Optical pulse dynamics in sub-wavelength nano-patterned silicon photonic wires

Spyros Lavdas

A dissertation submitted in partial fulfillment

of the requirements for the degree of

Doctor of Philosophy

of

University College London.

Electronic and Electrical Engineering

University College London

January 3, 2016

I, Spyros Lavdas, confirm that the work presented in this thesis is my own. Where information has been derived from other sources, I confirm that this has been indicated in the work.

Abstract

In this thesis, a comprehensive and rigorous theoretical model has been developed in order to study nonlinear optical pulse propagation in silicon nanowires and one-dimensional silicon photonic crystal waveguides. Our theoretical model includes all the linear and nonlinear effects, such as free-carrier dispersion, free-carrier absorption, self- and cross-phase modulation, cross-absorption modulation, and free-carrier generation that describe the pulse dynamics in such photonic waveguides. This work presents results pertaining to pulse reshaping and optical signal processing using optical nonlinearities of silicon photonic wires with subwavelength cross-section. We have considered different waveguide configurations, such as adiabatically tapered waveguides, long-period width-modulated Bragg waveguides, and photonic crystal waveguides. In particular, we have illustrated how optical nonlinearity and dispersion engineering of tapered photonic wires can be employed to generate optical similaritons and achieve more than 10 times pulse compression. We also discuss the properties of four-wave mixing pulsed amplification and frequency conversion efficiency in long-period Bragg waveguides and photonic crystal waveguides. In the latter case, a comparison between device performance in the slow- and fast-light regimes is also presented.

.

"Ω απέραντη νοσταλγία για κάτι που πότε δεν ζήσαμε
κι όμως αυτό υπήρξε όλη η ζωή μας ..."

Τ. Λειβαδίτης

Acknowledgements

Firstly, I would like to express my sincere gratitude to my supervisor Dr. Nicolae C. Panoiu for the continuous support of my Ph.D study and related research, for his patience, motivation, and immense knowledge. His guidance helped me in all the time of research and writing of this thesis. I will be indebted to him for the rest of my professional carreer.

Besides my supervisor, I would like to thank my second supervisor Benn Thomsen and Dr. Philip Watts for insightful comments and encouragement but also for the hard questions that I was asked during my transfer viva in order to widen and improve my research from various perspectives. I would also like to thank Dr. David Selviah for the time he spent in order to check that all the minor corrections, that I was asked to do after my viva examination, were carried out to a good level.

My sincere thanks also goes to the photonics group under the supervisor Prof. Richard Osgood of Columbia University in New York and Bio-nano company for our excellent cooperation and their constructive comments in many aspects of my current research.

I thank my fellow colleagues (Abiola Oladipo, Ahmed Al-Jarro, Jie You, Martin Weismann, Dan Timbrell, Wei Wu) for the stimulating discussions, for the sleepless nights we were working together before deadlines, and for all the fun we have had in the last years. Also last but not the least, I would like to thank my family: my parents and to my brother for supporting me spiritually throughout writing this thesis and my life in general.

Journal articles related to the PhD Thesis

1. S. Lavdas, J. B. Driscoll, H. Jiang, R. R. Grote, R. M. Osgood, and N. C. Panoiu, *"Generation of parabolic similaritons in tapered silicon photonic wires: comparison of pulse dynamics at telecom and mid-infrared wavelengths,"* Opt. Lett. **38**, 3953-3956 (2013).

2. S. Lavdas, J. B. Driscoll, R. R. Grote, R. M. Osgood, Jr., and N. C. Panoiu, *"Generation and collision of optical similaritons in dispersion engineered silicon photonic nanowires,"* Proc. of SPIE **8816**, San Diego (2013).

3. S. Lavdas, J. B. Driscoll, R. R. Grote, R. M. Osgood, and N. C. Panoiu, *"Pulse compression in adiabatically tapered silicon photonic wires,"* Opt. Express **22**, 6296-6312 (2014).

4. S. Lavdas, S. Zhao, J. B. Driscoll, R. R. Grote, R. M. Osgood, and N. C. Panoiu, *"Wavelength conversion and parametric amplification of optical pulses via quasi-phase-matched four-wave mixing in long-period Bragg silicon waveguides,"* Opt. Lett. **39**, 4017-4020 (2014).

5. S. Lavdas, J. B. Driscoll, R. R. Grote, R. M. Osgood, and N. C. Panoiu, *"Optical pulse amplification via four-wave-mixing in periodically modulated silicon photonic nanowires,"* Proc. of SPIE **9133**, Brussels (2014).

6. S. Lavdas and N. C. Panoiu, *"Theory of Pulsed Four-Wave-Mixing in One-dimensional Silicon Photonic Crystal Slab Waveguides,"* Phys. Rev. B (submitted).

7. S. Lavdas and N. C. Panoiu, *"Comparative analysis of four-wave mixing of optical pulses in slow and fast light regimes of a silicon photonic crystal waveguide,"* Opt. Lett. **40**, 4233–4236 (2015).

8. S. Lavdas, J. You, R. M. Osgood, and N. C. Panoiu, *"Optical pulse engineering and processing using optical nonlinearities of nanostructured waveguides made of silicon,"* Proc. SPIE **9546**, Active Photonic Materials VII, (2015).

Journal articles not directly related to the PhD Thesis

1. A. O. Oladipo, M. Kasper, S. Lavdas, G. Gramse, F. Kienberger, and N. C. Panoiu, *"Three-dimensional finite-element simulations of a scanning microwave microscope cantilever for imaging at the nanoscale,"* Appl. Phys. Lett. **103**, 213106 (2013).

2. A. O. Oladipo, M. Kasper, S. Lavdas, G. Gramse, F. Kienberger, and N. C. Panoiu, *"Analysis of a transmission mode scanning microwave microscope for subsurface imaging at the nanoscale,"* Appl. Phys. Lett. **105**, 133112 (2014).

3. J. You, S. Lavdas, and N. C. Panoiu, *"Comparison of BER in Multi-channel Systems With Stripe and Photonic Crystal Silicon Waveguides,"* IEEE J. Sel. Topics Quantum Electron. (submitted).

Conference papers related to the PhD Thesis

1. S. Lavdas, J. B. Driscoll, R. R. Grote, R. M. Osgood, Jr., and N. C. Panoiu, *"Soliton pulse compression in adiabatically tapered silicon photonic wires,"* SPIE Europe, Munich (2013).

2. S. Lavdas, J. B. Driscoll, R. R. Grote, R. M. Osgood, Jr., and N. C. Panoiu, *"Generation of parabolic optical pulses in dispersion-engineered silicon photonic nanowires,"* SPIE Optics+Photonics, San Diego (2013).

3. S. Lavdas, J. B. Driscoll, R. R. Grote, R. M. Osgood, and N. C. Panoiu, *"Quasi-phase-matched four-wave mixing of optical pulses in periodically modulated silicon photonic wires,"* SPIE Europe, Brussels (2014).

4. S. Lavdas and N. C. Panoiu, *"Quasi-phase-matched four-wave-mixing of optical pulses using silicon Bragg waveguides with normal or anomalous dispersion,"* Photon14, London (2014).

5. R. M. Osgood, X. Liu, S. Lavdas, J. Dadap, B. Souhan, J. Driscoll, R. Grote, B. Kuyken, G. Roelkens, N. C. Panoiu, R. Baets, and W. M. J. Green, *"Mid-IR Nonlinear Integrated Photonics: Physics and Devices,"* Summer Topicals Meeting Series (2014). (Invited)

6. S. Lavdas and N. C. Panoiu, *"Four-wave mixing of optical pulses in silicon photonic crystal waveguides: a comparison between the slow and fast light regimes,"* IEEE NANO 2015, Rome (2015).

7. N. C. Panoiu, S. Lavdas, and J. You, *"Optical pulse engineering using nonlinearities of nanostructured silicon photonic wires,"* 24th International Laser Physics Workshop (LPHYS'15), Shanghai (2015). (Invited) 8. N. C. Panoiu, S. Lavdas, J. You, and R. M. Osgood, *"Optical pulse engineering and processing using nonlinearities of tapered*

and photonic crystal waveguides made of silicon," Proc. SPIE **9546-70**, Active Photonic Materials VII, (2015).

Conference papers not directly related to the PhD Thesis

1. A. O. Oladipo, M. Kasper, S. Lavdas, G. Gramse, F. Kienberger, and N. C. Panoiu, *"Finite-element Simulations of a Volumetric Scanning Microwave Probe for Imaging at the Nanoscale,"* 7th International Congress on Advanced Electromagnetic Materials in Microwaves and Optics Metamaterials, Bordeaux (2013).

2. A. O. Oladipo, M. Kasper, S. Lavdas, G. Gramse, F. Kienberger, and N. C. Panoiu, *"Characterization of a Scanning Microwave Microscope using 3D finite element method,* Agilent Conference in Electrical Measurements, Cambridge (2014).

3. A. Oladipo, A. Lucibello, M. Kasper, S. Lavdas, G. M. Sardi, E. Proietti, F. Kienberger, M. Romolo, and N. C. Panoiu, *"Nanoscale Imaging of a Transmission Mode Scanning Microwave Microscope Investigated by a 3D Finite-element Method,"'* Piers, Guangzhou (2014).

4. A. O. Oladipo, A. Lucibello, M. Kasper, S. Lavdas, G. M. Sardi, E. Proietti, F. Kienberger, R. Marcelli, and N. C. Panoiu, *"Analysis of a transmission mode scanning microwave microscope for subsurface imaging at the nanoscale,"* Photon14, London (2014).

5. J. You, L. Spyros, and N. C. Panoiu, *"Bit error rate calculation in optical systems containing stripe and slow-light photonic crystal waveguides made of silicon,"* Asia Communications and Photonics Conference, Hong Kong (accepted) (2015).

LIST OF NOTATIONS AND ACRONYMS

c	speed of light in vacuum $(2.99792458 \times 10^8\ m/s)$
$\hbar$	reduced Planck constant $(1.05457162853 \times 10^{-34}\ kg/s)$
ε_0	electric permittivity of vacuum $(8.854 \times 10^{12} F/m)$
ε	electric permittivity
ε_r	relative electric permittivity $(\varepsilon/\varepsilon_0)$
Si	silicon
Si-PhNW	Silicon photonic nanowire
Si-PhCW	Silicon photonic crystal waveguide
β	propagation constant
α_{in}	intrinsic losses
α_{FC}	free-carrier losses
GV	group velocity
GVD	group-velocity dispersion
TOD	third-order dispersion
SPM	self phase modulation
TPA	two-photon absorption
XPM	cross-phase modulation
XAM	cross-phase absorption
FWM	four-wave mixing
FC	free carrier
FCD	free-carrier dispersion
FCA	free-carrier absorption
FCC	free-carrier chirp
SS	self-steepening
NLSE	nonlinear Schrödinger equation
SSF	split-step Fourier
FFT	fast-Fourier transformation
PWE	plain wave expansion
FWHM	full-width-half-maximum
CE	conversion efficiency
PhC	photonic crystal

LIST OF NOTATIONS AND ACRONYMS

CW	continuous wave
$\chi^{(1)}$	first-order nonlinear susceptibility
$\chi^{(2)}$	second-order nonlinear susceptibility
$\chi^{(3)}$	third-order nonlinear susceptibility
γ	effective nonlinear waveguide coefficient
Γ	effective nonlinear susceptibility
τ_s	characteristic response time of the nonlinearity
τ_c	recombination time of free-carriers
Δ	walk-off parameter
ε_I	similariton misfit parameter
Ψ	normalized pulse amplitude
Λ	grating period
A_{nl}	effective mode area
κ	overlap integral
Δw	width modulation

Contents

List of Figures

List of Tables

Chapter 1

Introduction

In recent years, the field of optics has attracted a great deal of attention due to a stringent need for solutions to challenges raised by chip-scale applications. Photonics is found to be an essential discipline tool for many technological areas, such as telecommunications systems, computer networks as well as biomedical science for healthcare purposes (e.g. diagnostic or therapeutic). It is for this reason that intensive research has been carried out over the last decade, focused originally on in-depth understanding of light propagation in different types of optical media and waveguiding devices and also on efficient fabrication techniques for sub-wavelength structures. Such structures can exploit efficiently the physical properties of light, giving rise to intriguing linear and nonlinear optical phenomena. One well established optical guiding structure is silica fibre, which has been studied and fabricated extensively since 1960s.

Optical fibres are widely used in fibre-optic communications chiefly because low propagating loss and are immune to electromagnetic interference. Despite the remarkable properties of optical fibres, there is a physical limitation for scaling fibres in photonic integrated circuits due to their large characteristic lengths. The latter limitation can be eliminated by employing silicon photonic nanowires (Si-PhNW), which can be easily fabricated due to the recent progress in CMOS technology. Such structures exhibit ultra-small waveguide cross-section leading to tight optical confinement. As a result, the linear and nonlinear properties of silicon nanowires are enhanced significantly thus having shorten characteristic lengths, in the range of a few millimeters. The enhanced optical nonlinearity of silicon also allows for optical propagation of low input power signals. Consequently, silicon nanowires offer an abundance of nonlinear optical effects that can be used to generate and process optical signals with low power

in low-cost ultracompact chips.

A higher degree of device functionality can be achieved by employing an one-dimensional (1D) silicon waveguide formed in a silicon photonic crystal (SiPhC). In particular, the photonic crystal consists of an hexagonal lattice of air holes in a silicon slab. The silicon waveguide is formed by filling one row of holes, which is also known as line defect-waveguide. Such type of waveguides shorten the characteristic linear and nonlinear lengths from a few millimetres to a few hundreds of microns. This comes from the fact that SiPhCs exhibit a much larger frequency dispersion and enhanced optical field confinement as compared to uniform waveguides. In addition, specific propagating modes can be localized into a band gap exhibiting interesting linear and nonlinear optical effects. One important linear effect is the strong dependence of the group velocity on the wavelength of the propagation signal. This physical phenomenon is responsible for the existence of slow and fast light regimes, which plays a critical role in novel applications such as optical interconnects on silicon chips, optical delay lines and optical buffers. These functionalities suggest that the bandwidth and the efficiency of on chip optical networks could be significantly improved in the near future.

Regarding the potential applications of silicon nanowires and photonic crystals, a large body of research has been carried out over the last decades. Very interesting and potentially useful nonlinear optical phenomena have emerged and been investigated, such as cross-phase modulation (XPM), self-phase modulation (SPM), four-wave mixing (FWM) and generation of optical solitons and similaritons. Equally important, nonlinear effects are induced by the generation of free carriers (FCs) through the TPA mechanism. These carriers can add linear absorption or cause a wavelength-dependent change in the index and implicitly in the phase of the propagating pulses. Such interaction will be shown to have a critical influence in specific nonlinear processes.

Most of the research on optical waveguides has been performed theoretically and experimentally in the context of silica optical fibres. It has also been suggested many optical schemes that could enhance the efficiency of these nonlinear processes. However, silica fibres exhibit some limitations, which are mainly related to the lack of flexible geometry and to their large linear and nonlinear characteristic lengths as it has been stated earlier. Although the research work on this field has revealed interesting nonlinear phenomena, there are still new important nonlinear dynamics that occur when

optical pulses propagate in media such as silicon nanowires and photonic crystals. Such nonlinear optical dynamics can inspire novel applications in the field of computer and communication systems and on-chip optical signal processing. The main characteristic of such applications would be their ultra-compact size being useful for chip to chip communications. The next section will present the main objectives that prompted the current research project.

1.1 Main objectives of the work

The objectives of this work can be divided into two main sets, which are related to the silicon photonic nanowires and silicon photonic crystal waveguides. Each set of objectives can also be separated in additional sections which are related to the development of numerical and semi-analytical theoretical models for a detailed investigation of nonlinear pulse dynamics. In this section, we will outline and briefly discuss the main objectives of our work.

To begin with, we will use a rigorous theoretical model, which describes the propagation of pulses in Si-PhNWs, and comprehensive numerical simulations to demonstrate that optical similaritons with parabolic shape can be generated in millimeter-long, dispersion engineered Si-PhNWs. In particular, we have used an exponential and a linear taper profile of silicon nanowire. In order to gain a better understanding of the underlying physics of similariton generation, we will present a comparative analysis of the pulse dynamics in two spectral domains relevant for technological applications, namely telecom ($\lambda = 1.55$ μm) and mid-IR ($\lambda = 2.2$ μm) spectral regions. A next step is to study and present the collision between such optical pulses.

Further to the previous objectives, we will analyze theoretically the compression of optical pulses upon propagation in tapered Si-PhNWs (hyperbolic tangent and linear taper profile), with a special focus on two compression methods: the soliton compression technique and pulse compression in Si-PhNWs whose group-velocity dispersion (GVD) coefficient β_2 changes sign during pulse propagation. While the first approach can be employed only at relatively large peak pulse power, namely in the soliton propagation regime, the latter one can be used to compress pulses whose power is below the soliton formation threshold as well. Our theoretical model rigorously describes the effects of the adiabatic variation of the cross-section of Si-PhNWs on the pulse dynamics

by fully accounting for the influence of this variation on the linear and nonlinear optical coefficients of the waveguide. For the sake of completeness, we consider the pulse dynamics at the optical communications wavelength, $\lambda = 1.55$ μm, and at mid-infrared wavelengths ($\lambda \gtrsim 2.1$ μm).

Besides the pulse compression in SiPhNW we will show that efficient quasi-phase matched (QPM) FWM of pulses can be achieved in Si-PNWs whose width varies periodically along the waveguide. To be more specific, we will focus on the QPM FWM of pulses that propagate in the normal dispersion regime, as in this case one cannot apply alternative phase matching methods based on nonlinearly induced phase-shifts.

The second set of the objectives is, essentially, an extension of the previous one. To this purpose we will introduce a rigorous theoretical model that describes FWM in SiPhCs. Our model will capture the influence on the FWM process of linear optical effects, including waveguide loss, FC dispersion (FCD) and FC absorption (FCA), nonlinear optical effects such as SPM, XPM, TPA, and cross-absorption modulation (XAM), as well as the mutual interaction between FCs and the optical field. We will also illustrate how our model can be applied to investigate the characteristics of FWM in the slow- and fast-light regimes, showing among other things that by incorporating the effects of FCs on the optical pulse dynamics new physics emerge. One noteworthy example in this context is that the well-known linear dependence of FCA on v_g^{-1} is replaced in the slow-light regime by a v_g^{-3} power-law dependence.

Based on our previous general theoretical model, we will present a study of FWM of optical pulses co-propagating in Si-PhCWs, highlighting the main differences between the scaling and strength of linear and nonlinear optical effects that influence the FWM in the slow- and fast-light regimes. Our theoretical analysis rigorously accounts for the explicit dependence of linear and nonlinear optical effects on GV and their implicit variation with the GV through the spatial profile of the optical modes, as well as the influence of these dispersive effects on FC dynamics.

It is worth mentioning that the common objective of the present research work, either when silicon nanowires or in SiPhC are considered to explore the influence of FC-generation on optical pulse dynamics. Note, here, that free carriers are not present in silica fibres. That means that there may be new interesting nonlinear properties based on FC-generation which have not been studied yet. In order to reveal the crucial role of

free carriers on pulse propagation different propagation scenarios will be investigated in frequency regimes where TPA and, consequently, FC-generation will have either dominant or negligible effects.

A more detailed summary of this work will be presented in the next section.

1.2 Outline

In Chapter 2, a general description of the properties of silicon photonic waveguides will be presented. Based on the optical properties of these devices, we describe the main concepts and ideas which will be used in further chapters. At the same time, a detailed review of the evolution of silicon photonics over the last decades is given through relevant references to the large body of published work.

Chapters 3 and 4 are focused on the generation of parabolic pulses (similariton generation) and their particle-like behaviour when they collide with each other, respectively. A theoretical model is also introduced, a model that, with small adjustments, is used throughout the following chapters. In particular, the model consists of a nonlinear Schrödinger equation, which describes all the linear and nonlinear optical pulse dynamics effects, is coupled to a rate equation which governs the free carrier dynamics. The dependence of similariton generation and collision on many pulse parameters have been investigated revealing the main physics.

In Chapter 5 the nonlinear process of optical pulse compression in dispersion engineered silicon nanowire is presented. An analytical model has also been developed in order to provide a deeper insight in the behaviour of several pulse parameters along the propagation distance. Different optical schemes of optical pulse compression are discussed in this chapter highlighting the effectiveness and flexibility of silicon nanowires.

The nonlinear process of quasi-phase matched FWM in a periodically width modulated silicon nanowire (Bragg nanowire) is presented in Chapter 6. A comparative analysis of the efficiency of FWM between a uniform and a Bragg silicon nanowire is demonstrated in this chapter. We demonstrate that by properly designing the optical waveguide such that the interacting pulses copropagate with the same group velocity, a conversion efficiency enhancement of more than 15 dB, as compared to a uniform waveguide, can readily be achieved. We also analyze the dependence of the conversion efficiency and FWM gain on the pulse width, time delay, walk-off parameter, and grat-

ing modulation depth.

Chapter 7 describes a very general theoretical model for interacting optical pulses in silicon photonic crystals. This rigorous model includes all relevant linear and nonlinear optical effects and their dependence on the group-velocity, as well as the influence of free-carriers on pulse dynamics. Based on this model an in-depth study of four-wave mixing of optical pulses in silicon photonic crystal waveguides is presented in every detail in Chapter 8. In particular, the key differences between FWM in the slow- and fast-light regimes and how they are related to the physical parameters of the pulses and waveguide are presented. Finally, we illustrate how these results can be used to design waveguides with optimized FWM conversion efficiency.

Finally, the main conclusions and the contributions of this work to the field of silicon photonics are outlined in Chapter 9. The future prospects of the current project are also presented in this concluding chapter.

Chapter 2

Background

2.1 Introduction

A series of important optical effects occur when light propagates into silicon nanowires or silicon photonic crystal waveguides due to the specific optical properties of silicon. Silicon presents a band gap near 1.12 eV, which makes it nearly transparent in a spectral region extending from 1.2 μm to mid-infrared (mid-IR) regime ($\lambda \geq 2$ μm) [2. 1–3]. Silicon waveguides also exhibit ultra-small cross section, of about $0.1\mu m^2$, which leads to a tight confinement of light and consequently strong nonlinear optical phenomena, such as TPA, SPM, third-order dispersion (TOD), and self-steepening (SS). Such nonlinear phenomena provide new functionalities in many applications pertaining to silicon photonics [2. 4–24]. Moreover, recent advances in fabrication techniques combined with the excellent electrical properties of silicon have enabled the demonstration of ultra compact passive and active silicon photonic components with very low optical losses. Such type of silicon components can be employed to computer and communication systems increasing the bandwidth in servers and racks, the improvement of data transfer speeds and reduced of datacentre complexity. In order for this potential to be fulfilled, many researchers have been working on silicon technology since mid of 1980s.

Silicon photonics has started to emerge as a field of research in 1980s with the pioneering work of Soref [2. 25, 26]. However, many problems emerged, such as high propagation and coupling losses. At that time it was not clear whether the losses are induced by surface scattering or by some other mechanisms. In addition, researchers were mainly concerned to scale down the device size and power consumption of de-

vices as well as to increase their characteristic response time. This would allow silicon photonics to be fully integrated with silicon electronics. However, in order to achieve a seamless integration, losses had to be reduced drastically. Initially, the losses were reduced to 3 dB/cm [2. 27, 28] then further to 0.026 dB/ cm [2. 29–32]. The fabrication of tapered silicon waveguides also largely eliminated the coupling losses [2. 33, 34]. The dramatic increase in research in silicon photonics was facilitated by the use of CMOS manufacturing [2. 35]. The CMOS technology reduced drastically the propagation losses, which were mainly caused by sidewall roughness of silicon nanowires. In addition, many interesting effects have been studied and demonstrated experimentally, such as spontaneous Raman emission [2. 36, 37], Raman amplification [2. 38–44], four-wave mixing [2. 45–49], SPM [2. 50–53], XPM and cross absorption modulation (XAM) [2. 54, 55], TPA [2. 13, 18], supercontinuum generation [2. 56]. These nonlinear effects can be employed in a wide range of applications in the field of optics.

In order to gain a deeper understanding of how linear and nonlinear optical effects determine the light propagation in silicon nanowires and silicon photonic crystals we will present in what follows the mathematical set of equations that govern the pulse propagation in these waveguiding devices.

2.2 Fundamental theoretical model

In order to gain a complete understanding of the rich linear and nonlinear optical properties of silicon nanowires and photonic crystals, it is necessary to describe the optical pulse and free carrier dynamics as the pulse propagates along the waveguide. Thus, we will present a detailed description of our theoretical model in this section. One should note here that although the propagation equations are similar to those of standard fibre optics, there are key differences [2. 57]. One major difference is that silicon requires its nonlinear optical susceptibilities to be treated as tensors and not as scalar variables that are used to describe isotropic glass fibres. Besides this difference, the strong optical confinement and the dependence of nonlinear pulse parameters on the wavelength requires a different mathematical approach to the pulse dynamics.

Before deriving the system of equations that governs the dynamics of optical pulses in silicon devices it is worth to mention that there is a similar approach to study optical pulse propagation in silicon nanowires and silicon photonic crystals. The main

difference arises from the fact that the propagating electromagnetic mode of silicon nanowire is determined by the cross section of the guiding device whereas the periodicity of the silicon photonic crystal slab waveguide plays a crucial role in the evolution of the electromagnetic field. Keeping in mind this difference, we will present briefly the theoretical approach for deriving the differential equations describing the optical pulse propagation in silicon nanowires. This differential equation, which holds for both cases, is the well-known perturbed nonlinear Schrödinger equation.

The description of optical pulse propagation in silicon wires and photonic crystals begins from the Maxwell equations, which in the frequency domain are:

$$\vec{\nabla} \times \vec{E}(\vec{r},\omega) = i\omega\mu\vec{H}(\vec{r},\omega) \tag{2.1a}$$

$$\vec{\nabla} \times \vec{H}(\vec{r},\omega) = -i\omega\varepsilon_c(\vec{r},\omega)\vec{E}(\vec{r},\omega) - i\omega\vec{P}_{pert}(\vec{r},\omega), \tag{2.1b}$$

where $\vec{E}(\vec{r},\omega)$ and $\vec{H}(\vec{r},\omega)$ are the electric and magnetic field of the propagating mode, respectively and ω is the frequency of the propagating mode. Regarding the total polarization of the mode $\vec{P}_{pert}$ it consists of two components, namely the linear and nonlinear part. The general expression that describes the polarization of the mode can be written as:

$$\begin{aligned}\vec{P} = \vec{P}_{linear} + \vec{P}_{nonlinear} = \varepsilon_0\chi^{(1)} \cdot \vec{E}(\vec{r},\omega) + \varepsilon_0\chi^{(2)} : \vec{E}(\vec{r},\omega)\vec{E}(\vec{r},\omega) \\ + \varepsilon_0\chi^{(3)} \vdots \vec{E}(\vec{r},\omega)\vec{E}(\vec{r},\omega)\vec{E}(\vec{r},\omega) + ...,\end{aligned} \tag{2.2}$$

where : and $\vdots$ indicates the dot product between two- and three- order tensors. Because the Si-crystal is invariant to an inversion symmetry transformation, as it belongs to the point group symmetry $m3m$, the second order susceptibility vanishes within the dipole approximation; that is, $\chi^{(2)} \equiv 0$. According to this, the linear and nonlinear part of the polarization of the mode is described by the following:

$$\vec{P}_{linear} = \varepsilon_0\chi^{(1)} \cdot \vec{E}(\vec{r},\omega) \tag{2.3a}$$

$$\vec{P}_{nonlinear} = \varepsilon_0 \chi^{(3)} \vdots \vec{E}(\vec{r},\omega)\vec{E}(\vec{r},\omega)\vec{E}(\vec{r},\omega) \tag{2.3b}$$

Equation-(2.2) can have a similar formulation regarding the physical effects that each part of the polarization describes. To this end, the linear and nonlinear part of the polarization is expressed as:

$$\vec{P}_{pert} = \vec{P}_{linear} + \vec{P}_{nonlinear} = \delta\varepsilon_{FC}\vec{E}(\vec{r},\omega) + \delta\vec{P}_{Kerr}(\vec{r},\omega), \tag{2.4}$$

where the linear contribution is described by:

$$\delta\varepsilon_{FC} = \frac{i\varepsilon_0 cn\alpha_{in}}{\omega} + 2\varepsilon_0 n\delta n_{FC} + \frac{i\varepsilon_0 cn\alpha_{FC}}{\omega}, \tag{2.5}$$

where δn_{FC} is the free-carrier-induced change in the refractive index, α_{FC} is the FCA coefficient and the nonlinear contribution in frequency domain reads

$$\vec{P}_{Kerr}(\omega) = \frac{3}{4}\varepsilon_0 \chi^{(3)}(\omega;\omega,-\omega,\omega) \vdots \vec{E}(\omega)\vec{E}^*(\omega)\vec{E}(\omega), \tag{2.6}$$

where $\chi^{(3)}(\omega;\omega,-\omega,\omega)$ is the third-order susceptibility tensor of silicon. Moreover, ε_0 is the vacuum permittivity and α_{in} is the intrinsic loss coefficient, determined both by the material losses and the optical field scattering at the silicon/silicon-oxide interfaces. Note here that we consider that the sum-frequencies processes are not phase matched, and thus their contribution to nonlinear polarization can be neglected. The phase-matched contribution will be presented extensively in Chapter 6. The coefficients δn_{FC}, $\delta\alpha_{FC}$ are described by [2. 25]:

$$\delta n_{FC} = -\frac{e^2}{2\varepsilon_0 n\omega^2}\left(\frac{N}{m^*_{ce}} + \frac{N^{0.8}}{m^*_{ch}}\right), \tag{2.7}$$

$$\alpha_{FC} = \frac{e^3 N}{\varepsilon_0 cn\omega^2}\left(\frac{1}{\mu_e m^*_{ce}} + \frac{1}{\mu_h m^{*2}_{ch}}\right), \tag{2.8}$$

where N is the carrier density, $m^*_{ce} = 0.26m_0$ and $m^*_{ch} = 0.39m_0$ are the effective masses of the electron and the hole, respectively, with m_0 as the mass of the electron, and $\mu_e(\mu_h)$ is the electron (hole) mobility.

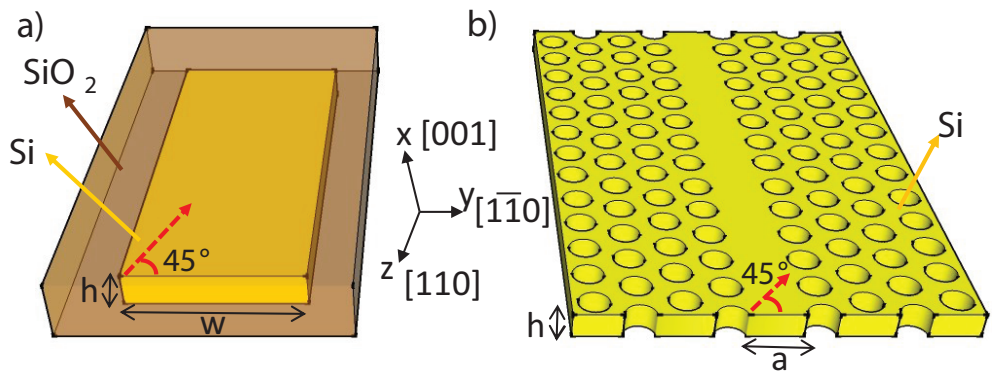

Figure 2.1: a) Sketch of silicon photonic nanowire burried in SiO_2 and b) geometry of silicon photonic crystal slab waveguide.

Equations (2.1)-(2.8) should take into account the properties of the physical geometry of our problem as shown in Fig. 2.1. Figure 2.1(a) shows a rectangular silicon core oriented along the $[1\bar{1}0]$ direction and burried into a SiO_2 substrate. The dimensions (h-height of the Si-PhNW and Si-PhCW, w-width of the silicon core) are in submicron region. From a physical point of view, the waveguide can be divided in an unperturbed and perturbed part. The perturbed part is determined by the polarization induced in the silicon core. Based on this physical assumption, we continue our analysis by using the reciprocity theorem:

$$\frac{\partial}{\partial z}\int_{A_\infty}\vec{F}_c\cdot\hat{e}_z dA=\int_{A_\infty}\vec{\nabla}\cdot\vec{F}_c dA, \tag{2.9}$$

where $\vec{F}_c$ is the following vector function:

$$\vec{F}_c=\vec{E}_1^*\times\vec{H}_2+\vec{E}_2\times\vec{H}_1^*, \tag{2.10}$$

where * denotes complex conjugate and $(\vec{E}_1,\vec{H}_1)\equiv(\vec{E}_0,\vec{H}_0)$ are the electromagnetic fields in the unperturbed waveguide while $(\vec{E}_2,\vec{H}_2)\equiv(\vec{E},\vec{H})$ corresponds to the perturbed waveguide. Accordingly, the fields $\vec{E}$ and $\vec{H}$ are guiding modes, which have been affected not only by nonlinear effects, such as Kerr effect or TPA, but also by the change of the dielectric constant induced by linear losses and generation of free carriers. Solving the source-free Maxwell equations (Eq. 2.1) for a fixed wavelength (λ) and including in Eq. (2.10), we deduce that:

$$\vec{\nabla}\cdot\vec{F}_c=i\frac{2\pi c}{\lambda}\left(n^2-n^{*2}\right)\varepsilon_0\vec{E}_0\cdot\vec{E}^*, \tag{2.11}$$

where c is the speed of light and the refractive index is $n = \sqrt{\varepsilon}$. In this way, Eq. (2.9) becomes as,

$$\frac{\partial}{\partial z}\int_{A_\infty}\left(\vec{E}_0^* \times \vec{H} + \vec{E} \times \vec{H}_0^*\right) dA = i\omega \int_{A_\infty} \vec{P}_{pert}\vec{E}_0 dA. \tag{2.12}$$

As a next step, we define the electromagnetic fields for the unperturbed waveguide as:

$$\vec{E}_0 = \frac{1}{2}\sqrt{\frac{Z_0 P_0}{A_0}}\vec{e}(\vec{r}_t, \omega_0)e^{i(\beta_0 z - \omega_0 t)}, \tag{2.13}$$

$$\vec{H}_0 = \frac{1}{2}\sqrt{\frac{P_0}{Z_0 A_0}}\vec{h}(\vec{r}_t, \omega_0)e^{i(\beta_0 z - \omega_0 t)}, \tag{2.14}$$

where $Z_0 = \sqrt{\mu_0/\varepsilon_0}$ as the free-space impedance and $\vec{e}(r_t)$, $\vec{h}(r_t)$ correspond to cross-sectional components of the electromagnetic field. The waveguide modes $\vec{e}$ and $\vec{h}$ are also normalized according to the following formula:

$$\frac{1}{4A_0}\int_\infty \left(\vec{e} \times \vec{h}^* + \vec{e}^* \times \vec{h}\right) \cdot \hat{e}_z dA = 1. \tag{2.15}$$

This normalization ensures the total power of the electric field of the unperturbed waveguide to be P_0. In addition, we define a slowly varying normalized complex envelope $u(z,\omega)$, such that in the time domain, its input peak amplitude is equal to 1. Accordingly, the total energy of the electromagnetic field $\vec{E}$, $\vec{H}$ of the perturbed waveguide is $P_0|u(z,\omega)|^2$. Using these definitions the fields $\vec{E}$ and $\vec{H}$ are written as:

$$\vec{E} = \frac{1}{2}\sqrt{\frac{Z_0 P_0}{A_0}}u(z,\omega)\vec{e}(\vec{r}_t, \omega)e^{i(\beta z - \omega t)}, \tag{2.16}$$

$$\vec{H} = \frac{1}{2}\sqrt{\frac{P_0}{Z_0 A_0}}u(z,\omega)\vec{h}(\vec{r}_t, \omega)e^{i(\beta z - \omega t)}. \tag{2.17}$$

As a next step we insert Eqs. (2.13), (2.14), (2.16), (2.17) into Eq. (2.12) and by taking into account the normalization expression of Eq. (2.15), we derive the following formula:

$$\frac{\partial u(z,\omega)}{\partial z} = B(z,\omega)u(z,\omega) + \frac{i\omega}{4P_0}\int_S \vec{e}^*(r_t,\omega)\cdot\vec{P}_{\text{pert}}(\mathbf{r},\omega)dS \tag{2.18}$$

where

$$B(z,\omega) = \frac{i}{4P_0}\int_S \left[\mu_0(\omega-\omega_0)|\vec{h}(r_t,\omega)|^2 + (\omega\bar{\varepsilon}_c(r,\omega)-\varepsilon_c\omega_0)|\vec{e}(r_t,\omega)|^2\right] dS. \quad (2.19a)$$

Here, $\bar{\varepsilon}_c(r,\omega)$ is the dielectric constant of the waveguide. The final step is to expand Eq. (2.19a) in Taylor series around ω_0. According to Taylor expansion Eq. 2.19a becomes:

$$B(z,\omega) \equiv \sum_{n\geq 1} \frac{i\beta_n}{n!}(\Delta\omega)^n \quad (2.20)$$

where

$$\beta_1(z) = \frac{\delta(z)}{v_g}, \quad (2.21a)$$

$$\beta_n(z) = \delta(z)\frac{\partial^{n-1}}{\partial\omega^{n-1}}\left(\frac{1}{v_g}\right),\ n\geq 2. \quad (2.21b)$$

Here, $\Delta\omega = \omega-\omega_0$ and the average of $\delta(z)$ over the propagation distance is equal to one. By taking into account Eqs (2.19), (2.21) and (2.4) we can take the Fourier transform of Eq. (2.18) deriving the following partial differential equation for the normalized amplitude $u(z,t)$ known as perturbed nonlinear Schrödinger equation (NLSE):

$$i\left(\frac{\partial u}{\partial z}+\frac{1}{v_g}\frac{\partial u}{\partial t}\right) - \frac{\beta_2}{2}\frac{\partial^2 u}{\partial t^2} - i\frac{\beta_3}{6}\frac{\partial^3 u}{\partial t^3} = -\frac{ic\kappa}{2nv_g}(\alpha_{in}+\alpha_{FC})u - \frac{\omega\kappa}{nv_g}\delta n_{FC}u - \gamma|u|^2u, \quad (2.22)$$

where the parameters $\beta_1 = 1/v_g$ (v_g is the group velocity of the mode), β_2 is the group velocity dispersion coefficient, β_3 is the third order coefficient (TOD) parameter, β_n are the higher order dispersion coefficients, which are defined in Eq. (2.21). One should note here that the propagation constant $\beta(\omega)$ can be expanded in a Taylor series around the carrier/pump frequency ω_0 as:

$$\beta(\omega) = \beta_0 + (\omega-\omega_p)\beta_1 + \frac{1}{2}(\omega-\omega_p)^2\beta_2 + \frac{1}{6}(\omega-\omega_p)^3\beta_3 + \frac{1}{24}(\omega-\omega_p)^4\beta_4 + .. \quad (2.23)$$

Otherwise, the Taylor series need higher-order terms in order to accurately describe the

propagation constant. For the current project we keep up to the fourth order term (β_4).

Moreover, the parameters κ and γ are the overlap integral between the guiding devices and the spatial field of the propagating mode and the effective nonlinearity, respectively. At this point, we should stress that there is an essential difference in calculating the latter nonlinear parameters in case of silicon nanowires and silicon photonic crystals. To be more specific, the nonlinear properties of a silicon nanowire are determined by its cross section, whereas the nonlinear properties of a silicon photonic crystal are strongly dependent on the period of the unit cell as it is clearly seen from the following equations [2. 58, 59]:

$$k_{nw} = \frac{n^2 \int_{A_0} |e(r_t)|^2 dA}{\int_{A_\infty} n^2(r_t)|e(r_t)|^2 dA}, \tag{2.24a}$$

$$k_{pc} = \frac{an^2 \int_{A_0} |e(r)|^2 dA}{\int_{V_{cell}} n^2(r)|e(r)|^2 dV}, \tag{2.24b}$$

and

$$\gamma_{nw} = \frac{3\omega\Gamma}{4\varepsilon_0 A_0 v_g^2} \tag{2.25a}$$

$$\gamma_{pc} = \frac{3\omega\Gamma}{4\varepsilon_0 a^2 v_g^2}. \tag{2.25b}$$

where a is the period of the photonic crystal as it is shown in Fig. 2.1(b) and the subscripts nw and pc denotes nanowire and photonic crystal respectively. The effective nonlinear susceptibility Γ for silicon nanowire or photonic crystals is described by the following formula:

$$\Gamma_{nw} = \frac{A_0 \int_{A_0} e^*(r_t;\omega) x^{(3)}(r_t;-\omega,\omega,-\omega,\omega) \vdots e(r_t;\omega) e^*(r_t;\omega) e(r_t;\omega) dA}{\left(\int_{A_\infty} n^2(r_t)|e(r_t,\omega)|^2 dA\right)^2}, \tag{2.26a}$$

$$\Gamma_{pc} = \frac{a^4 \int_{A_0} e^*(r_t;\omega) x^{(3)}(r_t;-\omega,\omega,-\omega,\omega) \vdots e(r_t;\omega) e^*(r_t;\omega) e(r_t;\omega) dA}{\left(\int_{V_{cell}} n^2(r)|e(r,\omega)|^2 dV\right)^2}. \tag{2.26b}$$

Equally important is to emphasize some of the assumptions on which Eq. (2.22)

is based. Thus, we have assumed that the variation of the dielectric constant (refractive index) is small enough to consider that the propagating electromagnetic modes in perturbed and unperturbed waveguide are the same. Moreover, by making the slowly varying envelope approximation for $u(z,t)$ and assuming small perturbations, the optical field propagates without experiencing backward reflections.

Moreover, we also have used the relation $P_0 = v_g W_t$ in order to derive Eq. (2.22). The parameter W_t is the mode energy defined separately for silicon nanowire and silicon photonic crystal slab waveguide as:

$$W_{t,nw} = \frac{1}{2}\int_{A_\infty} \varepsilon_0 n^2(r_t)|\vec{e}(r_t)|^2 dA. \tag{2.27}$$

Note that in order to derive Eq. (2.27) we have used the fact that the mode has equal amounts of electric and magnetic energy. A detailed expression of the mode energy for silicon photonic crystal slab waveguides will be provided in Chapter 7.

The last step of the derivation of the theoretical model is to formulate the rate equation, which describes the free carrier dynamics in silicon waveguides. This rate equation will be coupled to the nonlinear Schrödinger equation Eq. (2.22). The derivation of the free carrier generation starts from Eq. (2.22), the final result being:

$$\frac{\partial N_{nw}}{\partial t} = -\frac{N}{t_c} + \frac{3{\beta_1}^2 \Gamma''}{4\varepsilon_0 \hbar A_0^2}|u|^4, \tag{2.28}$$

where t_c is the characteristic lifetime of free carriers and $\hbar$ is the reduced Planck constant.

It should be emphasized that the temporal variation of free carriers density is dependent on the imaginary part Γ'' as it is expected, on t_c as well as on the square power of the propagating mode. One should note that only a fraction of the power of the electromagnetic mode contributes to the generation of free carriers as the mode profile only partially overlaps with the silicon waveguide. The characteristic lifetime, for silicon nanowires commonly used for photonic applications, varies from sub-nanosecond to tens of nanoseconds, while for silicon photonic crystal slab waveguides is in the range of few hundred of picoseconds.

It is worth mentioning that the effective nonlinear susceptibility described by Γ,

Eq. 2.26, accounts not only for the free-carrier generation but also for all nonlinear phenomena that occur along the waveguide. Therefore, we will present briefly in the next section how this susceptibility is calculated.

2.3 Nonlinear response of crystalline silicon

The nonlinear optical response of crystalline silicon is strongly dependent on the electric polarization, $\vec{P}(r,t)$ in the medium. In order to gain a deeper insight into this matter, we use power series for the electric field as follows:

$$\vec{P} = \vec{D} - \varepsilon\vec{E} = \varepsilon_0(\chi^{(1)} \cdot \vec{E} + \chi^{(2)} : \vec{E}\vec{E} + \chi^{(3)} \vdots \vec{E}\vec{E}\vec{E} + ...), \tag{2.29}$$

where $\vec{D}$ is the electric displacement field and $\chi^{(i)}$ is the ith-order optical susceptibility. The optical susceptibilities $\chi^{(i)}$ depend on the structure of the crystal. In particular for silica fibres the $\chi^{(i)}$ are represented as scalar variables whereas for silicon crystals as an (i+1)th-rank tensors. It is worth mentioning that the crystalline silicon lattice is invariant to an inversion symmetry transformation, as it belongs to the point group symmetry m3m, so that the second-order susceptibility $\chi^{(2)} = 0$.

The tensor $\chi^{(3)}$ has 21 nonzero elements, of which only 4 are independent, namely, $\chi^{(3)}_{1111}$, $\chi^{(3)}_{1122}$, $\chi^{(3)}_{1212}$, and $\chi^{(3)}_{1221}$. Additional symmetry properties lead to $\chi^{(3)}_{1122} = \chi^{(3)}_{1221}$. Kleimann symmetry relations also imply that $\chi^{(3)}_{1122} = \chi^{(3)}_{1212}$. Consequently, the parameters $\chi^{(3)}_{1111}$ and $\chi^{(3)}_{1122}$ are the remaining independent components of the susceptibility tensor. These nonlinear components of the susceptibility have been measured recent experiments across a broad range of wavelengths, between 1.2 and 2.4 μm [2. 60]–[2. 61]. These experiments suggest that the ratio of these two components is constant, that is, $\chi^{(3)}_{1111}$=2.36$\chi^{(3)}_{1122}$. One should note that the frequency dispersion of $\chi^{(3)}$ has been incorporated in the calculations of the nonlinear waveguide parameters used in this work at Columbia University.

Note, that in all of our work we have calculated the effective susceptibility $\chi^{(3)}_{eff}$ defined by:

$$\begin{aligned}\chi^{(3)}_{eff} =& \chi^{(3)}_{1122}[(\hat{a}^* \cdot \hat{b})(\hat{c} \cdot \hat{d}) + (\hat{a}^* \cdot \hat{c})(\hat{b} \cdot \hat{d}) + (\hat{a}^* \cdot \hat{d})(\hat{b} \cdot \hat{c})] \\ &+ (\chi^{(3)}_{1111} - \chi^{(3)}_{1122}) \sum_{i=1}^{3} \hat{a}^*_i \hat{b}_i \hat{c}_i \hat{d}_i\end{aligned} \tag{2.30}$$

Here $\hat{a}$ is a unit vector along the direction of the induced polarization, $\hat{b}$, $\hat{c}$, and $\hat{d}$ are unit vectors along the polarization direction of the interacting fields, and $\hat{a}_i$, $\hat{b}_i$, $\hat{c}_i$, and $\hat{d}_i$ are the direction cosines of these unit vectors.

Before we continue with the study of the linear and nonlinear dispersive properties of silicon nanowires and photonic crystal waveguides we mention that the linear and nonlinear pulse dynamics are strongly dependent on the initial shape of the propagating optical pulses. Consequently, the different pulse envelopes that have been used in this project, namely Gaussian, super-Gaussian, and hyperbolic secant pulses, are described in detail in the following section.

2.4 Definition of Gaussian, super-Gaussian and hyperbolic secant pulses

The majority of the commercial lasers emit pulses that can be approximated by a Gaussian profile. However, there are specific lightwave systems that use as bits hyperbolic secant or super-Gaussian shapes. To this end, we have taken into account all of these pulse profiles in our work thus being able to study the dependence on the input pulse shape of the pulse dynamics. These pulse shapes are defined as:

$$u_G(t,z=0) = \sqrt{\frac{E}{\sqrt{\pi}\tau}} e^{-i\Omega(t-T)-(1+iC)\frac{(t-T)^2}{2\tau^2}}, \tag{2.31}$$

$$u_{SG}(t,z=0) = \sqrt{\frac{E}{\sqrt{\pi}\tau}} e^{-i\Omega(t-T)-(1+iC)\frac{(t-T)^4}{2\tau^4}}, \tag{2.32}$$

$$u_s(t,z=0) = \sqrt{\frac{E}{2\tau}} \mathrm{sech}\left(\frac{t-T}{\tau}\right) e^{-i\Omega(t-T)-iC\frac{(t-T)^2}{2\tau^2}}, \tag{2.33}$$

where E, τ, C, Ω, and T are the pulse energy, pulse width, chirp coefficient, shift of the pulse carrier frequency, and temporal shift of the pulse, respectively. The pulse width τ and its full-width at half-maximum, T_{FWHM}, are related by $T_{\mathrm{FWHM}} = 1.665\tau$, $T_{\mathrm{FWHM}} = 1.824\tau$ and $T_{\mathrm{FWHM}} = 1.763\tau$ for Gaussian u_G, super-Gaussian u_{SG} and hyperbolic secant u_s pulses, respectively.

Note, that Eqs. (2.31)-(2.33) describe the pulse profile only at the input of silicon Si-PhNW/SiPhCW but not along the waveguides. Most of the times, the propagating

pulse does not preserve its shape due to the influence of linear and nonlinear effects. However, Eqs. (2.31)-(2.33) provide qualitative information about the variation of specific features of the pulse, such as its energy E and pulse width τ. In addition, a more in-depth analysis of linear and nonlinear pulse dynamics can be conducted through the mathematical expression of the pulse envelope as each linear and nonlinear phenomena affect specific pulse parameters. It is for this reason that a comprehensive semi-analytic method that describes these effects has been developed in this thesis and it will be presented in Chapter 5.

The next section is focused on which and to what extent each of the linear and nonlinear parameters of Eq. (2.22) affect the pulse shape along the propagation distance.

2.5 Dispersive properties of silicon waveguides

As it has already been mentioned silicon nanowires and silicon slab waveguides are characterized by their submicrometer cross-section and high-index contrast, which leads to strong optical confinement and waveguide dispersion. Therefore, great care needs to be taken during the design and fabrication of silicon waveguides. Moreover, the waveguide dispersion is derived from the propagation constant, $\beta(\omega)$, which is strongly dependent on the specific waveguide geometry. Note also that each coefficient of the Taylor series expansion of Eq. (2.23) has a different and a unique influence on the pulse evolution along the waveguide.

To be more specific, the first order parameter β_1 determines the group velocity. In particular, β_1 plays a crucial role on the interaction between optical pulses that co-propagate in an optical medium. The significance of β_1 is revealed by the analysis of nonlinear phenomena, such as FWM or similariton collision, which will be described in the Chapters 3 and 4, respectively.

The most important dispersion coefficient is β_2, which represents frequency dispersion of the group velocity and is responsible for the variation of the pulse width. In order to quantify the effect of GVD, a dispersion parameter D is defined as follows:

$$D = \frac{d\beta_1}{d\lambda} = -\frac{2\pi c}{\lambda^2}\beta_2. \tag{2.34}$$

The coefficients β_3 and β_4 are known as third and fourth order dispersion coefficients, respectively. Their effects are negligible for pulse widths of picoseconds and larger. Third order dispersion (TOD) coefficient is more important in the case of ultra short pulses while β_4 plays a crucial role in many parametric processes in optics, such as FWM.

The effects of GVD and TOD are presented in the subsections 2.5.1 and 2.5.2, respectively. However, we will not provide a comprehensive description of dispersive effects but only a brief qualitative presentation of the dispersive effects induced by GVD and TOD. More specifically, the fundamental phenomena induced by GVD and TOD properties are qualitatively the same for silica fibres, nanowires and photonic crystal slab waveguides. However, the extension to which the effects contribute to the pulse reshaping is significantly different in each of these cases. In particular, as the study of optical pulse propagation shifts from silica fibres to silicon nanowires and then to silicon photonic crystal slab waveguides the dispersive characteristic lengths are significantly reduced due to the increase of the optical pulse confinement. This means that all the linear dispersive effects are enhanced in the case of silicon nanowires and slab photonic crystal waveguides as compared to the case of silica fibres.

2.5.1 Group velocity dispersion effects

Group-velocity dispersion is the dependence of the group velocity of light propagating in a transparent medium on the optical frequency (or wavelength). Specifically, the phase of an optical pulse changes differently for each frequency component as the pulse propagates in the waveguide. Furthermore, there are cases where the phase also depends on whether the pulse experiences normal or anomalous dispersion. To be more specific, when a pulse is unchirped ($C = 0$), the phase is affected by the same amount for a pulse propagation in normal or anomalous dispersion regime. However, in the case of a chirped pulse ($C \neq 0$), the sign of β_2 has an important influence on the evolution of the pulse shape. Many qualitative features arise from the dependence of GVD on the particular nature of dispersion, such as pulse compression or generation of parabolic pulses.

The effects of GVD are strongly dependent on the propagation distance of the pulse. A dispersion length, L_D, is defined, in order to provide a length scale over which

dispersive effects become important as far as the pulse evolution is concerned:

$$L_D = \frac{\tau^2}{|\beta_2|}. \tag{2.35}$$

When the propagation distance is much shorter than the dispersion length ($L \ll L_D$) GVD plays no significant role during pulse propagation. However, the opposite occurs when the length of the silicon nanowire is such that $L_D \ll L$. In addition, ultrashort pulses in the femotsecond regime broaden much more than in picosecond regime because of a smaller dispersion length as Eq. (2.35) suggests. For instance, let us assume two pulses with the same value of β_2=1.11 ps^2 m^{-1} and different pulse widths τ_1=200 fs and τ_2=2 ps have L_{D1}=3.6 cm, and L_{D2}=3.6 m, respectively. An interesting question is raised regarding to which extent GVD affects the pulse propagation. The answer depends on the profile of the propagating pulse. For an initially unchirped pulse profile, GVD broadens the pulse during propagation. Pulse broadening can be understood better by taking into account that different frequency components of a pulse travel with different speeds through the silicon nanowire. For instance, red components (low frequency components) travel faster than blue components (high frequency

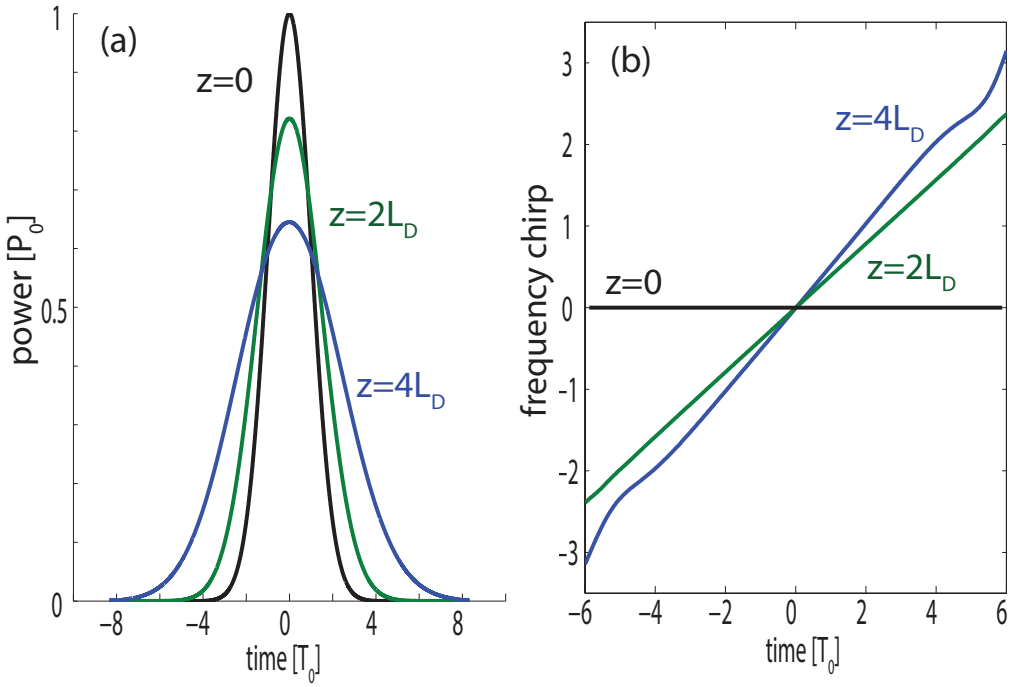

Figure 2.2: a) Pulse intensity and b) chirp as functions of normalized time for a Gaussian pulse at $z = 2L_D$ and $z = 4L_D$ propagating in the normal dispersion regime.

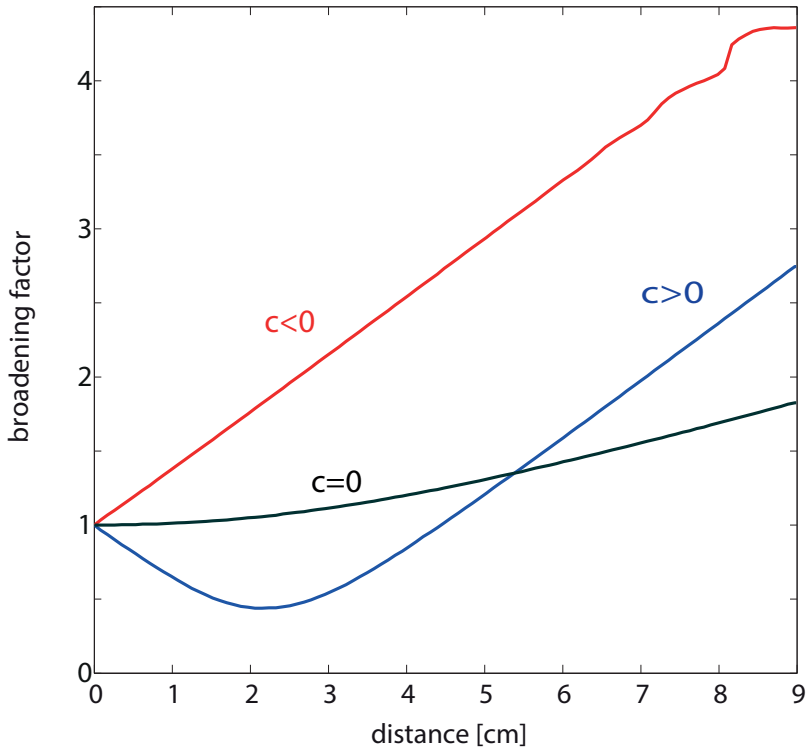

Figure 2.3: Broadening factor as a function of distance propagating at anomalous dispersion regime.

components) for $\beta_2 > 0$ while the opposite happens for $\beta_2 < 0$. Therefore, the pulse will not maintain its shape when all the spectral components do not arrive at the same time. In any other case, an unchirped pulse will broaden. One should note that GVD produces a linear chirp across the pulse even though the initial pulse was unchirped. The dispersion induced pulse broadening for an unchirped Gaussian pulse as well its dispersion induced linear chirp are shown in Fig. 2.2.

Figure 2.2 shows that the dispersion-induced linear chirp switches from positive to negative values. This feature plays a crucial role on pulse evolution in case of initially chirped pulses. More specifically, chirped pulses may broaden or compress depending on whether β_2 or C have the same or opposite signs. A chirped pulse broadens at a faster rate than that of an unchirped pulse when $\beta_2 C > 0$. On the other hand, a chirped pulse can be compressed for a certain propagation distance if $\beta_2 C < 0$. The evolution of the broadening factor, final pulse width divided by the input pulse width, determined for Gaussian pulse is presented in Fig. 2.3.

A complete theoretical analysis of pulse compression is provided in Chapter 5,

where we provide the analytical expressions that describe the evolution of different pulse profiles in silicon nanowires.

2.5.2 Third order dispersion effects

As it has been mentioned in the previous sections, TOD can be neglected in many cases of practical interest. However, there are certain cases where it is necessary to take into account the TOD effects. For example, if the pulse wavelength corresponds to zero group velocity dispersion (ZGVD, $\beta_2 = 0$) wavelength, the TOD becomes the dominant dispersive effect influencing the pulse propagation. In addition, when the pulse width (τ) is in the femtosecond range, it is necessary to incorporate β_3 into the mathematical model because $\Delta\omega \ll \omega_0$ is no longer valid so that the truncation of Eq. (2.23) is no longer justified.

Similar to the case of the dispersion length L_D, it is useful to introduce a dispersion length associated with TOD as

$$L_D^{'} = \frac{\tau^3}{|\beta_3|}. \tag{2.36}$$

According to this equation, TOD plays an important role when $L_D^{'} \approx L_D$. Thus TOD contributes significantly to pulse reshaping, making the pulse profile to be assymetric. In such cases, TOD is the main source of pulse distortion. Specifically, when $\beta_3 > 0$ an oscillatory structure appears at the trailing edge of the pulse whereas in the case when $\beta_3 < 0$ it appears at the leading edge of the pulse. The pulse assymetry is elliminated when $L_D = L_D^{'}$. The physical effects of TOD on the pulse shape are depicted in Fig. 2.4.

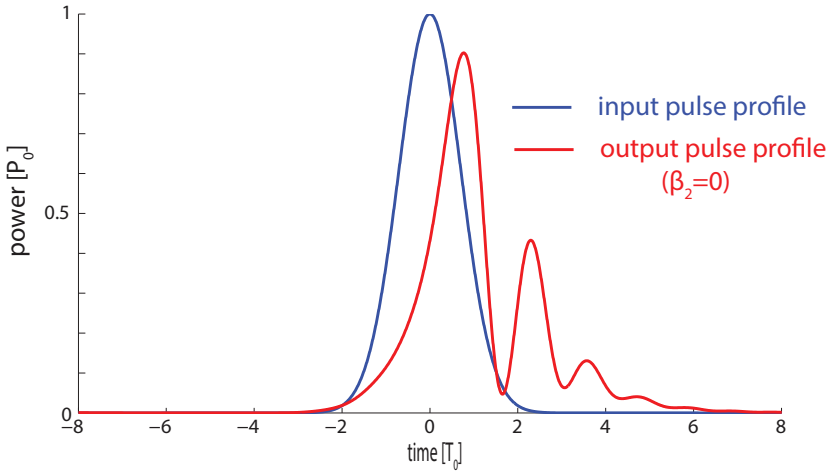

Figure 2.4: Gaussian shapes at $z = 0$ and $z = 2$ m for the case of $\beta_2 = 0$.

Note, that for the case of extremely short pulse widths of a few femtoseconds β_4 and higher order terms in Eq. (2.23) should be taken into consideration. Regarding some of the problems studied in this thesis, higher-order terms up to the fourth-order term (β_4) have been included in the rigorous theoretical model of Eq. (2.22) even when hundreds of femtoseconds or a few picoseconds pulse widths have been used. In addition, β_4 plays a significant role in the nonlinear process of FWM. This is due to the fact that β_4 is one of the terms that defines the phase-matching condition for an efficient FWM. A detailed study of FWM in silicon nanowires and silicon photonic crystal slab waveguides is provided in Chapters 6 and 7, respectively.

It is important to mention, that not only the linear effects determine the evolution of an optical pulse but also the nonlinear properties of the silicon nanowire. Thus, a description of nonlinear effects in the silicon waveguides is presented in the following section 5.2.

2.6 Nonlinear properties of silicon nanowires

Optical pulse propagation in silicon photonic waveguides exhibits rich nonlinear dynamics. This feature is mainly derived from the large third-order susceptibility $\chi^{(3)}$ of silicon. More specifically, third-order susceptibility has two dominant contributions, one comes from the instantaneous response of bound electrons (Kerr effect) and the other one from the optical field interaction with optical phonons (Raman effects).

The effective nonlinear waveguide coefficient γ is strongly dependent on the operating wavelength as well as on the geometry of the propagation media. The sub-micron cross section of silicon nanowires as well as the even smaller dimensions of silicon photonic crystal slab waveguides lead to large values of γ because of the tight light confinement. As a result, such type of silicon waveguides are expected to have also strong nonlinear frequency dispersion, too.

The nonlinear coefficient γ has a significant impact on optical pulse reshaping. Thus real part of γ (γ') is directly related to the nonlinear change of the refractive index n while the imaginary part governs the TPA phenomenon. The real part of γ governs the SPM phenomenon, which is a nonlinear process characterized by an induced optical phase delay due to Kerr effect. This can be described as a change in the refractive index. As a result, an additional chirp is produced during the pulse propagation re-

sulting in spectral pulse broadening. Furthermore, the interplay between the effects of SPM and GVD can lead to the generation of pulses with unique properties. Examples of such type of pulses are the well known solitons, which can preserve their shape along many characteristic lengths under certain circumstances, and similaritons, which are pulses that self-preserve their shape during propagation. More information about solitons is provided in Section 2.6.2. In addition to the solitons generation, an in-depth investigation of the generation and collision between similaritons in silicon nanowires is presented in Chapter 4.

As mentioned earlier, the imaginary part of γ is responsible for the TPA phenomenon, which is a process where two photons are absorbed simultaneously from the optical pulse. The specific process generates free electrons-hole pairs (free carriers, FC), which not only absorb light but also induce a wavelength-dependent change in the refractive index. A main conclusion that can be drawn from this is that the phase of a propagating pulse in a silicon nanowire is not only affected by SPM effects but also by free carrier generation. To be more specific, carrier density is not constant through the pulse propagation as free carriers can recombine. Note, that the temporal variation in carrier density strongly depends on the relation between carrier relaxation time t_c and pulse width τ. For pulse widths larger than the relaxation time, the free carrier density provides strong contribution to pulse reshaping, particularly to the trailing edge of the pulse. The leading part of the pulse generates free carriers and as a result, an additional complex linear susceptibility $\chi_{FC}^{(1)}$ is induced. In this way, the imaginary part of $\chi_{FC}^{(3)}$ corresponds to light absorption due to free carrier (FCA). Moreover, the real part of $\chi_{FC}^{(1)}$ is responsible for a phase shift of the pulse, which occurs due to a free-carrier-induced variation of the index of refraction.

The influence of each of the previous nonlinear effects is summarized in Fig. 2.5, where a long pulse width is considered. Red curves correspond to the case when both FCA and FCC assuming negligible density of free carriers. Black curves include FCA but neglect FCC, while the green curves correspond to the case when both effects are included. First, notice that the free carries have a significant influence on the spectral components of the pulse as they introduce considerable spectral asymmetry. Note, also, the additional losses induced by free carries (FCA) (black curves). An important feature illustrated by Fig. 2.5 is the existence of a spectral shift towards shorter wavelengths

when all the nonlinear effects are included. This can be explained by the nonlinear phase shift, which switches from positive to negative values because of free carrier effects. The nonlinear phase shift is limited if the lifetime of free carries is shorter than the pulse width.

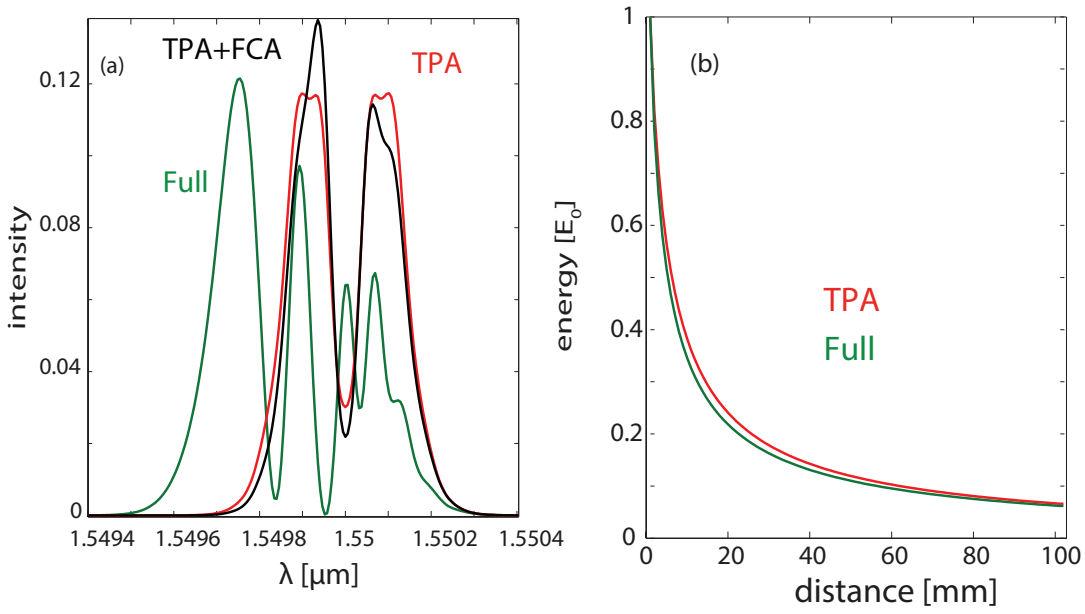

Figure 2.5: a) SPM-broadened spectra and nonlinear phase shift showing the impact of nonlinear effects, such as TPA, FCA and FCC, on pulse spectrum. b) Evolution of the pulse energy along propagation distance without (red curves) and with (green curves) FCA.

The effects of SPM are characterized by a nonlinear length, L_{NL}, defined as:

$$L_{NL} = \frac{1}{\gamma' P_0} \tag{2.37}$$

where P_0 is the peak power of the input pulse and γ' is the real part of γ. As the values of γ are large in silicon waveguides, the nonlinear length can become short. Therefore, strong nonlinear effects can occur over a propagation distance of only a few millimetres (in silicon nanowires) or even less than millimeters (in silicon photonic crystals).

Unlike silica fibres, Si-PhNW/Si-PhCW can be employed in chip scale devices. To illustrate this idea, we provide a comparison of characteristic lengths of a Si-PhNW, Si-PhCW and a single-mode optical fibre in Table-2.1. This table reveals many key features of the nonlinear properties of Si-PhNWs and Si-PhCWs. Firstly, the dispersion lengths in SiPhNWs (Si-PhCWs) is 2 ($\approx$ 5) orders of magnitude shorter than in optical

Dispersion and nonlinear parameters	Si-PhNW $T_0 = 200\ fs$	Si-PhCW $T_0 = 200\ fs$	silica fibre $T_0 = 200\ fs$
β_2	$1.11\ ps^2m^{-1}$	$-138.3\ ps^2m^{-1}$	$0.02ps^2m^{-1}$
L_D	$3.6\ cm$	$262\ \mu m$	2 m
γ	$= 107.12\ W^{-1}m^{-1}$	$= 754\ W^{-1}m^{-1}$	$= 0.003\ W^{-1}m^{-1}$
L_{NL} for $P_0 = 0.2\ mW$	$4.6\ cm$	$6.6\ mm$	2 km

Table 2.1: Comparison of characteristic lengths for ultrashort (200 fs) and long (10 fs) pulses and γ parameter in a Si-PhNW (dimensions $h \times w = 220 \times 4500$ nm^2) and Si-PhCW (dimensions $h = 0.6\,a, a = 412$ nm) and a single mode optical fibre for $\lambda = 1550$ nm.

fibres. Moreover the nonlinear factor γ in silicon photonic crystals is 5 orders of magnitude larger than in optical fibres. As a result, the nonlinear length L_{NL} is much shorter in the case of SiPhNW/Si-PhCW than that of optical fibres. One should note that the effective nonlinear parameter γ can be much larger than the one presented in Table-2.1 for the case of Si-PhCW. This comes from the fact that, Si-PhCWs exhibit specific wavelengths regimes, which are known as slow-light regimes, where the nonlinearity is dramatically increased, as discussed in Section 2.6.5. Therefore, the nonlinear length for Si-PhCW could amount to just a few microns for specific wavelengths. An additional general property of the nonlinear length is its independence on pulse width while it is fully determined by the peak power of the pulse.

The appropriate manipulation of the linear and nonlinear properties presented in Section 2.5 and Section 5.2 can lead to interesting nonlinear phenomena, such as soliton and similariton generation, Raman scattering or FWM. Such type of nonlinear phenomena are used in the development of optical interconnects for chip to chip communications. A brief presentation of such nonlinear effects follows in the next subsections.

2.6.1 Self-steepening

Although Eq. (2.22) is a rigorous theoretical model providing detailed information about the evolution of pulse profile in silicon nanowires, it does not include fully the large variation of nonlinear coefficient γ with frequency. Frequency variation of γ leads to a large characteristic optical shock time, which induces rich nonlinear effects on ultra short optical pulses. In order to investigate in more detail the contribution of characteristic optical shock time on pulse dynamics of ultra short optical pulses, we need to modify Eq. (2.22) in order to incorporate the frequency dependence of the nonlinear coefficient γ. Similar to Eq. (2.23), we expand $\gamma(\omega)$ in a Taylor series around

a fixed frequency ω_0 as:

$$\gamma(\omega) = \gamma(\omega_0) + \gamma_1(\omega - \omega_0) + \frac{1}{2}\gamma_2(\omega - \omega_0)^2 + ..., \tag{2.38}$$

where $\gamma_m = (\frac{d^m\gamma}{d\omega^m})_{\omega=\omega_0}$. In most cases of practical interest it is sufficient to keep the first two terms in this expansion.

Keeping in mind that during the Fourier-transform to time domain, $\omega - \omega_0$ is replaced by the differential operator $i\partial/\partial t$, the modified Eq. (2.22), written in a reference system moving with the pulse group velocity v_g, becomes as:

$$\begin{aligned} i\frac{\partial u}{\partial z} - \frac{\beta_2}{2}\frac{\partial^2 u}{\partial t^2} - i\frac{\beta_3}{6}\frac{\partial^3 u}{\partial t^3} = &-\frac{ic\kappa}{2nv_g}(\alpha_{in} + \alpha_{FC} - \frac{\omega\kappa}{nv_g}\delta n_{FC})u \\ &- \frac{3\omega P_0\Gamma}{4\varepsilon_0 A_0 v_g^2}\left[1 + i\left(\frac{1}{\omega_0} + \frac{\partial \ln[g(\omega)]}{\partial\omega}|_{\omega=\omega_0}\right)\frac{\partial}{\partial t}\right]|u|^2 u, \end{aligned} \tag{2.39}$$

where ω_0 is the carrier frequency and $g(\omega) = \Gamma/v_g^2$.

Equation (2.39) reveals an additional nonlinear phenomenon, the so-called self-frequency shift (or self-steepening). More specifically, if we combine the RHS terms of Eq. (2.39) that contains the derivative $\partial/\partial t$, we find that γ forces the group velocity to depend on the optical intensity and leads to the phenomenon of self-steepening. As a result, the refractive index is different across the pulse width depending on the local power. Hence, there is a phase shift for the different frequent components of the pulse. The broader in spectral domain the optical pulse is, the stronger the effect of self-steepening is.

Figure (2.6) shows the influence of self-steepenig on the pulse profile of an optical pulse. The dependence of the group velocity on the pulse intensity forces the peak of the pulse to move at a lower speed than the wings. This feature is responsible for the observed pulse asymmetry, not only in the time domain but also in the frequency domain. Note, that the induced shift in the group velocity of the spectral components leads to spectral broadening, similar to the effects induced by SPM. The strength of the self steepening phenomena is determined by the characteristic time τ_s, which is defined as

$$\tau_s = \frac{\partial \ln[g(\omega)]}{\partial\omega}|_{\omega=\omega_0} = \tau_0 + \tau_{wm}, \tag{2.40}$$

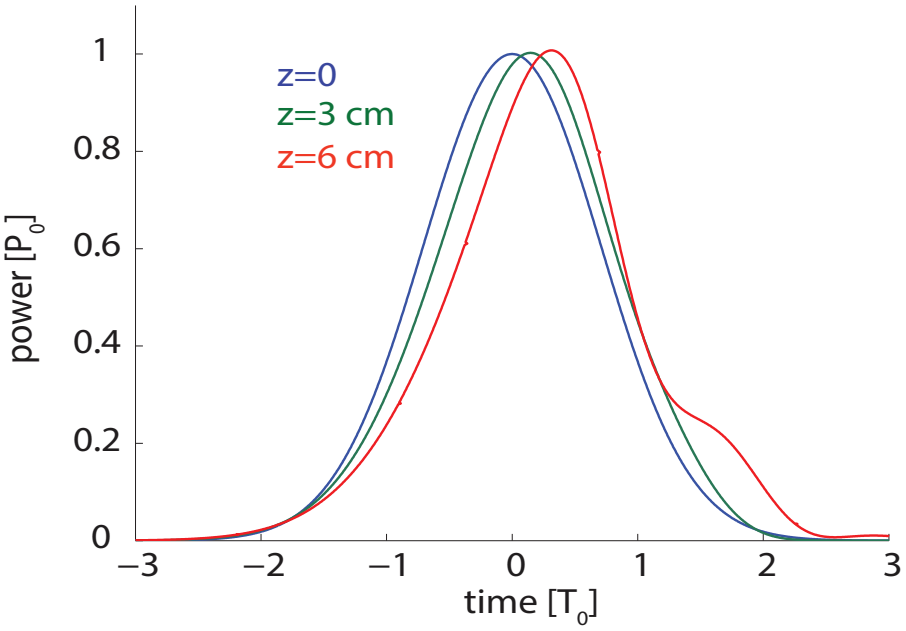

Figure 2.6: Self steepening of a Gaussian pulse at different propagation distances. Blue curve corresponds to the input pulse at $z = 0$.

where $\tau_0 = 1/\omega_0$ is related to the frequency-dependent response of the nonlinearity in a bulk crystal and $\tau_{wm} = \tau_r + i\tau_i$ quantifies the waveguide contribution including that due to $\chi^{(3)}(\omega)$. It should be mentioned that the parameter τ_i is equal to zero in the case of optical fibres. One should also note that , especially in silicon waveguides, τ_{wm} plays a significant role only in the case of ultra short pulses (femtosecond pulse widths).

Equations (2.27)-(2.39) provide the information required to determine the pulse dynamics upon its propagation in silicon waveguides. Based on these equations, we can investigate in detail many interesting phenomena, such as soliton and similariton generation.

2.6.2 Generation of optical solitons

The interplay between dispersive and nonlinear effects in Si-PhNW and Si-PhCW determines the evolution of the pulse shape as it propagates along the waveguide. An appropriate control of both effects can lead to the generation of pulses unique properties. One example of such type of pulse is the soliton, namely a pulse which preserves its shape along its propagation. Solitons are primarily characterized by the soliton

number, N, which is equal to:

$$N = \sqrt{\frac{L_D}{L_{NL}}} = \sqrt{\frac{\gamma P_0 \tau^2}{|\beta_2|}}. \tag{2.41}$$

The case of $N = 1$ corresponds to the fundamental soliton whereas $N > 1$, higher-order solitons, where the pulse profile of the soliton follows a periodic pattern in time and frequency domains as it is shown in Fig. 2.7. In order to investigate further the properties of a soliton, we should focus on the physical meaning of soliton number N. The soliton number reveals the dominant linear or nonlinear effect during the pulse propagation. In the case of a fundamental soliton, the GVD and SPM effects act equally on the pulse shape enforcing the pulse to preserve its pulse profile. This feature amounts to the cancellation of SPM and GVD effects. As SPM always produces a positive chirp, GVD should produce a negative chirp in order to compensate for that generated by SPM. Accordingly, soliton formation requires that β_2 should be negative. It is for this reason, that one should propagate pulses in the anomalous dispersion regime in order to generate solitons. Note, also, that recent experiments revealed that solitons are dependent on the initial chirp of the pulse[2. 57]. This comes from the fact that, solitons are generally stable under weak perturbations. However the fundamental soliton could be generally destroyed if $|C|$ exceeds a critical value [2. 57].

It is not sufficient to launch a pulse in the anomalous dispersion regime in order to generate solitons. If the soliton number is less than unity, solitons can not be formatted meaning that the soliton generation is a threshold effect. The physical meaning of this feature is the existence of a power threshold over which a soliton can propagate in a medium that exhibits anomalous dispersion regime. Moreover, a large value of the soliton numbers ensures that the input power is large enough for the input pulse to contain more than one soliton. However, large values of soliton number constitutes the main source of pulse degradation as the larger the N is, the more energy is wasted in the developed pedestals of the pulse.

The main concern regarding the generation of solitons in silicon waveguides is the large losses due to nonlinear optical effects, such as TPA and FCA. This means that the pulse can not preserve its shape for long propagation distances. However, soliton-like pulses are formatted in long millimetres silicon nanowires due to strong GVD and SPM

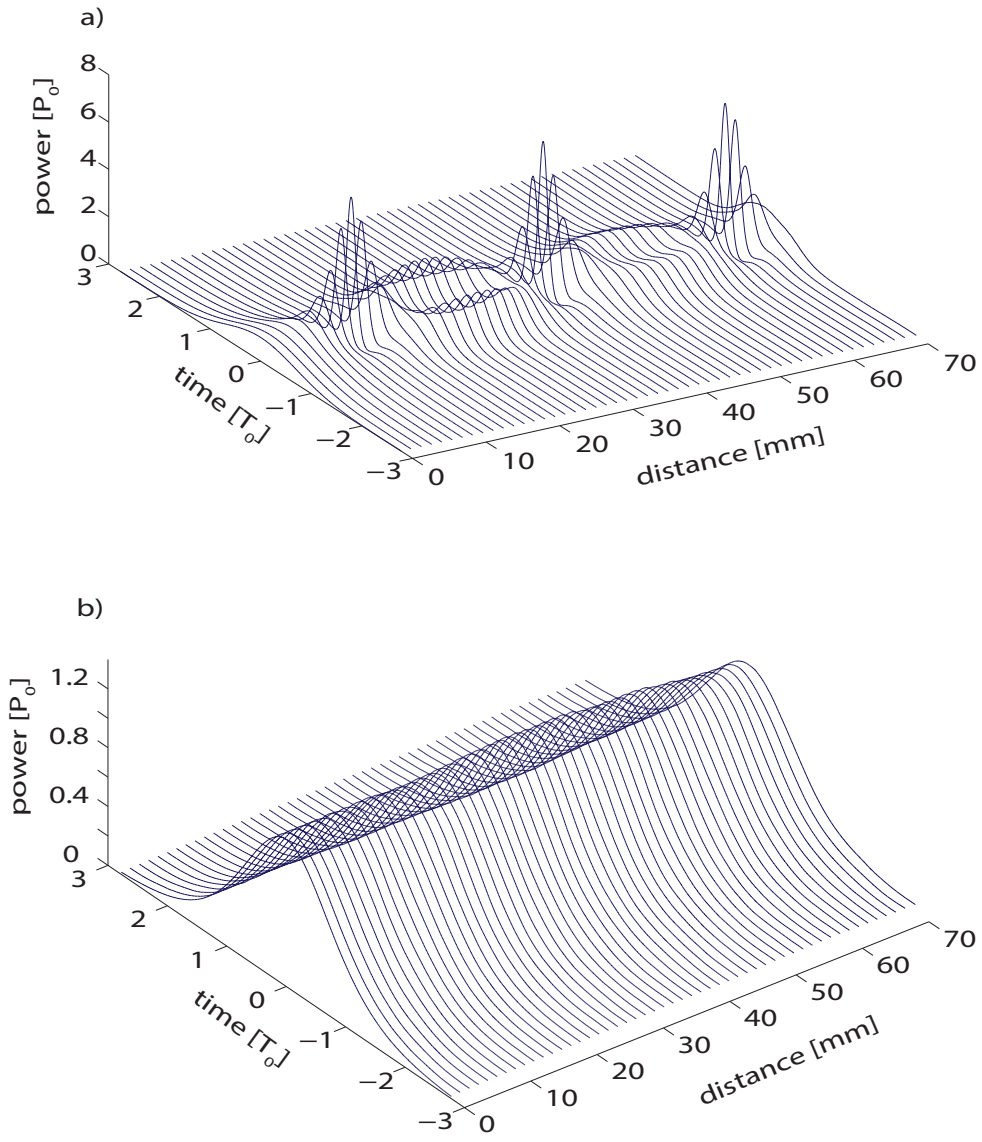

Figure 2.7: a) Periodic evolution of higher-order solitons, $N = 3$, pulse profile in time domain. b) Temporal pulse evolution for a fundamental soliton $N = 1$.

effects when the characteristic linear and nonlinear absorption lengths are much larger than the soliton length.

A nonlinear effect similar effect to soliton formation is the similariton generation, which occurs in the normal dispersion regime. This nonlinear optical process is described in the following subsection.

2.6.3 Generation of optical similaritons

Unlike solitons, which require a threshold power to form, no constraints have to be imposed on the pulse energy, initial shape, or optical phase profile to generate similaritons. These type of pulses maintain a certain relation (scaling) among changing power, pulse width, and chirp, generally leading to a parabolic intensity profile. It has been demonstrated that parabolic pulses represent an asymptotic solution of the nonlinear Schrödinger equation [see Section 2.2 for more details about NLSE] with a gain term for an optical pulse propagating in the normal dispersion regime.

The generation of parabolic pulses is strongly dependent on the interplay among the gain, dispersion and nonlinearity. From a practical point of view, in many optical fibres applications, amplifiers as source of gain are not preferred because their use increases the cost and the complexity of the whole system. Alternatively, similariton generation schemes have been suggested in recent years based on dispersion decreasing silicon or silica tapered fibres [2. 62–64] because decreasing dispersion acts in a similar way as gain.

The essential feature of a parabolic similariton pulse is that its induced chirp has a linear dependence on time. This property is responsible for the self-similar evolution of parabolic pulses along the waveguide. This self-similar behaviour of optical similaritons is fully determined by the interplay between the GVD and SPM. As a consequence, the process of parabolic pulse generation in silicon waveguides is strongly dependent on the input pulse width and power. To be more specific, there is an optimum combination between pulse width and input power, which forces the temporal chirp to vary linearly across the pulse. When the chirp does not have monotonic linear time dependence across the optical pulse, the pulse is subject to wave-breaking upon its propagation [2. 65].

It can be shown that by taking advantage of the characteristics of the linear and nonlinear properties of silicon waveguides, the generation of parabolic pulses requires relatively short propagation distances. For instance, our recent work [2. 66, 67] on similaritons in silicon nanowires suggests than only a few millimetres of pulse propagation are needed in order to generate a parabolic pulse, while in the case of optical fibres this distance can be a few meters or longer. This is due to the large values of the linear and nonlinear optical waveguide coefficients of silicon waveguides. Note, also, that

there are additional parameters that affect the efficiency of the similariton generation process, such as the input pulse shape and the input power. A detailed analysis of the generation of parabolic pulses in silicon nanowires is provided in Chapter 3.

2.6.4 Four-wave-mixing in silicon waveguides

So far, we have described different nonlinear phenomena in silicon waveguides, which greatly affect the optical pulse dynamics, both in the time and frequency domains. In this section we discuss, an additional nonlinear process, which generally involves the interaction of four waves with different frequencies. This generic nonlinear process is called four-wave mixing. During this nonlinear process an energy transfer among the co-propagating pulses occurs. In order to maximize this energy transfer, a phase match between the co-propagating pulses is required. Generally, there are two types of FWM based on the number of the pumps beams. The first type describes the energy transfer of three photons $\omega_1, \omega_2, \omega_3$ to a single photon at the frequency, $\omega_4 = \omega_1 + \omega_2 + \omega_3$. The special case where $\omega_1 = \omega_2 = \omega_3$ corresponds to the phenomenon of third-harmonic generation. However, it is difficult to eliminate the phase mismatch of such process.

The second type of FWM corresponds to the case where two photons with frequencies ω_1 and ω_2 are annihilated and generate two photons at frequencies ω_3 and ω_4 such that

$$\omega_1 + \omega_2 = \omega_3 + \omega_4. \tag{2.42}$$

In case where $\omega_1 = \omega_2$ FWM is initiated with just one pump, which will generate two frequency components with ω_3 and ω_4) such that:

$$\Omega_s = \omega_1 - \omega_3 = \omega_4 - \omega_1. \tag{2.43}$$

This nonlinear process is known as degenerate FWM. From a practical point of view, it is more useful the pump co-propagates with an additional pulse, which is employed as a carrier of information (signal). In this way, a down or an up conversion of information can be achieved (a process called also wavelength conversion) or amplification of initial signal could be obtained as well. In order to achieve this, the phase mismatch among the pump (ω_p), the signal (ω_s) and the third frequency component, known as idler (ω_i), should be eliminated.

Let us now consider and see what physical aspects should be considered when investigating the FWM. Firstly, let us assume that an unchirped Gaussian pump and signal pulse are launched in the waveguide

$$u(z_0,t) = \frac{\sqrt{P_p}}{\sqrt{P_p}+\sqrt{P_s}} e^{-\frac{t^2}{2\tau^2}} + \frac{\sqrt{P_s}}{\sqrt{P_p}+\sqrt{P_s}} e^{-\frac{t^2}{2\tau^2} - i\Delta\omega t} \tag{2.44}$$

where P_p and P_s are the peak power of the pump and signal, respectively, and $\Delta\omega = \omega_s - \omega_p$. The value of $\Delta\omega$ plays a crucial role for the accuracy of the computational method. In order to solve a single equation describing both pulses, it is required that the time-step is much shorter than $\pi/\Delta\omega$. This requirement makes it necessary to incorporate into Eq. (2.39) additional dispersive coefficients, such as β_3 and β_4. In this way, cubic and higher order terms in the expansion of Eq. (2.23) must satisfy the condition $(\beta_4/\beta_3)\Delta\omega \ll 1$ and $(\beta_3/\beta_2)\Delta\omega \ll 1$.

Further to this, the efficiency of the degenerate FWM process is governed by the conservation of energy and momentum, which are expressed as:

$$2\omega_p = \omega_s + \omega_i, \tag{2.45}$$

and

$$\Delta\beta = 2\gamma P_p - (2\beta_p - \beta_s - \beta_i) = 0, \tag{2.46}$$

where $P_p,\ \beta_p,\ \beta_s,\ \beta_i$ stands for the pump power and propagation constants for pump, signal and idler, respectively. Note, that we assume that the powers of the signal and the idler are much smaller than the pump power, such that the nonlinear Kerr phase shift is completely determined by the pump pulse. The phase-mismatch is mainly derived from the material and waveguide dispersion. Due to phase-mismatch, in general only a small fraction of the pump energy is transferred to the signal and idler. Therefore the phase-mismatch should be eliminated, as it was mentioned earlier, in order to maximize the energy transfer.

The basic idea employed to overcome this problem is to design a silicon waveguide for which the difference among the propagation constants of the three pulses is compensated. This wavevector mismatch can be canceled by using a periodically width modulated silicon photonic nanowire, as has been suggested in [2. 68]. According to

Eq. (2.46), in this case the phase match condition becomes:

$$\Delta\beta = 2\gamma P_p - (2\beta_p - \beta_s - \beta_i) \pm \frac{2\pi}{\Lambda} = 0, \tag{2.47}$$

where Λ denotes the period of the width modulated waveguide.

As it has been discussed, the propagation constant β and the nonlinear coefficient γ are strongly dependent on the operational frequency, as well as on the physical geometry of the guiding medium. Consequently, β and γ exhibit a periodical variation along the waveguide, which is derived from the periodical width modulation of the silicon nanowire.

According to Eq. (2.47), a practical question is raised, namely is it possible to calculate the optimum period of the width modulated waveguide in order to increase the efficiency of degenerate FWM? In order to answer this question, the coefficients β_p, β_s and β_i are expanded in Taylor series around the pump frequency ω_p, which corresponds to the pump frequency, such that:

$$\beta(\omega_s) = \beta_0 + \beta_1(\omega_s - \omega_p) + \frac{1}{2!}\beta_2(\omega_s - \omega_p)^2 + .., \tag{2.48}$$

and

$$\beta(\omega_i) = \beta_0 + \beta_1(\omega_i - \omega_p) + \frac{1}{2!}\beta_2(\omega_i - \omega_p)^2 + .. \tag{2.49}$$

Equations $(2.48) - (2.49)$ can be expressed in a more general form as:

$$\beta(\omega_s) = \sum \frac{1}{n!}\frac{dn^n\beta}{d\omega^n}|_{\omega=\omega_p}(\omega_s - \omega_p)^n, \tag{2.50}$$

and

$$\beta(\omega_i) = \sum \frac{1}{n!}\frac{dn^n\beta}{d\omega^n}|_{\omega=\omega_p}(\omega_i - \omega_p)^n. \tag{2.51}$$

By taking the sum of Eqs. $(2.50) - (2.51)$ and substituting it in Eq. (2.47), the final form of the mismatch condition becomes:

$$|2\gamma P_p + \beta_{2,p}\Delta\omega^2 + \frac{1}{12}\beta_{4,p}\Delta\omega^4| = \frac{2\pi}{\Lambda}. \tag{2.52}$$

One should note that Eq. (2.52) holds for small $\Delta\omega$ as the previously described Taylor

expansion is valid for small $\Delta\omega$. Equation (2.52) reveals that the period Λ is determined by $\Delta\omega$, the pulse and the waveguide parameters. To be more specific, the mathematical formula that describes the relation between $\Delta\omega$ and Λ, derived from Eq. (2.52), can be written as:

$$\Delta\omega^2 = \frac{6[-\beta_{2,p} \pm \sqrt{\beta_{2,p}^2 - \frac{\beta_{4,p}}{3}(2\gamma P_p \pm \frac{2\pi}{\Lambda})}]}{\beta_{4,p}} \tag{2.53}$$

It is clear that the phase-matching condition is strongly dependent on the input power, on the nonlinear parameter γ and on the even-order dispersive coefficients determined by the pump pulse. An additional parameter that has influence on the phase-matching condition is the period of the width modulation thus allowing for large design flexibility. In this way it is convenient to pick the desired pairs of wavelengths for which the FWM process is meant to be quasi-phase matched, and then calculate the corresponding period, Λ.

An alternative approach to calculate the period Λ, is the calculation of each propagation constant β separately for pump, idler and signal pulse. After the incorporation of the propagation constants into Eq. (2.47), the period Λ can be found as:

$$\Lambda = \pm\frac{2\pi}{2\gamma P_p - (2\beta_p - \beta_s - \beta_i)} \tag{2.54}$$

Following this approach, one can calculate a relation between the three wavelengths, λ_p, λ_s, and λ_i and the period Λ.

2.6.5 Slow light in silicon photonic crystal waveguides

One of the most exciting characteristic of Si-PhCWs is that they possess specific frequency regimes, known as slow light regimes, where the group velocity of the pulse becomes significantly smaller than the speed of light. This physical property of silicon photonic crystals has been actively investigated over the last decade [2. 69]-[2. 71], particularly due to its potential applications. Thus, the photonic band theory allows the study of the dispersion characteristics of photonic crystals by providing the band diagram of such multidimensional periodic structures. For instance, a generic silicon photonic crystal slab waveguide and its band diagram are shown in Fig. 2.8.

Figure 2.8(b) shows that the slow light regime is located for both modes in region where the band is almost flat as the group velocity of light is given by the inverse of

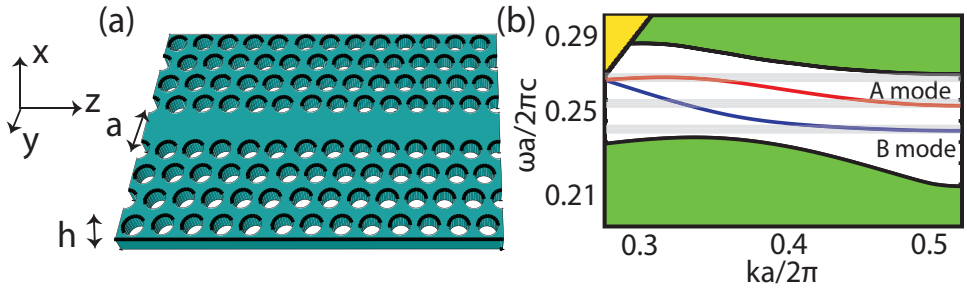

Figure 2.8: a) Geometry of a silicon photonic crystal slab waveguide b) Projected band structure. Dark yellow and green ares correspond to slab leaky and guiding modes, respectively. The red and blue curves represent the guiding modes propagating into the defect line.

the first-order dispersion $(dk/d\omega)^{-1}$, where k and ω are the wavenumber and angular frequency. In addition, slow light spectral regions can always be found at the edge of the photonic bands ($k = 0.5\ 2\pi/a$) because in these regions $d\omega/d\kappa \approx 0$.

There are two key optical properties that should be considered in the slow light regimes. The first is the bandwidth for which the slow light regime holds. This is an important parameter, which is essential for many applications. For instance, applications related to the information storage and adjustment of timing of optical packets (optical buffers) require a certain slow light bandwidth in order to accommodate the temporal pulse widths. Further, the slow light bandwidth implicitly determines the capacity of the buffer. Although a wide bandwidth is an ideal goal for many applications, it comes at the expense of a smaller time delay.

A second important property is the higher order of dispersion that characterizes the slow light regimes. Such feature defines the shape of the propagating pulse as the high dispersion usually accounts for strong pulse re-shaping. One should note here that the nonlinearity also increases in the slow light regime leading to large SPM. Therefore, the pulse starts to undergo significant TPA. The increase of linear and nonlinear dispersion could be an advantage of Si-PhCWs but also an important limit for specific applications, such as amplifiers or wavelength converters.

Regarding the high frequency dispersion, which mainly distorts the pulse shape along the propagation distance, there are effective ways to overcome this problem [2. 73–78]. The common purpose of these techniques is either to suppress the high-order dispersion using the so-called zero-dispersion periodic structures, or to compensate this higher-order dispersion by structuring the waveguide. The main concept of this

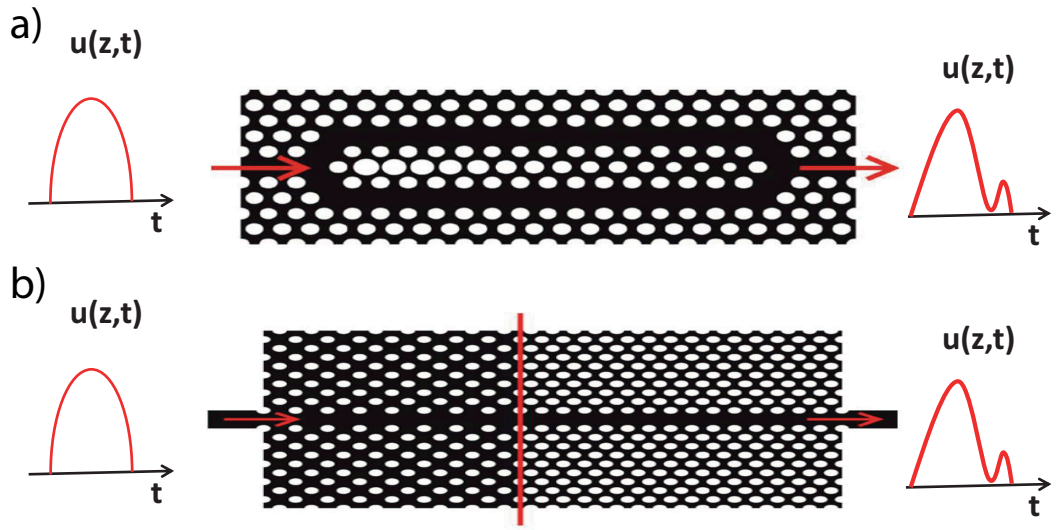

Figure 2.9: a) Dispersion compensated structure by changing the radius of the holes along the length of the middle structure b) Suppressing the high order dispersion using a zero-dispersion structure. The first part of the device produces positive GVD while the second exhibits negative GVD [2. 72].

idea is to gradually change the propagation constant of the guiding mode. One of the most well known techniques is to change either the size or the position of the holes, which form the boundary of the defect line [2. 72]. Equally important technique, is to combine appropriately two structures with positive and negative GVD. Such type of optical schemes are shown in Fig. 2.9.

The nonlinear effects occurring in the slow light regime are mainly employed in applications for controlling optical signals in the time domain. Such applications find their use primarily to optical interconnects for high data rate transmission in optical networks. However, there is a multitude of efficient applications based not only on the nonlinear properties of silicon waveguides but also on their linear properties. In this context, the next section will briefly present state-of-the-art applications employing Si-PhNW and Si-PhCW.

2.7 Applications of silicon waveguides

Optical interconnects for high performance computing is probably the most important application of silicon photonic waveguides. The main objective is to connect different parts of a computer system by silicon waveguides. It is possible to have a chip-to-chip Si-PhNW/Si-PhCW interconnect, enhancing the transmission of data [2. 79, 80]. A recent experiment demonstrates a low error-transmission of 1.28 Tb/s stream through

5 cm long wire waveguide of 3 dB/cm losses [2. 81]. The computing power of optical computers can further be enhanced by optical pulse compression. A Gaussian pulse can be compressed by an order of magnitude, increasing the information capacity that usual computer connections can manipulate [2. 82].

Silicon photonics are also employed for nonlinear optical conversion, which is a key functionality in telecommunications. A well-known technique for parametric optical conversion is FWM. A usual set up for parametric gain is shown in as shown in Fig. 2.10. In a recent experiment a 10 Gbit/s non-return-to-zero data train was converted across C band from 1535 to 1566 nm with minimal degradation of the signal quality [2. 83]. In addition, there are many experiments that have improved the process of FWM in order a multiband operation to be realized over a broad spectral region. For instance, in the experiment of Q. Lin [2. 49], spectral region extends from 1390 nm to 1730 nm. However, most of these applications make use of continuous waves as pump and signal inducing losses due to TPA and FC. In order to overcome these obstacles we have suggested an optical scheme where we launch optical pulses as pump and signal into a periodically modulated SiPhNW [2. 84]. Our work demonstrates under these circumstances a conversion enhancement of 20 dB as compared to the case of a constant width nanowire. However, it is not only high conversion efficiency that can be achieved via FWM but also pulse reshaping and regeneration, taking advantage of the intense nonlinearities of SiPhNW. For instance, an optical clock recovery system that uses TPA in a silicon photodiode to sychronize a 10 GHz optical clock to an 80 Gb/s RZ data signal has already been suggested [2. 85].

The common feature of the previous applications is the use of dispersion engineered silicon nanowires with few millimetres length. Thus, they can be incorporated into future ultradense multichannel telecommunication systems. These features point to be a potential application of silicon nanowires for lightwave systems. Super continuum generation and optical spectral broadening also constitute essential components within and outside the field of optical communications. These type of functionalities strongly depend on the interaction between different nonlinear processes. As silicon nanowires are characterized by strong nonlinearities, it is expected to play a crucial role to such type of applications. Recently, a spectral broadening of more than 350 nm upon propagation of ultrashort 1.3 μm wavelength optical pulses in a 4.7 mm SiPhNW

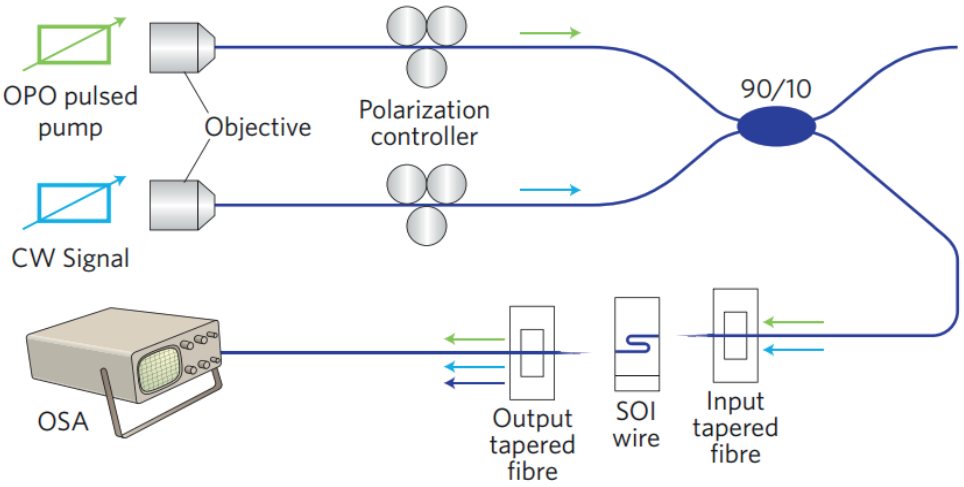

Figure 2.10: Set-up of FWM based parametric gain. A strong pump pulse is launched into a silicon nanowire together with a continuous signal wave. Energy is transferred from the pump to the signal [2. 88].

has been observed [2. 56]. Spectral broadening can also be experienced via the mechanism of soliton fission. This process has already been presented in photonic crystal fibres [2. 86]. Such type of spectral broadbands has been proposed as a simple way to create multiwavelength division multiplexing (WDM) applications. Therefore, supercontinuum generation can be employed in optical transceivers, in emerging on chip optical networks for multiprocessor-chips, in optical coherence tomography [2. 87] and optical frequency metrology. The essential requirements of these applications are the low power consumption as well as the ultra compact dimension of the optical devices.

Further to the previous applications, there is a number of technological areas which are relevant to mid-infrared wavelengths ($2-14\ \mu m$). Such type of applications include environmental monitoring, personalized results-driven healthcare, and public safety. This optical spectrum is often referred to as the molecular fingerprinting spectrum, as it includes the fundamental vibrational absorption lines of many molecules of practical interest. It is for this reason that mid-IR spectroscopic sensors are superior from a sensitivity standpoint and they are mainly used for medical diagnostic (e.g. tomography) [2. 89–92]. One should note here, that holmium and thulium lasers offer advanced performance at mid-IR wavelengths. More specifically, holmium and thulium lasers make endoscopic procedures safer and less invasive than the traditional surgical procedures. Furthermore, free-carrier dispersion-based electrooptic Mach-Zehnder

modulators have recently been characterized at mid-IR wavelengths near 2.2 μm, illustrating that design methodologies previously applied to telecom-band modulators can also be effective at longer wavelengths [2. 93]. Finally, a mid-IR photodetection device which spectrally translates signals near 2.4 m to the telecom-band near 1.6 μm with simultaneous amplification of 19 dB, has also been demonstrated [2. 94].

The applications that have been mentioned so far are mainly based on the advantageous linear (GVD, TOD) and nonlinear (SPM, TPA) effects of silicon photonics. However, there is an intensive research effort to exploit the slow light regimes of silicon photonics, especially silicon photonic crystals waveguides, to real applications. One target application is the all-optical routers, which will be able to store and identify optical data packets. In order to achieve this, the propagating pulses should be slowed down (the longest delay so far is 80-pulsewidths, [2. 95]-[2. 96]). This is beneficial for telecommunication systems since they need to consume large power for the electronic-optical conversion. One should note, that the electronic-optical conversion limits the bandwidth of the interchanging information. In the same context, slow light effect facilitates many application in quantum optics [2. 97]. In particular, the storage of the quantum state of light for long time is necessary in order to create correlated photons, which forms the basic building blocks of a quantum processor. Besides quantum optics, all optical demultiplexing based on FWM in Si-PhCWs is another key application for converting high speed signals to lower bit rates that can be electronically processed.

One of the well known applications, which is also based on FWM in silicon photonic crystals is the (green light) spectrum. The main goal of this application is to convert three photons of energy $\hbar\omega$ into a single photon of energy $3\hbar\omega$. The main challenge of this process is the single photon of $3\hbar\omega$ not to be absorbed from the silicon due to large nonlinear losses. The large enhancement of the electric field in the Si-PhCW and the appropriate design of the geometry ensured the success of this application as shown in Fig. 2.11.

As such silicon photonics seem to be the most suitable platform for integration of optical circuits due to the availability of waveguides with sub-micron transverse size.

In order to analyze the previous applications and design novel photonic devices a rigorous mathematical method should be employed. In the current project, a highly efficient numerical technique, which is known as split step Fourier (SSF) method is

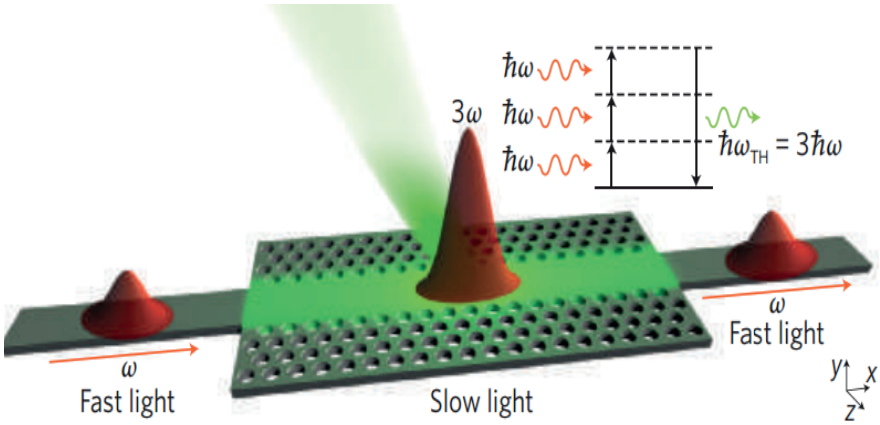

Figure 2.11: Schematic of generation green light in a slow light Si-PhCW [2. 98].

adopted. A description of this technique is presented in the following section.

2.8 Split-step Fourier method

The SSF method falls under the category of pseudospectral numerical methods, characterized by fast speed as compared to other methods, such as time-domain techniques. Time-domain techniques take into account the carrier frequency of the waves while SSF drops the carrier frequency from the derivation of Eq. (2.22). Thus, time-domain techniques can account for forward and backward propagating waves while SSF can describe only one-directional propagation. The disadvantages of the SSF method do not affect our analysis as the extra cost for this advantage of time-domain techniques is the increase in the computation time. However, in all instances analyzed in this project backward waves are not generated because the width variations of the waveguides are small and smooth.

The computation speed of the SSF is due to the calculation of the dispersion contribution to the pulse propagation in the frequency domain, thus avoiding any numerical derivatives. Equally important, the use of fast Fourier transform (FFT) method to move between frequency and time domain significantly speeds up the computations. Specifically, the basic idea that governs the SSF method is the separation of Eq. (2.39) in linear and nonlinear terms as follows:

$$\frac{\partial u}{\partial t} = (\hat{D} + \hat{N})u, \tag{2.55}$$

where $\hat{D}$ is a differential operator related to linear properties and $\hat{N}$ denotes the nonlinear features of SiNW/Si-PhCW. These operators are written in the following form:

$$\hat{D} = \frac{\beta_2}{2}\frac{\partial^2 u}{\partial t^2} + i\frac{\beta_3}{6}\frac{\partial^3 u}{\partial t^3} - \frac{ic\kappa}{2nv_g}\alpha_{in}u, \tag{2.56}$$

$$\hat{N} = -\gamma P_0\left[1 + i\tau_s\frac{\partial}{\partial t}\right]|u|^2 u - \frac{ic\kappa}{2nv_g}\alpha_{FC}u - \frac{\omega\kappa}{nv_g}\delta n_{FC}u. \tag{2.57}$$

One should make clear here that the second (a_{FC}) and third (δn_{FC}) RHS terms of Eq. (2.57) are strongly dependent on the free-carrier generation described by Eq. (2.28). This means that they are indeed nonlinear terms as the free-carrier generation is proportional to the square power of the mode.

From a physical point of view, the linear and nonlinear effects are coupled via the pulse envelope. The SSF method assumes that both effects act independently on each other over the short length of an integration step. More specifically, the propagation from z to $z+h$ is carried out in two steps. Firstly, the linear effects act alone ($\hat{D} \neq 0$, $\hat{N} = 0$) and secondly only the nonlinear effects act on the pulse ($\hat{N} \neq 0$, $\hat{D} = 0$).

According to Eqs. (2.56) and (2.57) the solution of the next spatial step of Eq. (2.22) has the following formulation:

$$u(z+h,t) \approx e^{h(\hat{D}+\hat{N})}u(z,t) \tag{2.58}$$

where

$$e^{h(\hat{D}+\hat{N})} \approx e^{h\hat{D}}e^{h\hat{N}}. \tag{2.59}$$

One should note here that the primary source of error in SSF emerges from the fact that the operators $\hat{D}$ and $\hat{N}$ do not commute. Thus, the approximation of Eq. (2.60) will provide solution accurate to second-order in the step-size, h. In order to improve the accuracy of the solution a symmetrized split-step Fourier method [2. 99] is employed. In particular, the expansion of Eq. (2.60) can be formulated using the Baker-Hausdorff formulae as:

$$e^{h\hat{D}}e^{h\hat{N}} = h(\hat{D}+\hat{N}+\frac{h}{2}[\hat{D},\hat{N}]+\frac{h^2}{12}[\hat{D}-\hat{N},[\hat{D},\hat{N}]]+...). \tag{2.60}$$

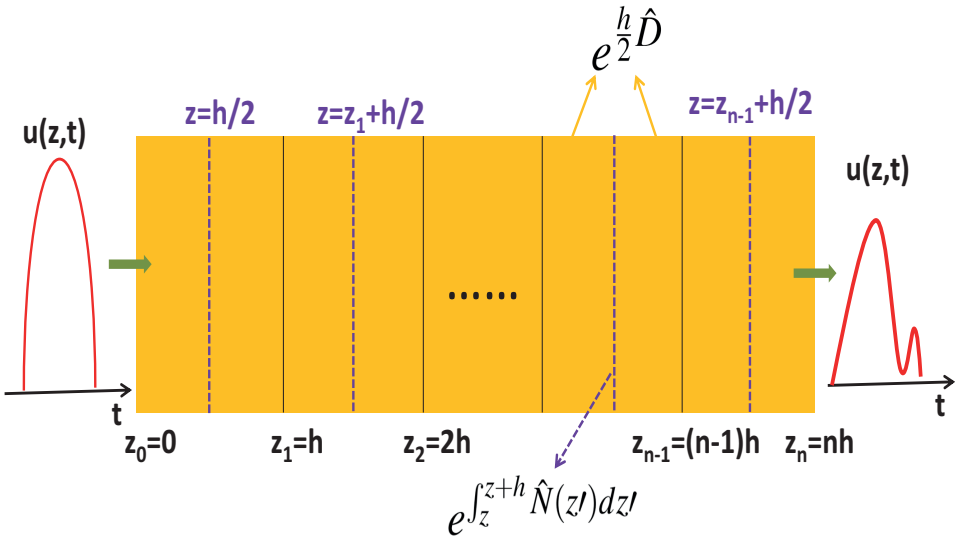

Figure 2.12: Schematic illustration of the symmetrized split-step Fourier method used for numerical simulations.

By keeping up to the second term of the latter formulation, the error is of third-order in terms of step-size h. According to this observation the solution can be cast as:

$$u(z+h,t) \approx e^{\frac{h}{2}\hat{D}} e^{\int_z^{z+h}\hat{N}(z')dz'} e^{\frac{h}{2}\hat{D}} u(z,t). \tag{2.61}$$

This mathematical procedure is illustrated in Fig. 2.12 where the whole propagation distance has been divided in a series of small steps. Each segment has a length equal to h. According to the symmetrized formulation of SSF, the linear effects are calculated for a distance of $h/2$. Note, here that the optical field is calculated in the frequency domain for the linear case. At the midplane, $z+h/2$, the field $u(z,t)$ is multiplied by a nonlinear factor that represents the effect of nonlinearity over the whole segment h. Finally, the field is calculated for the remaining distance $h/2$ assuming that only the linear effects act.

Equation (2.61) describes an iterative algorithm, where the calculation of the field at each distance step h needs the field at the end of the previous step. The iterations begin at $z = 0$, where the input pulse shape is set up. One should note, that we have adopted a more advanced mathematical scheme of SSF method in our theoretical model as we need to take into account the generation and dynamics of free-carriers. Consequently there is an additional intermediate computational step between the linear and

nonlinear step. To be more specific, the field calculated in the linear step is used to compute the generation of free carriers through the rate equation (2.28). Following this approach we incorporate the nonlinear effects related to the free-carriers (FCA and FCD) into our initial NLSE Eq. (2.22) leading to a system of coupled differential equations, which is solved through a Runge-Kutta method of 5^{th} order.

It is important to mention that the nonlinear part of the SSF method, which also includes the implicit nonlinearity of free carrier generation, is calculated in the time domain, as the nonlinearity is dependent on the square of the electric field magnitude. On the other hand, the linear part of SSF is calculated in the frequency domain. In this way, the use of the FFT algorithm [2. 100] makes the numerical evaluation of Eq. (2.39) relatively fast. It is for this reason that the split-step Fourier method can be faster by up to two orders of magnitude as compared with most finite-difference schemes [2. 101] as it has already been mentioned.

The accuracy of the SSF method needs to satisfy certain mathematical requirements. For instance, SSF implicitly imposes periodic boundary conditions at the boundaries of the computational time window. Hence, the width of the temporal window must be large enough in order to accommodate any temporal or spectral broadening due to linear and nonlinear dispersion. An appropriate boundary will also absorb the energy reaching the edge of the window, preventing its reflections back into the computational domain. One way to estimate the width of the time window would be to estimate in advance the temporal and spectral pulse broadening. However, this is not a convenient technique especially in cases of studying super-continuum generation. In order to overcome such type of inconveniences an adequate number of time-points should be chosen. The temporal sample array of $u(z,t)$ for each z should be $M = 2^m$, which is required by FFT. The most accurate way to ensure that correct parameter values (M, h, time window) have been chosen is to change these parameters for a specific simulation until the solution has converged. However, these parameters (M, h, time window) are not the same for each simulation as the propagation distance, the pulse width and, in general, the pulse dynamics change significantly for each application. One common characteristic of our simulations was that, in most cases the step length was much shorter than ($1.0\ \mu m$).

The previous conditions are not enough to verify that the results of our developed

software are reliable. We have checked the code in many test cases in order to ensure that it is rigorous and valid. Initially, we checked that the energy is conserved along the propagation distance when the intrinsic and nonlinear losses are not taken into account. Everytime, we incorporate a nonlinear parameter in the NLSE we checked and verified its effect against published results. This can be seen in Fig.2.5. The same results are published in Agrawal's paper about silicon nanowires[2. 102]. The next step was to check if well known phenomena such as soliton generation have the same properties in silicon nanowires as in optical fibres. Indeed, our simulations as shown in Figs 2.2-2.7 verify that our results are similar to what has been published in the well-known Agrawal's book on nonlinear fibre optics [2. 57].

The last condition that we have to take into account is our assumption that the propagating optical field is assumed to be quasi-monochromatic. That means that the pulse spectrum centered at ω_0, is assumed to have a spectral width $\Delta\omega$ such that $\Delta\omega/\omega_0 << 1$. This assumption is valid for pulses as short as 100 fs. It is for this reason that the shortest pulse width used in our simulations is 180 fs and so we could develop our mathematical model based on the slowly varying envelope approximation.

One should also note here that SSF method has been developed in the current work in such a way to incorporate all the changes of linear and nonlinear parameters that occur along the propagation distance. These changes are due to the variation of the width of the silicon nanowire and those of the optical pulse. As it will be presented, we change the width of the silicon nanowire in different ways such as exponential, hyperbolic tangent or linear one. The choice of different taper profiles is based on the fact that we want to study to what extent the optical pulse dynamics are affected when the linear and nonlinear parameters change along the propagation distance. Particularly, when similariton generation or soliton pulse compression is studied, the change of the width of the silicon nanowire is important because such nonlinear phenomena have their origin in the interplay between GVD and SPM. As a result, we tried different taper profiles in order to gain a more complete view of the latter nonlinear phenomena. Another important issue should be emphasized here. Throughout the study, we have not tried to find the most efficient taper profile. This is because the linear and nonlinear dispersion maps vary significantly for different heights of silicon nanowires or by using different material for substrate. That means that the effects of width modulation are

specific to the silicon nanowire configuration. However, we have considered only taper profiles that can be easily fabricated, thus anchoring our work into the world of practical applications. In particular, the most natural transition between two waveguides with constant width follows a hyperbolic tangent profile.

One interesting note for this work is to emphasize on how all the simulation input parameters have been chosen throughout the thesis. It should be clear that all the parameters have been chosen in order the current work to be able to focus on the nonlinearities of silicon. For example, powers and wavelengths are chosen in order to show the differences in pulse dynamics between telecom and mid-IR regimes or in the chapters related to FWM all the input parameters are selected in order to attain the phase matching condition. Besides that, the whole theoretical model is implemented in a C++ code. I should mention that I have taken and edited some functions from [2. 103] and added a few more features. The simulation time is not the same for each propagation scenario. It depends on the temporal sampling of the time window and on the number of the distance steps. For example, one simple propagation scenario of launching one pulse in a silicon nanowire needs about a minute in order to be completed. However, for the case of three co-propagating pulses in the slow light regime of a silicon photonic crystal it requires more than 40 minutes.

References

[2. 1] L. Pavesi, and D. J. Lockwood, *Silicon Photonics* (Springer, New York, 2004).

[2. 2] G. T. Reed, and A. P. Knights, *Silicon Photonics: An introduction* (Wiley, Hoboken, NJ, 2004).

[2. 3] R. A. Soref, "The past, Present, and Future of Silicon Photonics," IEEE J. Sel. Top. Quantum Electron. **12**, 1678–1687 (2006).

[2. 4] N. C. Panoiu, X. Liu, and R. M. Osgood "Self steepening of ultra short pulses in Si photonic nanowires," Opt. Lett. **34**, 947–949 (2009).

[2. 5] O. Boyraz, T. Indukuri, and B. Jalali, "Self-phase-modulation induced spectral broadening in silicon waveguides," Opt. Express **12**, 829–834 (2004).

[2. 6] E. Dulkeith, Y. A. Vlasov, X. Chen, N. C. Panoiu, and R. M. Osgood, Jr, "Self-phase-modulation in submicron silicon-on-insulator photonic wires," Opt. Express **14**, 5524–5534 (2006).

[2. 7] I.-W. Hsieh, X. Chen, J. I. Dadap, N. C. Panoiu, R. M. Osgood, S. J. McNab, and Y. A. Vlasov, "Ultrafast-pulse self-phase modulation and third-order dispersion in Si photonic wire-waveguides," Opt. Express **14**, 12380–12387 (2006).

[2. 8] I.-W. Hsieh, X. Chen, J. I. Dadap, N. C. Panoiu, R. M. Osgood, S. J. McNab, and Y. A. Vlasov, "Cross-phase modulation-induced spectral and temporal effects on co-propagating femtosecond pulses in silicon photonic wires," Opt. Express **15**, 1135–1146 (2007).

[2. 9] V. R. Almeida, C.A. Barrios, R. R. Panepucci, and M. Lipson, "All-optical control of light on a silicon chip," Nature **431**, 1081–1084 (2004).

[2. 10] T. Tanabe, M. Notomi, S. Mitsugi, A. Shinya, and E. Kuramochi, "All-optical switches on a silicon chip realized using photonic crystal nanocavities," Appl. Phys. Lett. **87**, 151112 (2005).

[2. 11] S. R. Preble, Q. Xu, B. S. Schmidt, and M. Lipson, "Ultrafast all-optical modulation on a silicon chip," Opt. Lett. **30**, 2891–2893 (2005).

[2. 12] T. G. Eusera, and W. L. Vos, "Spatial homogeneity of optically switched semiconductor photonic crystals and of bulk semiconductors," Appl. Phys. Lett. **97**, 043102 (2005).

[2. 13] C. Manolatou, and M. Lipson, "All-optical silicon modulators based on carrier injection by two-photon absorption," IEEE J. Lightwave Technol. **24**, 1433–1439 (2006).

[2. 14] F. Gan, F. J. Grawert, J. M. Schley, S. Akiyama, J. Michel, K. Wada, L. C. Kimerling, and F. X. Kartner, "Design of all-optical switches based on carrier injection in Si/SiO_2 split-ridge waveguides (SRWs)," IEEE J. Lightwave Technol. **24**, 3454–3463 (2006).

[2. 15] K. Ikeda, and Y. Fainman, "Nonlinear Fabry-Perot resonator with a silicon photonic crystal waveguide," Opt. Lett. **31**, 3486–3488 (2006).

[2. 16] T. K. Liang, L. R. Nunes, T. Sakamoto, K. Sasagawa, T. Kawanishi, M. Tsuchiya, G. R. A. Priem, D. Van Thourhout, P. Dumon, R. Baets, and H. K. Tsang, "Ultrafast all-optical switching by cross-absorption modulation in silicon wire waveguides," Opt. Express **13**, 7298–7303 (2005).

[2. 17] D. J. Moss, L. Fu, I. Littler, and B. J. Eggleton, "Ultrafast all-optical modulation via two-photon absorption in silicon-on-insulator waveguides," Electron. Lett. **41**, 320–321 (2005).

[2. 18] T. K. Liang, L. R. Nunes, M. Tsuchiya, K. S. Abedin, T. Miyazaki, D. Van Thourhout, W. Bogaerts, P. Dumon, R. Baets, and H. K. Tsang, "High speed logic gate using two-photon absorption in silicon waveguides," Opt. Commun. **265**, 171–174 (2006).

[2. 19] A. Liu, H. Rong, M. Paniccia, O. Cohen, and D. Hak, "Net optical gain in a low loss silicon-on-insulator waveguide by stimulated Raman scattering," Opt. Express **12**, 4261–4268 (2004).

[2. 20] H. Rong, A. Liu, R. Nicolaescu, M. Paniccia, O. Cohen, and D. Hak, "Raman Gain and nonlinear optical absorption measurement in a low-loss silicon waveguide," Appl. Phys. Lett. **85**, 2196–2198 (2004).

[2. 21] T. K. Liang, and H. K. Tsang, "Efficient Raman amplification in silicon-on-insulator waveguides," Appl. Phys. Lett. **85**, 3343–3345 (2004).

[2. 22] T. K. Liang, and H. K. Tsang, "Role of free carriers from two-photon absorption in Raman amplification in silicon-on-insulator waveguides," Appl. Phys. Lett. **84**, 2745–2747 (2004).

[2. 23] R. Claps, V. Raghunathan, D. Dimitropoulos, and B. Jalali, "Influence of nonlinear absorption on Raman amplification in silicon waveguides," Opt. Express **12**, 2774–2780 (2004).

[2. 24] T. K. Liang, and H. K. Tsang, "Nonlinear absorption and Raman scattering in silicon-on-insulator optical waveguides," IEEE J. Quantum Electron. **10**, 1149–1153 (2004).

[2. 25] R. A. Soref, and J. P. Lorenzo, "Single-crystal silicon: a new material for 1.3 and 1.6 μm integrated-optical components," Electron. Lett. **21**, 953–954 (1985).

[2. 26] R. A. Soref, and J. P. Lorenzo, "All-silicon active and passive guided-wave components for $\lambda = 1.3$ and $\lambda = 1.6$ μm," IEEE J. Quantum Electron. **22**, 873–879 (1986).

[2. 27] Y. A. Vlasov, and S. J. McNab, "Losses in single-mode silicon-on-insulator strip waveguides and bends," Opt. Express **12**, 1622–1631 (2004).

[2. 28] K. K. Lee, "Transmission and routing of optical signals in on-chip waveguides for silicon microphotonics," Ph.D. dissertation, Dept. Materials Science Eng., Mass. Inst. Technol., Cambridge (2001).

[2. 29] F. Xia, L. Sekaric, and Y. A. Vlasov, "Ultracompact optical buffers on a silicon chip," Nat. Photonics **1**, 6571 (2007).

[2. 30] M. P. Nezhad, O. Bondarenko, M. Khajavikhan, A. Simic, and Y. Fainman, "Etch-free low loss silicon waveguides using hydrogen silsesquioxane oxidation masks," Opt. Express **19**, 18827–18832 (2011).

[2. 31] G. Li, J. Yao, Y. Luo, H. Thacker, A. Mekis, X. Zheng, I. Shubin, J.-H. Lee, K. Raj, J. E. Cunningham, and A. V. Krishnamoorthy, "Ultralow-loss, high-density SOI optical waveguide routing for macrochip interconnects," Opt. Express **20**, 12035–12039 (2012).

[2. 32] H. Lee, T. Chen, J. Li, O. Painter, and K. J.Vahala, "Ultra-low-loss optical delay line on a silicon chip", Nat Commun., **3**, 860–867 (2012).

[2. 33] V. R. Almeida, R. R. Panepucci, and M. Lipson, "Nanotaper for compact mode conversion," Opt. Lett. **28**, 1302–1304 (2003).

[2. 34] T. Shoji, T. Tsuchizawa, T. Watanabe, K. Yamada, and H. Morita, "Low loss mode size converter from 0.3 μm square Si wire waveguides to singlemode fibres," Electron. Lett. **38**, 1669–1670 (2002).

[2. 35] W. Bogaerts, R. Baets, P. Dumon, V. Wiaux, S. Beckx, D. Taillaert, B. Luyssaert, J. van Campenhout, P. Bienstman, and D. van Thourhout, "Nanophotonic waveguides in silicon-on-insulator fabricated with CMOS technology," IEEE J. Lightwave Technol. **23**, 401–412 (2005).

[2. 36] R. Claps, D. Dimitropoulos, Y. Han, and B. Jalali, "Observation of Raman emission in silicon waveguides at 1.54 μm," Opt. Express **10**, 1305–1313 (2002).

[2. 37] J. I. Dadap, R. L. Espinola, R. M. Osgood, Jr, S. J. McNab, and Y. A. Vlasov, "Spontaneous Raman scattering in ultrasmall silicon waveguides," Opt. Lett. **29**, 2755–2757 (2004).

[2. 38] R. Claps, D. Dimitropoulos, V. Raghunathan, Y. Han, and B. Jalali, "Observation of stimulated Raman amplification in silicon waveguides," Opt. Express **11**, 1731–1739 (2003).

[2. 39] R. L. Espinola, J. I. Dadap, R. M. Osgood, Jr, S. J. McNab, and Y. A. Vlasov, "Raman amplification in ultrasmall silicon-on-insulaator wire waveguides," Opt. Express **12**, 3713–3718 (2004).

[2. 40] O. Boyraz, and B. Jalali, "Demonstration of 11 dB fibre-to-fibre gain in a silicon Raman amplifier," IEICE Electron. Express **1**, 429–434 (2004).

[2. 41] Q. Xu, V. R. Almeida, and M. Lipson, "Demonstration of high Raman gain in a submicrometer-size silicon-on-insulator waveguide," Opt. Lett. **30**, 35–37 (2005).

[2. 42] R. Claps, V. Raghunathan, O. Boyraz, P. Koonath, D. Dimitropoulos and B. Jalali, "Raman amplification and lasing in SeGe waveguides," Opt. Express **13**, 2459–2466 (2005).

[2. 43] S. G. Cloutier, P. A. Kossyrev, and J. Xu, "Optical gain and stimulated emisson in perriodic nanopatterned crystalline silicon," Nat. Mater. **4**, 887–891 (2005).

[2. 44] J. F. McMillan, X. Yang, N. C. Panoiu, R. M. Osgood, and C. W. Wong, "Enhanced stimulated Raman scattering in slow-light photonic crystal waveguides," Nat. Mater. **31**, 1235–1237 (2006).

[2. 45] Q. Xu, V. R. Almeida, and M. Lipson, "Micrometer-scale all-optical wavelength converter on silicon," Opt. Lett. **30**, 2733–2735 (2005).

[2. 46] Y.-H. Kuo, H. Rong, V. Sih, S. Xu, M. Paniccia, and O. Cohen, "Demonstration of wavelength conversion at $40Gb/s$ data rate in silicon waveguides," Opt. Express **14**, 11721–11726 (2006).

[2. 47] M. A. Foster, A. C. Turner, J. E. Sharping, B. S. Schmidt, M. Lipson, and A. L. Gaeta, "Broad-band optical parametric gain on a silicon photonic chip," Nature **441**, 960–963 (2006).

[2. 48] K. Yamada, H. Fukuda, T. Tsuchizawa, T. Watanabe, T. Shoji, and S. Itabashi "All-optical efficient wavelength conversion using silicon photonic wire waveguide," IEEE Photon. Technol. Lett. **18**, 1046–1048 (2006).

[2. 49] Q. Lin, J. Zhang, P. M. Fauchet, and G. P. Agrawal, "Ultrabroadband parametric generation and wavelength conversion in silicon waveguides," Opt. Express **14**, 4786–4799 (2006).

[2. 50] H. K. Tsang, C. S. Wong, T. K. Liang, I. E. Day, S. W. Roberts, A. Harpin, J. Drake, and M. Asghari, "Optical dispersion, two-photon absorption and self-phase modulation in silicon waveguides at 1.5 μm wavelength," Appl. Phys. Lett. **80**, 416–418 (2002).

[2. 51] G. W. Rieger, K. S. Virk, and J. F. Young, "Nonlinear propagation of ultrafst 1.5 μm pulses in high-index-contrast silicon-on-insulator waveguides," Appl. Phys. Lett. **84**, 900–902 (2004).

[2. 52] A. Cowan, G. Rieger, and J. Young, "Nonlinear trasnission on 1.5 μm pulses through single-mode silicon-on-insulator waveguide structures," Opt. Express **12**, 1611–1621 (2004).

[2. 53] H. Yamada, M. Shirane, T. Chu, H. Yokoyama, S. Ishida, and Y. Arakawa, "Nonlinear-optic silicon-nanowire waveguides," Jpn. J. Appl. Phys., Part 1 **44**, 6541–6545 (2005).

[2. 54] R. Dekker, A. Driessen, T. Wahlbrink, C. Moormann, J. Niehusmann, and M. Forst, "Ultrafast Kerr-induced all-optical wavelength conversion in silicon waveguides using 1.55 μm femtosecond pulses," Opt. Express **14**, 8336–8346 (2006).

[2. 55] O. Boyraz, P. Koonath, V. Raghunathan, and B. Jalali, "All optical switching and continuum generation in silicon waveguides," Opt. Express **12**, 4094–4102 (2004).

[2. 56] I.-W. Hsieh, X. Chen, X. Liu, J. I. Dadap, N. C. Panoiu, C. -Y. Chou, F. Xia, W. M. Green, Y. A. Vlasov, and R. M. Osgood, "Supercontinuum generation in silicon photonic wires," Opt. Express **15**, 15242–15249 (2007).

[2. 57] G. P. Agrawal, "Nonlinear Fibre Optics," 4th ed., Academic Press (2006).

[2. 58] Osgood, R. M. , Panoiu, N. C., Dadap, J. I., Liu, X., Chen, X., Hsieh, I-W, Dulkeit, E., Green, W. M. J., and Vlassov, Y. A., Engineering nonlinearities in nanoscale optical systems: physics and applications in dispersion engineered silicon nanophotonics wires, Adv.Opt.Photon. **1**, 162–235 (2009).

[2. 59] S. Lavdas and N. C. Panoiu, *"Theory of Pulsed Four-Wave-Mixing in One-dimensional Silicon Photonic Crystal Slab Waveguides,"* Phys. Rev. B (submitted).

[2. 60] R. W. Boyd, "Nonlinear Optics," 2nd ed., Academic Press (2002).

[2. 61] J. Zhang, Q. Lin, G. Piredda, R. W. Boyd, G. P. Agrawal, and P. M. Fauchet, "Anisotropic nonlinear response of silicon in the near-infrared region," Appl. Phys. Lett. **91**, 071113 (2007).

[2. 62] V. I. Kruglov, A. C. Peacock, J. D. Harvey and J. M Dudley, "Self-Similar propagation of parabolic pulses in normal-dispersion fibre amplifiers," J. Opt. Soc. Am. B. **19**, 461–469 (2002).

[2. 63] N. Healy, J. R. Sparks, P. J. A. Sazio, J. V. Badding, and A. C. Peacock, "Tapered silicon optical fibres," Opt. Express **18**, 7596–7601 (2010).

[2. 64] A. Peacock and N. Healy, "Parabolic pulse generation in tapered silicon fibres," Opt. Lett. **35**, 1780–1782 (2010).

[2. 65] C. Finot, L. Provost, P. Petropoulos, and D. J. Richardson, "Parabolic pulse generation through passive nonlinear pulse reshaping in a normally dispersive two segment fibre device," Opt. Express **15**, 852–864 (2006).

[2. 66] S. Lavdas, J. B. Driscoll, H. Jiang, R. R. Grote, R. M. Osgood, Jr., and N. C. Panoiu, "Generation of parabolic similaritons in tapered silicon photonic wires: comparison of pulse dynamics at telecom and mid-infrared wavelengths," Opt. Lett. **38**, 3953–3956 (2013).

[2. 67] S. Lavdas, J. B. Driscoll, R. R. Grote, R. M. Osgood, Jr., and N. C. Panoiu, "Generation and collision of optical similaritons in dispersion engineered silicon photonic nanowires," Spie Proceedings **8816**, (2013).

[2. 68] J. B. Driscoll, N. Ophir,R. R. Grote,J. I. Dadap, N. C. Panoiu, K. Bergman, and R. M. Osgood, Jr., "Width-modulation of Si photonic wires for quasi-phase-matching of four-wave-mixing: experimental and theoretical demonstration," Opt. Express **38**, 9227–9242 (2012).

[2. 69] K. Ohtaka, "Energy band of photons and low-energy photon diffraction," Phys. Rev. B **19**, 5057-5067 (1979).

[2. 70] E. Yablonovich, "Inhibited spotaneous emission in solid-state physics and electronics," Phys. Rev. Lett. **58**, 2059-2063 (1987).

[2. 71] S. John, "Strong localization of photons in certain disordered dielectric superlattice," Phys. Rev. Lett. **58**, 2059-2063 (1987).

[2. 72] S. A. Schulz, L. O'Falain, D. M. Beggs, T. P. White, A. Melloni, and T. F. Krauss, "Dispersion engineered slow light in photonic crystals: a comparison," J. Opt. **12**, 104004 (2010)

[2. 73] Baba T., Mori D., Inoshita K., and Kuroki Y., "Light localizations in photonic crystal line defect waveguides," IEEE J. Sel. Top. Quantum Electron. **10**, 484 (2004).

[2. 74] L. H. Frandsen, A. V. Lavrinenko, J. Fage-Pedersen, and P. I. Borel, "Photonic crystal waveguides with semi-slow light and tailored dispersion properties,"Opt. Express **14**, 9444 (2006).

[2. 75] A. Y. Petrov and M. Eich, "Zero dispersion at small group velocities in photonic crystal waveguides," Appl. Phys. Lett. , **85**, 4866 (2004).

[2. 76] M. Notomi, K. Yamada, A. Shinya, J. Takahashi, C. Takahashi, and I. Yokohama, "Extremely large group-velocity dispersion of line-defect waveguides in photonic crystal slabs,"Phys. Rev. Lett. **87**, 253902 (2001).

[2. 77] A. Petrov, M. Krause and M. Eich, "Backscattering and disorder limits in slow light photonic crystal waveguides," Opt. Express , vol. **17**, 8676 (2009).

[2. 78] J. M. Brosi, C. Koos, L. C. Andreani, M. Waldow, J. Leuthold, and W. Freude, "High-speed low-voltage electro-optic modulator with a polymer-infiltrated silicon photonic crystal waveguide," Opt. Express **16**, 4177 (2008).

[2. 79] D. A. B. Miller, "Rationale and challenges for optical interconnects to electronic chips," Proc. IEEE **88**, 728–749 (2000).

[2. 80] A. Shacham, K. Bergman, and L. P. Carloni, "On the design of a photonic network-on-chip," Proceeding of the IEEE International Symposium on Networks-on-Chip (NOCS'07)(IEEE,2007), paper 2.1.

[2. 81] B. G. Lee, X. G. Chen, A. Biberman, X. P. Liu, I.-W. Hsieh, C. Y. Chou, J. I. Dadap, F. N. Xia, W. M. J. Green, L. Sekaric, Y. A. Vlasov, R. M. Osgood and K. Bergman, "Ultrahigh-bandwidth silicon photonic nanowire waveguides for on-chip networks," IEEE Photon. Technol. Lett. **20**, 398–400 (2008).

[2. 82] S. Lavdas, J. B. Driscoll, R. R. Grote, R. M. Osgood, Jr., and N. C. Panoiu, "Pulse compression in adiabatically tapered silicon photoni wires," Opt. Lett. (submitted), (2013).

[2. 83] M. A. Foster, A. C. Turner, R. Salem, M. Lipson, and A. L. Gaeta, "Broad-band continuous-wave parametric wavelength conversion in silicon nanowaveguides," Opt. Express **15**, 12949–12958 (2007).

[2. 84] S. Lavdas, S. Zhao, J. B. Driscoll, R. R. Grote, R. M. Osgood, Jr., and N. C. Panoiu, "Wavelength conversion of optical pulses using quasi-phase-matching of four wave mixing in Si photonic nanowires," (to be submitted) (2014).

[2. 85] R. Salem, G. E. Tudury, T. U. Horton, G. M. Carter, and T. E. Murphy, "Polarization-insensitive optical clock recovery at 80 Gb/s using a silicon photodiode," IEEE Photon. Technol. Lett. **17**, 1968–1970 (2005).

[2. 86] J. M. Dudley, G. Genty, and S. Coen, "Supercontinuum generation in photonic crystal fibre," Rev. Mod. Phys. **78**, 1135–1184 (2006).

[2. 87] W. Drexler, "Ultrahigh-resolution optical coherence tomography," J. Biomed. Opt. **9**, 47–74 (2004).

[2. 88] J. Leuthold, C. Koos, and W. Freude, "Nonlinear silicon photonics," Nat. Photonics **4**, 535–544 (2010).

[2. 89] U. Willer, M. Saraji, A. Khorsandi, P. Geiser, and W. Schade, "Near- and mid-infrared laser monitoring of industrial processes, environment and security applications," Opt. Laser Eng. **44**, 699–710 (2006).

[2. 90] K. Namjou, C. B. Roller, and P. J. McCann, “The Breathmeter: A new laser device to analyze your health,” IEEE Circuits & Devices Magazine, 22–28, (2006).

[2. 91] J. A. Seeley and J. M. Richardson, “Early warning chemical sensing,” Lincoln Laboratory Journal **17**, 85–99 (2007).

[2. 92] R. Furstenberg, C. A. Kendziora, J. Stepnowski, S. V. Stepnowski, M. Rake, M. R. Papantonakis, V. Nguyen, G. K. Hubler, and R. A. McGill, “Stand-off detection of trace explosives via resonant infrared photothermal imaging,” Appl. Phys. Lett. **93**, 224103 (2008).

[2. 93] M. A. Van Camp, S. Assefa, D. M. Gill, T. Barwicz, S. M. Shank, Y. A. Vlasov, and W. M. J. Green, “Silicon nanophotonic mid-IR MachZehnder electrooptic modulator,” presented at the Conference on Lasers and Electro-Optics San Jose, USA, 2012.

[2. 94] X. Liu, B. Kuyken, G. Roelkens, R. Baets, J. Osgood, R. M., and W. M. J. Green, “Bridging the mid-infrared-to-telecom gap with silicon nanophotonic spectral translation,” Nature Photon. **6**, 667-671 (2012).

[2. 95] J. E. Sharping, Y. Okawachi, J. van Howe, C. Xu, Y. Wang, A. E. Willner, and A. L. Gaeta, “All-optical,wavelength and bandwidth preserving, pulse delay based on parametric wavelength conversion and dispersion,” Opt. Express **13**, 7872-7877 (2005).

[2. 96] E. Parra and J. R. Lowell, “Toward applications of slow-light technology,” Opt. Photon. News **18**, 4145 (2007).

[2. 97] M. D. Lukin and A. Imamoglu, “Nonlinear Optics and Quantum Entanglement of Ultraslow Single Photons,” Phys. Rev. Lett. **84**, 1419 (2000)

[2. 98] B. Corcoran, C. Monat, C. Grillet, D. J. Moss, B. J. Eggleton, T. P. White, L. O’Faolain, and T. F. Krauss, “Green light emission in silicon through slow-light enhanced third-harmonic generation in photonic-crystal waveguides,” Nat. Photonics **3**, 206 - 210 (2009).

[2. 99] J. A. Fleck, J. R. Morris, M. D. Feit, “Time-Dependent Propagation of High Energy Laser Beams through the Atmosphere,” Appl. Phys. **10**, 129–160 (1976).

[2. 100] J. W. Cooley, and J. W. Tukey, “An algorithm for the machine calculation of complex Fourier series,” Math. Comp. **19**, 297301 (1965).

[2. 101] T. R. Taha, and M. J. Ablowitz, ”Analytical and numerical aspects of certain nonlinear evolution equations. II. Numerical, nonlinear Schrdinger equation”J. Comput. Phys. **55**, 203230 (1984).

[2. 102] Q. Lin, O. J. Painter, and G. P. Agrawal, “Nonlinear optical phenomena in silicon waveguide: Modelling and applications,” Opt. Express **15**, 16604–16644 (2007).

[2. 103] William H. Press and Saul A. Teukolsky, William T. Vetterling, and Brian P. Flannery, “Numerical Recipes in C: The Art of Scientific Computing”, Cambridge University Press, (1992).

Chapter 3

Similariton generation in silicon photonic nanowires

3.1 Introduction

Generation of pulses with specific spectral and temporal characteristics is a key functionality needed in many applications in ultrafast optics, optical signal processing, and optical communications. One type of such pulses are those that preserve their shape upon propagation. Solitons are the most ubiquitous example of such a pulse that form in the anomalous GVD regime, whereas their counterpart in the normal GVD region are self-similar pulses, called similaritons [3. 1–3]. Unlike solitons, which require a threshold power, no constraints have to be imposed on the pulse energy, initial shape, or optical phase profile to generate similaritons in silicon nanowires [3. 4, 5]. Due to their self-similar propagation, similaritons do not undergo wave breaking and the linear chirp they acquire during their formation makes it easy to employ dispersive pulse compression techniques to generate nearly transform-limited pulses. These remarkable properties of similaritons have provided a strong incentive for their study, and optical similaritons have been demonstrated in active optical fibre systems such as Yb-doped fibre amplifiers [3. 3, 6], using passive schemes based on dispersion-managed or tapered silica fibres [3. 7–10], and high-power fibre amplifiers [3. 11–13].

Driven by the ever growing demand for enhanced integration of complex optoelectronic architectures that process increasing amounts of data, finding efficient ways to extend the regime of self-similar pulse propagation to chip-scale photonic devices is becoming more pressing. One promising approach, based on silicon (Si) fibres with

micrometre-sized core dimensions [3. 14], has recently been proposed [3. 15]. A further degree of device integration can be achieved by employing Si-PhNWs with submicrometer transverse size fabricated on a silicon-on-insulator material system [3. 16]. In addition to the enhanced optical nonlinearity, which allows for increased device integration, Si-PhNWs enable seamless integration with complementary metal-oxide semiconductor technologies. The use of Si-PhNWs can be extended to the mid-infrared (mid-IR) region ($\lambda \gtrsim 2.2\ \mu$m) [3. 17], where silicon provides superior functionality due to low TPA and, thus, reduced free-carrier absorption (FCA). In fact, it has already been shown that nonlinear optical effects such as modulational instability [3. 18, 19], frequency dispersion of the nonlinearity [3. 21], and supercontinuum generation [3. 19, 22–24], can be used to achieve significant pulse reshaping in millimeter-long Si-PhNWs (for a review, see [3. 25]). Before we continue with our theoretical model we should mention that we have used a linear and an exponential taper profile in the current chapter in order to study how the width variation of the silicon nanowire affect the efficiency of the similariton generation process.

3.2 Mathematical formulation

The pulse dynamics that emerge during the optical pulse propagation in silicon nanowires are described by the following equation [3. 21, 26–28]:

$$i\frac{\partial u}{\partial z}+\sum_{n=1}^{3}\frac{i^n\beta_n(z)}{n!}\frac{\partial^n u}{\partial t^n}=-\frac{ic\kappa(z)}{2nv_g(z)}\alpha_{\mathrm{FC}}(z)u-\frac{\omega\kappa(z)}{nv_g(z)}\delta n_{\mathrm{FC}}(z)u - \gamma(z)\left[1+i\tau(z)\frac{\partial}{\partial t}\right]|u|^2u, \tag{3.1}$$

where $u(z,t)$ is the pulse envelope, measured in $\sqrt{\mathrm{W}}$, z and t are the distance along the Si-PhNW and time, respectively, $\beta_n(z)=d^n\beta/d\omega^n$ is the nth order dispersion coefficient, $\kappa(z)$ quantifies the overlap between the optical mode and the active area of the waveguide, $v_g(z)$ is the group-velocity, $\delta n_{\mathrm{FC}}(z)$ [$\alpha_{\mathrm{FC}}(z)$] are the free-carrier (FC) induced index change (losses) and are given by $\delta n_{\mathrm{FC}}(z)=-e^2/2\varepsilon_0 n\omega^2\left[N(z)/m^*_{ce}+N(z)^{0.8}/m^*_{ch}\right]$ and $\alpha_{\mathrm{FC}}(z)=e^3N(z)/\varepsilon_0 cn\omega^2(1/\mu_e {m^*_{ce}}^2+1/\mu_h {m^*_{ch}}^2)$, respectively, where N is the FC density, $m^*_{ce}=0.26m_0$ ($m^*_{ch}=0.39m_0$) is the electrons (holes) effective mass, with m_0 the electron mass, and μ_e (μ_h) the elec-

tron (hole) mobility. One should note here that the intrinsic losses have not been taken into account as their characteristic length is much longer than the propagation distance studied in this work. According to this, intrinsic losses do not have any influence in parabolic pulse generation process.

The nonlinear properties of the waveguide are described by the nonlinear coefficient, $\gamma(z) = 3\omega\Gamma(z)/4\varepsilon_0 A(z)v_g^2(z)$, where $A(z)$ and $\Gamma(z)$ are the cross-sectional area and the effective third-order susceptibility of the waveguide, respectively. Nonlinear optical effects higher than the third-order are not considered here although at high peak power they might become important. One interesting part of Eq. (3.1) is the shock time scale, *i.e.* the characteristic response time of the nonlinearity, $\tau(z)$. The explicit formula of $\tau(z)$ is the following one:

$$\tau(z) = \partial \ln \gamma(z)/\partial\omega, \tag{3.2}$$

We should stress at that point that we have expressed the characteristic response time of the nonlinearity in such a way in order to make the initial NLSE, Eq. (2.39), shorter. We also want to show the dependence of the shock time on $\gamma(z)$. If one wants to formulate Eq. (2.39) then $\gamma(z)$ should be replaced into Eq. (3.1) as it follows:

$$\tau(z) = (\frac{1}{\omega} + \frac{\partial\Gamma}{\Gamma\partial\omega}). \tag{3.3}$$

By multiplying and dividing the term $\frac{\partial\Gamma}{\Gamma\partial\omega}$ with v_g^2, Eq. (3.3) is formulated as it follows:

$$\tau(z) = (\frac{1}{\omega} + \frac{\partial g(\omega)}{g(\omega)\partial\omega}), \tag{3.4}$$

where $g(\omega) = \frac{\Gamma}{v_g^2}$. By replacing Eq. (3.4) into Eq. (3.1) one can derive the initial NLSE, Eq. (2.39). Besides that, our model is completed by a rate equation for the FC density,

$$\frac{\partial N}{\partial t} = -\frac{N}{t_c} + \frac{3\Gamma''(z)}{4\varepsilon_0\hbar A^2(z)v_g^2(z)}|u|^4, \tag{3.5}$$

where Γ'' (Γ') is the imaginary (real) part of Γ and t_c is the FCs recombination time (in this work, $t_c = 1$ ns).

3.3 Dispersion properties of Si-PhNWs

The system (3.1)-(3.5) provides a rigorous description of pulse propagation in Si-PhNWs with adiabatically varying transverse size since the z-dependence of the waveguide parameters is fully incorporated in our model *via* the implicit dependence of the modes of the Si-PhNW on its transverse size. Thus, we consider a tapered ridge waveguide with a silicon rectangular core buried in SiO_2, with height, $h = 250$ nm, and width, w, varying from w_{in} to w_{out} between the input and output facets, respectively. Our colleagues in Columbia university used a finite-element mode solver to determine the propagation constant, $\beta(\lambda)$, and the fundamental TE-like mode, for $1.3\ \mu\text{m} \leq \lambda \leq 2.3\ \mu\text{m}$ and for 51 values of the waveguide width ranging from 500 nm to 1500 nm. The dispersion coefficients are calculated by fitting $\beta(\lambda)$ with a 12th order polynomial and subsequently calculating the derivatives with respect to ω. Alternatively, direct numerical differentiation can be used [3. 29] or other rigorous and efficient

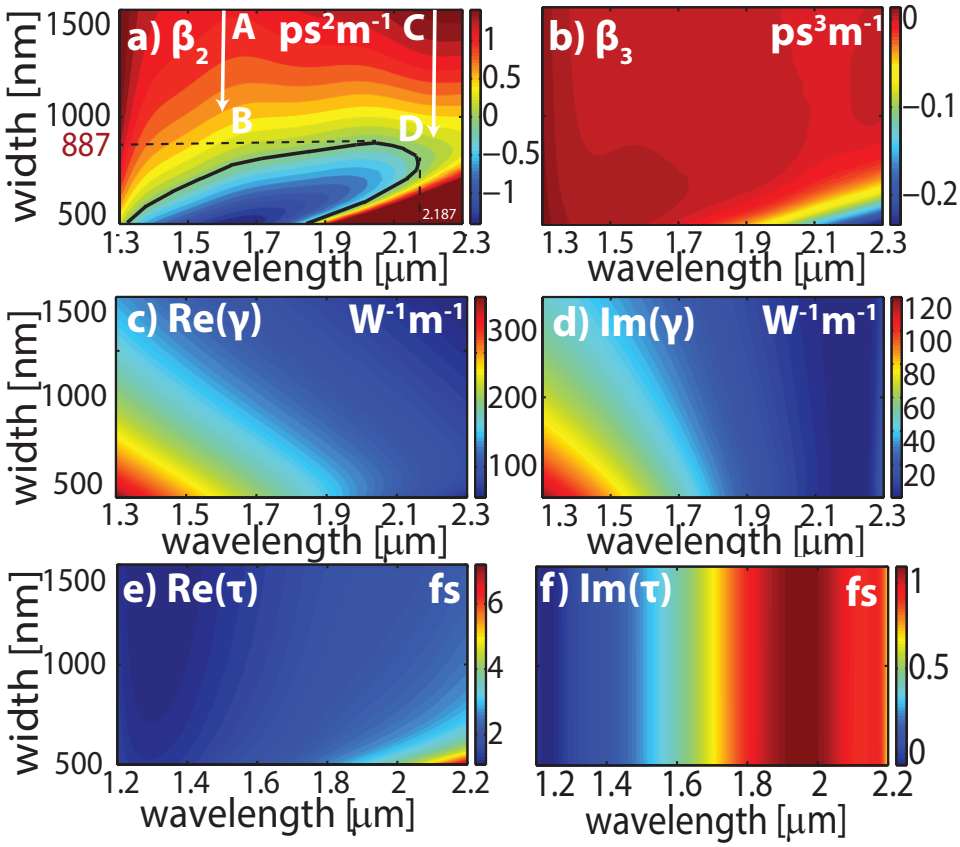

Figure 3.1: Dispersion maps of a) GVD coefficient, β_2, b) third-order dispersion coefficient, β_3, c) self-phase modulation coefficient, γ', d) TPA coefficient, γ'', and e) real and f) imaginary part of the shock-time, τ. In a), $\beta_2 = 0$ on the black contour and arrows indicate the limits of w, at $\lambda = 1.55\ \mu$m and $\lambda = 2.2\ \mu$m.

numerical methods can be employed [3. 20]. Using these results and the optical modes, the parameters, κ, γ, and τ, are computed for all values of w. Their z-dependence is then found by polynomial interpolation.

3.4 Results

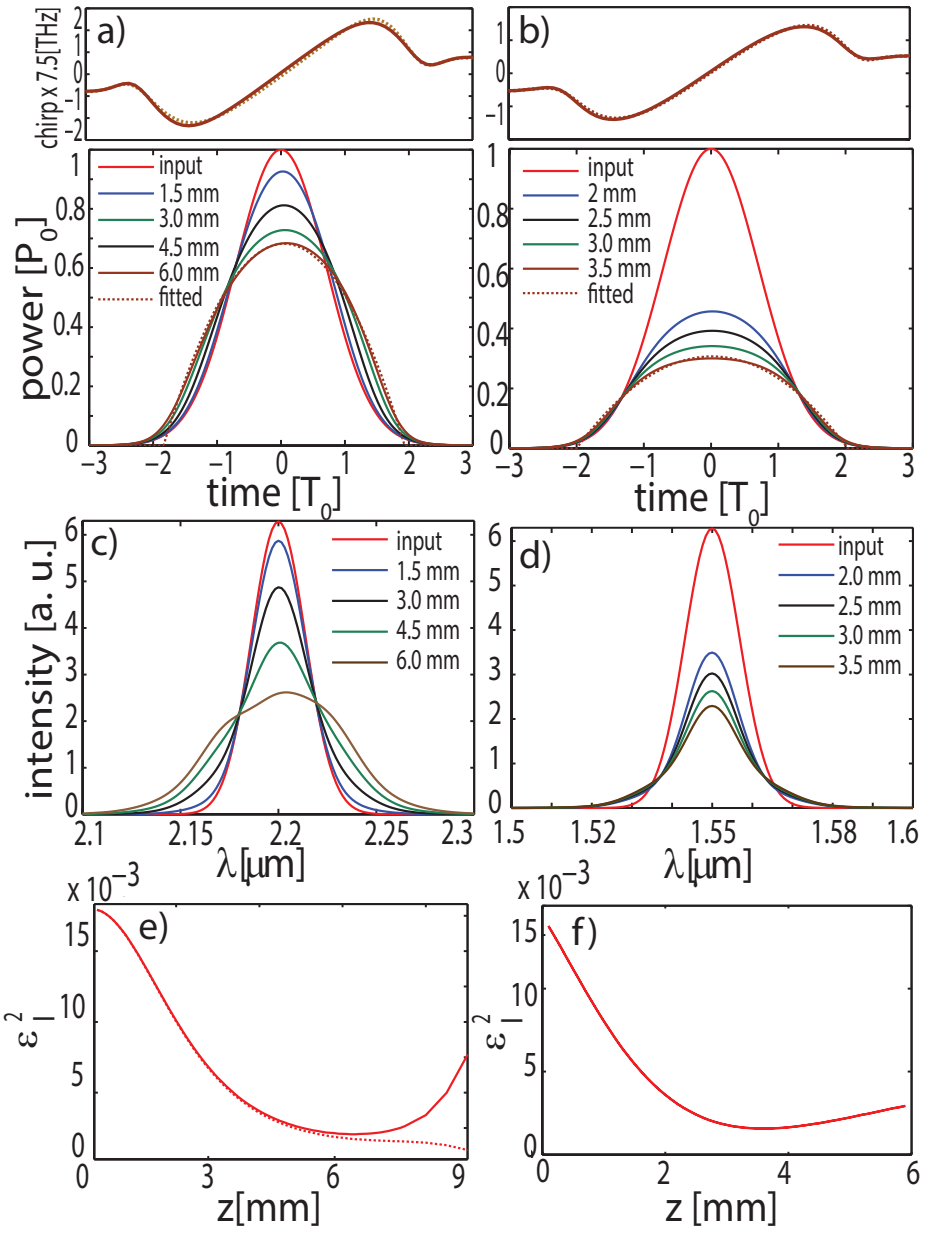

Figure 3.2: Temporal pulse shape (normalized to input power $P_0 = 7\ W$) with increasing z and the chirp of the output pulse, calculated for the full model (solid line) and for $\beta_3 = 0$ and $\tau = 0$ (dotted line) (top panels) and the corresponding pulse spectra (bottom panels). e)-f) ε_I^2 *vs.* z, for the full model (solid line) and for $\beta_3 = 0$ and $\tau = 0$ (dotted line). Left (right) panels correspond to $\lambda = 2.2\ \mu$m ($\lambda = 1.55\ \mu$m).

The results of this analysis are summarized in Fig. 3.1, where we plot the disper-

sion maps of the waveguide parameters. Thus, Fig. 3.1(a) shows that if $w < 887$ nm the Si-PhNW has two zero GVD wavelengths, defined by $\beta_2(\lambda, w) = 0$, whereas if $w > 887$ nm the Si-PhNW has normal GVD in the entire spectral domain. In addition, if $\lambda > 2187$ nm the waveguide has normal GVD for any w. Important properties of the Si-PhNW are revealed by the dispersion maps of the nonlinear coefficients as well. Specifically, the strength of the nonlinearity, $\gamma'(\lambda, w)$, decreases with both increasing w and λ, meaning that in the range of wavelengths and waveguide widths explored here, nonlinear effects in Si-PhNWs are stronger if narrow waveguides are used at lower wavelengths. On the other hand the TPA coefficient, $\gamma''(\lambda, w)$, and consequently nonlinear losses, decrease with w and λ, which suggests that the waveguide parameters and wavelength must be properly chosen for optimum device operation. Finally, as seen in Fig. 3.1(e), the shock time $\tau'(\lambda, w)$ has large values at long wavelengths but decreases with w.

physical parameters	$\lambda = 1.55\mu m$	$\lambda = 2.2\mu m$
T_{FWHM} $[fs]$	220	220
P_0 $[W]$	7	7
$\alpha_{in}[dB\ cm^{-1}]$	0	0
w_{in} $[nm]$	1500	1500
w_{out} $[nm]$	1080	850
β_{TPA} $[cm/GW]$	$1.3{\cdot}10^{-11}$	$1.5{\cdot}10^{-13}$
n_2 $[cm^2/W]$	$5.37{\cdot}10^{-18}$	$1.04{\cdot}10^{-17}$
$\beta_1(in)$ $[ps/m]$	$1.26{\cdot}10^{4}$	$1.21{\cdot}10^{4}$
$\beta_2(in)$ $[ps^2/m]$	1.11	1.53
$\beta_3(in)$ $[ps^3/m]$	$0.5{\cdot}10^{-3}$	$-2.9{\cdot}10^{-3}$
$\gamma'(in)$ $[W^{-1}m^{-1}]$	107.2	59.26
$\gamma''(in)$ $[W^{-1}m^{-1}]$	32.63	0.3
$\tau'(in)$ $[fs]$	1.36	2.24
$\tau''(in)$ $[fs]$	0.34	0.6
$\beta_1(out)$ $[ps/m]$	$1.27{\cdot}10^{4}$	$1.25{\cdot}10^{4}$
$\beta_2(out)$ $[ps^2/m]$	$79{\cdot}10^{-2}$	$88{\cdot}10^{-3}$
$\beta_3(out)$ $[ps^3/m]$	$1.4{\cdot}10^{-3}$	$-1.37{\cdot}10^{-3}$
$\gamma'(out)$ $[W^{-1}m^{-1}]$	141.23	74.95
$\gamma''(out)$ $[W^{-1}m^{-1}]$	44.16	$387{\cdot}10^{-3}$
$\tau'(out)$ $[fs]$	1.44	2.55
$\tau''(out)$ $[fs]$	$3.38{\cdot}10^{-1}$	$59{\cdot}10^{-2}$
L $[mm]$	3.5	6

Table 3.1: Input pulse parameters for the two cases presented in Fig. 3.1(a) (arrow $A-B$ and arrow $C-D$).

To investigate the formation of self-similar pulses, we launch a Gaussian pulse, $u(t) = \sqrt{P_0}e^{-t^2/2T_0^2}$, in an exponentially tapered Si-PhNW, $w(z) = w_{\text{in}}e^{-az}$. We study similariton generation in telecom and mid-infrared wavelengths. All the input pulse parameters which used for our simulations are presented in Table-3.1. In Fig. 3.2 we plot the pulse profile and its spectrum, calculated for several values of z. As expected, the pulse decay is stronger at $\lambda = 1.55$ μm as compared to that at $\lambda = 2.2$ μm, due to larger TPA. The stronger nonlinear effects at $\lambda = 2.2$ μm are also revealed by the spectral ripples that start to form at $z \gtrsim 5$ mm (no such modulations are seen at $\lambda =$ 1.55 μm). Also, the pulse becomes more asymmetric at $\lambda = 2.2$ μm, due to increased τ [3. 21]. However, the most important phenomenon revealed by Fig. 3.2 is that at both wavelengths the pulse evolves into a parabolic one, $|u_p(t)|^2 = |u_p(t_0)|^2[1-(t-t_0)^2/T_p^2]$ for $|t-t_0| < T_p$ and $u_p(t) = 0$ otherwise, where $u_p(t_0)$, t_0, and T_p are the amplitude, time shift, and pulse width, respectively.

The generation of parabolic pulses can be quantitatively characterized by the intensity misfit parameter, ε_I, which provides a global measure of how close the pulse profile is to a parabolic one; it is defined as [3. 15]:

$$\varepsilon_I^2 = \frac{\int[|u(t)|^2 - |u_p(t)|^2]^2 dt}{\int |u(t)|^4 dt}. \tag{3.6}$$

Figures 3.2(e) and 3.2(f) show that at both wavelengths there is a certain optimum waveguide length at which ε_I^2 reaches a minimum value, *i.e.* $\varepsilon_I^2 = 1.67 \times 10^{-3}$ ($\varepsilon_I^2 = 1.57 \times 10^{-3}$) at $\lambda = 2.2$ μm ($\lambda = 1.55$ μm). The small values of ε_I^2 provide clear evidence of the formation of parabolic pulses. The pulse becomes closer to a parabolic pulse at $\lambda = 1.55$ μm because the effects that induce pulse asymmetry are smaller at this wavelength. This can also be seen by comparing the dependence $\varepsilon_I^2(z)$ in the case of the full model (3.1)-(3.5) and when higher-order effects are neglected ($\beta_3 = 0$ and $\tau = 0$). Thus, at $\lambda = 1.55$ μm, $\varepsilon_I^2(z)$ is almost unaffected if one neglects these effects, whereas in the same conditions, at $\lambda = 2.2$ μm, the minimum of $\varepsilon_I^2(z)$ decreases considerably to 0.41×10^{-3} (and is reached at $z = 9.52$ mm).

A fundamental characteristic of parabolic pulses is that across the pulse the frequency chirp varies linearly with time. The pulses generated in our numerical experiments clearly have this property, as illustrated in the top panels of Figs. 3.2(a) and

3.2(b). These figures also show that, at both wavelengths, this linear time dependence of the chirp is preserved even in the presence of higher-order effects, which demonstrates the robustness against perturbations of the parabolic pulse generation.

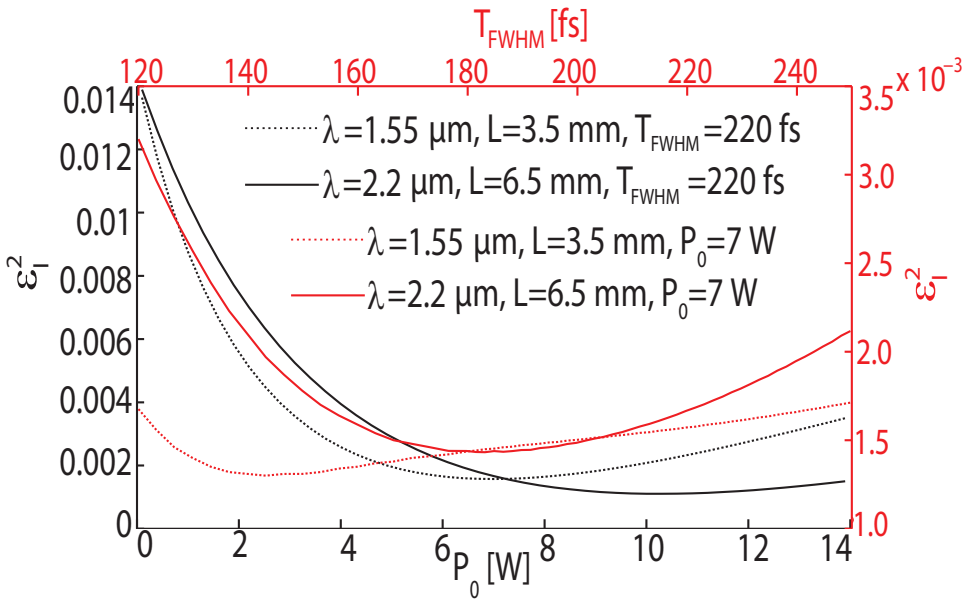

Figure 3.3: Dependence of ε_I^2 on pulse width and power.

The dependence of the similariton generation on the pulse parameters is particularly important when assessing the effectiveness of this optical process. In order to study this dependence, we have determined ε_I^2, at both wavelengths, as a function of pulse parameters, T_{FWHM} and P_0. The results of our analysis, summarized in Fig. 3.3, show that for a given waveguide length there is an optimum power at which ε_I^2 reaches a minimum, which is explained by the fact that the similariton formation length increases with P_0. In the same context, T_{FWHM} plays a critical role in similariton formation. As we can see in Fig. 3.3 (red curves) ε_I^2 presents a minimum at $T_{\mathrm{FWHM}} = 140$ fs for telecom wavelength and at at $T_{\mathrm{FWHM}} = 200$ fs for mid-infrared wavelength. For long pulse widths the induced effects of free carrier generation such as free carrier absorption and induced free carrier chirp start to degradate the pulse shape. As it is expected, shorter pulse widths in telecom regime affect more the similariton formation than in mid-infrared since the nonlinear parameter γ is much stronger in telecom wavelengths than of this in mid-infrared. The relation between the input pulse parameters and the similariton generation can be further explored by considering pulses with different shapes. Our results regarding this dependence are summarized in Fig. 3.4, where

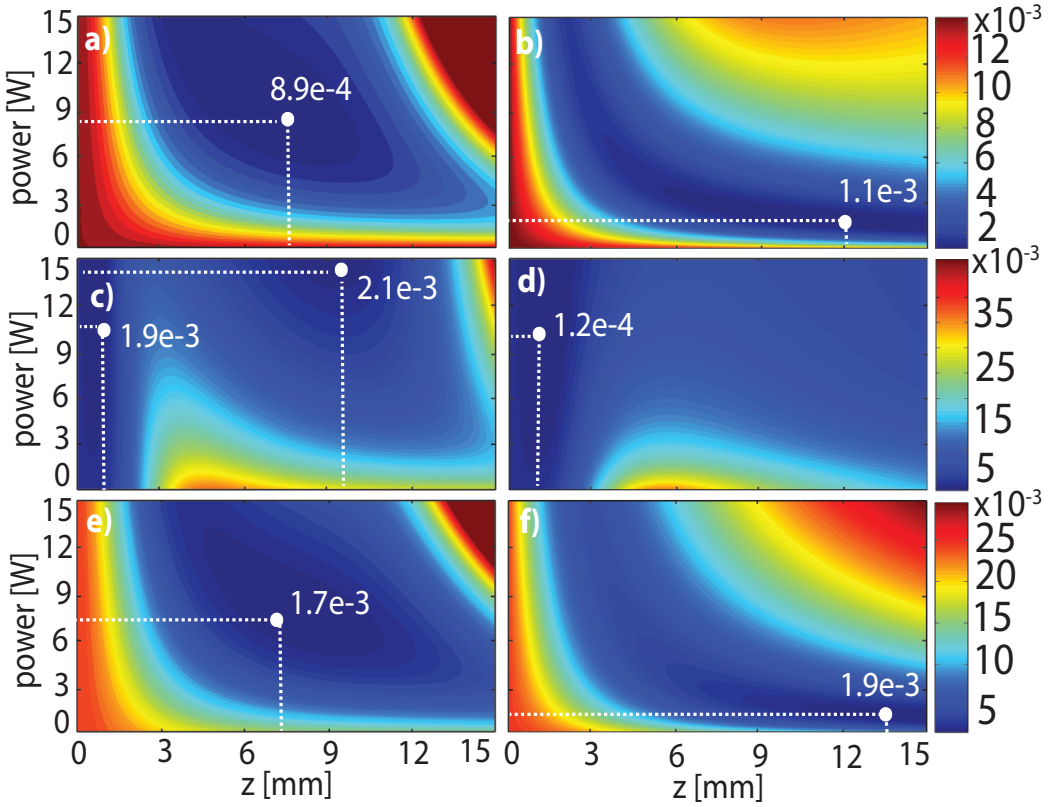

Figure 3.4: Dependence of ε_I^2 on z and pulse power, calculated for a Gaussian pulse (top panels), supergaussian with $m = 2$ (middle panels), and sech pulse (bottom panels). In all cases $T_{\mathrm{FWHM}} = 220$ fs. Left (right) panels correspond to $\lambda = 2.2$ μm ($\lambda = 1.55$ μm). White dots indicate the lowest value of ε_I^2 for each case.

we plot the evolution of $\varepsilon_I^2(z)$, determined for varying P_0. In order to gain a more complete view of the self similaritons we study the effects of different input pulse shapes in parabolic pulse generation. Although pulses emitted from many lasers can be approximated by a Gaussian shape, it is necessary to consider other pulse shapes such as super-Gaussian ($u(t) = \sqrt{P_0}e^{-t^{2m}/2T_0^{2m}}$ with $m = 2$ $T_{\mathrm{FWHM}} = 1.824T_0$), and hyperbolic secant ($u(t) = \sqrt{P_0}\mathrm{sech}(t/T_0)$, where $T_{\mathrm{FWHM}} = 1.763T_0$). The main idea is to see how the time dependence of the phase affects the generation of similaritons. At this point we should remind that the time dependence of the phase (essentially the chirp) plays a key role for the generation of parabolic pulses. In all of our propagation scenarios $T_{\mathrm{FWHM}} = 220$ fs. There are several revealing conclusions that can be drawn from the maps in Fig. 3.4. First, the Gaussian pulse leads to the lowest values of $\varepsilon_I^2(z)$, which suggests that this pulse shape is the most efficient one for generating similaritons. Second, in the case of Gaussian and sech pulses there is a band of low values of $\varepsilon_I^2(z)$, which is narrower at $\lambda = 1.55$ μm as compared to its width at $\lambda = 2.2$ μm. One should

physical parameters	$\lambda = 1.55\mu m$	$\lambda = 2.2\mu m$
$T_{FWHM}\ [fs]$	220	220
$P_0\ [W]$	7	7
$\alpha_{in}[dB\ cm^{-1}]$	0	0
$w_{in}\ [nm]$	1500	1500
$w_{out}\ [nm]$	1080	850
$\beta_{TPA}\ [cm/GW]$	$1.31{\cdot}10^{-11}$	$1.5{\cdot}10^{-13}$
$n_2\ [cm^2/W]$	$5.37{\cdot}10^{-18}$	$1.04{\cdot}10^{-17}$
$\beta_1(in)\ [ps/m]$	$1.26{\cdot}10^{4}$	$1.216{\cdot}10^{4}$
$\beta_2(in)\ [ps^2/m]$	1.11	1.53
$\beta_3(in)\ [ps^3/m]$	$0.5{\cdot}10^{-3}$	$-2.9{\cdot}10^{-3}$
$\gamma'(in)\ [W^{-1}m^{-1}]$	107.2	59.26
$\gamma''(in)\ [W^{-1}m^{-1}]$	32.63	0.3
$\tau'(in)\ [fs]$	1.36	2.24
$\tau''(in)\ [fs]$	0.34	0.6
$\beta_1(out)\ [ps/m]$	$1.27{\cdot}10^{4}$	$1.3{\cdot}10^{4}$
$\beta_2(out)\ [ps^2/m]$	0.79	$463{\cdot}10^{-2}$
$\beta_3(out)\ [ps^3/m]$	$1.4{\cdot}10^{-3}$	-6.8
$\gamma'(out)\ [W^{-1}m^{-1}]$	179.76	89.43
$\gamma''(out)\ [W^{-1}m^{-1}]$	54.67	$46.38{\cdot}10^{-2}$
$\tau'(out)\ [fs]$	1.51	2.825
$\tau''(out)\ [fs]$	$338{\cdot}10^{-3}$	0.576
$L\ [mm]$	15	15

Table 3.2: Input pulse parameters for the case of similariton generation for telecom and mid-infrared wavelengths corresponding to the results presented in Fig. 3.5.

note that as P_0 increases for the case of supergaussian pulses there are two bands of low values of $\varepsilon_I^2(z)$ at $\lambda = 2.2\ \mu$m whereas there is only one at $\lambda = 1.55\ \mu$m. Finally, pulses with a supergaussian shape evolve into a similariton over the shortest distance, because of the three pulse profiles, the supergaussian one is closest to a parabolic pulse.

Due to its practical relevance, we also studied the generation of similaritons in Si-PhNW tapers with different profiles. To this end, we considered a linear taper and exponential ones with different z-variation rate, in all cases the (Gaussian) pulse parameters and w_{in} and w_{out} being the same [see Fig. 3.5(a)]. All the input pulse parameters are presented in the following Table-3.2.

The results of this analysis, which are presented in Fig. 3.5, show that although similaritons are generated irrespective of the taper profile, the efficiency of this process does depend on the shape of the taper. In particular, overall the linear taper is the most effective for similariton generation, whereas in the case of exponential tapers

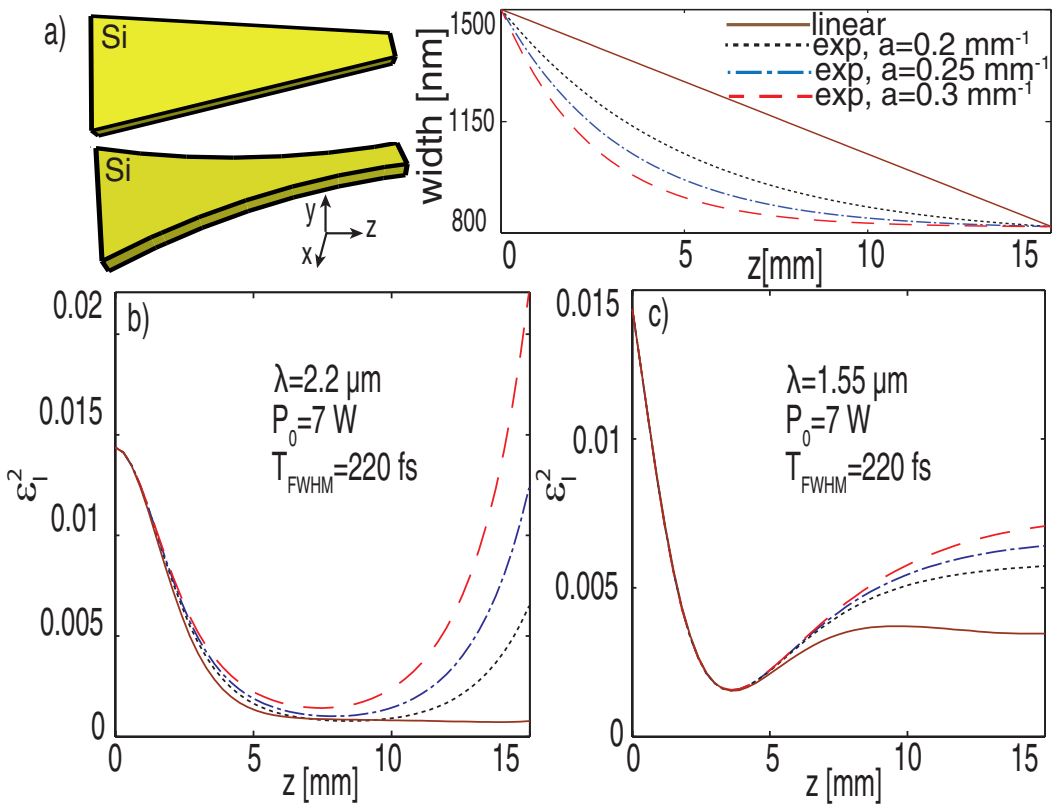

Figure 3.5: a) Schematics and dependence $w(z)$ for a linear and exponential tapers, $w(z) = w_{\text{in}} + (w_{\text{out}} - w_{\text{in}})(1 - e^{-az})/(1 - e^{-aL})$. In all cases $w_{\text{in}} = 1500$ nm and $w_{\text{out}} = 820$ nm. b) and c) show ε_I^2 *vs.* z, for the tapers in a).

the steeper their profile the more inefficient they are. These conclusions qualitatively remain valid at both $\lambda = 2.2$ μm and $\lambda = 1.55$ μm, although the overall pulse dynamics do depend on wavelength. In particular, ε_I^2 is smaller at $\lambda = 2.2$ μm and the pulse preserves a parabolic shape for a longer distance, in agreement with the results in Fig. 3.4.

3.5 Conclusion

In conclusion, we have demonstrated that parabolic pulses can be generated in millimeter-long tapered Si-PhNWs with engineered decreasing normal GVD. Our analysis showed that using this approach optical similaritons can be generated at both telecom and mid-IR wavelengths, irrespective of the pulse shape and taper profile. However, our investigations have revealed that the efficiency of the similariton generation is strongly dependent on the wavelength at which the device operates, pulse parameters and its temporal profile, as well as the particular shape of the Si-PhNW taper.

In order to gain a deeper insight in the particle-like behaviour of similaritons, we

will present in the next chapter all the pulse dynamics that emerge when similaritons collide with each other.

References

[3. 1] D. Anderson, M. Desaix, M. Karlsson, M. Lisak, and M. L. Quiroga-Teixeiro, "Wave-breaking-free pulses in nonlinear-optical fibres," J. Opt. Soc. Am. B. **10**, 1185–1190 (1993).

[3. 2] K. Tamura and M. Nakazawa, "Pulse compression by nonlinear pulse evolution with reduced optical wave breaking in erbium-doped fibre amplifiers," Opt. Lett. **21**, 68 (1996).

[3. 3] M. E. Fermann, V. I Kruglov, B. C. Thomsen, J. M. Dudley and J. D. Harvey, "Self-Similar Propagation and Amplification of Parabolic Pulses in Optical fibres," Phys. Rev. Lett. **84**, 6010–6013 (2000).

[3. 4] Ponomarenko, S. A., and Agrawal, G. P., "Optical similaritons in nonlinear waveguides," *Opt. Lett.* **32**, 1659–1661 (2007).

[3. 5] Agrawal, G. P., "Optical solitons, Autosoliton and similaritons," Tutorial of Institute of Optics, Rochester University, 1–49 (2008).

[3. 6] V. I. Kruglov, A. C. Peacock, J. D. Harvey and J. M Dudley, "Self-Similar propagation of parabolic pulses in normal-dispersion fibre amplifiers," J. Opt. Soc. Am. B. **19**, 461–469 (2002).

[3. 7] T. Hirooka and M. Nakazawa, "Parabolic pulse generation by use of a dispersion-decreasing fibre with normal group-velocity dispersion," Opt. Lett. **29**, 498–500 (2004).

[3. 8] B. Kibler, C. Billet, P. A. Lacourt, R. Ferriere, L. Larger, and J. M. Dudley, "Parabolic pulse generation in comb-like profiled dispersion decreasing fibre," Electron. Lett. **42**, 965–966 (2006).

[3. 9] A. I. Latkin, S. K. Turitsyn, and A. A. Sysoliatin, "Theory of parabolic pulse generation in tapered fibre" Opt. Lett. **32**, 331–333 (2007).

[3. 10] C. Finot, L. Provost, P. Petropoulos, and D. J. Richardson, "Parabolic pulse generation through passive nonlinear pulse reshaping in a normally dispersive two segment fibre device," Opt. Express **15**, 852–864 (2007).

[3. 11] J. Limpert, T. Schreiber, T. Clausnitzer, K. Zollner, H. J. Fuchs, E. B. Kley, H. Zellmer, and A. Tunnermann, "High-power femtosecond Yb-doped fibre amplifier," Opt. Express **10**, 628–638 (2002).

[3. 12] A. Malinowski, A. Piper, J. H. V. Price, K. Furusawa, Y. Jeong, J. Nilsson, and D. J. Richardson, "Ultrashort-pulse Yb3+-fibre-based laser and amplifier system producing >25 W average power," Opt. Express **29**, 2073–2075 (2004).

[3. 13] S. Lefrancois, C.-H. Liu, M. L. Stock, T. S. Sosnowski, A. Galvanauskas, and Frank W. Wise, "High-energy similariton fibre laser using chirally coupled core fibre," Opt. Lett. **38**, 43–45 (2013).

[3. 14] N. Healy, J. R. Sparks, P. J. A. Sazio, J. V. Badding, and A. C. Peacock, "Tapered silicon optical fibres," Opt. Express **18**, 7596–7601 (2010).

[3. 15] A. Peacock and N. Healy, "Parabolic pulse generation in tapered silicon fibres," Opt. Lett. **35**, 1780–1782 (2010).

[3. 16] K. K. Lee, D. R. Lim, H. C. Luan, A. Agarwal, J. Foresi, and L. C. Kimerling, "Effect of size and roughness on light transmission in a Si/SiO_2 waveguide: Experiments and model," Appl. Phys. Lett. **77**, 1617–1619 (2000).

[3. 17] R. Soref, "Mid-infrared photonics in silicon and germanium," Nat. Photonics **4**, 495–497 (2010).

[3. 18] N. C. Panoiu, X. Chen, and R. M. Osgood, "Modulation instability in silicon photonic nanowires," Opt. Lett. **31**, 3609–3611 (2006).

[3. 19] B. Kuyken, X. P. Liu, R. M. Osgood, R. Baets, G. Roelkens, and W. M. J. Green, "Mid-infrared to telecomband supercontinuum generation in highly nonlinear silicon-on-insulator wire waveguides," Opt. Express **19**, 20172–20181 (2011).

[3. 20] R. Mussina, D. R. Selviah, F. A. Fernandez, A. G. Tijhuis, and B. P. de Hon, "A rapid accurate technique to calculate the group delay, dispersion and dispersion slope of arbitrary radial refractive index profile weakly-guiding optical fibres," Progress In Electromagnetics Research **145**, 93–113 (2014).

[3. 21] N. C. Panoiu, X. Liu, and R. M. Osgood, "Self-steepening of ultrashort pulses in silicon photonic nanowires," Opt. Lett. **34**, 947–949 (2009).

[3. 22] O. Boyraz, P. Koonath, V. Raghunathan, and B. Jalali, "All optical switching and continuum generation in silicon waveguides," Opt. Express **12**, 4094–4102 (2004).

[3. 23] L. Yin, Q. Lin, and G. P. Agrawal,"Soliton fission and supercontinuum generation in silicon waveguides," Opt. Lett. **32**, 391–393 (2007).

[3. 24] I. W. Hsieh, X. Chen, X. P. Liu, J. I. Dadap, N. C. Panoiu, C. Y. Chou, F. Xia, W. M. Green, Y. A. Vlasov, and R. M. Osgood, "Supercontinuum generation in silicon photonic wires," Opt. Express **15**, 15242–15249 (2007).

[3. 25] R. M. Osgood, N. C. Panoiu, J. I. Dadap, X. Liu, X. Chen, I-W. Hsieh, E. Dulkeith, W. M. J. Green, and Y. A. Vlassov, "Engineering nonlinearities in nanoscale optical systems: physics and applications in dispesion-engineered silicon nanophotonic wires," Adv. Opt. Photon. **1**, 162–235 (2009).

[3. 26] X. Chen, N. C. Panoiu, and R. M. Osgood, "Theory of Raman-mediated pulsed amplication in silicon-wire waveguides," IEEE J. Quantum Electron. **42**, 160–170 (2006).

[3. 27] N. C. Panoiu, J. F. McMillan, and C. W. Wong, "Theoretical analysis of pulse dynamics in silicon photonic crystal wire waveguides," IEEE J. Sel. Top. Quantum Electron. **16**, 257–266 (2010).

[3. 28] J. B. Driscoll, N. Ophir, R. R. Grote, J. I. Dadap, N. C. Panoiu, K. Bergman, and R. M. Osgood, "Width-modulation of Si photonic wires for quasi-phase-matching of four-wave-mixing: experimental and theoretical demonstration," Opt. Express **20**, 9227–9242 (2012) .

[3. 29] A. C. Turner, C. Manolatou, B. S. Schmidt, M. Lipson, M. A. Foster, J. E. Sharping, and A. L. Gaeta, "Tailored anomalous group-velocity dispersion in silicon channel waveguides," Opt. Express **14**, 4357–4362 (2006).

Chapter 4

Similariton collision in silicon photonic nanowires

4.1 Introduction

The rapid increase of data transmission rate in many optical communication systems has led to an intense interest in generating pulses that do not suffer from distortion and wave breaking phenomena upon propagation. An example of such type of pulses that preserve their shape during propagation and show particle-like behaviour are localized optical waves also known as solitons. They exist in the anomalous GVD regime, namely when the second-order dispersion coefficient, $\beta_2 < 0$. Similar types of pulses that show particle-like properties and self-similar behaviour upon propagation are the so-called similaritons[4. 1–5]. Unlike solitons, they form primarily in the normal dispersion regime ($\beta_2 > 0$), although the existence of similaritons in the anomalous GVD regime has been demonstrated as well.[4. 6] Similaritons preserve their overall pulse energy and phase profiles, although specific pulse parameters, such as the pulse width, amplitude, and frequency chirp vary during propagation. As a result, similaritons are not affected by destructive effects, such as pulse distortion, radiative damping, and wave breaking phenomena. More importantly, from a practical point of view, in order to generate optical similaritions no specific constraints have to be imposed on the physical parameters describing the initial pulse. The generation of optical similaritons and their physical properties have already been studied and demonstrated in optical fibre systems such as Yb-doped fibre amplifiers,[4. 2] using passive schemes based on dispersion managed or tapered silica fibres,[4. 4] and high-power amplifiers[4. 7].

The constant drive towards increased photonic systems integration makes it necessary to develop innovative approaches to generate at chip-scale optical pulses that are not distorted when propagated in subwavelength wave guiding photonic devices. Recent studies[4. 8] in which it is demonstrated that similaritons can form in silicon (Si) fibres with micrometer sized core represent an important step towards this goal. However, device fabrication considerations suggest that the silicon-on-insulator (SOI) material platform[4. 9, 10] provides a more flexible and cost-effective solution to further decrease the device footprint. By scaling down the transverse device size to submicrometer range, the enhanced optical field confinement not only leads to larger modal frequency dispersion but also increases considerably the effective optical nonlinearity of the waveguide. As such, significant pulse reshaping effects can be achieved over relatively short propagation distance. For example, soliton generation in Si-PhNWs has already been demonstrated experimentally in chip-scale devices.[4. 11] Other important nonlinear optical effects that can be used efficiently to engineer the intensity and phase profiles of optical pulses, such as supercontinuum generation,[4. 12–14] pulse self-steepening,[4. 15] and modulational instability,[4. 16] have been demonstrated both at telecom ($\lambda = 1.55$ μm) and mid-IR ($\lambda \gtrsim 2.2$ μm) wavelengths (see Refs. [[4. 17–19]] and references therein for more information on nonlinear optical effects in Si waveguides). The latter spectral domain provides an additional advantage for using Si as material platform for integrated nonlinear photonic devices, namely, the TPA of Si is dramatically reduced.

4.2 Dispersion properties of silicon photonic wire waveguides

The Si-PhNW considered in this study consists of a Si rectangular core with an adiabatically varying width, $w(z)$, which is buried in SiO_2. The height of the waveguide is assumed to be constant, $h = 250$ nm. In order to incorporate in our model the z-dependence of the optical parameters of the waveguide we determine the fundamental (TE-like) optical mode and its propagation constant following the same procedure that was presented in Chapter 3. However, for convenience we will briefly present some key characteristics of the dispersion properties of Si-PhNW.

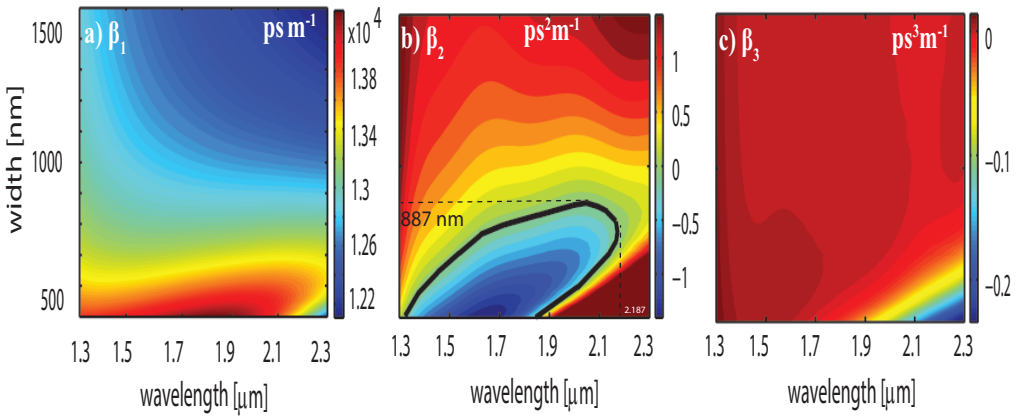

Figure 4.1: Width dependence of the spectra of the waveguide dispersion coefficients: a) β_1, b) β_2, and c) β_3. The black solid curve in b) corresponds to $\beta_2 = 0$.

The width dependence of the spectra of the waveguide dispersion coefficients are presented in Fig. 4.1. These plots show that the linear waveguide parameters depend strongly on both w and λ, which provides increased flexibility in choosing the regime in which the device operates. In particular, it can be seen that if $w < 887$ nm the Si-PhNW has two zero GVD wavelengths, defined by the relation $\beta_2(\lambda, w) = 0$. In contrast, when $w > 887$ nm the Si-PhNW has normal GVD in the entire spectral domain. However, if $\lambda > 2187$ nm the waveguide has normal GVD for any width. Moreover, within the range of the waveguide parameters investigated here, β_2 decreases monotonically with w if $\lambda < 1.78\ \mu$m, whereas if $\lambda > 1.78\ \mu$m the dependence $\beta_2(w)$ has a minimum point. A strong dependence on the waveguide width is also shown by $\beta_1 = 1/v_g$, namely, β_1 decreases as w increases.

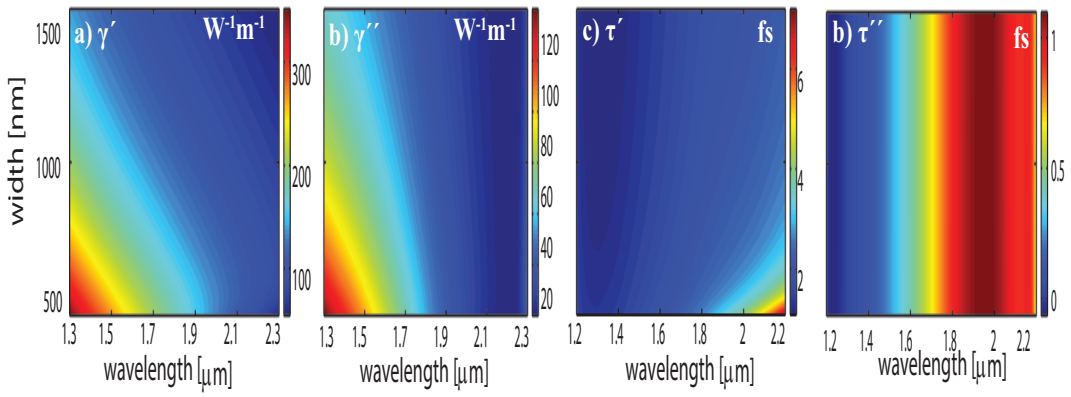

Figure 4.2: Width dependence of the spectra of the nonlinear waveguide coefficients: a) SPM parameter, γ', b) TPA coefficient, γ'', c) shock time coefficient (real part), τ', and d) shock time coefficient (imaginary part), τ''.

Pulse propagation in Si-PhNWs is not only determined by the waveguide dispersion coefficients but also by the nonlinear coefficients, which are plotted in Fig. 4.2. Specifically, the magnitude of the real and imaginary parts of the waveguide nonlinearity coefficient, γ, which describe the SPM and TPA effects, respectively, increase as w and λ decrease. As a result, it is expected that pulse reshaping phenomena induced by optical nonlinear effects will be more intense at lower wavelengths in Si-PhNWs with smaller w. On the other hand, the shock time parameter shows a different dependence on the waveguide width. Specifically, whereas τ' increases as w decreases, τ'' varies only slightly with w. Note that τ' and τ'' are time scales associated with different nonlinear effects, namely, SPM and TPA, respectively.

It is clear that an appropriate combination between the size of a silicon nanowire and the operational wavelength of the propagating pulse can enhance efficiently different nonlinear phenomena. Such type of flexibility is of great importance nowadays as long as there is urgent need for multi-tasking devices in the field of telecommunications. In particular, a silicon nanowire with width $w < 887$ nm does not have the same influence on the pulse shape in the regime of $\lambda \approx 1.55\ \mu m$ where the GVD is negative as in the regime of $\lambda \approx 2.1\ \mu m$ where the GVD is positive. That means that we can take advantage of different nonlinear phenomena with the same device. One such type of nonlinear phenomena is the parabolic pulse generation which was studied extensively in the previous Chapter 3. This work will focus in an interesting aspect of parabolic pulses which is their particle like behaviour when the collide between each other. Interesting conclusions follow in the next section.

4.3 Collision of optical similaritons

The results presented in Chapter 3 revealed that parabolic similaritons can be easily generated in tapered Si-PhNWs. However, one important physical property of such pulses, which is particularly relevant to technological applications, is that similaritons display particle-like behaviour during collision. It should be noted that one expects that the knowledge pertaining to similaritons collision in regular or photonic crystal fibres[4. 23, 24] cannot be simply translated to the context of Si-PhNWs, as the basic optical properties of these optical guiding systems make them quite distinct from each other. For example, the presence of FCs in Si-PhNWs means that optical similaritons

collide in these waveguides in the presence of nonlinear loss emerging by the TPA, whereas in the case of silica based optical fibres optical losses depend linearly on the pulse amplitude.

In order to study the collision of optical similaritons in Si-PhNWs we use the theoretical model described in Section 3.2. Accordingly we launch two similaritons with different carrier frequencies, namely, $\Omega_0 + \Delta\Omega$ and $\Omega_0 - \Delta\Omega$. This amounts to the two pulses having different group-velocities. The pulses are temporally separated by Δt, which can be arbitrarily chosen. We consider first the case of normal GVD, so that, for simplicity, we assume that the width of the waveguide is constant, $w = 900$ nm. The initial profile of the optical field is then given by:

$$u_p(t) = A_{01}\sqrt{1-\frac{(t-\bar{t})^2}{T_0^2}}e^{i[\phi(t-\bar{t})+\Delta\Omega(t-\bar{t})]} + A_{02}\sqrt{1-\frac{(t+\bar{t})^2}{T_0^2}}e^{i[\phi(t+\bar{t})-\Delta\Omega(t+\bar{t})]}, \quad (4.1)$$

where A_{01} and A_{02} are the amplitudes of the two similaritons and $\bar{t} = \Delta t/2$. In order to calculate the parameters of the similaritons we assume that we have one propagating similariton described by the following expression:

$$u_p(t) = A_0\sqrt{1-\frac{(t-\bar{t})^2}{T_0^2}}e^{i[\phi(t-\bar{t})+\Delta\Omega(t-\bar{t})]}, \quad (4.2)$$

where $|t| \leq T_0$ and $A_0 = 0$ for $|t| > T_0$. The input energy of the pulse is calculated by taking the following integral

$$E_{in} = \int_{-T_0}^{T_0} |u_p(t)|^2 dt = \frac{8}{3}A_0^2 T_0. \quad (4.3)$$

According to previously published works [4. 2, 3], the input energy of a similariton is equal to:

$$E_{in} = \frac{8\sqrt{\gamma\beta_2/2}A_0^3}{g}. \quad (4.4)$$

If we replace in this equation the gain, g, with the nonlinear loss coefficient, $\alpha_{\mathrm{nl}} = -2\gamma'' A_0^2$, Eq. (4.4) can be adapted to a waveguide with TPA. One should note here that the assumption of nonlinear losses is based on the fact that TPA is proportional to the square power of the amplitude of the propagating pulse. Taking into account the latter

assumption we combine Eqs. (4.3), (4.4) in order to derive the following expression:

$$\frac{8}{3}A_0T_0 = \frac{3\sqrt{\gamma\beta_2}}{2\sqrt{2}\gamma''}. \tag{4.5}$$

By inserting Eq. (4.5) in Eq. (4.3), we can derive the expression for A_0, Eq. (4.7b). In order to calculate T_0 we insert Eq. (4.7b) in the following equation [4. 2, 3]:

$$T_0 = \frac{6\sqrt{\gamma\beta_2/2}}{2\gamma''A_0}. \tag{4.6}$$

According to the previous manipulations one can have the related parameters for similaritons of Eq. 4.2 as it follows:

$$\phi(t) = \phi_0 - \frac{3\gamma'}{4\gamma''} + \frac{\gamma''A_0^2}{3\beta_2}t^2, \tag{4.7a}$$

$$A_0 = \frac{\gamma''E_{\text{in}}}{2\sqrt{2\gamma'\beta_2}}, \tag{4.7b}$$

$$T_0 = \frac{6\gamma'\beta_2}{\gamma''^2E_{\text{in}}}, \tag{4.7c}$$

where ϕ_0 is a constant phase. To determine the initial values of the parameters of the colliding similaritons we choose first the pulse width, T_0, assumed to be the same for the two similaritons, then using Eq. (4.7c) we calculate the initial pulse energy, E_{in}, and from Eq. (4.7b) we find the amplitude of the similaritons, A_0. Finally, the initial phase profile is determined from Eq. (4.7a). Since β_2 and γ are frequency dependent, the two similaritons will be characterized by different sets of parameters. We should stress here that the appropriate choice of input pulse wavelengths ensures that the pulses are located either in high or low TPA wavelength regime.

We have applied this procedure to study the collision of two parabolic similaritons with $\lambda_0 = 1.55$ μm and frequency shift $\Delta\Omega = 130.2$ THz, which means that the wavelengths of the two similaritons are $\lambda_1 = 1400$ nm and $\lambda_2 = 1736$ nm. We should make clear that the intrinsic losses have not been taken into account as the dominant loss mechanism for the propagation distances studied in this work is the nonlinear losses emerged from TPA and free carrier generation. All the input pulse parameters are shown in the following Table-4.1.

This choice of the parameters of the input pulses ensures that the wavelengths of

physical parameters	$\lambda = 1.400\mu m$	$\lambda = 1.736\mu m$
$T_0\ [fs]$	600	600
$P_0\ [mW]$	440.4	447.8
$\alpha_{in}[dB\ cm^{-1}]$	0	0
$w\ [nm]$	900	900
$\beta_{TPA}\ [cm/GW]$	$1.6{\cdot}10^{-11}$	$9.2{\cdot}10^{-12}$
$n_2\ [cm^2/W]$	$4.55{\cdot}10^{-18}$	$9.08{\cdot}10^{-18}$
$\beta_1\ [ps/m]$	$1.3{\cdot}10^{4}$	$1.29{\cdot}10^{4}$
$\beta_2\ [ps^2/m]$	$7.78{\cdot}10^{-1}$	$2.64{\cdot}10^{-1}$
$\beta_3\ [ps^3/m]$	$2.7{\cdot}10^{-3}$	$1.15{\cdot}10^{-3}$
$\gamma'\ [W^{-1}m^{-1}]$	197.17	137.13
$\gamma''\ [W^{-1}m^{-1}]$	65.99	31.8
$\tau'\ [fs]$	1.22	1.83
$\tau''\ [fs]$	0.1	$7.4{\cdot}10^{-1}$
$L\ [mm]$	50	50

Table 4.1: Input pulse parameters corresponding to the case presented in Fig. 4.3.

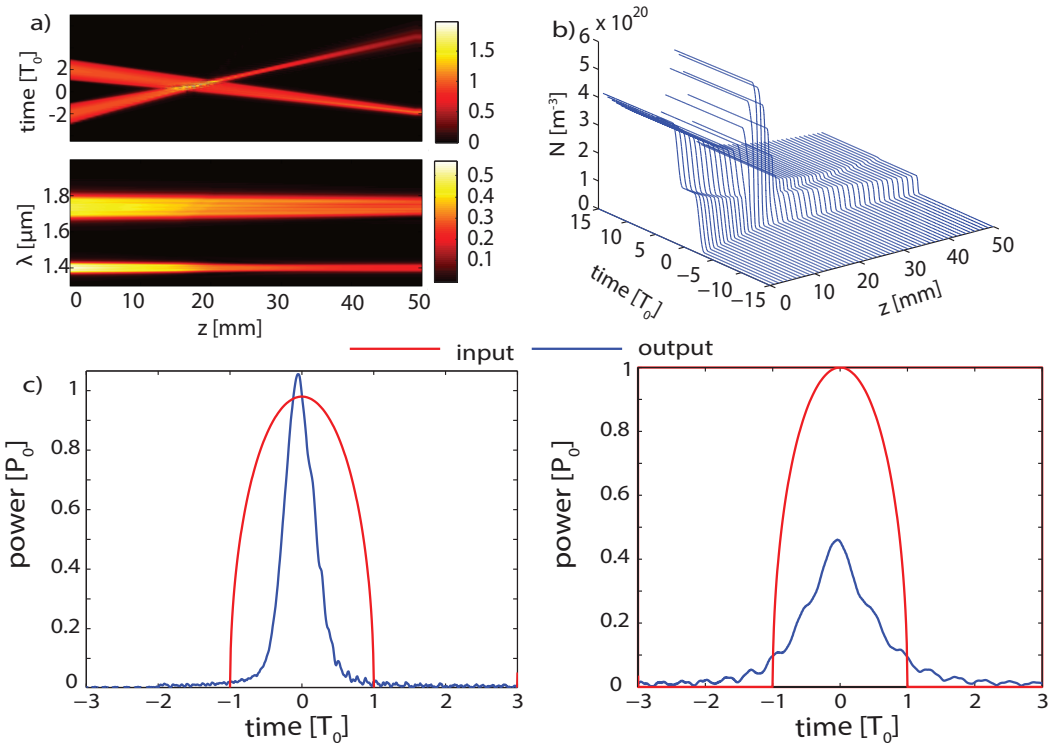

Figure 4.3: Collision of two parabolic similaritons propagating in the normal GVD regime and in the presence of large TPA. a) Temporal and spectral pulse evolution along propagation distance. b) Evolution of free-carrier density. c) Temporal pulse profile at the input and output of the silicon nanowire. The pulse width and power are normalized with respect to $T_0 = 600\ fs$ and $P_0 = 447.8\ mW$.

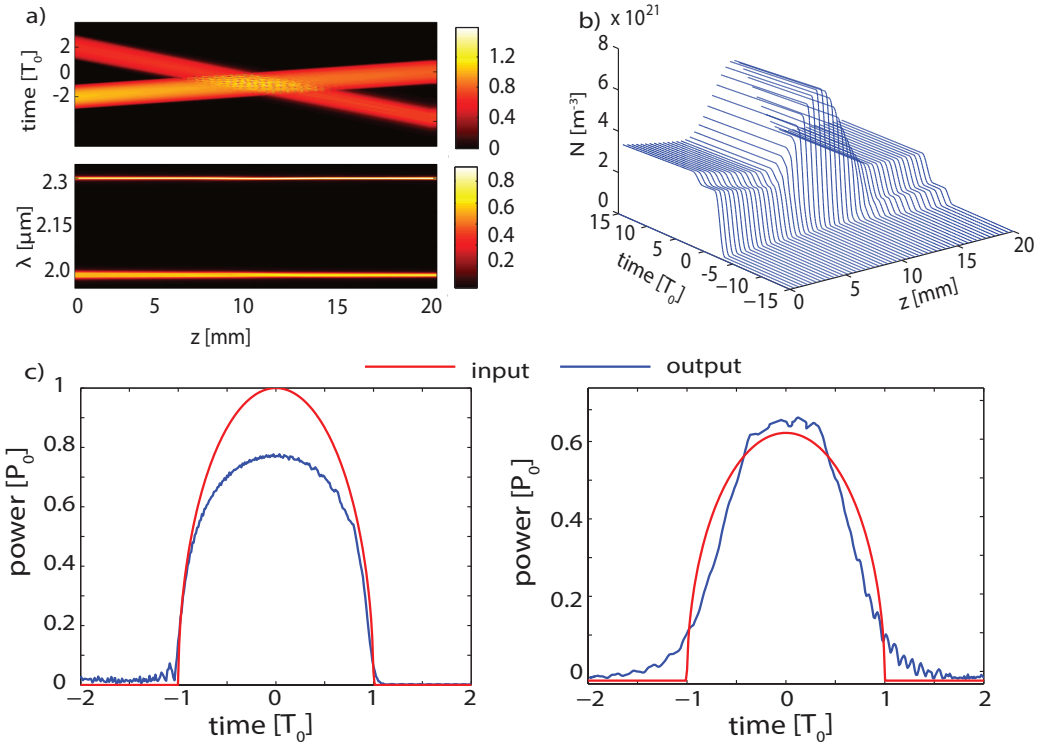

Figure 4.4: Collision of two parabolic similaritons propagating in the normal GVD regime and in the presence of weak TPA. a) Temporal and spectral pulse evolution along propagation distance. b) Evolution of free-carrier density. c) Temporal pulse profile at the input and output of the silicon nanowire. The pulse width and power are normalized with respect to $T_0 = 2500\ fs$ and $P_0 = 2540\ mW$.

both similaritons lie in a region of large TPA. The results of our simulations, presented in Fig. 4.3, clearly illustrate the particle-like behaviour of the similaritons upon the pulse collision. Specifically, it can be seen that, except of some slight interference effects observed in the overlap region, the similaritons pass through each other being practically unaffected by the collision process. In addition, the strong TPA leads to significant pulse absorption, which is also reflected in the dependence of the FC-density on the propagation distance. In particular, one can observe a significant decrease with z of the FC density, except, as expected, in the overlap region where a larger amount of FCs is generated as shown in Fig. 4.3(b). In addition to the collision of the similaritons, Fig. 4.3 also illustrates temporal compression This is clear from Fig. 4.3(c) which presents the input and output pulse profile. Due to to strong TPA and nonlinear effects, we can see that the pulse has been affected significantly after 50 *mm* of propagation distance.

We also considered the collision of parabolic similaritons propagating at mid-IR

wavelengths. Thus, we chose $\lambda_0 = 2.2$ μm and $\Delta\Omega = 57$ THz, the corresponding wavelengths of the two similaritons being $\lambda_1 = 2019$ nm and $\lambda_2 = 2300$ nm. All the input pulse parameters are shown in the following Table-4.2:

physical parameters	$\lambda = 2.019\mu m$	$\lambda = 2.3\mu m$
T_0 $[ps]$	2.5	2.5
P_0 $[W]$	2.54	1.62
$\alpha_{in}[dB\ cm^{-1}]$	0	0
w $[nm]$	530	530
β_{TPA} $[cm/GW]$	$1.48{\cdot}10^{-13}$	$1{\cdot}10^{-13}$
n_2 $[cm^2/W]$	$11.89{\cdot}10^{-18}$	$9.5{\cdot}10^{-18}$
β_1 $[ps/m]$	$1.4{\cdot}10^{4}$	$1.3{\cdot}10^{4}$
β_2 $[ps^2/m]$	3.0	20
β_3 $[ps^3/m]$	$-7.3{\cdot}10^{-2}$	$-2.3{\cdot}10^{-1}$
γ' $[W^{-1}m^{-1}]$	126.85	68.36
γ'' $[W^{-1}m^{-1}]$	10.39	24.65
τ' $[fs]$	4	6
τ'' $[fs]$	1.06	$5.4{\cdot}10^{-1}$
L $[mm]$	20	20

Table 4.2: Input pulse parameters for the case presented in Fig. 4.4.

Figure 4.4 illustrates the dynamics of the similaritons collision in this case. While the evolution of the optical field again shows that the similaritons are not destroyed as a result of their collision (Fig. 4.4(a)), the dynamics of FCs are more complex as compared to what we have observed in the previous case. Specifically, it can be seen that an increased amount of FCs is generated while the two similaritons collide, whereas the FC-density remains rather constant when the two pulses are temporally separated as shown in Fig. 4.4(b). Interestingly enough, the similariton at $\lambda_1 = 2019$ nm decays faster than the one at $\lambda_2 = 2300$ nm, although it probes a lower FC-density and thus smaller FC absorption. This result, explained by the reduced TPA experienced by the latter similariton, demonstrates that in this spectral regime and for pulse parameters considered here the TPA is significantly larger than the FC absorption.

In order to complete our analysis of similariton interaction in Si-PhNWs we considered the collision of similaritons that propagate in the anomalous GVD regime. Since in the mid-IR the waveguide has normal GVD for any width, in this case we only study the similaritons collision at $\lambda_0 = 1.55$ μm. Moreover, for the two pulses to propagate in the anomalous GVD regime we set $w = 510$ nm. In the case of anomalous

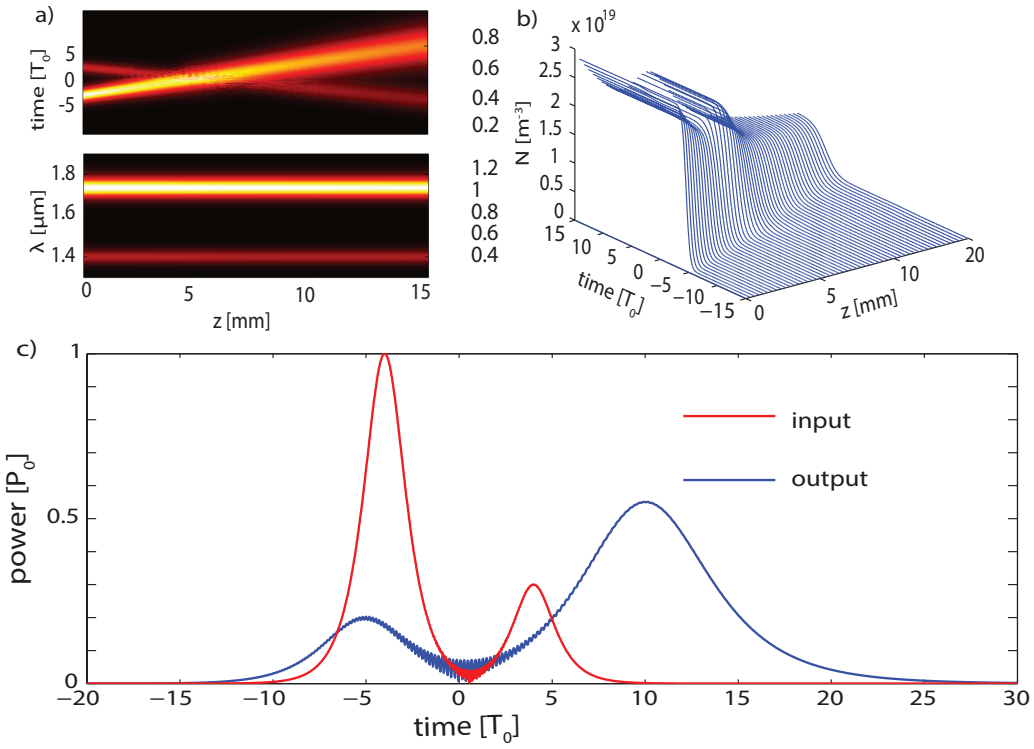

Figure 4.5: Collision of two hyperbolic secant similaritons propagating in the anomalous GVD regime and in the presence of large TPA. a) Temporal and spectral pulse evolution along propagation distance. b) Evolution of free-carrier density. c) Temporal pulse profile at the input and output of the silicon nanowire. The pulse width and power are normalized with respect to $T_0 = 200\ fs$ and $P_0 = 154\ mW$. One should notice that the red and blue curves are on the same horizontal scale but arbitrarily placed along the horizontal axis relative to one another.

GVD, the similariton profile is described by a hyperbolic secant function, so that the input pulse is written as:[4. 6]

$$u_p(t) = \frac{1}{T_0}\sqrt{\frac{|\beta_2(\lambda_1)|}{\gamma'(\lambda_1)}}\,\mathrm{sech}\left(\frac{t-\bar{t}}{T_0}\right)e^{i[\phi(t-\bar{t})+\Delta\Omega(t-\bar{t})]} + \frac{1}{T_0}\sqrt{\frac{|\beta_2(\lambda_2)|}{\gamma'(\lambda_2)}}\,\mathrm{sech}\left(\frac{t+\bar{t}}{T_0}\right)e^{i[\phi(t+\bar{t})-\Delta\Omega(t+\bar{t})]}. \tag{4.8}$$

Here, $\phi(t) = \phi_0 - (\gamma' P_0/\beta_2)t^2$, ϕ_0 being a constant phase. Note that in the case when the quadratic chirp term in this relation vanishes the corresponding sech pulses are the well-known solitons. They correspond to a case of a Si-PhNW with constant optical parameters and no optical losses or gain. As it is well known, solitons would propagate in such waveguides without any change in their shape or pulse parameters, whereas similaritons only preserve their shape upon propagation.

As in the case of normal GVD, we set the frequency shift $\Delta\Omega = 130.2$ THz, meaning that $\lambda_1 = 1400$ nm and $\lambda_2 = 1736$ nm. All the input pulse parameters are shown in the following Table-4.3:

physical parameters	$\lambda = 1400\mu m$	$\lambda = 1736\mu m$
$T_0\ [fs]$	200	200
$P_0\ [mW]$	48	154
$\alpha_{in}[dB\ cm^{-1}]$	0	0
$w\ [nm]$	510	510
$\beta_{TPA}\ [cm/GW]$	$1.6{\cdot}10^{-11}$	$9.2{\cdot}10^{-12}$
$n_2\ [cm^2/W]$	$4.55{\cdot}10^{-18}$	$9.084{\cdot}10^{-18}$
$\beta_1\ [ps/m]$	$1.38{\cdot}10^{4}$	$1.4{\cdot}10^{4}$
$\beta_2\ [ps^2/m]$	$-5.8{\cdot}10^{-1}$	-1.21
$\beta_3\ [ps^3/m]$	$5.5{\cdot}10^{-3}$	$6.7{\cdot}10^{-3}$
$\gamma'\ [W^{-1}m^{-1}]$	303.5	165.44
$\gamma''\ [W^{-1}m^{-1}]$	101.58	41.6
$\tau'\ [fs]$	1.42	2.28
$\tau''\ [fs]$	0.1	$7.4{\cdot}10^{-1}$
$L\ [mm]$	15	15

Table 4.3: Input pulse parameters for the case presented in Fig. 4.5.

The collision of sech similaritons, presented in Fig. 4.5, has several features that distinguish this case from that of parabolic similaritons. Before we continue with some useful comments of Fig. 4.5, we should make clear that the left blue pulse profile of Fig. 4.5(c) is the output pulse profile of the right red pulse profile and vice versa. This occurs because the pulses go through each other during the collision having as a result to sweep their positions in time domain. Figure 4.5(a) shows that the dynamics of FCs is chiefly determined by the propagation of just one of the two similaritons (Fig. 4.5(b)). This result is easily explained by the quadratic dependence of the generated FCs on the pulse power, combined with the fact that the optical power of one of the similaritons is more than three times larger than the peak power of the other one. Despite these differences, however, in this case too the sech similaritons show particle-like behaviour during collision.

4.4 Conclusions

In conclusion, we have demonstrated the collision of optical similaritons propagating in the normal and anomalous GVD regimes, in both cases the dynamics of the optical field

and those of photo-generated FCs being investigated. This analysis has demonstrated that although the optical similaritons are not destroyed in the collision process, the similaritons interaction is strongly dependent on the particular conditions in which the collision occurs, including the frequency dispersion regime, spectral domain, and pulse parameters.

The characteristic of similaritons not to be destroyed after their collision is very important for communication and computer systems. Based on this property one could increase the amount of pulsed information in a communication channel without degrading it. According to this approach, the bandwidth of the communication and computer channels could increase considerably. In the same context, the following chapter presents optical pulse compression in Si-PhNWs which could enhance the effectiveness of the currrent optical channels.

References

[4. 1] Anderson, D., Desaix, M., Karlsson, M., Lisak M., and Quiroga-Teheiro, M. L., "Wave breaking free pulses in nonlinear optical fibres," *J. Opt. Soc. Am. B* **10**, 1185–1190 (1993).

[4. 2] Kruglov, V. I., Peacock, A. C., Harvey, J. D., and Dudley, J. M., "Self-similar propagation of parabolic pulses in normal-dispersion fibre amplifiers," *J. Opt. Soc. Am. B* **19**, 461–469 (2002).

[4. 3] Fermann, M. E., Kruglov, V. I., Thomsen, B. C., Dudley, J. M., and Harvey, J. D., "Self-similar propagation and amplification of parabolic pulses in optical fibres," *Phys. Rev. Lett.* **84**, 6010–6013 (2000).

[4. 4] Hirooka, T., and Nakazawa, M., "Parabolic pulse generation by use of a dispersion-decreasing fibre with normal-group velocity dispersion," *Opt. Lett.* **29**, 498–500 (2004).

[4. 5] Ponomarenko, S. A., and Agrawal, G. P., "Optical similaritons in nonlinear waveguides," *Opt. Lett.* **32**, 1659–1661 (2007).

[4. 6] Kruglov, V. I., Peacock, A. C., and Harvey, J. D., "Exact self-similar solutions of the generalized nonlinear Schrödinger equation with distributed coefficients," *Phys. Rev. Lett.* **90**, 113902 (2003).

[4. 7] Limpert, J., Schreiber, T., Clausnitzer, T., Zollner, K., Fuchs, H. J., Kley, E. B., Zellmer, H., and Tunnermann, A., "High-power femtosecond Yb-doped fibre amplifier," *Opt. Express* **10**, 628–638 (2002).

[4. 8] Peacock, A., and Healy, N., "Parabolic pulse generation in tapered silicon fibres," *Opt. Lett.* **35**, 1780–1782 (2010).

[4. 9] Lee, K. K., Lim, D. R., Luan, H. C., Agarwal, A., Foresi, J., and Kimerling, L. C., "Effect of size and roughness on light transmission in a Si/SiO_2 waveguide: Experiments and model," *Appl. Phys. Lett.* **77**, 1617–1619 (2000).

[4. 10] R. U. Ahmad, F. Pizzuto, G. S. Camarda, R. L. Espinola, H. Rao, and R. M. Osgood, *IEEE Photon. Technol. Lett.* **14**, 65–67 (2002).

[4. 11] Hsieh, I. W., Chen, X., Dadap, J. I., Panoiu, N. C., Osgood, R. M., McNab, S. J., and Vlasov, Y. A., "Ultrafast-pulse self-phase-modulation and third-order dispersion in Si photonic wire-waveguides," *Opt. Express* **14**, 12380–12387 (2006).

[4. 12] Hsieh, I. W., Chen, X., Liu, X. P., Dadap, J. I., Panoiu, N. C., Chou, C. Y., Xia, F., Green, W. M., Vlasov, Y. A., and R. M. Osgood, "Supercontinuum generation in silicon photonic wires," *Opt. Express* **15**, 15242–15249 (2007).

[4. 13] Boyraz, O., Koonath, P., Raghunathan, V., and Jalali, B., "All optical switching and continuum generation in silicon waveguides," *Opt. Express* **12**, 4094–4102 (2004).

[4. 14] Kuyken, B., Liu, X. P., Osgood, R. M., Baets, R., Roelkens, G., and Green, W. M. J., "Mid-infrared to telecomband supercontinuum generation in highly nonlinear silicon-on-insulator wire waveguides," *Opt. Express* **19**, 20172–20181 (2011).

[4. 15] Panoiu, N. C., Liu, X., and Osgood, R. M., "Self-steepening of ultra short pulses in silicon photonic nanowires," *Opt. Lett.* **34**, 947–949 (2009).

[4. 16] Panoiu, N. C., Chen, X., and Osgood, R. M., "Modulation instability in silicon photonic nanowires," *Opt. Lett.* **31**, 3609–3611 (2006).

[4. 17] Lin, Q., Painter, O. J., and Agrawal, G. P., "Nonlinear optical phenomena in silicon waveguides: Modeling and applications," *Opt. Express* **15**, 16604–16644 (2007).

[4. 18] Dadap, J. I., Panoiu, N. C., Chen, X. G., Hsieh, I. W., Liu, X. P., Chou, C. Y., Dulkeith, E., McNab, S. J., Xia, F. N., Green, W. M. J., Sekaric, L., Vlasov, Y. A., and Osgood, R. M., "Nonlinear-optical phase modification in dispersion-engineered Si photonic wires," *Opt. Express* **16**, 1280–1299 (2008).

[4. 19] Osgood, R. M. , Panoiu, N. C., Dadap, J. I., Liu, X., Chen, X., Hsieh, I-W, Dulkeit, E., Green, W. M. J., and Vlassov, Y. A., "Engineering nonlinearities in nanoscale optical systems: physics and applications in dispersion engineered silicon nanophotonics wires," *Adv. Opt. Photon.* **1**, 162–235 (2009).

[4. 20] Chen, X., Panoiu, N. C., and Osgood, R. M., "Theory of Raman-mediated pulsed amplification in silicon-wire waveguides," *IEEE J. Quantum Electron.* **42**, 160–170 (2006).

[4. 21] Panoiu, N. C., McMillan, J. F., and Wong, C. W., "Theoretical analysis of pulse dynamics in silicon photonic crystal wire waveguides," *IEEE J. Sel. Top. Quantum Electron.* **16**, 257–266 (2010).

[4. 22] Driscoll, J. B., Ophir, N., Grote, R. R., Dadap, J. I., Panoiu, N. C., Bergman, K., and Osgood, R. M., "Width-modulation of Si photonic wires for quasi-phase-matching of four-wave-mixing: experimental and theoretical demonstration," *Opt. Express* **20**, 9227–9242 (2012).

[4. 23] Finot, C., and Millot, G., "Collisions between similaritons in optical fibre amplifiers,"*Opt. Express* **13**, 7653–7663 (2005).

[4. 24] Ponomarenko, S. A., and Agrawal, G. P., "Nonlinear interaction of two or more similaritons in loss- and dispersion-managed fibres," *J. Opt. Soc. Am. B* **25**, 983–989 (2008).

Chapter 5

Pulse compression in silicon photonic nanowires

5.1 Introduction

Optical pulse compression techniques provide an essential functionality on which a broad array of optics and photonic applications rely, including broadband communication systems, nonlinear optics, optical coherence tomography for cross-sectional tissue imaging, materials processing, and nonlinear microscopy. Several schemes for optical pulse compression, based on either linear or nonlinear optical techniques, have been proposed, among the most successful and widely adopted being pulse compressors employing diffraction grating pairs [5. 1–3], synthetic quasi-phase-matching gratings [5. 4], interferometric systems based on nonlinear optical loop mirrors [5. 5–7], SPM and XPM induced pulse compression [5. 8–11], higher-order soliton pulse compression [5. 12–16], and adiabatic soliton compression [5. 17, 18]. The efficiency of these techniques can significantly be improved by tailoring the linear and nonlinear physical properties of the optical medium in which the pulse propagates, so that optical pulses with specific temporal and spectral characteristics are achieved. In particular, efficient pulse compression have been demonstrated in several types of optical fibres with dispersion engineered characteristics, such as dispersion decreasing fibres [5. 14, 17, 18], tapered holey fibres [5. 19, 20], and sub-micron tapered silicon and silica fibres [5. 16, 21–23]. Among all these alternative solutions, sub-wavelength waveguiding devices based on silicon (Si) are at the centre of the current research efforts geared towards achieving pulse compression at optical chip-scale.

Tapered Si-PhNWs with subwavelength transverse size [5. 24, 25] are photonic devices ideally suited for dispersion engineering. Thus, due to the combined effects of the large difference between the index of refraction of the silicon core ($n_{\mathrm{Si}} \approx 3.4$) and that of the cladding (usually air, $n_{\mathrm{air}} = 1$) and the subwavelength nature of the cross-sectional area of the waveguide, variations in the transverse size of the waveguide as small as only a few percent of the operating wavelength can induce changes of the mode propagation constant, β, which are large enough to significantly affect the temporal and spectral characteristics of optical pulses that propagate in such wire waveguides. In particular, by simply varying the waveguide width, one can readily design Si-PhNWs whose frequency dispersion changes within certain spectral regions between normal dispersion, where the second-order dispersion coefficient, $\beta_2(\omega) = \beta''(\omega) > 0$, and anomalous one ($\beta_2 < 0$) and which possess multiple zero-dispersion points, defined by $\beta_2(\omega) = 0$. Equally important, the large intrinsic third-order (Kerr) optical nonlinearity of Si, in conjunction with the strong field confinement achievable in high-index contrast waveguiding devices, makes it possible to attain strong nonlinear pulse interactions at low optical power and over short propagations distance. To be more specific, the dispersion length, L_D, and the nonlinear length, L_{nl}, of Si-PhNWs can be more than four orders of magnitude smaller than those of silica fibres [5. 26–28]. As a result, linear and nonlinear optical effects that normally require kilometer-long optical fibres to be observed can be achieved in milimetre-sized silicon devices, a few such examples being soliton pulse compression [5. 29, 30], modulational instability [5. 31], parametric amplification [5. 32, 33], supercontinuum generation [5. 34–36], pulse self-steepening [5. 37], and four-wave mixing [5. 38–42].

This chapter is organized as follows. In Section 5.2 we introduce the physical model we use to describe the coupled dynamics of the optical field and free carriers (FCs) upon pulse propagation in tapered Si-PhNWs. In order to gain a deeper understanding of the main physics governing these dynamics we also introduce a simplified semi-analytical model based on the method of moments, namely a model that describes the pulse dynamics simply as the time evolution of a small set of physical parameters defining the optical pulse. Then, in Section 5.3, we present the optical properties of the tapered Si-PhNWs considered in this work. In Section 5.4 and Section 5.5 we analyze the characteristics of optical pulse compression achieved via the soliton compression

technique and by using waveguides with sign-changing dispersion, respectively. In order to achieve the change of the dispersion sign we have used an hyperbolic tangent and a linear taper profile. Besides, we compare the pulse compression efficiency between the latter techniques. The main results and the conclusions of this work are summarized in Section 5.6.

5.2 Theoretical models for pulse propagation in sub-wavelength tapered silicon waveguides

In this section, we introduce a simplified semi-analytical mathematical model, based on the method of moments, in which the pulse propagation is reduced to a particle-like dynamics. One should note, here, that we will also use the general theoretical model of ultrashort pulse propagation in silicon nanowires that described in Section 3.2. One should note here, that although there are intrinsic losses of 0.1 dB/cm we have not incorporated them into our theoretical model. However, the linear losses effect do not have any influence in similariton generation as the attenuation parameter of 0.1 dB/cm is 2.3025 m^{-1}. That means that the characteristic length of the attenuation is 43 cm which is much longer than the whole propagation distance of our simulations.

5.2.1 Semi-analytical model

While the system (3.1)-(3.5) can provide detailed information about the pulse evolution, it is often more convenient to use a simplified approach based on a particle-like description of the pulse. In this approximation, also called the method of moments [5. 46], the pulse is characterized by a relatively small number of parameters, which are assumed to change adiabatically during pulse propagation. The physical quantities used in our analysis are defined as follows:

$$E = \int_{-\infty}^{\infty} |u|^2 dt, \tag{5.1a}$$

$$\tau^2 = \frac{\delta}{E} \int_{-\infty}^{\infty} (t-T)^2 |u|^2 dt, \tag{5.1b}$$

$$C = \frac{i\delta}{2E} \int_{-\infty}^{\infty} (t-T)\left(u^* u_t - u u_t^*\right) dt, \tag{5.1c}$$

$$\Omega = \frac{i}{2E} \int_{-\infty}^{\infty} \left(u^* u_t - u u_t^*\right) dt, \tag{5.1d}$$

$$T = \frac{1}{E}\int_{-\infty}^{\infty} t|u|^2 dt, \tag{5.1e}$$

where E, τ, C, Ω, and T are the pulse energy, pulse width, chirp coefficient, shift of the pulse carrier frequency, and temporal shift or the pulse, respectively. The parameter δ depends on the specific shape of the pulse, being equal to $12/\pi^2$ and 2 for hyperbolic secant and Gaussian pulses, respectively. These pulses are defined as:

$$u_s(t, z=0) = \sqrt{\frac{E}{2\tau}}\,\mathrm{sech}\left(\frac{t-T}{\tau}\right) e^{-i\Omega(t-T)-iC\frac{(t-T)^2}{2\tau^2}}, \tag{5.2a}$$

$$u_G(t, z=0) = \sqrt{\frac{E}{\sqrt{2\pi}\tau}}\, e^{-i\Omega(t-T)-(1+iC)\frac{(t-T)^2}{2\tau^2}}. \tag{5.2b}$$

The pulse width and its full-width at half-maximum, T_{FWHM}, are related by $T_{\mathrm{FWHM}} = 1.763\tau$ and $T_{\mathrm{FWHM}} = 1.665\tau$ for hyperbolic secant and Gaussian pulses, respectively.

In order to determine the pulse dynamics one calculates the z-derivative of the quantities in Eqs. (5.1a)-(5.1e) and use Eq. (3.1) to eliminate from the integrands the partial derivatives wrt z of $u(z,t)$. This leads to the following nonlinear system of ordinary differential equations:

$$\frac{d\mathbf{F}(z)}{dz} = \mathbb{A}(E, \tau, C, \Omega, T), \tag{5.3}$$

where $\mathbf{F}(z) = [E(z),\ \tau(z),\ C(z),\ \Omega(z),\ T(z)]^t$, t meaning the transpose operation, is a column vector containing the z-dependent parameters that characterize the pulse and $\mathbb{A}$ is a column vector that depends on the pulse parameters. The components of this vector depend on the specific shape of the pulse, their expressions for the two particular cases considered in this work being provided in the Appendix-*A*. The system (5.3) is solved by using a standard Runge-Kutta method of 5th order. Note that in our derivation of the system (5.3) the influence of FCs on the pulse dynamics is accounted for only through the TPA and nonlinear frequency dispersion terms in Eq. (3.1), that is, we have neglected the first two terms on the RHS of this equation. This means that the conclusions derived by using this simplified model must be validated by a full numerical integration of the rigorous theoretical model defined by Eqs. (3.1)-(3.5).

5.3 Dispersion maps of linear and nonlinear parameters of tapered silicon waveguides

In this work, we assume that optical pulses propagate in a silicon waveguide with rectangular core cross-section. The height of the waveguide is constant, $h = 250$ nm, whereas its width, w, varies adiabatically along the waveguide. The silicon core is placed on top of a SiO_2 substrate, the cladding being air (see Fig. 5.1).

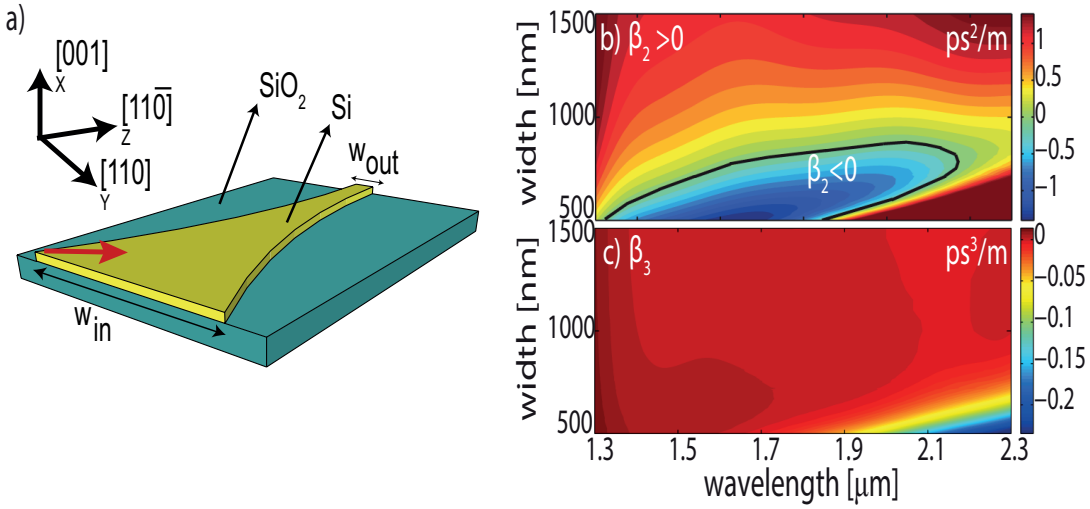

Figure 5.1: a) Sketch of a Si-PhNW oriented along the $1\bar{1}0$ direction (red arrow). Dispersion maps of b) second-order, β_2, and c) third-order dispersion coefficient, β_3. The black contour corresponds to zero-GVD, $\beta_2 = 0$.

The wavelength and width dependence of the waveguide parameters which are illustrated in Fig. 5.1 have been presented earlier in Chapter 3. However, we will emphasize some interesting features of the dispersion maps of the linear and nonlinear optical coefficients of the tapered Si-PhNW. These maps reveal an important property of the considered waveguide, namely in a broad range of frequencies the dispersion regime can be switched between the normal and anomalous by simply varying the waveguide width. These two regimes are separated by a zero-dispersion curve defined by $\beta_2(\lambda) = 0$, depicted in Fig. 5.1(b) as a black contour. Note that in the soliton regime the waveguide nonlinearity is relatively large, as per Fig. 5.2(a), because this regime is achieved for small w, namely when the optical field is strongly confined in the silicon core. This means that these silicon photonic wires readily provide the main ingredients needed for soliton pulse compression in dispersion-varying optical guiding devices. Moreover, since in this work we investigate the compression of pulses down to just

a few hundreds of femtoseconds, the influence of third-order dispersion (TOD) and frequency dispersion of the nonlinearity must be accounted for. The dispersion map of the TOD coefficient, $\beta_3(\lambda)$, is shown in Fig. 5.1(c), whereas the dispersive properties of the nonlinearity dispersion are illustrated in Figs. 5.2(c) and 5.2(d).

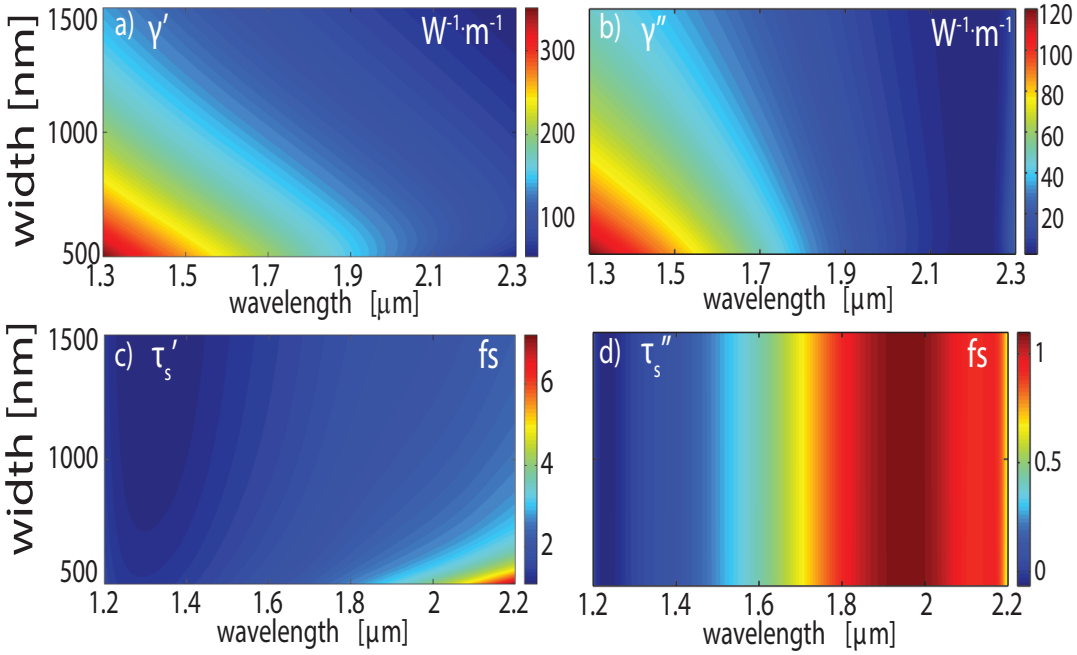

Figure 5.2: Dispersion maps of a) real and b) imaginary part of the nonlinear coefficient, γ, and the dispersion maps of c) real and d) imaginary part of the shock time coefficient, τ_s.

5.4 Soliton pulse compression in dispersion-varying tapered silicon waveguides

Generally, there are two main methods used to compress pulses that propagate in the soliton regime. The first one is based on the particle-like propagation of solitons, namely single solitons are propagated in a medium whose dispersion and nonlinearity changes adiabatically, leading to a slow decrease of the soliton width upon pulse propagation. The drawback of this method is that optical losses can affect its efficiency, which in the context of Si-PhNWs is an important aspect to be considered. The second method relies on the fact that higher-order solitons evolve periodically as they propagate, so that at certain distances their width is much smaller than the initial one. By properly choosing the waveguide length, significant pulse compression can be

achieved. Because it is much more effective, we consider here only this latter method.

To begin with, we launch a hyperbolic secant pulse described by Eq. (5.2a) with $\lambda = 1.55$ μm in a tapered Si-PhNW. The longitudinal z-variation of the width profile of the waveguide is assumed to be $w(z) = w_{\text{in}} + (w_{\text{out}} - w_{\text{in}})\tanh(az)/\tanh(aL)$, where $w_{\text{in}} = 700$ nm and $w_{\text{out}} = 660$ nm, are the initial and final width of the waveguide, respectively, $L = 9$ cm is the waveguide length, and $a = 80$ m^{-1}. This dependence ensures that the pulse propagates throughout into the soliton regime, $\beta_2 < 0$. The width of the input pulse is $\tau = 180$ fs and the input peak power, $P_0 = 1.4$ W, which means that the initial value of the soliton number, N_s, defined as $N_s^2 = L_D/L_{\text{nl}} = \gamma' P_0 \tau^2/|\beta_2|$, is $N_s = 10$. All the input parameters used for the simulations are presented in the following Table-5.1.

physical parameters	$\lambda = 1.55\mu m$	$\lambda = 2.1\mu m$
$\tau\ [fs]$	180	180
$P_0\ [W]$	1.4	2.07
$\alpha_{in}[dB\ cm^{-1}]$	0	0
$a[m^{-1}]$	80	80
$w_{in}\ [nm]$	700	850
$w_{out}\ [nm]$	600	750
$\beta_{TPA}\ [cm/GW]$	$1.31{\cdot}10^{-11}$	$3.5{\cdot}10^{-12}$
$n_2\ [cm^2/W]$	$5.37{\cdot}10^{-18}$	$11.46{\cdot}10^{-18}$
$\beta_1(in)\ [ps/m]$	$1.32{\cdot}10^{4}$	$1.29{\cdot}10^{4}$
$\beta_2(in)\ [ps^2/m]$	$-9.2{\cdot}10^{-1}$	$-8.1{\cdot}10^{-2}$
$\beta_3(in)\ [ps^3/m]$	$3.5{\cdot}10^{-3}$	$-2.7{\cdot}10^{-3}$
$\gamma'(in)\ [W^{-1}m^{-1}]$	202.4	97.7
$\gamma''(in)\ [W^{-1}m^{-1}]$	61.6	4.028
$\tau'(in)\ [fs]$	1.57	2.5
$\tau''(in)\ [fs]$	0.34	0.917
$\beta_1(out)\ [ps/m]$	$1.36{\cdot}10^{4}$	$1.32{\cdot}10^{4}$
$\beta_2(out)\ [ps^2/m]$	$-5.8{\cdot}10^{-1}$	$-3.2{\cdot}10^{-1}$
$\beta_3(out)\ [ps^3/m]$	$4.3{\cdot}10^{-3}$	$-7.4{\cdot}10^{-3}$
$\gamma'(out)\ [W^{-1}m^{-1}]$	225.3	104.5
$\gamma''(out)\ [W^{-1}m^{-1}]$	68.4	4.30
$\tau'(out)\ [fs]$	1.65	2.68
$\tau''(out)\ [fs]$	$3.4{\cdot}10^{-1}$	$9.12{\cdot}10^{-1}$
$L\ [mm]$	90	30

Table 5.1: Input pulse parameters for the case of soliton compression at telecom and mid-infrared wavelengths corresponding to the results presented in Fig. 5.3.

The temporal and spectral evolution of the pulse and FCs are presented in

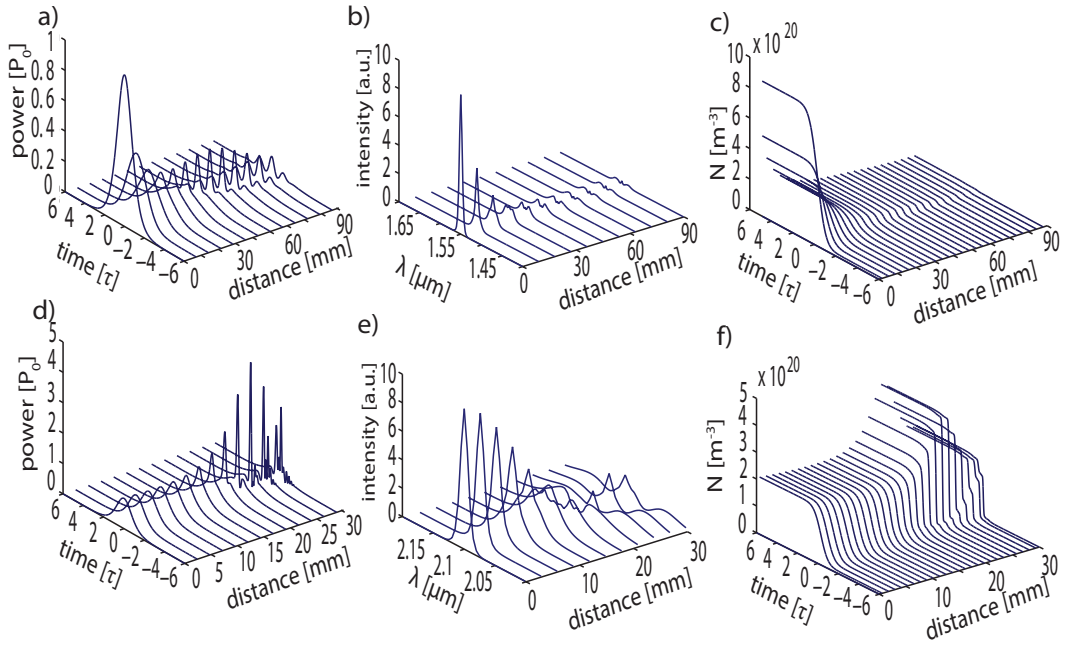

Figure 5.3: Temporal [a) and d)] and spectral [b) and e)] pulse evolution in a tapered Si-PhNW (see text for taper and pulse parameters) and the corresponding free-carriers dynamics [c) and f)]. Top and bottom panels correspond to $\lambda = 1.55$ μm and $\lambda = 2.1$ μm, respectively. One should note here that a) and d) are normalized to input power $P_0 = 1.4$ W and $P_0 = 2.07$, respectively. Further to that time is also normalized to the input pulse width $\tau = 180$ fs

Figs. 5.3(a)-5.3(c). These plots show that after an initial stage in which the pulse broadens ($z < 20$ mm) a significant pulse compression is observed beyond $z \simeq 20$ mm. It can be seen, however, that the pulse shape does not change periodically with z, which is due to the influence of effects other than the group-velocity dispersion (GVD) and SPM. Specifically, TPA induces strong pulse decay whereas the TOD leads to pulse breakup. The effect of TPA on the pulse dynamics is particularly strong in the initial propagation stage during which, as Fig. 5.3(c) suggests, most of the pulse energy is absorbed by photogenerated FCs. Nevertheless, a maximum of more than fivefold pulse compression is achieved at $z \simeq 60$ mm, which corresponds to a pulse duration of $\sim$36 fs.

Before we continue to present some interesting characteristics of pulse compression in silicon nanowires, I should comment that, to the best of my knowledge, I have not found some published work related to optical pulse compression in silicon nanowires in order to compare the published results with mine.

A common feature of pulses compressed through this method, which can also be

seen in our simulations for $z \gtrsim 60$ mm, is the generation of pedestals at the edges of the pulse. That means that the energy of the pulse does not remain in the main peak of the pulse but it is lost to the pedestals. In order to gain a more complete view about the energy that is wasted to the pedestals, we should mention that for the case of $\lambda = 1.55$ μm the energy of the main peak is three times larger than that lost to the pedestals at $z \simeq 60$ mm whereas $z \simeq 90$ mm the energy of the main peak is only 1.2 times larger than that wasted to the pedestals. However, for the case of $\lambda = 2.1$ μm the energy of the main peak at $z \simeq 20$ mm is six times larger than that to the pedestals whereas at $z \simeq 30$ mm is only 1.4 times larger than that to the pedestals.

In order to assess the degree to which the deleterious effects of TPA can be mitigated, we investigated the propagation of a hyperbolic secant pulse in the mid-IR regime, namely at $\lambda = 2.1$ μm. The tapered wire considered in this case is defined by $w_{\text{in}} = 850$ nm, $w_{\text{out}} = 750$ nm, $L = 3$ cm, and $a = 80$ m^{-1}, the pulse parameters being $\tau = 180$ fs and $P_0 = 2.07$ W ($N_s = 9$). Unlike the telecom case, the pulse decay is negligible at mid-IR wavelengths, its peak amplitude, in fact, increases considerably. This substantial increase in the peak power, illustrated in Fig. 5.3(d), is explained by the fact that although part of the pulse energy is absorbed via TPA, the pulse undergoes significant compression as well. In particular, it is compressed by more than $10\times$ at $z = 25$ mm, which obviously results in large enhancement of the peak power. As in the case of $\lambda = 1.55$ μm, pedestals are generated leading to the loss of energy from the main peak for propagation distances longer than 25 mm.

Unlike the case of regular or microstructured optical fibres, photogenerated FCs can affect, in a nontrivial way, the dynamics of optical pulses that propagate in silicon wires. This idea is clearly illustrated by the plots in Figs. 5.3(c) and 5.3(f). Thus, whereas at $\lambda = 1.55$ μm the FC density decreases monotonously with z, at $\lambda = 2.1$ μm there is a certain propagation distance, $z \simeq 20$ mm, at which a maximum amount of FCs is generated. This distance is roughly equal to the distance at which maximum pulse compression is observed. To understand this difference in pulse dynamics, note that at a given z the peak FC density can be estimated from Eq. (3.5) to be $\Delta N(z) \simeq P^2(z)\Gamma''(z)\tau(z)/A^2(z)v_g^2(z)$. Then, since the parameters Γ'', A, and v_g vary only slightly with z, the main contribution to $\Delta N(z)$ comes from the z-variation of the factor $P^2(z)\tau(z) \sim P(z)E(z)$. At mid-IR the pulse energy loss is rather small and

therefore the maximum amount of FCs is generated when the peak power reaches its maximum, that is, when the pulse compression is maximum as well.

More insights into the pulse dynamics are provided by the semi-analytical model described by the system (5.3). By integrating numerically this system of equations we determined the dependence of the pulse parameters on the propagation distance, under the assumption that the pulse propagates in a particle-like manner. In an alternative approach, we computed the pulse parameters by fitting with a sech-function given by Eq. (5.2a) the pulse obtained by direct integration of the rigorous model (3.1)-(3.5). The results obtained by these two methods are represented in Fig. 5.4 by the black and blue lines, respectively. For comparison, the pulse parameters were also calculated by inserting in the definitions in Eqs. (5.1) the solution obtained by numerical integration of the rigorous theoretical model (see the red curves in Fig. 5.4).

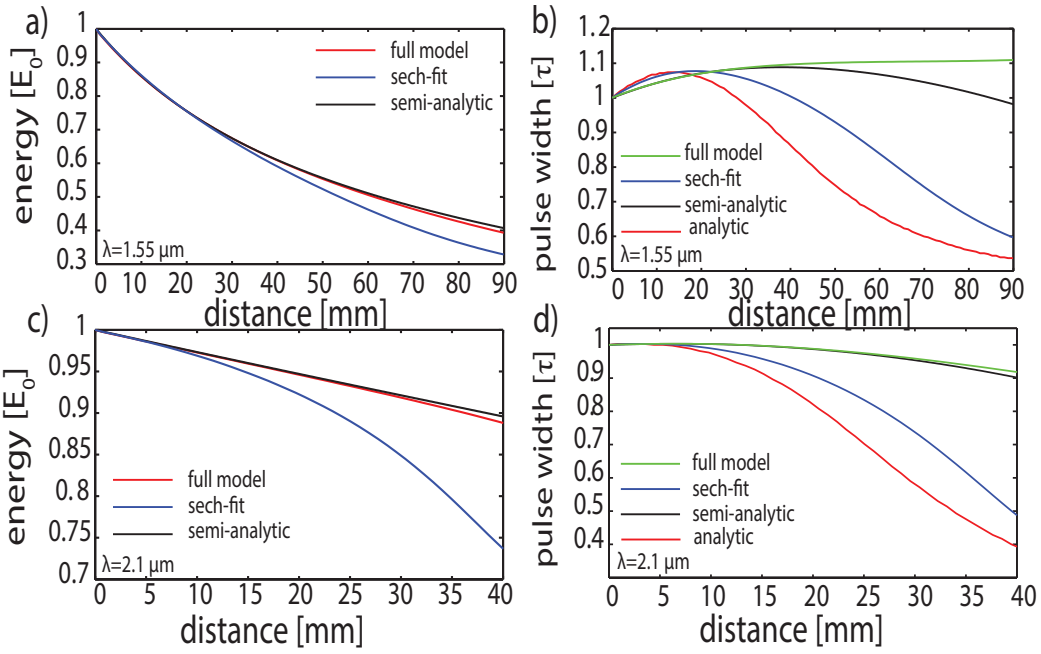

Figure 5.4: Evolution of pulse energy E and width τ *vs.* the propagation distance. Top panels correspond to $\lambda = 1.55\ \mu$m, $\tau = 180$ fs, and $P_0 = 0.2$ W, whereas the pulse parameters in the bottom panels are $\lambda = 2.1\ \mu$m, $\tau = 180$ fs, and $P_0 = 0.5$ W. The linear and nonlinear parameter are the same as presented in Table-5.1. $E_0 = 72\ fJ$ for top panels while $E_0 = 90\ fJ$ for bottom panels.

The results summarized in Fig. 5.4 show that, generally, there is a good agreement over a certain propagation distance between the predictions of the full theoretical model and the semi-analytical model. This proves that indeed in the initial stage of the propagation, the optical pulse can be viewed as a hyperbolic secant pulse undergo-

ing particle-like dynamics. This approximation breaks down after a certain propagation distance ($z \simeq 30$ mm at $\lambda = 1.55$ μm and $z \simeq 10$ mm at $\lambda = 2.1$ μm) as beyond this distance the optical pulse begins to split up. That means that our theoretical model is more accurate than the semi-analytical model as it keeps up with the emerged nonlinear pulse dynamics that occur along the propagation distance. One should mention here that the semi-analytical model can not describe strong compression due to the fact that as the pulse is compressed then its amplitude starts to increase enhancing the nonlinearities. Thus the pulse starts to change its initial profile making the initial assumption of the semi-analytical model that the pulse profile is constant along the propagation distance not to be valid. An additional feature of Fig. 5.4 is that, at both wavelengths, the pulse profile follows a similar evolution: initially the pulse broadens and then its width gradually decreases. To quantify the pulse compression after it breaks up, we determined its width by calculating the FWHM width of the main pulse, as per the green curves in Fig. 5.4. It can be seen that, contrary to the predictions of the semi-analytical model, the main pulse is compressed significantly, which proves the effectiveness of tapered Si-PhNWs in pulse reshaping applications.

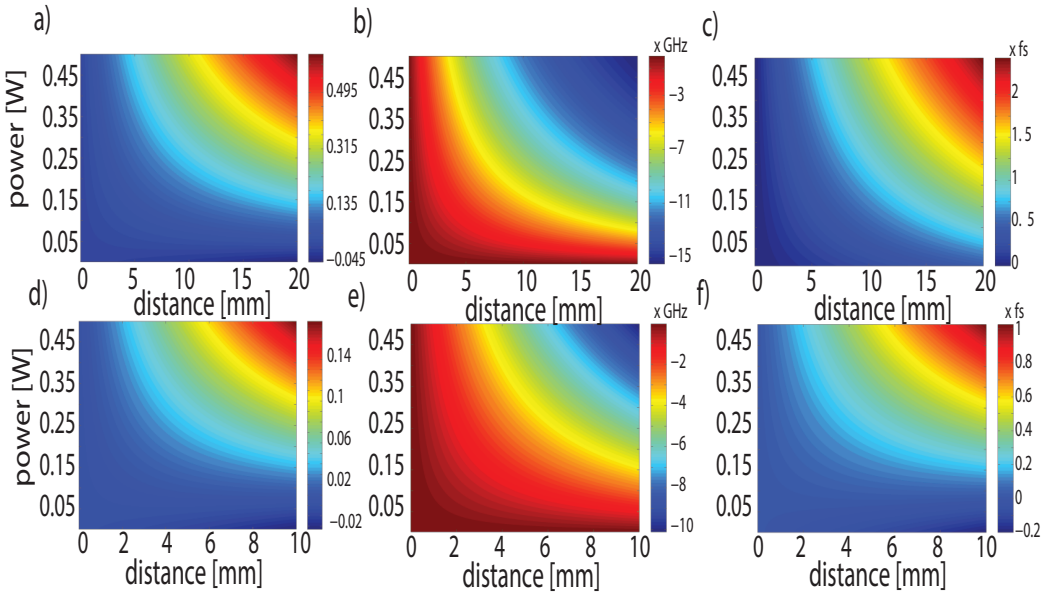

Figure 5.5: Evolution of the pulse chirp C (left panels), frequency shift Ω (middle panels), and temporal shift T (right panels), determined for different peak power. Top and bottom panels correspond to $\lambda = 1.55$ μm and $\lambda = 2.1$ μm, respectively, and throughout $\tau = 180$ fs.

To achieve a more complete understanding of of the pulse compression process, we also determined the z-dependence of the chirp, $C(z)$, centre frequency shift, $\Omega(z)$,

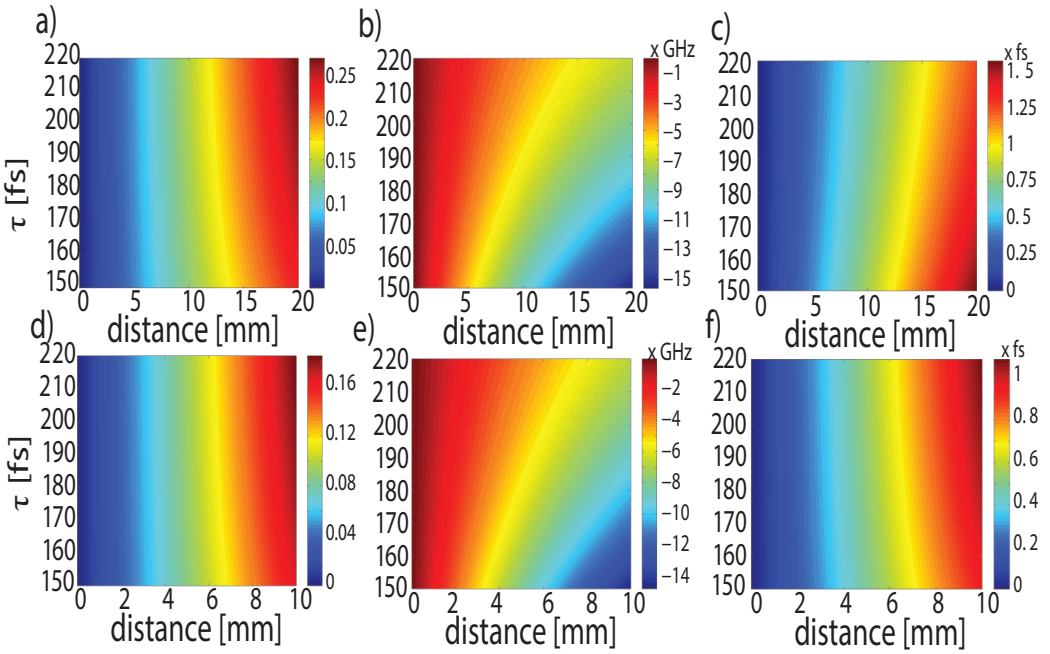

Figure 5.6: The same as in Fig. 5.5, the pulse parameters being determined as function of τ. The pulse power in the top ($\lambda = 1.55\ \mu m$) and bottom ($\lambda = 2.1\ \mu m$) panels is $P_0 = 1.4$ W and $P_0 = 2.07$ W, respectively.

and temporal shift, $T(z)$, calculated as function of the input pulse peak power P_0 and width τ, the results being presented in Fig. 5.5 and Fig. 5.6, respectively. These figures show that, except for relatively small peak power, the chirp is positive and increases monotonously with z, that is the positive chirp generated by SPM is larger than the negative one generated by the anomalous GVD. As a result, the initial propagation stage in which the pulse broadens is followed by a monotonous pulse compression. This is an expected behaviour of a pulse that propagates in the anomalous GVD regime, the z-dependence of the pulse chirp explaining why the pulse compression is preceded by an initial pulse broadening. Thus, initially the pulse broadens under the influence of the GVD but as the positive chirp induced by the SPM increases, the GVD begins to have an opposite effects, namely it compresses the pulse. As the pulse is compressed, the GVD and the peak power increase, so that the SPM and, consequently, the rate at which the chirp increases become larger, too. This leads to a further increase in the efficiency of the pulse compression process. A similar monotonous increase with the propagation distance, albeit extremely small ($T \simeq 1$ fs), is shown by the pulse temporal shift. This effect, whose magnitude is comparable to τ_s, is due to the frequency dispersion of the nonlinearity and the TOD. Finally, the centre frequency of the pulse is redshifted

because of the nonlinear effect of τ_s, the magnitude of this redshift increasing with z. As expected, the magnitude of the frequency shift increases with the peak power, P_0 (the strength of the nonlinearity dispersion increases with P_0) and decreases with the pulse width, τ (TOD increases as τ decreases).

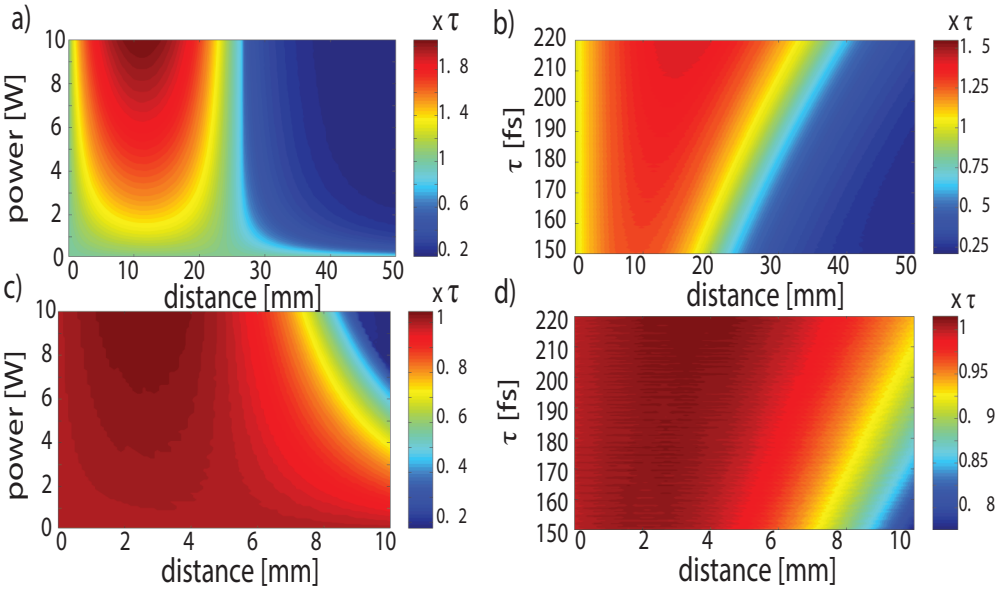

Figure 5.7: a) Dependence of the pulse width on P_0, determined for $\tau = 180$ fs and b) on τ, determined for $P_0 = 1.4043$ W. c) Dependence of the pulse width on P_0, determined for $\tau = 180$ fs and d) on τ, determined for $P_0 = 2.07$ W. The top and bottom plots correspond to $\lambda = 1.55$ μm and $\lambda = 2.1$ μm, respectively.

Since this study is primarily concerned with the investigation of pulse compression mechanisms in tapered Si-PhNWs and the physical effects that determine their efficiency, we focus now on a more detailed analysis of the dependence of the pulse compression factor on the pulse power and width. This is a natural choice as the main characteristic lengths that govern the pulse propagation are the linear and nonlinear lengths, which depend on τ and P_0, respectively. The results of this investigations are summarized in Fig. 5.7. Thus, comparing the results presented in the top and bottom panels in Fig. 5.7 one can see that the pulse compression is much more efficient at mid-IR frequencies, namely a shorter propagation distance is needed to achieve a certain compression factor. This can be easily explained using the characteristics of the pulse evolution we just discussed: the TPA is much weaker at mid-IR, which means that the positive SPM-induced chirp and hence the pulse compression is much larger in this frequency domain. Moreover, the maps plotted in Fig. 5.7 show that the compression factor increases with P_0 but decreases with τ. This finding has a simple explanation,

namely whereas the SPM is proportional to P_0, the strength of GVD effects is inverse proportional to τ^2. Note, however, that if only waveguide tapering effects are considered both SPM and GVD increase with the propagation distance, as for the two tapers considered in this section both γ and $|\beta_2|$ increase with z.

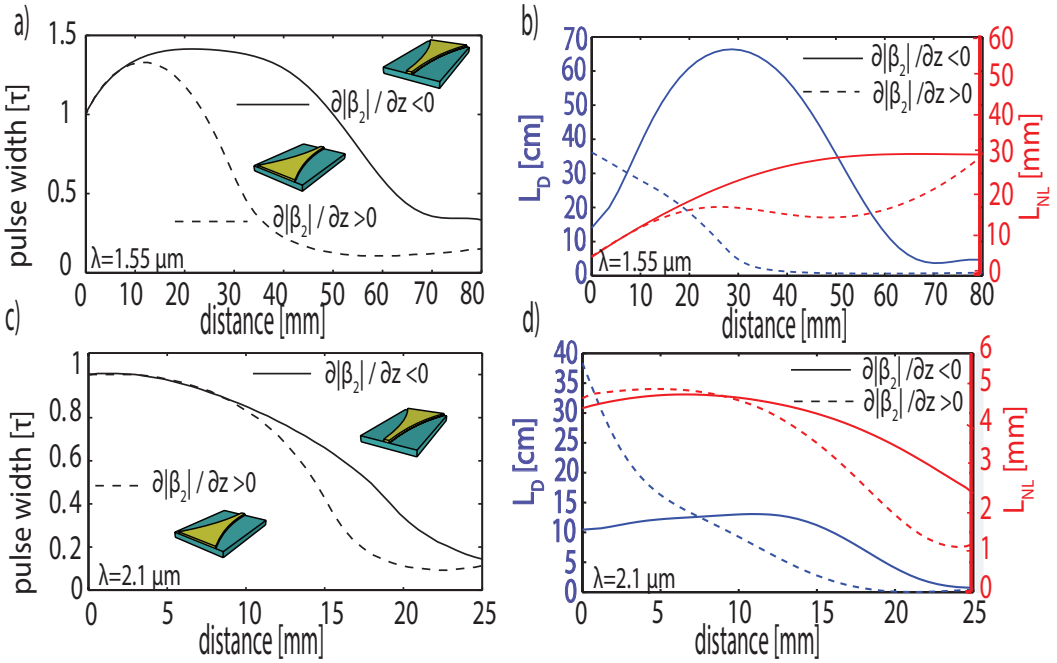

Figure 5.8: Evolution of pulse width (left panels) and L_D and $L_{\rm nl}$ (right panels) determined for tapered Si-PhNWs with increasing (dotted line) and decreasing (solid line) dispersion.

This analysis suggests that, surprisingly, pulse compression can be achieved even when the dispersion increases. To be more specific, previous studies that considered adiabatic soliton compression in dispersion-managed optical fibres have demonstrated that pulse compression in lossless fibres with constant nonlinearity can be achieved only if the dispersion $|\beta_2|$ decreases. Indeed, under these circumstances, for the soliton number $N_s^2 = \gamma P_0 \tau^2/|\beta_2|$ to remain constant while the pulse duration, τ, decreases, the GVD coefficient $|\beta_2|$ must decrease as well. In tapered Si-PhNWs, however, the increase of the GVD coefficient can be offset by the increase of γ (γ increases as the waveguide width decreases, as per Fig. 5.2), so that soliton pulse compression can be achieved even in dispersion-increasing tapered waveguides. These ideas are illustrated in Fig. 5.8, where we show the dependence of the pulse width on the propagation distance in tapers with increasing as well as decreasing dispersion. Thus, we launch a pulse with $P_0 = 1.4$ W ($P_0 = 2.07$ W) in a tapered Si-PhNWs with $w_{\rm in} = 700$ nm

($w_{\text{in}} = 850$ nm), $w_{\text{out}} = 660$ nm ($w_{\text{out}} = 750$ nm), and $L = 90$ mm ($L = 30$ mm), the wavelength being $\lambda = 1.55\ \mu$m ($\lambda = 2.1\ \mu$m). In both cases $\tau = 180$ fs and $a = 80\ \text{m}^{-1}$. The z-dependence of the pulse width, as well as that of L_D and L_{nl}, are depicted in Fig. 5.8 with dotted lines. The solid lines in this figure correspond to the pulse propagation in the inverted taper, namely to the case in which the roles of w_{in} and w_{out} are interchanged while the pulse parameters are kept unchanged. As a result, in the first case the dispersion increases (in absolute value), whereas the latter one corresponds to decreasing dispersion. Nevertheless, in both cases, the soliton is significantly compressed, as per Figs. 5.8(a) and 5.8(c). A closer analysis of the interplay between the two main characteristic lengths describing the soliton dynamics leads us to the same conclusion. Thus, Figs. 5.8(b) and 5.8(d) show that for both tapers $L_D > L_{\text{nl}}$, that is the nonlinear effects are stronger. A consequence of this fact is that, as discussed above, the total chirp is positive. As the pulse propagates in the anomalous GVD regime, this results in pulse compression.

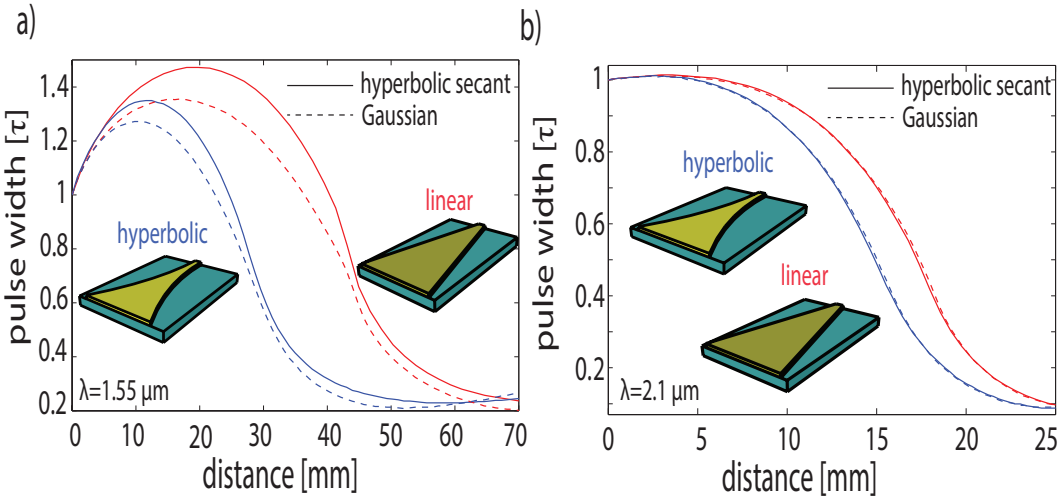

Figure 5.9: a) Evolution of the pulse width for two taper profiles, calculated for $P_0 = 1.4$ W and $\lambda = 1.55\ \mu$m and b), for $P_0 = 2.07$ W and $\lambda = 2.1\ \mu$m. In both cases the initial pulse width is $\tau = 180$ fs.

From a practical point of view, it is important to understand to what degree the taper profile affects the efficiency of the pulse compression process. While we did not try to find the optimum taper profile that leads to maximum compression, we have considered the pulse propagation in hyperbolically and linearly tapered Si-PhNWs, that are, two of the commonly used taper profiles. The z-profile of the linear taper is defined by $w(z) = w_{\text{in}} - (w_{\text{in}} - w_{\text{out}})z/L$. The input and output widths were the same in both

cases: at $\lambda = 1.55$ μm, $w_{\text{in}} = 700$ nm, $w_{\text{out}} = 660$ nm, and $L = 90$ mm, whereas at $\lambda = 2.1$ μm, $w_{\text{in}} = 850$ nm, $w_{\text{out}} = 750$ nm, and $L = 30$ mm. The pulse peak power was $P_0 = 1.4$ W ($P_0 = 2.07$ W) at $\lambda = 1.55$ μm ($\lambda = 2.1$ μm), whereas in both cases $\tau = 180$ fs and $a = 80$ m^{-1}. The results of our analysis, summarized in Fig. 5.9, suggests that whereas the pulse width follows a similar evolution as it propagates in the two tapers, specific differences imply that the hyperbolic taper is more efficient for pulse compression. This finding can be explained by the fact that in the case of the hyperbolic taper there is a more rapid transition to the waveguide region with large nonlinearity, as compared to the case of linear taper, which means that the generated positive chirp that induces pulse compression is larger in the former case.

5.5 Pulse compression below the soliton power threshold

One of the conclusions of the preceding section was that large pulse compression can be achieved when a pulse with positive chirp propagates in the anomalous GVD regime. One drawback of this approach is that if $\beta_2 < 0$, the chirp induced by the GVD is negative, which reduces the chirp generated by the SPM. One possible solution to this problem, which can be easily implemented by using tapered Si-PhNWs, is to propagate first the pulse in a section with large normal GVD of a tapered waveguide until the pulse accumulates a large positive chirp then propagate the chirped pulse in a waveguide section with large anomalous GVD, where the pulse is compressed. In a practical setting, this scheme can be implemented by simply using a tapered Si-PhNW whose width is varied in such a way that the waveguide has normal and anomalous GVD within its input and output sections, respectively [see Fig. 5.1(b)]. Importantly, this pulse compression method can be applied to pulses with low peak power as well, as it does not require that the pulse propagates in the soliton regime.

The semi-analytical model described by Eq. (5.3) provides an intuitive picture of the pulse compression. Thus, if one considers a hyperbolic secant pulse given by Eq. (5.2a) and neglects TPA effects and the higher-order terms in Eq. (3.1), that is,

$\gamma'' = 0$, $\beta_3 = 0$, and $\tau_s = 0$, Eqs. (A2b)-(A2c) become [5. 46]:

$$\frac{d\tau}{dz} = \frac{\beta_2 C}{\tau}, \tag{5.4a}$$

$$\frac{dC}{dz} = \left(\frac{4}{\pi^2} + C^2\right)\frac{\beta_2}{\tau^2} + \frac{2\gamma' E}{\pi^2 \tau}, \tag{5.4b}$$

where the pulse energy, E, is conserved upon propagation. This system shows that when the pulse propagates in the waveguide section with normal GVD, $\beta_2 > 0$, both terms in the RHS of Eq. (5.4b) increase the chirp. When the pulse then propagates in the waveguide section with anomalous GVD, $\beta_2 < 0$, the RHS of Eq. (5.4a) is negative, and therefore the pulse is compressed.

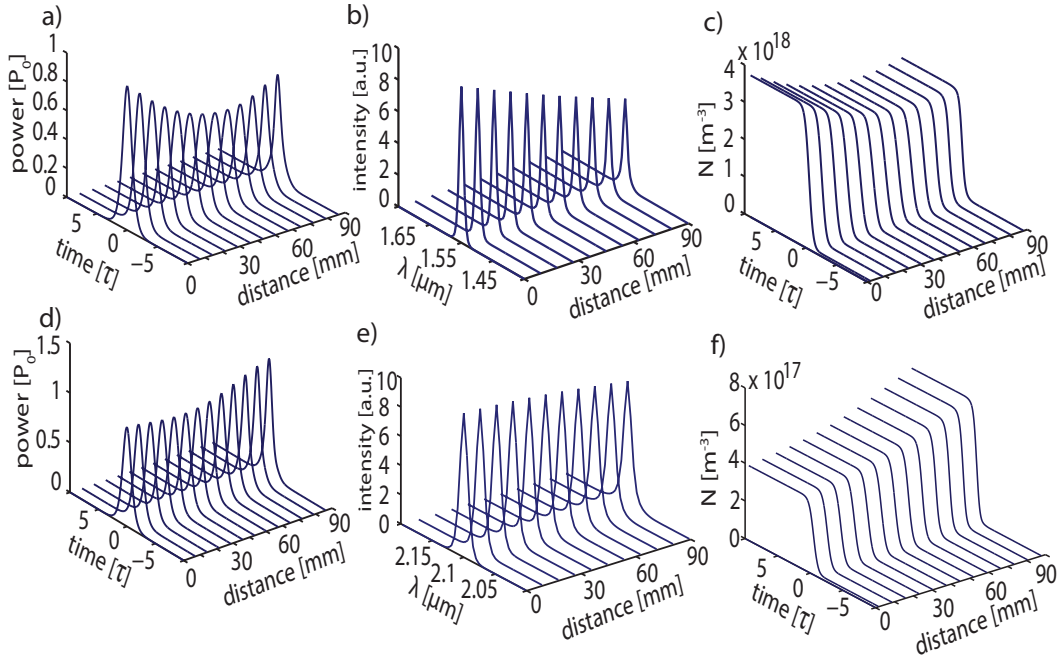

Figure 5.10: Temporal [a) and d)] and spectral [b) and e)] pulse evolution in a tapered Si-PhNWs whose dispersion changes from normal to anomalous (see text for taper and pulse parameters) and the corresponding free-carriers dynamics [c) and f)]. Top and bottom panels correspond to $\lambda = 1.55$ μm and $\lambda = 2.1$ μm, respectively.

To illustrate these ideas, we consider the propagation of optical pulses in tapered Si-PhNWs whose dispersion changes from normal to anomalous. For this, we considered two tapered Si-PhNWs defined by the following parameters: $w_{\text{in}} = 850$ nm and $w_{\text{out}} = 610$ nm, at $\lambda = 1.55$ μm, and $w_{\text{in}} = 980$ nm and $w_{\text{out}} = 735$ nm, at $\lambda = 2.1$ μm. In both cases $a = 80$ m^{-1}, $L = 90$ mm, and $\tau = 180$ fs, whereas the pulse power was $P_0 = 90$ mW at $\lambda = 1.55$ μm and $P_0 = 100$ mW at $\lambda = 2.1$ μm. This choice of waveg-

uide and pulse parameters ensured that at both wavelengths $N_s(z=0)=0.9<1$. All the input pulse parameters used for the current simulation are presented in the following Table-5.2.

physical parameters	$\lambda = 1.55\mu m$	$\lambda = 2.1\mu m$
$\tau\ [fs]$	180	180
$P_0\ [W]$	$9{\cdot}10^{-2}$	0.1
$\alpha_{in}[dB\ cm^{-1}]$	0	0
$a[m^{-1}]$	80	80
$w_{in}\ [nm]$	850	980
$w_{out}\ [nm]$	610	735
$\beta_{TPA}\ [cm/GW]$	$1.31{\cdot}10^{-11}$	$3.5{\cdot}10^{-12}$
$n_2\ [cm^2/W]$	$5.37{\cdot}10^{-18}$	$11.46{\cdot}10^{-18}$
$\beta_1(in)\ [ps/m]$	$1.29{\cdot}10^{4}$	$1.26{\cdot}10^{4}$
$\beta_2(in)\ [ps^2/m]$	$-3.9{\cdot}10^{-1}$	$-4.1{\cdot}10^{-1}$
$\beta_3(in)\ [ps^3/m]$	$2.4{\cdot}10^{-3}$	$-1.58{\cdot}10^{-3}$
$\gamma'(in)\ [W^{-1}m^{-1}]$	174.8	88.1
$\gamma''(in)\ [W^{-1}m^{-1}]$	53.25	3.63
$\tau'(in)\ [fs]$	1.57	2.5
$\tau''(in)\ [fs]$	$33.8{\cdot}10^{-2}$	$91.8{\cdot}10^{-2}$
$\beta_1(out)\ [ps/m]$	$1.35{\cdot}10^{4}$	$1.33{\cdot}10^{4}$
$\beta_2(out)\ [ps^2/m]$	$-53.8{\cdot}10^{-2}$	$-31.3{\cdot}10^{-2}$
$\beta_3(out)\ [ps^3/m]$	$4.2{\cdot}10^{-3}$	$-9.7{\cdot}10^{-3}$
$\gamma'(out)\ [W^{-1}m^{-1}]$	228.8	105.2
$\gamma''(out)\ [W^{-1}m^{-1}]$	67.8	4.37
$\tau'(out)\ [fs]$	1.64	2.70
$\tau''(out)\ [fs]$	$33.7{\cdot}10^{-2}$	$91.7{\cdot}10^{-2}$
$L\ [mm]$	90	90

Table 5.2: Input pulse parameters for the case of pulse compression at telecom and mid-infrared wavelengths of Fig. 5.10.

The evolution of the temporal and spectral profile of the pulse, as well as that of FC-density, at both wavelengths, are presented in Fig. 5.10. This figure show that the pulse is compressed at both wavelengths; however, the compression factor is significantly smaller than in the case of soliton compression. In addition, as expected, TPA has different impact on the pulse compression at the two wavelengths. At $\lambda = 1.55\ \mu$m, where the TPA is large, the pulse propagates in a lossy medium and therefore its width initially increases, before undergoing compression in the waveguide section with $\beta_2 < 0$, namely beyond $z \simeq 40$ mm. By contrast, at $\lambda = 2.1\ \mu$m the TPA is weak, so that the width of the pulse remains approximately constant for $z \lesssim 30$ mm and then

begins to decrease. Since the peak power is relatively small in this case, the amount of generated FCs is small as well (compare the FC-densities in Fig. 5.3 and Fig. 5.10) and consequently the z-dependence of FCs is similar to that of the pulse power.

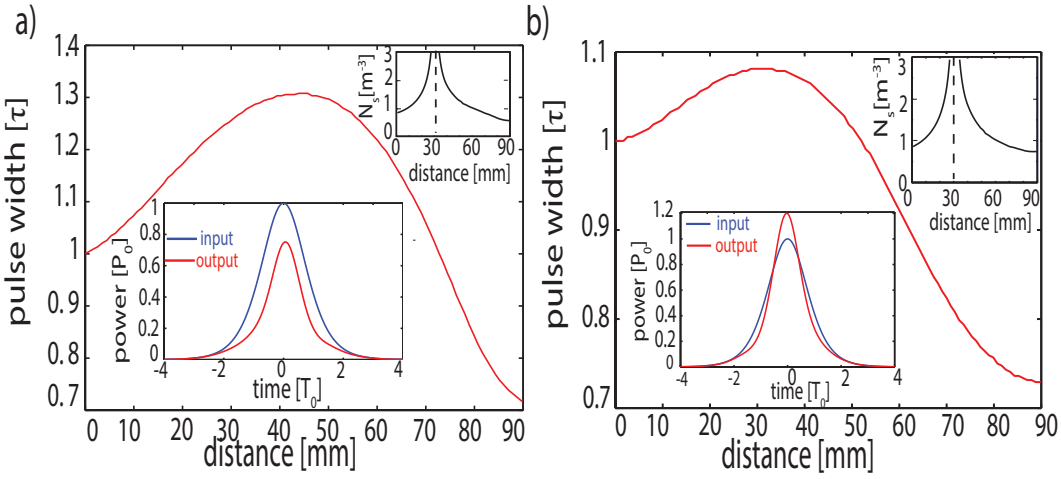

Figure 5.11: Evolution of the pulse width upon propagation in a tapered Si-PhNWs whose dispersion changes from normal to anomalous, determined for a), $\lambda = 1.55$ μm and b), $\lambda = 2.1$ μm. Insets depict the evolution of the soliton number N_s as well as the input and output pulse profiles.

A more quantitative description of the pulse compression is presented in Fig. 5.11, where we show the evolution of the pulse width *vs.* the propagation distance. Thus, it can be seen that the pulse broadens while it propagates in the section of the waveguide with normal GVD (the zero-GVD point is located at $z = 30$ mm) and subsequently undergoes significant compression. In particular, the pulse width decreases by 29% at $\lambda = 1.55$ μm and by 27% at $\lambda = 2.1$ μm, after a total propagation distance of 90 mm. The input pulse width is $\tau = 180$ fs and the input power is $P_0 = 90$ mW at $\lambda = 1.55$ μm and $P_0 = 100$ mW at $\lambda = 2.1$ μm, which ensures that $N_s(z = 0) < 1$, namely the input pulse does not have enough energy to form a soliton. However, as the pulse approaches the zero-GVD point, N_s increases considerably since β_2 becomes very small. After the pulse passes the zero-GVD point N_s begins to decrease and becomes again less than 1 in the final propagation stage.

The dependence of the compression factor on the pulse parameters, determined for the same pair of tapers as that corresponding to Fig. 5.10, is summarized in Fig. 5.12. Note that we chose the input power in these simulations such that the soliton number remains smaller than 1 for the most part of the propagation. The main conclusion illustrated by these plots is that pulse compression can be achieved for a broad spectrum

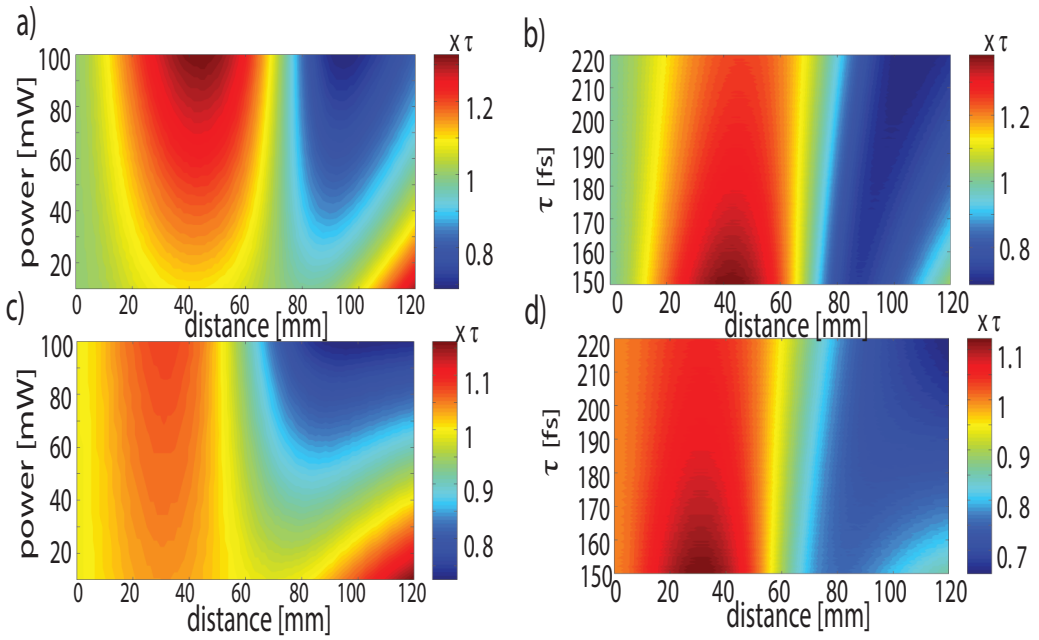

Figure 5.12: a) Dependence of the pulse width *vs.* peak power P_0, determined for $\tau = 180$ fs, and b), *vs.* τ, determined for $P_0 = 90$ mW. c) Dependence of the pulse width *vs.* peak power P_0, determined for $\tau = 180$ fs and d), *vs.* τ, determined for $P_0 = 100$ W. Top and bottom panels correspond to $\lambda = 1.55$ μm and $\lambda = 2.1$ μm, respectively.

of pulse widths and powers. For all values of the pulse parameters one requires a certain propagation distance (waveguide length) in order to achieve pulse compression, as initially the pulse broadens. It can also be seen that the compression factor depends rather weakly on the pulse parameters or the operation wavelength. In particular, for a given propagation distance, the compression factor increases with the pulse power and decreases with the pulse width. This conclusion can be derived from the dependence on the pulse parameters of the SPM and GVD chirps, namely, as suggested by Eq. (5.4b), the SPM chirp increases with the pulse power whereas the GVD chirp increases when the pulse width decreases.

5.6 Conclusion

Large pulse compression has been obtained in long millimetre SiPhNW. A rigorous numerical and semi-analytical model have been developed in order to study in detail the propagation of pulses either in soliton or normal regime. In order to gain a complete physical insight of pulse compression, we focused on different parameters that have influence on compression proccess such as input power and pulse width, taper profiles.

In general, we showed that a generation of ultra short pulses is possible on chip scale devices.

An equally important nonlinear phenomenon that could also be employed in chip scale optical applications is FWM. Such applications could be signal amplification, signal regeneration and a multitude of other important applications in various fields of optics. It is for this reason that we provide a detailed analysis of FWM in a periodically width modulated Si-PhNW in the next chapter.

References

[5. 1] E. B. Treacy, "Optical pulse compression with diffraction gratings," IEEE J. Quantum Electron. **QE 5**, 454–458 (1969).

[5. 2] O. E. Martinez, J. P. Gordon, and R. L. Fork, "Negative group-velocity dispersion using refraction," J. Opt. Soc. Am. A. **1**, 1003–1006 (1984).

[5. 3] A. M. Weiner, "Femtosecond pulse shaping using spatial light modulators," Rev. Sci. Instrum. **71**, 1929–1960 (2000).

[5. 4] G. Imeshev, A. Galvanauskas, D. Harter, M. A. Arbore, M. Proctor, and M. M. Fejer, "Engineerable femtosecond pulse shaping by second-harmonic generation with Fourier synthetic quasi-phase-matching gratings," Opt. Lett. **23**, 864–866 (1998).

[5. 5] N. J. Doran and D. Wood, "Nonlinear-optical loop mirror," Opt. Lett. **13**, 56–58 (1988).

[5. 6] K. Smith, N. J. Doran, and P. G. J. Wigley, "Pulse shaping, compression, and pedestal suppression employing a nonlinear-optical loop mirror," Opt. Lett. **15**, 1294–1296 (1990).

[5. 7] M. D. Pelusi, Y. Matsui, and A. Suzuki, "Pedestal suppression from compressed femtosecond pulses using a nonlinear fibre loop mirror," IEEE J. Quantum Electron. **35**, 867–874 (1999).

[5. 8] W. J. Tomlinson, R. H. Stolen, and C. V. Shank, "Compression of optical pulses chirped by self-phase modulation in fibres," J. Opt. Soc. Am. B. **1**, 139–149 (1984).

[5. 9] M. Nisoli, S. De Silvestri, O. Svelto, R. Szipocs, K. Ferencz, Ch. Spielmann, S. Sartania, and F. Krausz, "Compression of high-energy laser pulses below 5 fs," Opt. Lett. **22**, 522–524 (1997).

[5. 10] J. T. Manassah, "Pulse compression of an induced-phase-modulated weak signal," Opt. Lett. **13**, 755–757 (1988).

[5. 11] G. P. Agrawal, P. L. Baldeck, and R. R. Alfano, "Optical wave breaking and pulse compression due to cross-phase modulation in optical fibres," Opt. Lett. **14**, 137–139 (1989).

[5. 12] L. F. Mollenauer, R. H. Stolen, J. P. Gordon, and W. J. Tomlinson, "Extreme picosecond pulse narrowing by means of soliton effect in single-mode optical fibres," Opt. Lett. **8**, 289–291 (1983).

[5. 13] K. A. Ahmed, K. C. Chan, and H. F. Liu, "Femtosecond pulse generation from semiconductor laser using the soliton effect compression technique," IEEE J. Sel. Top. Quantum Electron. **1**, 592–600 (1995).

[5. 14] M. D. Pelusi and H. F. Liu, "Higher order soliton pulse compression in dispersion-decreasing optical fibres," IEEE J. Quantum Electron. **33**, 1430–1439 (1997).

[5. 15] A. A. Amorim, M. V. Tognetti, P. Oliveira, J. L. Silva, L. M. Bernardo, F. X. Kartner, and H. M. Crespo, "Sub-two-cycle pulses by soliton self-compression in highly nonlinear photonic crystal fibres," Opt. Lett. **34**, 3851–3853 (2009).

[5. 16] A. C. Peacock, "Mid-IR soliton compression in silicon optical fibres and fibre tapers," Opt. Lett. **37**, 818-820 (2012).

[5. 17] S. V. Chernikov, E. M. Dianov, D. J. Richardson, and D. N. Payne, "Soliton pulse compression in dispersion-decreasing fibre," Opt. Lett. **18**, 476–478 (1993).

[5. 18] M. Nakazawa, E. Yoshida, H. Kubota, and Y. Kimura, "Generation of a 170 fs, 10 GHz transform-limited pulse train at 1.55 μm using a dispersion decreasing, erbium-doped active soliton compressor," Electron. Lett. **30**, 2038–2040 (1994).

[5. 19] J. Hu, B. S. Marks, C. R. Menyuk, J. Kim, T. F. Carruthers, B. M. Wright, T. F. Taunay, and E. J. Friebele, "Pulse compression using a tapered microstructure optical fibre," Opt. Express **14**, 4026–4036 (2006).

[5. 20] M. L. V. Tse, P. Horak, J. H. V. Price, F. Poletti, F. He, and D. J. Richardson, "Pulse compression at 1.06 μm in dispersion-decreasing holey fibres," Opt. Lett. **31**, 3504–3506 (2006).

[5. 21] A. C. Peacock, "Soliton propagation in tapered silicon core fibres," Opt. Lett. **35**, 3697–3699 (2010).

[5. 22] L. Tong, R. Gattass, J. Ashcom, S. He, J. Lou, M. Shen, I. Maxwell, and E. Mazur, "Subwavelength-diameter silica wires for low-loss optical wave guiding," Nature **426**, 816–819 (2003).

[5. 23] M. Foster, A. Gaeta, Q. Cao, and R. Trebino, "Soliton-effect compression of supercontinuum to few-cycle durations in photonic nanowires," Opt. Express **13**, 6848–6855 (2005).

[5. 24] K. K. Lee, D. R. Lim, H. C. Luan, A. Agarwal, J. Foresi, and L. C. Kimerling, "Effect of size and roughness on light transmission in a Si/SiO_2 waveguide: Experiments and model," Appl. Phys. Lett. **77**, 1617–1619 (2000).

[5. 25] R. U. Ahmad, F. Pizzuto, G. S. Camarda, R. L. Espinola, H. Rao, and R. M. Osgood, "Ultracompact corner-mirrors and T-branches in silicon-on-insulator," IEEE Photon. Technol. Lett. **14**, 65–67 (2002).

[5. 26] Q. Lin, O. J. Painter, and G. Agrawaal, "Nonlinear optical phenomena in silicon waveguides: modelling and applications," Opt. Express **15**, 16604–16644 (2007).

[5. 27] J. I. Dadap, N. C. Panoiu, X. G. Chen, I. W. Hsieh, X. P. Liu, C. Y. Chou, E., Dulkeith, S. J., McNab, F. N. Xia, W. M. J. Green, L. Sekaric, Y. A. Vlasov, and R. M. Osgood, "Nonlinear-optical phase modification in dispersion-engineered Si photonic wires," Opt. Express **16**, 1280–1299 (2008).

[5. 28] R. M. Osgood, N. C. Panoiu, J. I. Dadap, X. Liu, X. Chen, I-W. Hsieh, E. Dulkeith, W. M. J. Green, and Y. A. Vlassov, "Engineering nonlinearities in nanoscale optical systems: physics and applications in dispersion-engineered silicon nanophotonic wires," Adv. Opt. Photon. **1**, 162–235 (2009).

[5. 29] X. Chen, N. C. Panoiu, I. W. Hsieh, J. I. Dadap, and R. M. Osgood, "Third-order dispersion and ultrafast-pulse propagation in silicon wire waveguides," IEEE Photon. Technol. Lett. **18**, 2617–2619 (2006).

[5. 30] M. Mohebbi, "Silicon photonic nanowire soliton-effect compressor at 1.5 μm," IEEE Photon. Technol. Lett. **20**, 921–923 (2008).

[5. 31] N. C. Panoiu, X. Chen, and R. M. Osgood, "Modulation instability in silicon photonic nanowires," Opt. Lett. **31**, 3609–3611 (2006).

[5. 32] M. A. Foster, A. C. Turner, J. E. Sharping, B. S. Schmidt, M. Lipson, and A. L. Gaeta, "Broad-band optical parametric gain on a silicon photonic chip," Nature **441**, 960–963 (2006).

[5. 33] X. Liu, R. M. Osgood, Y. A. Vlasov, and W. M. J. Green, "Mid-infrared optical parametric amplifier using silicon nanophotonic waveguides," Nat. Photonics **4**, 557–560 (2010).

[5. 34] O. Boyraz, P. Koonath, V. Raghunathan, and B. Jalali, "All optical switching and continuum generation in silicon waveguides," Opt. Express **12**, 4094–4102 (2004).

[5. 35] I. W. Hsieh, X. Chen, X. P. Liu, J. I. Dadap, N. C. Panoiu, C. Y. Chou, F. Xia, W. M. Green, Y. A. Vlasov, and R. M. Osgood, "Supercontinuum generation in silicon photonic wires," Opt. Express **15**, 15242–15249 (2007).

[5. 36] L. Yin, Q. Lin, and G. P. Agrawal,"Soliton fission and supercontinuum generation in silicon waveguides," Opt. Lett. **32**, 391–393 (2007).

[5. 37] N. C. Panoiu, X. Liu, and R. M. Osgood, "Self-steepening of ultrashort pulses in silicon photonic nanowires," Opt. Lett. **34**, 947–949 (2009).

[5. 38] H. Fukuda, K. Yamada, T. Shoji, M. Takahashi, T. Tsuchizawa, T. Watanabe, J. Takahashi, and S. Itabashi, "Four-wave mixing in silicon wire waveguides," Opt. Express **13**, 4629–4637 (2005).

[5. 39] R. Espinola, J. Dadap, R. M. Osgood, Jr., S. McNab, and Y. Vlasov, "C-band wavelength conversion in silicon photonic wire waveguides," Opt. Express **13**, 4341–4349 (2005).

[5. 40] M. A. Foster, A. C. Turner, R. Salem, M. Lipson, and A. L. Gaeta, "Broad-band continuous-wave parametric wavelength conversion in silicon nanowaveguides," Opt. Express **15**, 12949–12958 (2007).

[5. 41] S. Zlatanovic, J. S. Park, S. Moro, J. M. C. Boggio, I. B. Divliansky, N. Alic, S. Mookherjea, and S. Radic, "Mid-infrared wavelength conversion in silicon waveguides using ultracompact telecom-band-derived pump source," Nat. Photonics **4**, 561–564 (2010).

[5. 42] J. B. Driscoll, N. Ophir, R. R. Grote, J. I. Dadap, N. C. Panoiu, K. Bergman, and R. M. Osgood, "Width-modulation of Si photonic wires for quasi-phase-matching of four-wave-mixing: experimental and theoretical demonstration," Opt. Express **20**, 9227–9242 (2012).

[5. 43] X. Chen, N. C. Panoiu, and R. M. Osgood, "Theory of Raman-mediated pulsed amplification in silicon-wire waveguides," IEEE J. Quantum Electron. **42**, 160–170 (2006).

[5. 44] N. C. Panoiu, J. F. McMillan, and C. W. Wong, "Theoretical analysis of pulse dynamics in silicon photonic crystal wire waveguides," IEEE J. Sel. Top. Quantum Electron. **16**, 257–266 (2010).

[5. 45] S. Lavdas, J. B. Driscoll, H. Jiang, R. R. Grote, R. M. Osgood, and N. C. Panoiu, "Generation of parabolic similaritons in tapered silicon photonic wires: comparison of pulse dynamics at telecom and mid-IR wavelengths," Opt. Lett. **38**, 3953–3956 (2013).

[5. 46] G. P. Agrawal, *Nonlinear Fibre Optics* (Academic Press, San Diego, USA, 2007).

Chapter 6

Quasi-phase matched four-wave mixing in silicon photonic nanowires

6.1 Introduction

Frequency generation in optical systems is the main underlying process in a series of key applications, including all-optical signal processing, optical amplification, and wavelength multiplexing. One of the most facile approaches to achieve this functionality is via optical-wave interaction in nonlinear media. In the case of media with cubic nonlinearity, the simplest such interaction is FWM, a nonlinear process in which two photons combine and generate a pair of photons with different frequencies. Due to its simplicity and effectiveness, FWM has been at the centre of intense research, from the early days of nonlinear fibre optics [6. 1, 2] to the recent studies of FWM in ultra-compact silicon (Si) devices [6. 3–16, 18–20]. Silicon photonic nanowires are particularly suited to achieve highly efficient FWM, as silicon has extremely large cubic nonlinearity over a broad frequency domain. Equally important in this context, due to the deep-subwavelength size of the cross-section of Si-PhNWs, the parameters quantifying their optical properties depend strongly on wavelength and waveguide size [6. 19, 20]. As a result, one can easily control the strength and phase-matching of the FWM. These ideas have inspired intense research in chip-scale devices based on FWM in Si waveguides, with optical parametric amplifiers [6. 7, 8, 13], frequency converters [6. 10–12, 14–16, 18], sources of quantum-correlated photon pairs [6. 21], and optical signal regenerators [6. 22] being demonstrated.

6.2 Geometry and dispersion properties of Si-PhNWs

One of the main properties of Si-PhNWs, which makes them particularly suitable to achieve efficient FWM, is that by properly designing the waveguide geometry one can easily engineer the dispersion to be either normal or anomalous within specific spectral domains. More specifically, Si-PhNWs with relatively large cross-sections have normal dispersion, which precludes phase matching of the FWM. This drawback can be circumvented by scaling down the waveguide size to a few hundred of nanometers as then the dispersion becomes anomalous. The price one pays for this small crossection is that the device operates at reduced optical power. An alternate promising approach to achieve phase-matched FWM in the normal dispersion regime is to employ QPM techniques, i.e. to cancel the linear and nonlinear phase mismatch of the interacting waves by periodically varying the waveguide cross-section. This technique has been recently used for *cw* optical beams [6. 18], yet in many cases of practical importance it is desirable to achieve FWM in the pulsed regime. In addition, at large power *cw* beams are strongly depleted by TPA, which results in the detuning of the FWM.

The optical waveguide considered here consists of a silicon core with constant height, $h = 250\,\text{nm}$, and periodically modulated width, $w(z)$, buried in SiO_2. We assume a sinusoidal dependence, $w(z) = w_0 + \Delta w \sin(2\pi z/\Lambda)$, where w_0, Δw, and Λ are the average width, amplitude of the width modulation, and its period, respectively, but more intricate profiles $w(z)$ can be readily investigated by our method described in Section 3.2. One should note that we have incorporated in Eq. (3.1) linear dispersion terms up to the fourth order. It should be reminded that we use a slowly varying envelope approximation which was described in detail in Section 2.2. However, there are alternative semi-analytical techniques such as those introduced in [6. 17] where bound-mode propagation is calculated by Fourier decomposition method. But for pulses with pulse width much longer than optical cycles the slowly varying envelope approximation is more convenient method. Before we continue with the results of our work, we have to mention that the intrinsic losses, α_{in}, have not been included in our theoretical model since their characteristic length is much shorter than our propagation distance. That means that the intrinsic losses do not have influence in our results. In addition to that, the nonlinear losses emerged from TPA and free carrier generation is the dominant loss mechanism in the current work.

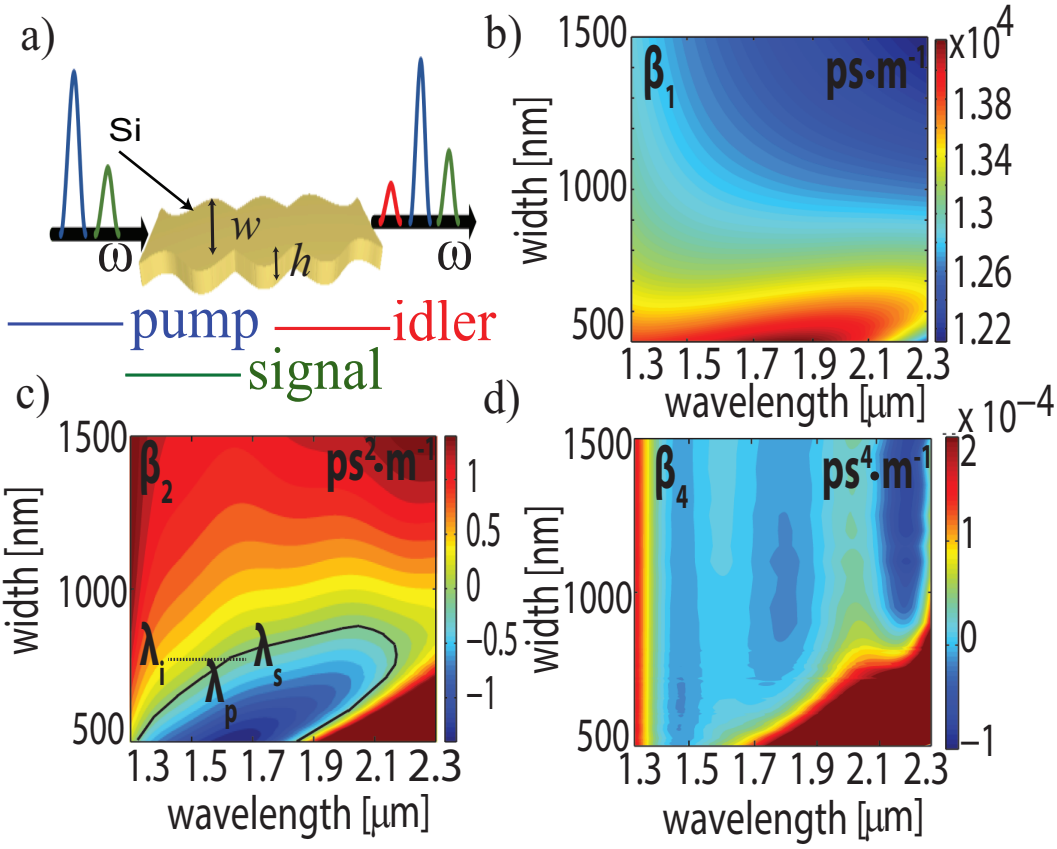

Figure 6.1: (a) Schematics showing a periodically width-modulated Si-PhNW and the configuration of a pulsed seeded degenerate FWM set-up. Dispersion maps of dispersion coefficients: (b) β_1, (c) β_2, and (d) β_4.

6.3 Degenerate FWM in Si-PhNWs

As illustrated in Fig. 6.1(a), here we consider the case of degenerate FWM, in which two photons at the pump frequency, ω_p, interact with the nonlinear medium and generate a pair of photons at the signal and idler frequencies, *i.e.* ω_s and ω_i, respectively. This FWM process is most effective when the following relation holds:

$$\left|2(\beta_p - \gamma' P_p) - \beta_s - \beta_i\right| = K_g, \tag{6.1}$$

where $K_g = 2\pi/\Lambda$ is the Bragg wave vector, P_p is the pump peak power, and $\beta_{p,s,i}(\omega)$ are the mode propagation constants evaluated at the frequencies of the co-propagating pulses. Note that in Eq. (6.1) all width-dependent quantities are evaluated at $w = w_0$.

If $\Delta\omega \equiv \omega_s - \omega_p = \omega_p - \omega_i \ll \omega_p$, Eq. (6.1) can be cast to a form that makes it more suitable to find the wavelengths of the quasi-phase-matched pulses by expanding in Taylor series the functions $\beta_{p,s,i}(\omega)$, around ω_p. Keeping the terms up to the fourth-

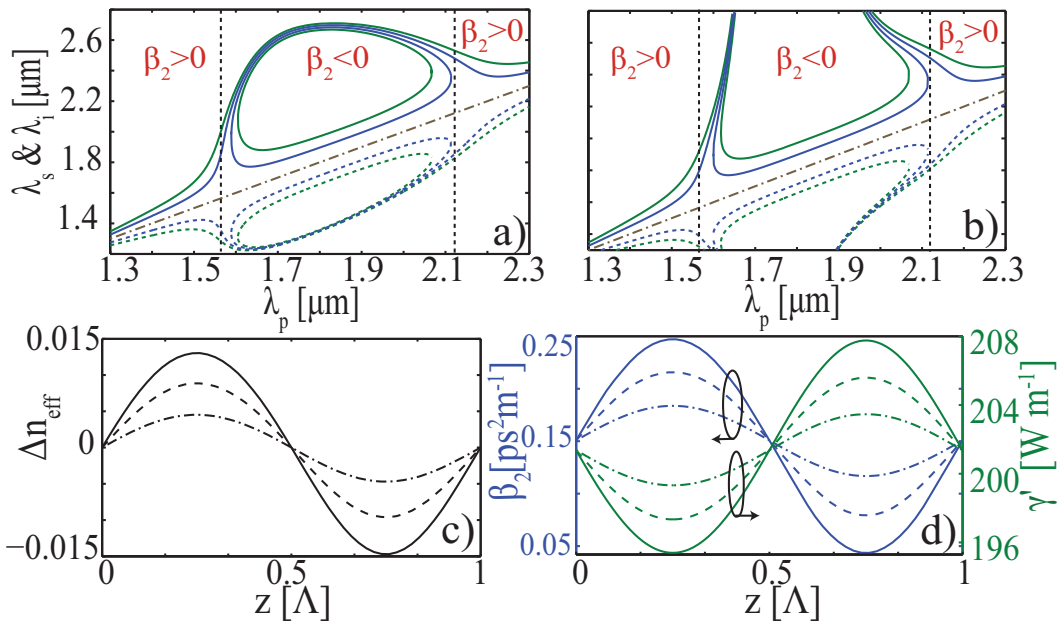

Figure 6.2: (a), (b) Wavelength diagrams defined by the phase-matching conditions (6.1) and (6.2), respectively. Solid (dashed) lines correspond to the signal (idler) and green (blue) lines correspond to $\Lambda = 2\,\text{mm}$ ($\Lambda = 6\,\text{mm}$). Dash-dot lines correspond to $\lambda_p = \lambda_s = \lambda_i$ and the vertical dotted lines indicate where $\beta_2(\lambda) = 0$. Dependence of Δn_{eff}, (c), and β_2, and γ', (d), on z, shown for one period, Λ. In (c) and (d) the lines correspond to $\Delta w = 10\,\text{nm}$ (dash-dot), $\Delta w = 20\,\text{nm}$ (dashed), and $\Delta w = 30\,\text{nm}$ (solid). In all panels $w_0 = 740\,\text{nm}$.

order, Eq. (6.1) becomes:

$$\left| 2\gamma' P_p + \beta_{2,p}\Delta\omega^2 + \frac{1}{12}\beta_{4,p}\Delta\omega^4 \right| = K_g. \tag{6.2}$$

The dispersive properties of the Si-PhNW, summarized in Fig. 6.1, define the spectral domain, in which efficient FWM can be achieved. The width dependence of the dispersion coefficients and other relevant waveguide parameters, i.e. γ, κ, and τ, was obtained by using a method described in detail in [6. 18, 25]. Importantly, with a proper choice of the operating wavelength or waveguide width, the photonic wire can have both normal and anomalous GVD. The wavelengths, for which the FWM is quasi-phase-matched and determined from Eqs. (6.1) and (6.2), are plotted in Figs. 6.2(a) and 6.2(b), respectively. These results show that, as expected, for relatively small $\Delta\omega$, Eqs. (6.1) and (6.2) lead to similar predictions, whereas they disagree for large $\Delta\omega$. Interestingly enough, Fig. 6.2(a) shows that for certain λ_p's FWM can be achieved at more than one pair of wavelengths, (λ_s, λ_i), a feature that suggests that optical bistability could readily be observed in this system. The corresponding z-variation over

one period of the effective modal refractive index, Δn_{eff}, β_2, and γ', is presented in Figs. 6.2(c) and 6.2(d).

The wavelength conversion efficiency and parametric amplification gain are determined from the pulse spectrum. Thus, we launch into the waveguide pulses whose temporal profile, $u(0,t) = \sqrt{P_p}[\exp(-t^2/2T_0^2) + \sqrt{\xi}\exp(-t^2/2T_0^2 - i\Delta\omega t)]$, is the superposition of a pump pulse and a weak signal, whose frequency is shifted by $\Delta\omega$. The ratio $\xi = P_s/P_p$ is set to 10 % and 1 % in the cases of wavelength conversion and parametric amplification, respectively, so that in the latter case the signal is too weak to affect the pump. We also assume that the signal and the pump have the same temporal width, T_0.

6.4 Results of degenerate FWM in Si-PhNWs

A generic example of pulse evolution in a uniform and Bragg Si-PhNW, where the latter is designed such that condition (6.1) holds, is presented in Fig. 6.3. We considered a pulse with $T_0 = 500$ fs, $P_p = 200$ mW, $P_s = 20$ mW, $\lambda_p = 1518$ nm, and $\lambda_s = 1623$ nm, so that one expects an idler pulse to form at $\lambda_i = 1426$ nm. The waveguide parameters are $w_0 = 740$ nm, $\Delta w = 30$ nm, and $\Lambda = 6$ mm. All the input pulse parameters are presented in the following Table-6.1.

physical parameters	$\lambda_p = 1.518\mu m$	$\lambda_s = 1.623\mu m$	$\lambda_s = 1.426\mu m$
$T_0\ [fs]$	500	500	0
$P_0\ [W]$	0.2	$2{\cdot}10^{-2}$	0
$\alpha_{in}[dB\ cm^{-1}]$	0	0	0
$w_0\ [nm]$	740	740	740
$\beta_{TPA}\ [cm/GW]$	$1.39{\cdot}10^{-11}$	$0.17{\cdot}10^{-11}$	$6.48{\cdot}10^{-11}$
$n_2\ [cm^2/W]$	$5.02{\cdot}10^{-18}$	$6.48{\cdot}10^{-18}$	$4.59{\cdot}10^{-18}$
$\Delta w\ [nm]$	30	30	30
$\beta_1\ [ps/m]$	$1.314{\cdot}10^{4}$	$1.314{\cdot}10^{4}$	$1.36{\cdot}10^{4}$
$\beta_2\ [ps^2/m]$	$1.5{\cdot}10^{-1}$	$-8.6{\cdot}10^{-2}$	$4.1{\cdot}10^{-1}$
$\beta_3\ [ps^3/m]$	$3.02{\cdot}10^{-3}$	$3.079{\cdot}10^{-3}$	$3.0{\cdot}10^{-3}$
$\beta_4\ [ps^4/m]$	$-6.1{\cdot}10^{-7}$	$-1.2{\cdot}10^{-5}$	$-4.21{\cdot}10^{-7}$
$\gamma'\ [W^{-1}m^{-1}]$	201.4	177.1	221.78
$\gamma''\ [W^{-1}m^{-1}]$	62.25	49.7	73.48
$\tau'\ [fs]$	1.5	1.7	1.32
$\tau''\ [fs]$	$28{\cdot}10^{-2}$	$46.6{\cdot}10^{-2}$	$13.5{\cdot}10^{-2}$
$L\ [mm]$	60	60	60

Table 6.1: Input pulse parameters for the case of degenerate FWM of Fig. 6.3.

The evolution of the temporal pulse profile, shown in Figs. 6.3(a) and 6.3(b), suggests that the pulse propagates with a group-velocity, v_g, slightly larger than $v_g(\omega_p)$. Indeed, the pulse propagates in the normal dispersion regime and its average frequency is smaller than ω_p, which means that $v_g > v_g(\omega_p)$. In the case of the Bragg waveguide, additional temporal oscillations of the pulse are observed. This effect is traced to the periodic variation $v_g(z)$, which is due to the implicit dependence of v_g on a periodically varying width $w(z)$.

Due to its particular nature, it is more suitable to study the FWM in the frequency domain. In particular, the differences between the evolution of the pulse spectra in uniform and Bragg waveguides, illustrated by Figs. 6.3(c) and 6.3(d), respectively, underline the main physics of pulsed FWM in Si-PhNWs. Specifically, it can be seen that, in the Bragg waveguide, the idler energy builds up at a much higher rate as compared to the case of the uniform Si-PhNW, an indication of a much more efficient FWM interaction [see also Fig. 6.3(g)]. In both cases, however, we observe a gradual decrease of the pulse peak power, induced by the linear and nonlinear losses associated to the generated FCs. For the Bragg waveguide one can also observe a series of oscillations of the FC density with respect to z, which are due to the periodic variation with z of γ''. Importantly, the power decay leads to the detuning of the FWM [see Eqs. (6.1) and (6.2)] and, implicity, to the degradation of its efficiency.

A comparative study of the conversion efficiency (CE), $\eta(z) = 10\log[E_i(z)/E_s(0)]$, and FWM gain, $G(z) = E_s(z)/E_s(0)$, in a Bragg vs. a uniform Si-PhNWs is summarized in Fig. 6.4. The pulse energies of the idler, E_i, and signal, E_s, were calculated by integrating the power spectrum over a frequency domain containing the corresponding pulse. These results clearly show that the Bragg grating induces a dramatic increase of the CE. As expected, the CE enhancement increases with Δw, reaching 15 dB for $\Delta w = 30$ nm. Another key effect that can influence the CE is the quasi-periodic variation of $N(z)$, plotted in Fig. 6.4(b). Specifically, the oscillatory z-variation of $N(z)$ results in a quasi-periodic variation of the effective modal index, $n_{\text{eff}}(z)$, which adds to the periodic variation of n_{eff} due to the waveguide-width modulation. Note, however, that for the power values used in this analysis the former effect is an order of magnitude weaker than the latter one [compare Fig. 6.2(c) with the inset in Fig. 6.4(b)]. The CE also depends on T_0, as per Fig. 6.4(c). Indeed, one expects that the CE increases with

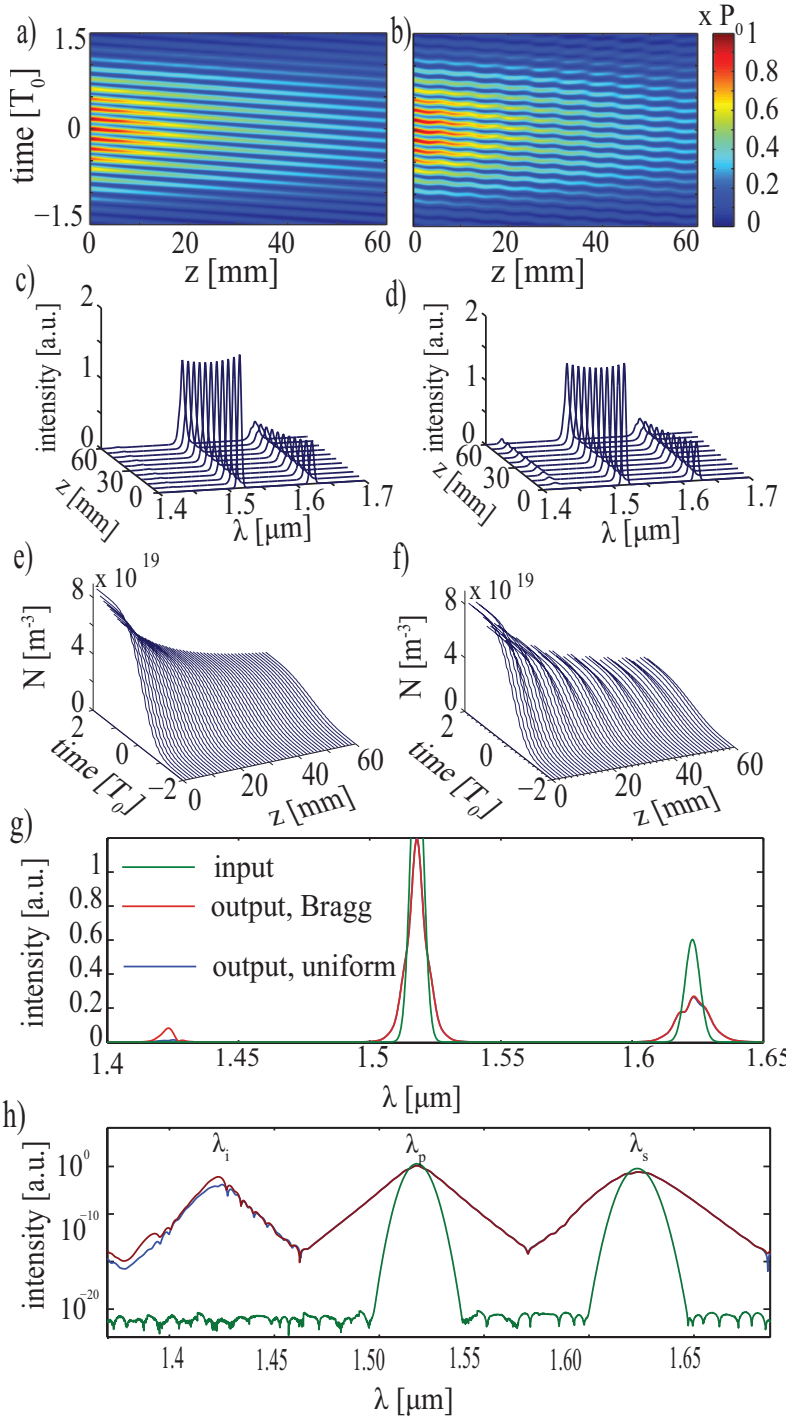

Figure 6.3: Left (right) panels show the evolution of an optical pulse in a uniform (quasi-phase-matched Bragg) waveguide (see the text for the values of the pulse and waveguide parameters). Top, middle, and bottom panels show the z-dependence of the temporal pulse profile, its spectrum, and the FC density, respectively. (g) Input and output pulse spectra corresponding to the two waveguides. (h) The log-plot of the same spectra.

T_0 since the Bragg waveguide is designed to phase-match the carrier frequencies of the pulses, meaning that spectrally narrower pulses are better phase-matched.

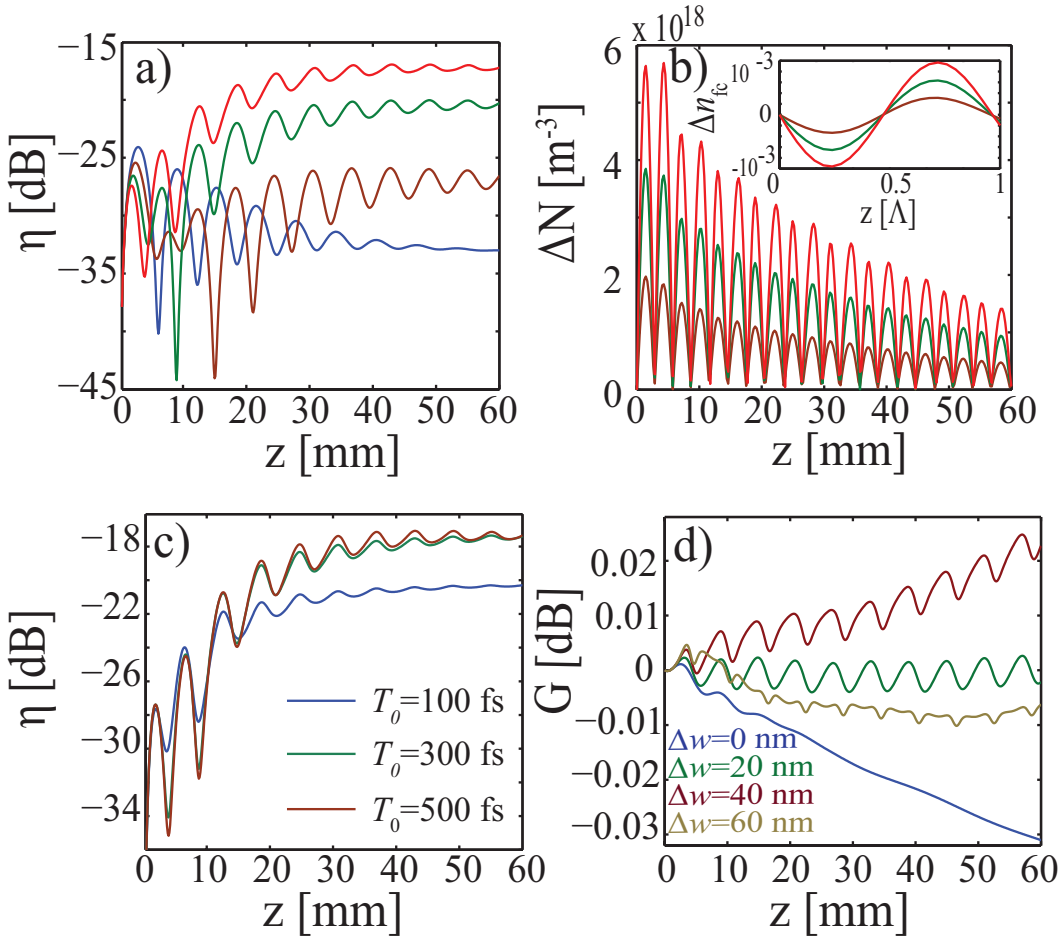

Figure 6.4: (a), (b) Dependence of CE and FC density on z, respectively. Inset shows the z-dependence of the FC induced variation of n_{eff}. The lines correspond to $\Delta w = 0$ (blue), $\Delta w = 10\,\text{nm}$ (brown), $\Delta w = 20\,\text{nm}$ (green), and $\Delta w = 30\,\text{nm}$ (red). (c) CE determined for different pulse widths. (d) FWM gain determined for different Δw.

The dependence of the FWM gain on the width modulation is shown in Fig. 6.4(d). One should note that we have chosen the signal to be in the mid-infrared wavelength region in order to limit the deleterious effects of TPA. Thus, the pulse has $T_0 = 500\,\text{fs}$, $P_p = 200\,\text{mW}$, $P_s = 2\,\text{mW}$, $\lambda_p = 2215\,\text{nm}$, and $\lambda_s = 2102\,\text{nm}$, meaning that the idler is formed at $\lambda_i = 2340\,\text{nm}$. The waveguide parameters were $w_0 = 720\,\text{nm}$, and $\Lambda = 6\,\text{mm}$. All the input pulse parameters used for this simulation are presented in the following Table-6.2.

The increased FWM efficiency in Bragg Si-PhNWs is clearly demonstrated by these numerical experiments namely, a transition from negative to positive net gain is observed when Δw increases from zero to 40 nm. However, the net gain is negative throughout the propagation distance when $\Delta w \geq 60\,\text{nm}$. This is expected as for large width modulations the width does not change adiabatically. That means that backward

physical parameters	$\lambda_p = 2.215\mu m$	$\lambda_s = 2.102\mu m$	$\lambda_s = 2.340\mu m$
$T_0\ [fs]$	500	500	0
$P_0\ [W]$	0.2	2e-2	0
$\alpha_{in}[dB\ cm^{-1}]$	0	0	0
$w_0\ [nm]$	720	720	720
$\beta_{TPA}\ [cm/GW]$	$1.5{\cdot}10^{-13}$	$1.3{\cdot}10^{-12}$	$1{\cdot}10^{-13}$
$n_2\ [cm^2/W]$	$10{\cdot}10^{-18}$	$11.5{\cdot}10^{-18}$	$9.5{\cdot}10^{-18}$
$\Delta w\ [nm]$	30	30	30
$\beta_1\ [ps/m]$	$1.332{\cdot}10^{4}$	$1.3329{\cdot}10^{4}$	$1.33{\cdot}10^{4}$
$\beta_2\ [ps^2/m]$	$43{\cdot}10^{-2}$	$-27.8{\cdot}10^{-2}$	1.306
$\beta_3\ [ps^3/m]$	$-21{\cdot}10^{-3}$	$-1{\cdot}10^{-2}$	$-37{\cdot}10^{-3}$
$\beta_4\ [ps^4/m]$	$3.4{\cdot}10^{-4}$	$1.8{\cdot}10^{-4}$	$7.9{\cdot}10^{-4}$
$\gamma'\ [W^{-1}m^{-1}]$	92.8	92.67	83.53
$\gamma''\ [W^{-1}m^{-1}]$	0.31	4.2	24.8
$\tau'\ [fs]$	3.1	2.1	3.4
$\tau''\ [fs]$	$71{\cdot}10^{-2}$	$91{\cdot}10^{-2}$	$64{\cdot}10^{-2}$
$L\ [mm]$	60	60	60

Table 6.2: Input pulse parameters for the case of degenerate FWM of Fig. 6.3.

waves appear which our mathematical model can not take under consideration. Large width modulation also means that the phase mismatch increases as β_2 and β_4 varries significantly along a period.

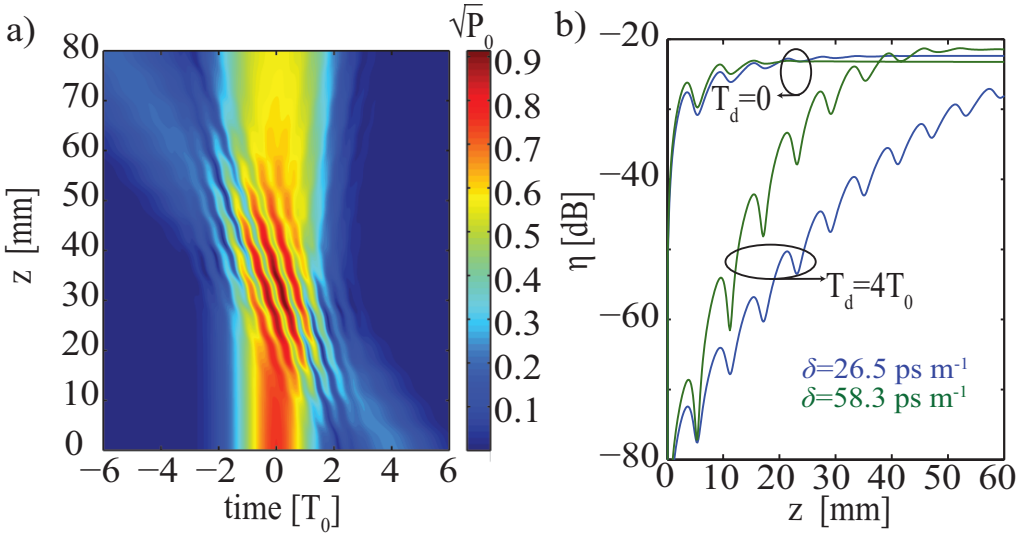

Figure 6.5: (a) Pulse evolution for $\lambda_s = 2181$ nm and $\lambda_i = 2066$ nm. (b) CE dependence on z. Green and blue lines correspond to the pulse in (a) and $\lambda_s = 2066$ nm and $\lambda_i = 2181$ nm, respectively. The other parameters in (a) and (b) are $w_0 = 600$ nm, $\Lambda = 6$ mm, $\lambda_p = 2122$ nm, $T_0 = 500$ fs, $P_p = 200$ mW, and $P_s = 20$ mW.

In Fig. 6.5(a) this propagation section corresponds to the region where one can

observe a series of intensity fringes, which are due to the frequency beating between the two pulses. Also, the CE increases rapidly as T_d decreases because for large T_d the pump decays more before it begins to interact with the signal, i.e. the FWM becomes more detuned. This suggests that the CE should increase with δ as well, in agreement with the results plotted in Fig. 6.5(b).

In our analysis so far we have designed the Si-PhNW so that the pump and signal have the same group-velocity, meaning that optimum FWM is then achieved. In Fig. 6.5, which also considers mid-IR pulses ($\lambda \gtrsim 2\,\mu$m), we present the CE determined in two cases when this condition is not satisfied, i.e. when the walk-off $\delta = |1/v_{g,p} - 1/v_{g,s}| \neq 0$, and for two different values of the pump-signal time delay, T_d. The main conclusion that can be drawn from these results is that when $\delta \neq 0$ FWM occurs only over a certain distance, which is related to the time necessary for the pump and signal pulses to pass through each other.

6.5 Conclusions

In conclusion, we showed that efficient FWM of pulses can be achieved in long-period Bragg silicon waveguides, which can be used to enhance the wavelength-conversion efficiency and pulse amplification, as compared to uniform waveguides. One of the striking features of this work is the crucial role of the periodicity of the width modulation in phase matching condition. A periodic waveguide enables phase matched wavelengths not only in anomalous dispersion regime, as this is the most usual case in fibres, but also in normal dispersion regime. So, our analysis revealed key dependencies between the pulse and waveguide parameters and the efficiency of the FWM, results which can be instrumental in guiding a practical implementation of these ideas.

This worked also highlighted the influence of nonlinearity in the efficiency of QPM FWM. This dependence on nonlinearity is the driving force to study the nonlinear phenomenon of FWM in another silicon platform which is the well-known silicon photonic crystal. According to this, we present, in the next chapter, the new mathematical formulation that is required for optical copropagating pulses in silicon photonic crystals as well as we focus on the wavelength dependence of the linear and nonlinear parameters that affect FWM.

References

[6. 1] R. H. Stolen, J. E. Bjorkholm, and A. Ashkin, "Phasematched threewave mixing in silica fibre optical waveguides," Appl. Phys. Lett. **24**, 308–310 (1974).

[6. 2] K. O. Hill, D. C. Johnson, B. S. Kawasaki, and R. I. MacDonald, "cw threewave mixing in singlemode optical fibres," J. Appl. Phys. **49**, 5098–5106 (1978).

[6. 3] R. Claps, V. Raghunathan, D. Dimitropoulos, and B. Jalali, "Anti-Stokes Raman conversion in silicon waveguides," Opt. Express **11**, 2862–2872 (2003).

[6. 4] D. Dimitropoulos, V. Raghunathan, R. Claps, and B. Jalali, "Phase-matching and nonlinear optical processes in silicon waveguides," Opt. Express **12**, 149–160 (2004).

[6. 5] H. Fukuda, K. Yamada, T. Shoji, M. Takahashi, T. Tsuchizawa, T. Watanabe, J. Takahashi, and S. Itabashi, "Four-wave mmixing in silicon wire waveguide," Opt. Express **13**, 4629–4637 (2005).

[6. 6] R. Espinola, J. Dadap, R. M. Osgood, Jr., S. McNab, and Y. Vlasov, "C-band wavelength conversion in silicon photonic wire waveguides," Opt. Express **13**, 4341 (2005).

[6. 7] M. A. Foster, A. C. Turner, J. E. Sharping, B. S. Schmidt, M. Lipson, and A. L. Gaeta, "Broad-band optical parametric gain on a silicon photonic chip," Nature **441**, 960–963 (2006).

[6. 8] Q. Lin, J. Zhang, P. M. Fauchet, and G. P. Agrawal, "Ultrabroadband parametric generation and wavelength conversion in silicon waveguides," Opt. Express **14**, 4786–4799 (2006).

[6. 9] N. C. Panoiu, X. Chen, and R. M. Osgood, "Modulation instability in silicon photonic nanowires," Opt. Lett. **31**, 3609–3611 (2006).

[6. 10] K. Yamada, H. Fukuda, T. Tsuchizawa, T. Watanabe, T. Shoji, and S. Itabashi, "All-Optical Efficient Wavelength Conversion Using Silicon Photonic Wire Waveguide," IEEE Photon. Technol. Lett. **18**, 1046–1048 (2006).

[6. 11] Y-H Kuo, H. Rong, V. Sih, S. Xu, M. Paniccia, and O. Cohen, "Demonstration of wavelength conversion at 40 Gb/s data rate in silicon waveguides," Opt. Express **14**, 11721–11726 (2006).

[6. 12] M. A. Foster, A. C. Turner, R. Salem, M. Lipson, and A. L. Gaeta, "Broad-band continuous wave parametric wavelength conversion in silicon nanowaveguides," Opt. Express **15**, 12949–12958 (2007).

[6. 13] X. Liu, R. M. Osgood, Y. A. Vlasov, and W. M. J. Green, "Mid-infrared optical parametric amplifier using silicon nanophotonic waveguides," Nat. Photonics **4**, 557–560 (2010).

[6. 14] S. Zlatanovic, J. S. Park, S. Moro, J. M. C. Boggio, I. B. Divliansky, N. Alic, S. Mookherjea, and S. Radic, "Mid-infrared wavelength conversion in silicon waveguides using ultracompact telecom-band-derived pump source," Nat. Photonics **4**, 561–564 (2010).

[6. 15] B. Kuyken, X. P. Liu, R. M. Osgood, R. Baets, G. Roelkens, and W. M. J. Green, "Mid-infrared to telecomband supercontinuum generation in highly nonlinear silicon-on-insulator wire waveguides," Opt. Express **19**, 20172–20181 (2011).

[6. 16] X. Liu, B. Kuyken, G. Roelkens, R. Baets, R. M. Osgood, and W. M. J. Green, "Bridging the mid-infrared-to-telecom gap with silicon nanophotonic spectral translation," Nat. Photonics **6**, 667 (2012).

[6. 17] I. Papakostantinou, R. James, and D. R. Selviah, "Radiation-and bound-mode propagation in rectangular, multimode dielectric, channel waveguides with sidewall and roughness," IEEE J. Lightwave Technol. **27**, 4151–4163 (2000).

[6. 18] J. B. Driscoll, N. Ophir, R. R. Grote, J. I. Dadap, N. C. Panoiu, K. Bergman, and R. M. Osgood, "Width Modulation of Si photonic wires for quasi-phase-matching of four wave mixing: experimental and theoretical demonstration," Opt. Express **20**, 9227–9242 (2012).

[6. 19] Q. Lin, O. J. Painter, and G. P. Agrawal, "Nonlinear optical phenomena in silicon waveguides: Modelling and applications," Opt. Express **15**, 16604–16644 (2007).

[6. 20] R. M. Osgood, N. C. Panoiu, J. I. Dadap, X. Liu, X. Chen, I-W. Hsieh, E. Dulkeith, W. M. J. Green, and Y. A. Vlassov, "Engineering nonlinearities in nanoscale optical systems: physics and applications in dispesion-engineered silicon nanophotonic wires," Adv. Opt. Photon. **1**, 162–235 (2009).

[6. 21] Q. Lin, and G. P. Agrawal, "Silicon waveguides for creating quantum-correlated photon pairs," Opt. Lett. **31**, 3140–3142 (2006).

[6. 22] R. Salem, M. A. Foster, A. C. Turner, D. F. Geraghty, M. Lipson, and A. L. Gaeta, "Signal regeneration using low-power four-wave mixing on silicon chip," Nat. Photonics **2**, 35–38 (2008).

[6. 23] X. Chen, N. C. Panoiu, and R. M. Osgood, "Theory of Raman-mediated pulsed amplification in silicon-wire waveguides," IEEE J. Quantum Electron. **42**, 160–170 (2006).

[6. 24] N. C. Panoiu, X. Liu, and R. M. Osgood, "Self-steepening of ultrashort pulses in silicon photonic nanowires," Opt. Lett. **34**, 947–949 (2009).

[6. 25] S. Lavdas, J. B. Driscoll, H. Jiang, R. R. Grote, R. M. Osgood, and N. C. Panoiu, "Generation of parabolic similaritons in tapered silicon photonic wires: comparison of pulse dynamics at telecom and mid-IR wavelengths," Opt. Lett. **38**, 3953–3956 (2013).

[6. 26] R. A. Soref and B. R. Bennett, "Electrooptical effects in silicon," IEEE J. Quantum Electron. **23**, 123–129 (1987).

Chapter 7

Theory of pulsed four-wave mixing in one-dimensional silicon photonic crystal waveguides

7.1 Introduction

One of the most promising applications of photonics is the development of ultra-compact optical interconnects for chip-to-chip and even intra-chip communications. The driving forces behind research in this area are the perceived limitations at high frequency of currently used copper interconnects [7. 1], combined with a rapidly increasing demand to move huge amounts of data within increasingly more confined yet increasingly intricate communication architectures. An approach showing great potential towards developing optical interconnects at chip scale is based on high-index contrast optical waveguides, such as silicon photonic waveguides (Si-PhWGs) implemented on the silicon-on-insulator material platform [7. 2, 3]. Among key advantages provided by this platform are the increased potential for device integration facilitated by the enhanced confinement of the optical field achievable in high-index contrast photonic structures, as well as the particularly large optical nonlinearity of silicon, which makes it an ideal material for active photonic devices. Many of the basic device functionalities required in networks-on-chip have in fact already been demonstrated using Si-PhWGs, including parametric amplification [7. 4–8], optical modulation [7. 9–11], pulse compression [7. 12, 13], supercontinuum generation [7. 14–16], pulse self-steepening [7. 17], modulational instability [7. 18], and four-wave mixing (FWM) [7. 19–24]; for a

review of optical properties of Si-PhWGs see [7. 25, 26]. However, since the parameter space of Si-PhWGs is rather limited, there is little room to engineer their optical properties.

A promising solution to this problem has its roots in the advent of photonic crystals (PhCs) in the late 80's [7. 27, 28]. Thus, by patterning an optical medium in a periodic manner, with the spatial periods of the pattern being comparable to the operating optical wavelength, the optical properties of the resulting medium can be modified and engineered to a remarkable extent. Following this approach, a series of photonic devices have been demonstrated using PhCs, including optical waveguides and bends [7. 29–33], optical micro-cavities [7. 34–39], and optical filters [7. 40–42]. One of the most effective approaches to modify the optical properties of PhCs is to vary the group-velocity (GV), v_g, of the propagating modes. Unlike the case of waves propagating in regular optical media, whose GV can hardly be altered, by varying the geometrical parameters of PhCs one can tune the corresponding GV over many orders of magnitude. Perhaps the most noteworthy implication of the existence of optical modes with significantly reduced GV, the so-called slow-light [7. 43–45], is that both linear and nonlinear optical effects can be dramatically enhanced in the slow-light regime [7. 46–54].

One of the most important nonlinear optical process, as far as nonlinear optics applications are concerned, is FWM [7. 55]. In the generic case, it consists of the combination of two photons with frequencies, ω_1 and ω_2, belonging to two pump continuous-waves (CWs) or pulses, followed by the generation of a pair of photons with frequencies ω_3 and ω_4. The energy conservation requires that $\omega_1 + \omega_2 = \omega_3 + \omega_4$. In practice, however, an easier to implement FWM configuration is usually employed, namely degenerate FWM. In this case one uses just one pump with frequency, ω_p, the generated photons belonging to a signal (ω_s) and an idler (ω_i) beam; in this case the conservation of the optical energy is expressed as: $2\omega_p = \omega_s + \omega_i$. Among the most important applications of degenerate FWM, it is noteworthy to mention optical amplification, wavelength generation and conversion, phase conjugation, generation of squeezed states, and supercontinuum generation. While FWM has been investigated theoretically and experimentally in PhC waveguides [7. 56–61] and long-period Bragg waveguides [7. 24, 62], a comprehensive theory of FWM in silicon PhC waveguides (Si-PhCWGs), which rigorously incorporates in a unitary way all relevant linear and

nonlinear optical effects as well as the influence of photogenerated free-carriers (FCs) on the pulse dynamics is not available yet.

In this chapter we introduce a rigorous theoretical model that describes FWM in Si-PhCWGs. Our model captures the influence on the FWM process of linear optical effects, including waveguide loss, FC dispersion and FC absorption, nonlinear optical effects such as self- and cross-phase modulation, two-photon absorption, and cross-absorption modulation, as well as the mutual interaction between FCs and optical field. Importantly, we present a first principles derivation of the formulae for the linear and nonlinear optical coefficients of the waveguide, as well as the spatially averaged expressions of these waveguide optical coefficients. We also illustrate how our model can be employed to investigate the characteristics of FWM in the slow- and fast-light regimes, showing among other things that by incorporating the effects of FCs on the optical pulse dynamics new physics emerge. One noteworthy example in this context is that the well-known linear dependence of FCA on v_g^{-1} is replaced in the slow-light regime by a v_g^{-3} power-law dependence.

Our theoretical model is based on several underlying assumptions, which hold in commonly employed experimental configurations. Thus, we assume that the duration of the optical cycle of pulses considered in our study is much smaller than the momentum relaxation time of FCs and as such we can assume that the FCs follow practically instantaneously the variations of the optical field. Moreover, we consider that the duration of the optical pulses is much larger than the response time of the electronic nonlinearity so that this (Kerr) nonlinear optical response is assumed to be instantaneous. In addition, the duration of the optical pulses and their spectral separation are large enough so that they do not overlap spectrally, meaning that treating the optical field as a superposition of optical pulses is a valid approximation. Finally, although in the particular cases considered in our numerical simulations the width of the pulses is much smaller than the FCs relaxation time, the theoretical model we derive in this work is valid when the two characteristic times have comparable values as well.

The remaining of the paper is organized as follows. In the next Section we present the optical properties of the PhC waveguide considered in this work. Then, in Section 7.3, we develop the theory of pulsed FWM in Si-PhCWGs whereas the particular case of degenerate FWM is analyzed in Section 7.4. Then, in Section 7.5, we apply

these theoretical tools to explore the physical conditions in which efficient FWM can be achieved. The results are subsequently used, in Section 7.6, to study via numerical simulations the main properties of pulsed FWM in Si-PhCWGs. We conclude our paper by summarizing in the last Section the main findings of our article and discussing some of their implications to future developments in this research area. Finally, an averaged model that can be used in the case of broad optical pulses is presented in an Appendix-*B*.

7.2 Description of the photonic crystal waveguide

In this section we present the geometrical and material properties of the PhC waveguide considered in this work, as well as the physical properties of its optical modes. Thus, our Si-PhCW consists of a one-dimensional (1D) waveguide formed by introducing a line defect in a two-dimensional (2D) honeycomb-type periodic lattice of air holes in a homogeneous slab made of silicon (a so-called W1 PhC waveguide). The line defect is oriented along the z-axis, which is chosen to coincide with one of the ΓK symmetry

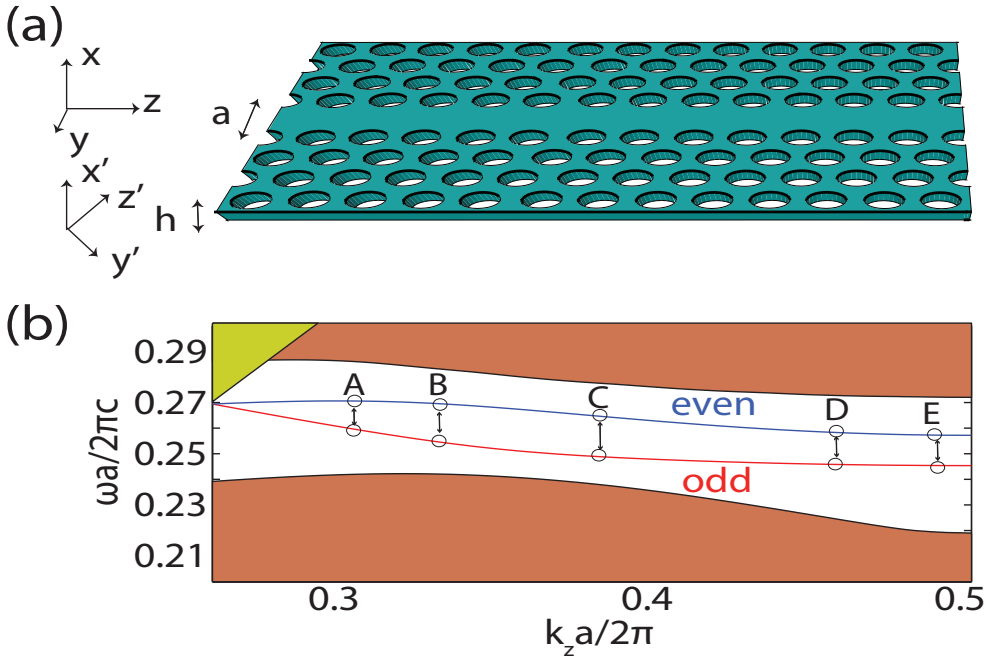

Figure 7.1: (a) Geometry of the 1D Si-PhC slab waveguide. The height of the slab is $h = 0.6a$ and the radius of the holes is $r = 0.22a$. The primed coordinate system shows the principal axes of the Si crystal with the input facet of the waveguide in the $(1\bar{1}0)$ plane of the Si crystal lattice. (b) Projected band structure. Dark yellow and brown areas correspond to slab leaky and guiding modes, respectively. The red and blue curves represent the guiding modes of the 1D waveguides.

axes of the crystal, and is created by filling in a row of holes [see Fig. 7.1(a)]. The slab height is $h = 0.6a$ and the radius of the holes is $r = 0.22a$, where $a = 412\,\text{nm}$ is the lattice constant, whereas the index of refraction of silicon is $n_{\text{Si}} \equiv n = 3.48$.

The defect line breaks the discrete translational symmetry of the photonic system along the y-axis, so that the optical modes of the waveguide are invariant only to discrete translation along the z-axis [7. 63]. Moreover, based on experimental considerations, we restrict our analysis to in-plane wave propagation, namely the wave vector, $\mathbf{k}$, lies in the $x = 0$ plane. The k_z component, on the other hand, can be restricted to the first Brillouin zone, $k_z \in [-\pi/a, \pi/a]$, which is an immediate consequence of the

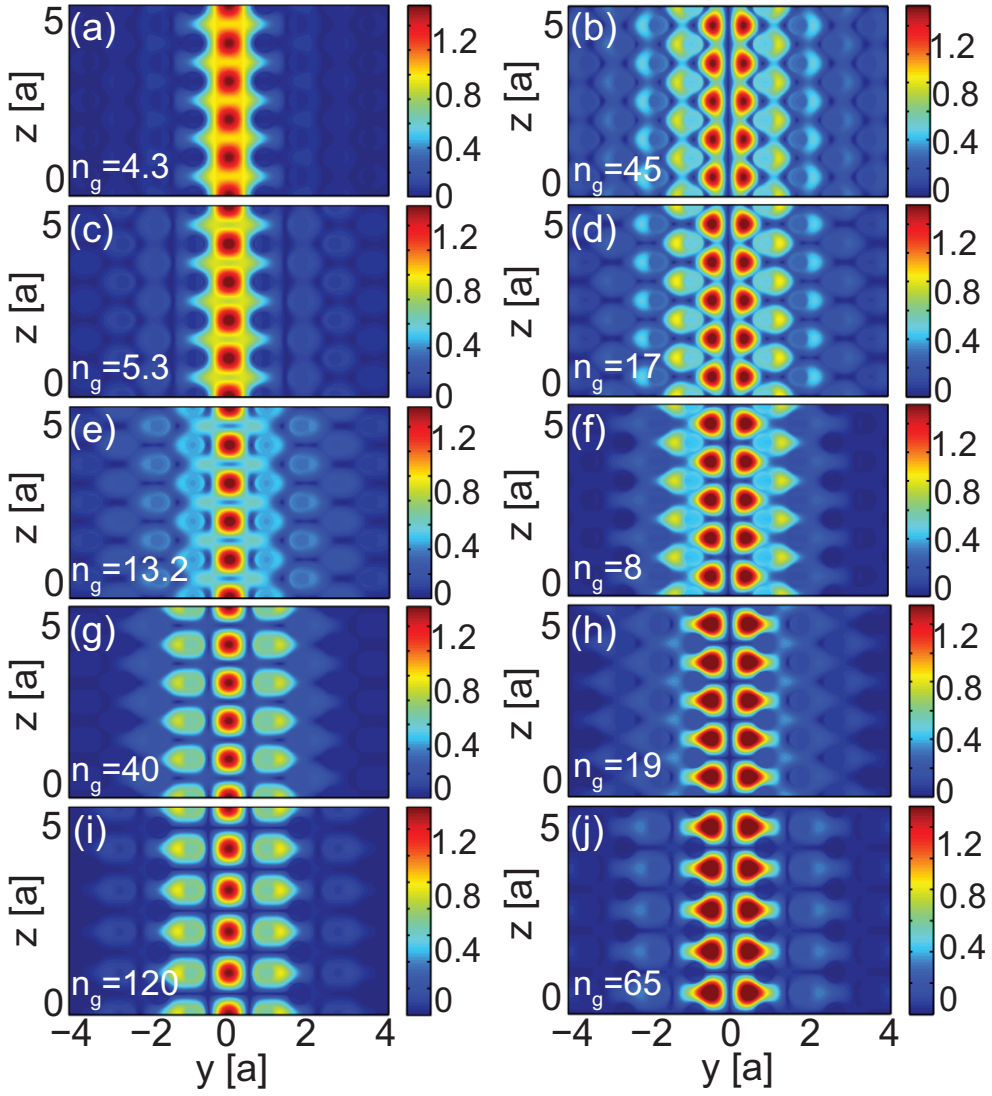

Figure 7.2: Left (right) panels show the amplitude of the normalized magnetic field H_x of the y-odd (y-even) mode, calculated in the plane $x = 0$ for five different values of the propagation constant, k_z. From top to bottom, the panels correspond to the Bloch modes indicated in Fig. 7.1(b) by the circles A, B, C, D, and E, respectively.

Bloch theorem. Under these circumstances, we determined numerically the photonic band structure of the system and the guiding optical modes of the waveguide using MPB, a freely available code based on the plane-wave expansion (PWE) method [7.64]. To be more specific, we used a supercell with size of $6a \times 19\sqrt{3}/2a \times a$ along the x-, y-, and z-axis, respectively, the corresponding step size of the computational grid being $a/60$, $a\sqrt{3}/120$, and $a/60$, respectively. Figure 7.1(b) summarizes the results of these calculations. Thus, the waveguide has two fundamental TE-like optical guiding modes located in the band-gap of the unperturbed PhC, one y-even and the other one y-odd.

In order to better understand the physical properties of the optical guiding modes, we plot in Fig. 7.2 the profile of the magnetic field H_x, which is its only nonzero component in the $x = 0$ symmetry plane. These field profiles, calculated for several values of k_z, show that although the optical field is primarily confined at the location of the defect (waveguide), for some values of k_z it is rather delocalized in the transverse direction. This field delocalization effect is particularly strong in the spectral domains where the modal dispersion curves are relatively flat, namely in the so-called slow-light regime, and increases when the group index of the mode, defined as $n_g = c/v_g$, increases.

The dispersion effects upon pulse propagation in the waveguide are characterized by the waveguide dispersion coefficients, defined as $\beta_n = d^n k_z/d\omega^n$. In particular, the first-order dispersion coefficient is related to the pulse GV via $\beta_1 = 1/v_g$, whereas the second-order dispersion coefficient, β_2, quantifies the GV dispersion (GVD) as well as pulse broadening effects. The wavelength dependence of the first four dispersion coefficients, determined for both guided modes, is presented in Fig. 7.3, the shaded areas indicating the spectral regions of slow-light. For the sake of clarity, we set the corresponding threshold to $c/v_g = 20$, that is the slow-light regime is defined by $n_g > 20$. As it can be seen in Fig. 7.3, the even mode possesses two slow-light regions, one located at the band-edge ($\lambda \approx 1.6\,\mu$m) and the other one at $k_z \approx 0.3(2\pi/a)$, i.e. $\lambda \approx 1.52\,\mu$m, whereas the odd mode contains only one such spectral domain located at the band-edge ($\lambda \approx 1.67\,\mu$m). Moreover, the even mode can have both positive and negative GVD, the zero-GVD point being at $\lambda = 1.56\,\mu$m, whereas the odd mode has normal GVD ($\beta_2 > 0$) throughout. Since usually efficient FWM can only be achieved in the anomalous GVD regime ($\beta_2 < 0$), we will assume that the interacting pulses

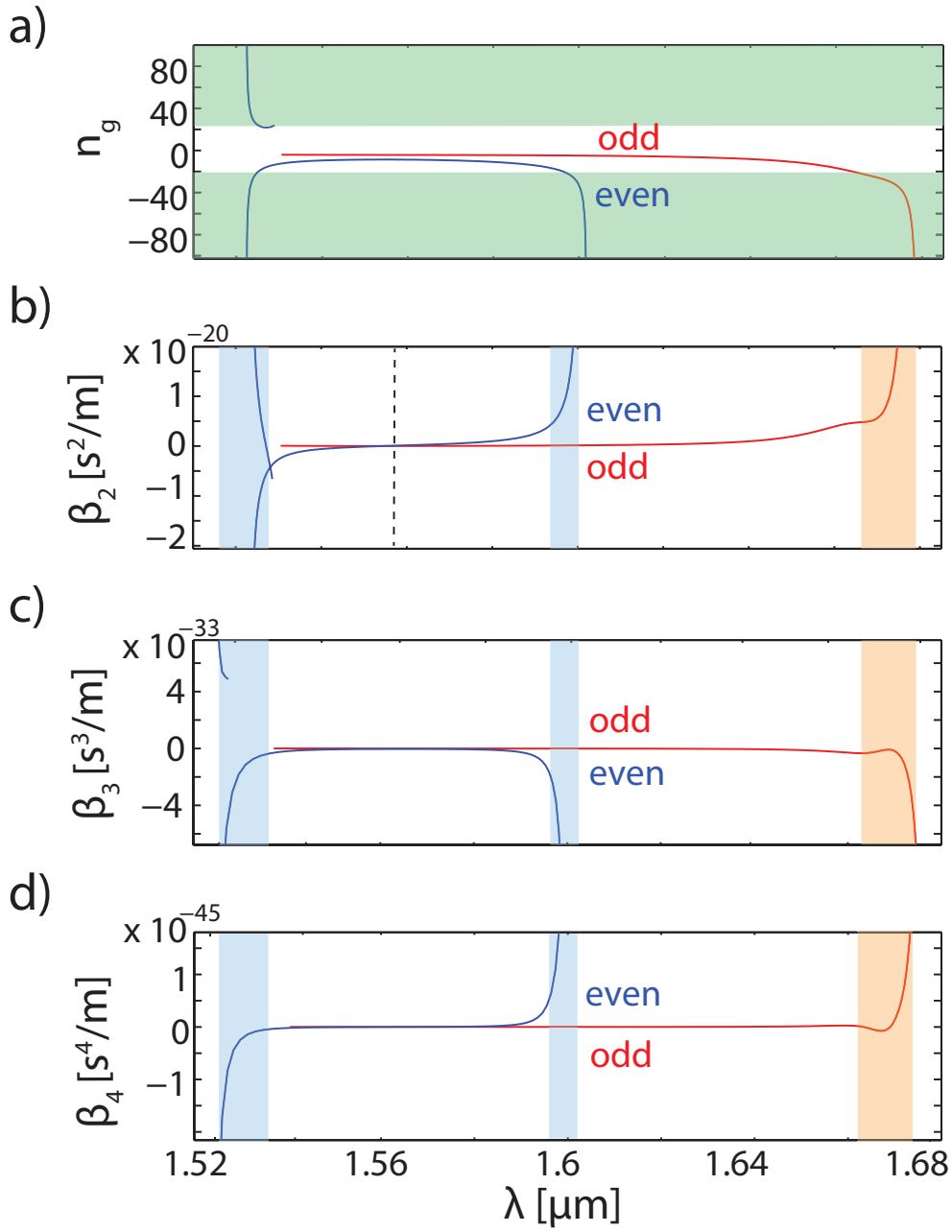

Figure 7.3: (a), (b), (c), and (d) Frequency dependence of waveguide dispersion coefficients n_g, β_2, β_3, and β_4, respectively, determined for the even and odd modes. Light green, blue, and red shaded regions correspond to slow-light regime, defined as $n_g > 20$. The dashed vertical line in panel (b) indicates the zero-GVD wavelength.

propagate in the even mode unless otherwise is specified.

7.3 Derivation of the mathematical model

This section is devoted to the derivation of a system of coupled-mode equations describing the co-propagation of a set of mutually interacting optical pulses in a Si-PhCW, as well the influence of photogenerated FCs on the pulse evolution. We will derive these

coupled-mode equations in the most general setting, namely the nondegenerate FWM, then show how they can be applied to a particular case most used in practice, the so-called degenerate FWM configuration. Our derivation follows the general approach used to develop a theoretical model for pulse propagation in silicon waveguides with uniform cross-section [7. 65] and Si-PhCWs [7. 66].

7.3.1 Optical modes of photonic crystal waveguides

In the presence of an external perturbation described by the polarization, $\mathbf{P}_{\text{pert}}(\mathbf{r},\omega)$, the electromagnetic field of guiding modes with frequency, ω, is described by the Maxwell equations, which in the frequency domain can be written in the following form:

$$\nabla \times \mathbf{E}(\mathbf{r},\omega) = i\omega\mu\mathbf{H}(\mathbf{r},\omega), \tag{7.1a}$$

$$\nabla \times \mathbf{H}(\mathbf{r},\omega) = -i\omega[\varepsilon_c(\mathbf{r},\omega)\mathbf{E}(\mathbf{r},\omega) + \mathbf{P}_{\text{pert}}(\mathbf{r},\omega)], \tag{7.1b}$$

where μ is the magnetic permeability, which in the case of silicon and other nonmagnetic materials can be set to $\mu = \mu_0$, $\varepsilon_c(\mathbf{r},\omega)$ is the dielectric constant of the PhC, and $\mathbf{E}$ and $\mathbf{H}$ are the electric and magnetic fields, respectively. In our case, $\mathbf{P}_{\text{pert}}$ is the sum of polarizations describing the refraction index change induced by photogenerated FCs and nonlinear (Kerr) effects.

In order to understand how the modes of the PhC waveguide are affected by external perturbations, let us consider first the unperturbed system, that is $\mathbf{P}_{\text{pert}} = 0$. Thus, let us assume that, at the frequency ω, the unperturbed PhC waveguide has M guiding modes. It follows then from the Bloch theorem that the fields of these modes can be written as:

$$\mathbf{E}_{m\sigma}(\mathbf{r},\omega) = \mathbf{e}_{m\sigma}(\mathbf{r},\omega)e^{i\sigma\beta_m z}, \quad m = 1,2,\ldots,M, \tag{7.2a}$$

$$\mathbf{H}_{m\sigma}(\mathbf{r},\omega) = \mathbf{h}_{m\sigma}(\mathbf{r},\omega)e^{i\sigma\beta_m z}, \quad m = 1,2,\ldots,M, \tag{7.2b}$$

where β_m is the mth mode propagation constant and $\sigma = +$ ($\sigma = -$) denotes forward (backward) propagating modes. Here, we consider that the harmonic time dependence of the fields was chosen as $e^{-i\omega t}$. The mode amplitudes $\mathbf{e}_{m\sigma}$ and $\mathbf{h}_{m\sigma}$ are periodic along the z-axis, with period a. Moreover, the forward and backward propagating modes obey

the following symmetry relations:

$$\mathbf{e}_{m-}(\mathbf{r},\omega) = \mathbf{e}^{*}_{m+}(\mathbf{r},\omega), \tag{7.3a}$$

$$\mathbf{h}_{m-}(\mathbf{r},\omega) = -\mathbf{h}^{*}_{m+}(\mathbf{r},\omega), \tag{7.3b}$$

where the symbol "*" denotes complex conjugation. As such, one only has to determine either the forward or the backward propagating modes.

The guiding modes can be orthogonalized, the most commonly used normalization convention being

$$\frac{1}{4}\int_{S}(\mathbf{e}_{m\sigma}\times\mathbf{h}^{*}_{m'\sigma'}+\mathbf{e}^{*}_{m'\sigma'}\times\mathbf{h}_{m\sigma})\cdot\hat{\mathbf{z}}dS = \sigma P_m\delta_{\sigma\sigma'}\delta_{mm'}, \tag{7.4}$$

where P_m is the power carried by the mth mode. This mode power is related to the mode energy contained in one unit cell of the PhC waveguide, W_m, via the relation:

$$P_m = \frac{W_m^{\mathrm{el}}+W_m^{\mathrm{mag}}}{a}v_g = \frac{2W_m^{\mathrm{el}}}{a}v_g = \frac{2W_m^{\mathrm{mag}}}{a}v_g, \tag{7.5}$$

where

$$W_m^{\mathrm{el}} = \frac{1}{4}\int_{V_{\mathrm{cell}}}\frac{\partial}{\partial\omega}(\omega\varepsilon_c)|\mathbf{e}_{m\sigma}(\mathbf{r},\omega)|^2dV, \tag{7.6a}$$

$$W_m^{\mathrm{mag}} = \frac{1}{4}\int_{V_{\mathrm{cell}}}\mu_0|\mathbf{h}_{m\sigma}(\mathbf{r},\omega)|^2dV, \tag{7.6b}$$

are the electric and magnetic energy of the mode, respectively, and V_{cell} is the volume of the unit cell. Note that in Eq. (7.5) we used the fact that the mode contains equal amounts of electric and magnetic energy. In particular, in the case of PhC waveguides the waveguide dispersion is much larger than the material dispersion so that in Eq. (7.6a) we can neglect the frequency dispersion of ε_c.

It should be stressed that the waveguide modes defined by Eqs. (7.2) are exact solutions of the Maxwell equations (7.1) with $\mathbf{P}_{\mathrm{pert}} = 0$, and thus they should not be confused with the so-called local modes of the waveguide. The latter modes correspond to waveguides whose optical properties vary adiabatically with z, on a scale comparable to the wavelength and have been used to describe, *e.g.*, wave propagation in tapered waveguides [7. 69] or pulse propagation in 1D long-period Bragg gratings [7. 70].

7.3.2 Perturbations of the photonic crystal waveguide

Due to the photogeneration of FCs and nonlinear optical effects, the dielectric constant of Si-PhCWs undergoes a certain local variation, $\delta\varepsilon(\mathbf{r})$, upon the propagation of optical pulses in the waveguide. The corresponding perturbation polarization, $\mathbf{P}_{\text{pert}}$ in Eq. (7.1b), can be divided in two components according to the physical effects they describe: the linear change of the dielectric constant *via* generation of FCs and the nonlinearly induced variation of the index of refraction.

Assuming an instantaneous response of the medium, the linear contribution to $\mathbf{P}_{\text{pert}}$, $\delta\mathbf{P}_{\text{lin}}(\mathbf{r},t)$, is written as:

$$\delta\mathbf{P}_{\text{lin}}(\mathbf{r},t) = [\delta\varepsilon_{\text{fc}}(\mathbf{r}) + \delta\varepsilon_{\text{loss}}(\mathbf{r})]\,\mathbf{E}(\mathbf{r},t), \tag{7.7}$$

where [7. 65]:

$$\delta\varepsilon_{\text{fc}}(\mathbf{r}) = \left(2\varepsilon_0 n\delta n_{\text{fc}} + i\frac{\varepsilon_0 cn}{\omega}\alpha_{\text{fc}}\right)\Sigma(\mathbf{r}), \tag{7.8a}$$

$$\delta\varepsilon_{\text{loss}}(\mathbf{r}) = i\frac{\varepsilon_0 cn}{\omega}\alpha_{\text{in}}\Sigma(\mathbf{r}). \tag{7.8b}$$

Here, α_{in} is the intrinsic loss coefficient of the waveguide and $\Sigma(\mathbf{r})$ is the characteristic function of the domain where FCs can be generated, namely $\Sigma = 1$ in the domain occupied by silicon and $\Sigma = 0$ otherwise. Based on the Drude model, the FC-induced change of the index of refraction, δn_{fc}, and FC losses, α_{fc}, are given by [7. 71]:

$$\delta n_{\text{fc}} = -\frac{e^2}{2\varepsilon_0 n\omega^2}\left(\frac{N_e}{m_{ce}} + \frac{N_h^{0.8}}{m_{ch}}\right), \tag{7.9a}$$

$$\alpha_{\text{fc}} = \frac{e^3}{\varepsilon_0 cn\omega^2}\left(\frac{N_e}{\mu_e m_{ce}^2} + \frac{N_h}{\mu_h m_{ch}^2}\right). \tag{7.9b}$$

Here, e is the charge of the electron, μ_e (μ_h) is the electron (hole) mobility, $m_{ce} = 0.26m_0$ ($m_{ch} = 0.39m_0$) is the conductivity effective mass of the electrons (holes), with m_0 the mass of the electron, and N_e (N_h) is the induced variation of the electrons (holes) density (in what follows, we assume that $N_e = N_h \equiv N$).

The nonlinear contribution to $\mathbf{P}_{\text{pert}}$, $\delta\mathbf{P}_{\text{nl}}(\mathbf{r},t)$, is described by a third-order non-

linear susceptibility, $\hat{\chi}^{(3)}(\mathbf{r})$, and can be written as:

$$\delta\mathbf{P}_{\mathrm{nl}}(\mathbf{r},t) = \varepsilon_0\hat{\chi}^{(3)}(\mathbf{r})\vdots\mathbf{E}(\mathbf{r},t)\mathbf{E}(\mathbf{r},t)\mathbf{E}(\mathbf{r},t). \tag{7.10}$$

The real part of the susceptibility $\hat{\chi}^{(3)}$ describes parametric optical processes such as SPM, XPM, and FWM, while the imaginary part of $\hat{\chi}^{(3)}$ corresponds to TPA and XAM. Note that in this study we neglect the stimulated Raman scattering effect as it is assumed that the frequencies of the interacting pulses do not satisfy the condition required for an efficient, resonant Raman interaction.

Since silicon belongs to the crystallographic point group $m3m$ the susceptibility tensor $\hat{\chi}^{(3)}$ has 21 nonzero elements, of which only 4 are independent, namely, χ_{1111}, χ_{1122}, χ_{1212}, and χ_{1221} [7. 72]. In addition, the frequency dispersion of the nonlinear susceptibility can be neglected as we consider optical pulses with duration of just a few picoseconds or larger. As a consequence, the Kleinman symmetry relations imply that $\chi_{1122} = \chi_{1212} = \chi_{1221}$. Moreover, experimental studies have shown that $\hat{\chi}^{(3)}_{1111} = 2.36\hat{\chi}^{(3)}_{1122}$ [7. 73] within a broad frequency range. Therefore, the nonlinear optical effects considered here can be described by only one element of the tensor $\hat{\chi}^{(3)}$.

Because of fabrication considerations, in many instances the waveguide is not aligned with any of the crystal principal axes and as such these axes are different from the coordinate axes in which the optical modes are calculated. Therefore, one has to transform the tensor $\hat{\chi}^{(3)}$ from the crystal principal axes into the coordinate system in which the optical modes are calculated [7. 65],

$$\hat{\chi}^{(3)}_{ijkl} = \hat{R}_{i\alpha}\hat{R}_{j\beta}\hat{R}_{k\gamma}\hat{R}_{l\delta}\hat{\chi}'^{(3)}_{\alpha\beta\gamma\delta}, \tag{7.11}$$

where $\hat{\chi}'^{(3)}$ is the nonlinear susceptibility in the crystal principal axes and $\hat{R}$ is the rotation matrix that transforms one coordinate system into the other. In our case, $\hat{R}$ is the matrix describing a rotation with $\pi/4$ around the x-axis (see Fig. 7.1).

7.3.3 Coupled-mode equations for the optical field

In order to derive the system of coupled-mode equations describing pulsed FWM in Si-PhCWs we employ the conjugated form of the Lorentz reciprocity theorem [7. 65–67, 75, 76]. To this end, let us consider two solutions of the Maxwell equations (7.1),

$[\mathbf{E}_a(\mathbf{r},\omega_a),\mathbf{H}_a(\mathbf{r},\omega_a)]$ and $[\mathbf{E}_b(\mathbf{r},\omega_b),\mathbf{H}_b(\mathbf{r},\omega_b)]$, which correspond to two different spatial distribution of the dielectric constant, $\varepsilon_a(\mathbf{r},\omega_a)$ and $\varepsilon_b(\mathbf{r},\omega_b)$, respectively. If we insert the vector $\mathbf{F}$, defined as $\mathbf{F}=\mathbf{E}_b\times\mathbf{H}_a^*+\mathbf{E}_a^*\times\mathbf{H}_b$, in the integral identity:

$$\int_S \nabla\cdot\mathbf{F}dS=\frac{\partial}{\partial z}\int_S \mathbf{F}\cdot\hat{\mathbf{z}}dS+\oint_{\partial S}\mathbf{F}\cdot\mathbf{n}dl, \tag{7.12}$$

where S is the transverse section at position, z, and ∂S is the boundary of S, and use the Maxwell equations, we arrive at the following relation:

$$\begin{aligned}\frac{\partial}{\partial z}\int_S \mathbf{F}\cdot\hat{\mathbf{z}}dS &= i\mu_0(\omega_b-\omega_a)\int_S \mathbf{H}_a^*\cdot\mathbf{H}_b dS\\ &+ i\int_S(\omega_b\varepsilon_b-\omega_a\varepsilon_a)\mathbf{E}_a^*\cdot\mathbf{E}_b dS-\oint_{\partial S}\mathbf{F}\cdot\mathbf{n}dl.\end{aligned} \tag{7.13}$$

Let us consider now a nondegenerate FWM process in which two pulses at carrier frequencies $\bar{\omega}_1$ and $\bar{\omega}_2$ interact and generate two optical pulses at carrier frequencies $\bar{\omega}_3$ and $\bar{\omega}_4$, with the energy conservation expressed as $\bar{\omega}_1+\bar{\omega}_2=\bar{\omega}_3+\bar{\omega}_4$. Then, in the Lorentz reciprocity theorem given by Eq. (7.13) we choose as the first set of fields a mode of the unperturbed waveguide ($\mathbf{P}_{\text{pert}}=0$), which corresponds to the frequency $\omega_a=\bar{\omega}_i$, where $\bar{\omega}_i$ is one of the carrier frequencies $\bar{\omega}_1$, $\bar{\omega}_2$, $\bar{\omega}_3$, or $\bar{\omega}_4$:

$$\mathbf{E}_a(\mathbf{r},\bar{\omega}_i)=\frac{\mathbf{e}_{n_i\rho_i}(\mathbf{r},\bar{\omega}_i)}{\sqrt{\bar{P}_{n_i}}}e^{i\rho_i\bar{\beta}_{n_i}z}, \tag{7.14a}$$

$$\mathbf{H}_a(\mathbf{r},\bar{\omega}_i)=\frac{\mathbf{h}_{n_i\rho_i}(\mathbf{r},\bar{\omega}_i)}{\sqrt{\bar{P}_{n_i}}}e^{i\rho_i\bar{\beta}_{n_i}z}, \tag{7.14b}$$

where $\rho_i=\pm1$ and n_i is an integer, $1\le n_i\le N_i$, $i=1,\ldots,4$, with N_i being the number of guiding modes at the frequency $\bar{\omega}_i$. In Eqs. (7.14), and in what follows, a bar over a symbol means that the corresponding quantity is evaluated at one of the carrier frequencies.

As the second set of fields we take those that propagate in the perturbed waveguide, at the frequency $\omega_b=\omega$. These fields are written as a series expansion of the guiding modes at frequencies $\bar{\omega}_i$, $i=1,\ldots,4$, thus neglecting the frequency dispersion of the guiding modes and the radiative modes that might exist at the frequency ω. This approximation is valid as long as all interacting optical pulses have narrow spectra centered at the corresponding carrier frequencies, that is the physical situation considered

in this work. In particular, this modal expansion becomes less accurate when any of the pulses propagates in the slow-light regime, as generally the smaller the GV of a mode is the larger its frequency dispersion is. Thus, the second set of fields are expanded as:

$$\mathbf{E}_b(\mathbf{r},\omega) = \sum_{j=1}^{4}\sum_{m_j\sigma_j} a^{(j)}_{m_j\sigma_j}(z,\omega)\frac{\mathbf{e}_{m_j\sigma_j}(\mathbf{r},\bar{\omega}_j)}{\sqrt{\bar{P}_{m_j}}}e^{i\sigma_j\bar{\beta}_{m_j}z}, \tag{7.15a}$$

$$\mathbf{H}_b(\mathbf{r},\omega) = \sum_{j=1}^{4}\sum_{m_j\sigma_j} a^{(j)}_{m_j\sigma_j}(z,\omega)\frac{\mathbf{h}_{m_j\sigma_j}(\mathbf{r},\bar{\omega}_j)}{\sqrt{\bar{P}_{m_j}}}e^{i\sigma_j\bar{\beta}_{m_j}z}. \tag{7.15b}$$

With the fields normalization used in Eqs. (7.15), the mode amplitudes $a^{(i)}_{m_i\sigma_i}(z,\omega)$, $i = 1,\ldots,4$, are measured in units of $\sqrt{\mathrm{W}}$. Note that since the optical pulses are assumed to be spectrally narrow, the mode amplitudes $a^{(i)}_{m_i\sigma_i}(z,\omega)$ have negligible values except when the frequency ω lies in a narrow spectral domain centered at the carrier frequency, $\bar{\omega}_i$.

The dielectric constant in the two cases is $\varepsilon_a = \bar{\varepsilon}_c(\mathbf{r},\bar{\omega}_i)$ and $\varepsilon_b = \varepsilon_c(\mathbf{r},\omega) + \delta\varepsilon(\mathbf{r},\omega)$, where $\varepsilon_c(\mathbf{r},\omega)$ is the dielectric constant of the unperturbed PhC. If the material dispersion is neglected, $\varepsilon_c(\mathbf{r},\omega) = \varepsilon_c(\mathbf{r},\bar{\omega}_i) = \bar{\varepsilon}_c(\mathbf{r})$. Inserting the fields given by Eqs. (7.14) and Eqs. (7.15) in Eq. (7.13), and neglecting the line integral in Eq. (7.13), which cancels for exponentially decaying guiding modes, one obtains the following set of coupled equations:

$$\begin{aligned}
&\rho_i\frac{\partial a^{(i)}_{n_i\rho_i}(z)}{\partial z} + \sum_{\substack{j=1\\ j\neq i}}^{4}\sum_{m_j\sigma_j} C^{ij}_{n_i\rho_i,m_j\sigma_j}(z)\times\left[\frac{\partial a^{(j)}_{m_j\sigma_j}(z)}{\partial z} + i(\sigma_j\bar{\beta}_{m_j} - \rho_i\bar{\beta}_{n_i})a^{(j)}_{m_j\sigma_j}(z)\right]\\
&= B^i_{n_i\rho_i}a^{(i)}_{n_i\rho_i}(z) + \sum_{jm_j\sigma_j}{}' D^{ij}_{n_i\rho_i,m_j\sigma_j}a^{(j)}_{m_j\sigma_j}(z) + \frac{i\omega e^{-i\rho_i\bar{\beta}_{n_i}z}}{4\sqrt{\bar{P}_{n_i}}}\int_S \bar{\mathbf{e}}^*_{n_i\rho_i}\cdot\mathbf{P}_{\mathrm{pert}}(\mathbf{r},\omega)dS,\\
&i = 1,\ldots,4,
\end{aligned} \tag{7.16}$$

where

$$C^{ij}_{n_i\rho_i,m_j\sigma_j}(z) = \frac{e^{i(\sigma_j\bar{\beta}_{m_j}-\rho_i\bar{\beta}_{n_i})z}}{4\sqrt{\bar{P}_{n_i}\bar{P}_{m_j}}}\times\int_S\left(\bar{\mathbf{e}}_{m_j\sigma_j}\times\bar{\mathbf{h}}^*_{n_i\rho_i} + \bar{\mathbf{e}}^*_{n_i\rho_i}\times\bar{\mathbf{h}}_{m_j\sigma_j}\right)\cdot\hat{\mathbf{z}}dS, \tag{7.17a}$$

$$B^i_{n_i\rho_i} = \frac{i}{4\bar{P}_{n_i}}\int_S\left[\mu_0(\omega-\bar{\omega}_i)|\bar{\mathbf{h}}_{n_i\rho_i}|^2 + (\omega\varepsilon_c - \bar{\varepsilon}_c\bar{\omega}_i)|\bar{\mathbf{e}}_{n_i\rho_i}|^2\right]dS, \tag{7.17b}$$

$$D^{ij}_{n_i\rho_i,m_j\sigma_j}(z) = \frac{ie^{i(\sigma_j\bar{\beta}_{m_j}-\rho_i\bar{\beta}_{n_i})z}}{4\sqrt{\bar{P}_{n_i}\bar{P}_{m_j}}}\int_S\left[\mu_0(\omega-\bar{\omega}_i)\times\bar{\mathbf{h}}_{m_j\sigma_j}\cdot\bar{\mathbf{h}}^*_{n_i\rho_i}\right]dS$$
$$+\frac{ie^{i(\sigma_j\bar{\beta}_{m_j}-\rho_i\bar{\beta}_{n_i})z}}{4\sqrt{\bar{P}_{n_i}\bar{P}_{m_j}}}\int_S\left[(\omega\varepsilon_c-\bar{\varepsilon}_c\bar{\omega}_i)\bar{\mathbf{e}}_{m_j\sigma_j}\cdot\bar{\mathbf{e}}^*_{n_i\rho_i}\right]dS. \tag{7.17c}$$

In Eq. (7.16) and what follows a prime symbol to a sum means that the summation is taken over all modes, except that with $j=i$, $m_j=n_i$, and $\sigma_j=\rho_i$. Moreover, in deriving the l.h.s. of Eq. (7.16) we used the orthogonality relation given by Eq. (7.4). As it will become more apparent later on, the coefficient $C^{ij}_{n_i\rho_i,m_j\sigma_j}$ describes the linear coupling between the modes characterized by parameters $\{n_i\rho_i\}$ and $\{m_j\sigma_j\}$, the coefficient $B^i_{n_i\rho_i}$ is related to the frequency dispersion the mode $\{n_i\rho_i\}$, whereas the coefficient $D^{ij}_{n_i\rho_i,m_j\sigma_j}$ describes the frequency dispersion of the optical coupling between the modes characterized by parameters $\{n_i\rho_i\}$ and $\{m_j\sigma_j\}$.

The time-dependent fields are obtained by integrating over all frequency components contained in the spectra of the system of interacting optical pulses:

$$\mathbf{E}(\mathbf{r},t) = \frac{1}{2}\int_0^\infty\sum_{j=1}^4\sum_{m_j\sigma_j}a^{(j)}_{m_j\sigma_j}(z,\omega)\frac{\mathbf{e}_{m_j\sigma_j}(\mathbf{r},\bar{\omega}_j)}{\sqrt{\bar{P}_{m_j}}}$$
$$\times e^{i(\sigma_j\bar{\beta}_{m_j}z-\omega t)}d\omega+c.c.\equiv\frac{1}{2}\left[\mathbf{E}^{(+)}(\mathbf{r},t)+\mathbf{E}^{(-)}(\mathbf{r},t)\right], \tag{7.18a}$$
$$\mathbf{H}(\mathbf{r},t) = \frac{1}{2}\int_0^\infty\sum_{j=1}^4\sum_{m_j\sigma_j}a^{(j)}_{m_j\sigma_j}(z,\omega)\frac{\mathbf{h}_{m_j\sigma_j}(\mathbf{r},\bar{\omega}_j)}{\sqrt{\bar{P}_{m_j}}}$$
$$\times e^{i(\sigma_j\bar{\beta}_{m_j}z-\omega t)}d\omega+c.c.\equiv\frac{1}{2}\left[\mathbf{H}^{(+)}(\mathbf{r},t)+\mathbf{H}^{(-)}(\mathbf{r},t)\right], \tag{7.18b}$$

where $\mathbf{E}^{(+)}(\mathbf{r},t)$, $\mathbf{H}^{(+)}(\mathbf{r},t)$ and $\mathbf{E}^{(-)}(\mathbf{r},t)$, $\mathbf{H}^{(-)}(\mathbf{r},t)$ are the positive and negative frequency parts of the spectrum, respectively.

Let us now introduce the envelopes of the interacting pulses in the time domain, $A^{(i)}_{n_i\rho_i}(z,t)$, defined as the integral of the mode amplitudes taken over the part of the spectrum that contains only positive frequencies,

$$A^{(i)}_{n_i\rho_i}(z,t) = \int_0^\infty a^{(i)}_{n_i\rho_i}(z,\omega)e^{-i(\omega-\bar{\omega}_i)t}d\omega. \tag{7.19}$$

With this definition, the time-dependent fields given in Eqs. (7.18) become:

$$\mathbf{E}(\mathbf{r},t) = \frac{1}{2}\sum_{j=1}^{4}\sum_{m_j\sigma_j} A^{(j)}_{m_j\sigma_j}(z,t) \times \frac{\bar{\mathbf{e}}_{m_j\sigma_j}(\mathbf{r},\bar{\omega}_j)}{\sqrt{\bar{P}_{m_j}}} e^{i(\sigma_j\bar{\beta}_{m_j}z-\bar{\omega}_j t)} + c.c., \tag{7.20a}$$

$$\mathbf{H}(\mathbf{r},t) = \frac{1}{2}\sum_{j=1}^{4}\sum_{m_j\sigma_j} A^{(j)}_{m_j\sigma_j}(z,t) \times \frac{\bar{\mathbf{h}}_{m_j\sigma_j}(\mathbf{r},\bar{\omega}_j)}{\sqrt{\bar{P}_{m_j}}} e^{i(\sigma_j\bar{\beta}_{m_j}z-\bar{\omega}_j t)} + c.c.. \tag{7.20b}$$

Following the same approach, the time-dependent polarization, too, can be decomposed in two components, which contain positive and negative frequencies, that is, it can be written as:

$$\mathbf{P}_{\text{pert}}(\mathbf{r},t) = \frac{1}{2}\int_0^\infty \mathbf{P}_{\text{pert}}(\mathbf{r},\omega)e^{-i\omega t}d\omega + c.c. \equiv \frac{1}{2}\left[\mathbf{P}^{(+)}_{\text{pert}}(\mathbf{r},t) + \mathbf{P}^{(-)}_{\text{pert}}(\mathbf{r},t)\right]. \tag{7.21}$$

The next step of our derivation is to Fourier transform Eq. (7.16) in the time domain. To this end, we first expand the coefficients $B^i_{n_i\rho_i}$ and $D^{ij}_{n_i\rho_i,m_j\sigma_j}$ in Taylor series, around the carrier frequency $\bar{\omega}_i$ [note that according to Eq. (7.17a), $C^{ij}_{n_i\rho_i,m_j\sigma_j}$ is frequency independent]:

$$B^i_{n_i\rho_i} = \sum_{q\geq 1}\frac{(\Delta\omega_i)^q}{q!}\left.\frac{\partial^q B^i_{n_i\rho_i}}{\partial\omega^q}\right|_{\omega=\bar{\omega}_i} \equiv \sum_{q\geq 1}\frac{i\beta^{(q)i}_{n_i\rho_i}}{q!}(\Delta\omega_i)^q, \tag{7.22a}$$

$$D^{ij}_{n_i\rho_i,m_j\sigma_j} = \sum_{q\geq 1}\frac{(\Delta\omega_i)^q}{q!}\left.\frac{\partial^q D^{ij}_{n_i\rho_i,m_j\sigma_j}}{\partial\omega^q}\right|_{\omega=\bar{\omega}_i} \equiv \sum_{q\geq 1}\frac{i\beta^{(q)ij}_{n_i\rho_i,m_j\sigma_j}}{q!}(\Delta\omega_i)^q, \tag{7.22b}$$

where $\Delta\omega_i = \omega - \bar{\omega}_i$, $i = 1,\ldots,4$. Combining Eqs. (7.22a), (7.17b), (7.5), and (7.6) leads to the following expression for the dispersion coefficients, $\beta^{(q)i}_{n_i\rho_i}$:

$$\beta^{(1)i}_{n_i\rho_i}(z) = \frac{\delta^i_{n_i}(z)}{v^i_{g,n_i}}, \tag{7.23a}$$

$$\beta^{(n)i}_{n_i\rho_i}(z) = \delta^i_{n_i}(z)\frac{\partial^{n-1}}{\partial\omega^{n-1}}\left(\frac{1}{v^i_{g,n_i}}\right),\ n\geq 2, \tag{7.23b}$$

where

$$\delta^i_{n_i}(z) = \frac{a}{4W_{m_i}}\int_S\left[\mu_0|\mathbf{h}_{n_i\rho_i}(\mathbf{r},\bar{\omega}_i)|^2 + \frac{\partial}{\partial\omega}(\omega\varepsilon_c)|\mathbf{e}_{n_i\rho_i}(\mathbf{r},\bar{\omega}_i)|^2\right]dS. \tag{7.24}$$

It can be easily seen from this equation that the average of $\delta^i_{n_i}(z)$ over one lattice

cell of the PhC waveguide is equal to 1, *i.e.*,

$$\tilde{\delta}^i_{n_i} \equiv \frac{1}{a}\int_z^{z+a} \delta^i_{n_i}(z')dz' = 1. \tag{7.25}$$

Here and in what follows the tilde symbol indicates that the corresponding physical quantity has been averaged over a lattice cell of the waveguide. With this notation, Eqs. (7.23) become:

$$\tilde{\beta}^{(1)i}_{n_i\rho_i} \equiv \beta^i_{1,n_i} = \frac{1}{v^i_{g,n_i}}, \tag{7.26a}$$

$$\tilde{\beta}^{(n)i}_{n_i\rho_i} \equiv \beta^i_{n,n_i} = \frac{\partial^{n-1}\beta^i_{1,n_i}}{\partial\omega^{n-1}},\ n \geq 2. \tag{7.26b}$$

These relations show that $\tilde{\beta}^{(n)i}_{n_i\rho_i} = \beta^i_{n,n_i}$ is the nth order dispersion coefficient of the waveguide mode characterized by the parameters $\{n_i,\rho_i\}$, evaluated at $\omega = \bar{\omega}_i$.

We now multiply Eq. (7.16) by $e^{-i(\omega-\bar{\omega}_i)t}$ and integrate over the positive-frequency domain. These simple calculations lead to the time-domain coupled-mode equations for the field envelopes, $A^{(i)}_{n_i\rho_i}(z,t)$:

$$\begin{aligned}
&\rho_i\frac{\partial A^{(i)}_{n_i\rho_i}}{\partial z} + \sum_{\substack{j=1\\ j\neq i}}^{4}\sum_{m_j\sigma_j} C^{ij}_{n_i\rho_i,m_j\sigma_j}e^{-i(\bar{\omega}_j-\bar{\omega}_i)t}\left[\frac{\partial A^{(j)}_{m_j\sigma_j}}{\partial z} + i(\sigma_j\bar{\beta}_{m_j} - \rho_i\bar{\beta}_{n_i})A^{(j)}_{m_j\sigma_j}\right]\\
&= i\sum_{q\geq 1}\frac{\beta^{(q)i}_{n_i\rho_i}}{q!}\left(i\frac{\partial}{\partial t}\right)^q A^{(i)}_{n_i\rho_i} + i\sum_{q\geq 1}\sum_{jm_j\sigma_j}{}'\frac{\beta^{(q)ij}_{n_i\rho_i,m_j\sigma_j}}{q!}e^{-i(\bar{\omega}_j-\bar{\omega}_i)t}\left(i\frac{\partial}{\partial t}\right)^q A^{(j)}_{n_j\rho_j}\\
&+ \frac{i\bar{\omega}_i e^{-i(\rho_i\bar{\beta}_{n_i}z-\bar{\omega}_i t)}}{4\sqrt{\bar{P}_{n_i}}}\int_S \bar{\mathbf{e}}^*_{n_i\rho_i}\cdot\mathbf{P}^{(+)}_{\text{pert}}(\mathbf{r},t)dS,\ i=1,\ldots,4,
\end{aligned} \tag{7.27}$$

The temporal width of the pulses considered in this analysis is much smaller as compared to the nonlinear electronic response time of silicon and therefore the latter can be approximated to be instantaneous. In addition, we assume that the spectra of the interacting pulses are narrow and do not overlap. Under these circumstances, the optical pulses can be viewed as quasi-monochromatic waves and their nonlinear interactions can be treated in the adiabatic limit. Separating the nonlinear optical effects contributing to the nonlinear polarization, one can express in the time domain this po-

larization as [7. 74]:

$$\delta\mathbf{P}_{\mathrm{nl},\bar{\omega}_i}(\mathbf{r},t) = \frac{3}{4}\sum_{m_i\sigma_i}\varepsilon_0\hat{\chi}^{(3)}(\bar{\omega}_i,-\bar{\omega}_i,\bar{\omega}_i)\vdots\bar{\mathbf{e}}_{m_i\sigma_i}(\mathbf{r},\bar{\omega}_j)\bar{\mathbf{e}}^*_{m_i\sigma_i}(\mathbf{r},\bar{\omega}_j)\bar{\mathbf{e}}_{m_i\sigma_i}(\mathbf{r},\bar{\omega}_j)$$
$$|A^{(i)}_{m_i\sigma_i}|^2 A^{(i)}_{m_i\sigma_i}\frac{e^{i\sigma_i\bar{\beta}_{m_i}z}}{\bar{P}_{m_i}\sqrt{\bar{P}_{m_i}}}$$
$$+\frac{3}{2}\sum_{m_i\sigma_i}\sum_{\substack{(p_i\rho_i)\neq(m_i\sigma_i)\\ p_i>m_i}}\varepsilon_0\hat{\chi}^{(3)}(\bar{\omega}_i,-\bar{\omega}_i,\bar{\omega}_i)\vdots\bar{\mathbf{e}}_{p_i\rho_i}(\mathbf{r},\bar{\omega}_i)\bar{\mathbf{e}}^*_{p_i\rho_i}(\mathbf{r},\bar{\omega}_i)\bar{\mathbf{e}}_{m_i\sigma_i}(\mathbf{r},\bar{\omega}_i)$$
$$|A^{(i)}_{p_i\rho_i}|^2 A^{(i)}_{m_i\sigma_i}\frac{e^{i\sigma_i\bar{\beta}_{m_i}z}}{\bar{P}_{p_i}\sqrt{\bar{P}_{m_i}}}$$
$$+\frac{3}{2}\sum_{\substack{j=1\\ j\neq i}}^{4}\sum_{\substack{m_i\sigma_i\\ p_j\rho_j}}\varepsilon_0\hat{\chi}^{(3)}(\bar{\omega}_j,-\bar{\omega}_j,\bar{\omega}_i)\vdots\bar{\mathbf{e}}_{p_j\rho_j}(\mathbf{r},\bar{\omega}_j)\bar{\mathbf{e}}^*_{p_j\rho_j}(\mathbf{r},\bar{\omega}_j)\bar{\mathbf{e}}_{m_i\sigma_i}(\mathbf{r},\bar{\omega}_i)$$
$$|A^{(j)}_{p_j\rho_j}|^2 A^{(i)}_{m_i\sigma_i}\frac{e^{i\sigma_i\bar{\beta}_{m_i}z}}{\bar{P}_{p_j}\sqrt{\bar{P}_{m_i}}}$$
$$+\frac{3}{2}\sum_{\substack{p_jq_km_l\\ \rho_j\tau_k\sigma_l}}\varepsilon_0\hat{\chi}^{(3)}(\bar{\omega}_j,-\bar{\omega}_k,\bar{\omega}_l)\vdots\bar{\mathbf{e}}_{p_j\rho_j}(\mathbf{r},\bar{\omega}_j)\bar{\mathbf{e}}^*_{q_k\tau_k}(\mathbf{r},\bar{\omega}_k)\bar{\mathbf{e}}_{m_l\sigma_l}(\mathbf{r},\bar{\omega}_l)$$
$$A^{(j)}_{p_j\rho_j}A^{(k)*}_{q_k\tau_k}A^{(l)}_{m_l\sigma_l}\times\frac{e^{i\left[(\rho_j\bar{\beta}_{p_j}-\tau_k\bar{\beta}_{q_k}+\sigma_l\bar{\beta}_{m_l})z-(\bar{\omega}_j-\bar{\omega}_k+\bar{\omega}_l)t\right]}}{\sqrt{\bar{P}_{p_j}\bar{P}_{q_k}\bar{P}_{m_l}}}\Bigg|_{\substack{j\neq k\neq l\neq i\\ \bar{\omega}_j-\bar{\omega}_k+\bar{\omega}_l=\bar{\omega}_i}} . \quad (7.28)$$

This expression for the nonlinear polarization accounts for the fact that the nonlinear susceptibility is invariant to frequency permutations. The first term in Eq. (7.28) represents SPM effects of the pulse envelopes, the second and third terms describe the XPM between modes with the same frequency and XPM between pulses propagating at different frequencies, respectively, whereas the last term describes FWM processes.

If one inserts in Eq. (7.27) the linear and nonlinear polarizations given by Eq. (7.7) and Eq. (7.28), respectively, then discards the fast time-varying terms, one obtains the following system of coupled equations that governs the dynamics of the mode envelopes:

$$\rho_i\frac{\partial A^{(i)}_{n_i\rho_i}}{\partial z} = i\sum_{q\geq1}\frac{\beta^{(q)i}_{n_i\rho_i}}{q!}\left(i\frac{\partial}{\partial t}\right)^q A^{(i)}_{n_i\rho_i} + i\sum_{q\geq1}\sum_{(m_i\sigma_i)\neq(n_i\rho_i)}\frac{\beta^{(q)ii}_{n_i\rho_i,m_i\sigma_i}}{q!}\left(i\frac{\partial}{\partial t}\right)^q A^{(i)}_{m_i\sigma_i}$$

$$+i\frac{\vartheta^i_{n_i\rho_i}(z)}{v^i_{g,n_i}}A^{(i)}_{n_i\rho_i}+i\sum_{(m_i\sigma_i)\neq(n_i\rho_i)}\frac{\vartheta^i_{n_i\rho_i,m_i\sigma_i}(z)}{\sqrt{v^i_{g,n_i}v^i_{g,m_i}}}A^{(i)}_{m_i\sigma_i}+\frac{3i\bar{\omega}_i}{16\varepsilon_0 a^2}\times$$

$$\Bigg\{\sum_{m_i\sigma_i}\Bigg[\frac{\Gamma^i_{n_i\rho_i,m_i\sigma_i}(z)}{v^i_{g,m_i}\sqrt{v^i_{g,m_i}v^i_{g,n_i}}}|A^{(i)}_{m_i\sigma_i}|^2A^{(i)}_{m_i\sigma_i}+\sum_{\substack{(p_i\rho_i)\neq(m_i\sigma_i)\\ p_i>m_i}}\frac{2\Gamma^i_{n_i\rho_i,m_i\sigma_i p_i\rho_i}(z)}{v^i_{g,p_i}\sqrt{v^i_{g,m_i}v^i_{g,n_i}}}|A^{(i)}_{p_i\rho_i}|^2A^{(i)}_{m_i\sigma_i}+$$

$$\sum_{\substack{j=1\\ j\neq i}}^{4}\sum_{p_j\rho_j}\frac{2\Gamma^{ij}_{n_i\rho_i,m_i\sigma_i p_j\rho_j}(z)}{v^j_{g,p_j}\sqrt{v^i_{g,m_i}v^i_{g,n_i}}}|A^{(j)}_{p_j\rho_j}|^2A^{(i)}_{m_i\sigma_i}\Bigg]+\sum_{\substack{p_jq_km_l\\ \rho_j\tau_k\sigma_l}}e^{i\Delta\bar{\beta}_{n_ip_jq_km_l}z}\frac{2\Gamma^{jkl}_{n_i\rho_i,p_j\rho_jq_k\tau_km_l\sigma_l}(z)}{\sqrt{v^j_{g,p_j}v^k_{g,q_k}v^l_{g,m_l}v^i_{g,n_i}}}$$

$$\times A^{(j)}_{p_j\rho_j}A^{(k)*}_{q_k\tau_k}A^{(l)}_{m_l\sigma_l}\Big|_{j\neq k\neq l\neq i}\Bigg\},\ i=1,\ldots,4, \tag{7.29}$$

where $\Delta\bar{\beta}_{n_ip_jq_km_l}=\rho_j\bar{\beta}_{p_j}-\tau_k\bar{\beta}_{q_k}+\sigma_l\bar{\beta}_{m_l}-\rho_i\bar{\beta}_{n_i}$ is the wavevector mismatch.

The coefficients $\vartheta^i_{n_i\rho_i}$ and $\vartheta^i_{n_i\rho_i,m_i\sigma_i}$ represent the wavevector shift of the optical mode (n_i,ρ_i) and the linear coupling constant between modes (n_i,ρ_i) and (m_i,σ_i), induced by the linear perturbations, respectively, $\Gamma^i_{n_i\rho_i,m_i\sigma_i}$ and $\Gamma^i_{n_i\rho_i,m_i\sigma_i p_i\rho_i}$ describe SPM and XPM-induced coupling between modes with the same frequency, $\bar{\omega}_i$, respectively, $\Gamma^{ij}_{n_i\rho_i,m_i\sigma_i p_j\rho_j}$ represents the XPM-induced coupling between modes with frequencies $\bar{\omega}_i$ and $\bar{\omega}_j$, and $\Gamma^{jkl}_{n_i\rho_i,p_j\rho_jq_k\tau_km_l\sigma_l}$ is related to the FWM interaction among the pulses. All these nonlinear coefficients have the meaning of z-dependent effective cubic susceptibilities. The linear and nonlinear coefficients in Eqs. (7.29) are given by the following relations:

$$\vartheta^i_{n_i\rho_i}(z)=\frac{\bar{\omega}_i a}{4\bar{W}^i_{n_i}}\int_S[\delta\varepsilon_{\rm fc}(\mathbf{r})+\delta\varepsilon_{\rm loss}(\mathbf{r})]|\mathbf{e}_{n_i\rho_i}(\bar{\omega}_i)|^2dS, \tag{7.30a}$$

$$\vartheta^i_{n_i\rho_i,m_i\sigma_i}(z)=\frac{\bar{\omega}_i e^{i(\sigma_i\bar{\beta}_{m_i}-\rho_i\bar{\beta}_{n_i})z}}{4\sqrt{\bar{W}^i_{n_i}\bar{W}^i_{m_i}}}$$

$$\times\int_S[\delta\varepsilon_{\rm fc}(\mathbf{r})+\delta\varepsilon_{\rm loss}(\mathbf{r})]\mathbf{e}^*_{n_i\rho_i}(\bar{\omega}_i)\cdot\mathbf{e}_{m_i\sigma_i}(\bar{\omega}_i)dS, \tag{7.30b}$$

$$\Gamma^i_{n_i\rho_i,m_i\sigma_i}(z)=\frac{\varepsilon_0^2a^4e^{i(\sigma_i\bar{\beta}_{m_i}-\rho_i\bar{\beta}_{n_i})z}}{\bar{W}^i_{m_i}\sqrt{\bar{W}^i_{m_i}\bar{W}^i_{n_i}}}\int_S\mathbf{e}^*_{n_i\rho_i}(\bar{\omega}_i)$$

$$\cdot\hat{\chi}^{(3)}(\bar{\omega}_i,-\bar{\omega}_i,\bar{\omega}_i)\vdots\mathbf{e}_{m_i\sigma_i}(\bar{\omega}_i)\mathbf{e}^*_{m_i\sigma_i}(\bar{\omega}_i)\mathbf{e}_{m_i\sigma_i}(\bar{\omega}_i)dS, \tag{7.30c}$$

$$\Gamma^i_{n_i\rho_i,m_i\sigma_ip_i\rho_i}(z)=\frac{\varepsilon_0^2a^4e^{i(\sigma_i\bar{\beta}_{m_i}-\rho_i\bar{\beta}_{n_i})z}}{\bar{W}^i_{p_i}\sqrt{\bar{W}^i_{m_i}\bar{W}^i_{n_i}}}\int_S\mathbf{e}^*_{n_i\rho_i}(\bar{\omega}_i)$$

$$\cdot\,\hat{\chi}^{(3)}(\bar{\omega}_i,-\bar{\omega}_i,\bar{\omega}_i)\vdots\mathbf{e}_{p_i\rho_i}(\bar{\omega}_i)\mathbf{e}^{*}_{p_i\rho_i}(\bar{\omega}_i)\mathbf{e}_{m_i\sigma_i}(\bar{\omega}_i)dS, \tag{7.30d}$$

$$\Gamma^{ij}_{n_i\rho_i,m_i\sigma_i p_j\rho_j}(z)=\frac{\varepsilon_0^2a^4e^{i(\sigma_i\bar{\beta}_{m_i}-\rho_i\bar{\beta}_{n_i})z}}{\bar{W}^j_{p_j}\sqrt{\bar{W}^i_{m_i}\bar{W}^i_{n_i}}}\int_S\mathbf{e}^{*}_{n_i\rho_i}(\bar{\omega}_i)$$

$$\cdot\,\hat{\chi}^{(3)}(\bar{\omega}_j,-\bar{\omega}_j,\bar{\omega}_i)\vdots\mathbf{e}_{p_j\rho_j}(\bar{\omega}_j)\mathbf{e}^{*}_{p_j\rho_j}(\bar{\omega}_j)\mathbf{e}_{m_i\sigma_i}(\bar{\omega}_i)dS, \tag{7.30e}$$

$$\Gamma^{jkl}_{n_i\rho_i,p_j\rho_j q_k\tau_k m_l\sigma_l}(z)=\frac{\varepsilon_0^2a^4}{\sqrt{\bar{W}^j_{p_j}\bar{W}^k_{q_k}\bar{W}^l_{m_l}\bar{W}^i_{n_i}}}\int_S\mathbf{e}^{*}_{n_i\rho_i}(\bar{\omega}_i)$$

$$\cdot\,\hat{\chi}^{(3)}(\bar{\omega}_j,-\bar{\omega}_k,\bar{\omega}_l)\vdots\mathbf{e}_{p_j\rho_j}(\bar{\omega}_j)\mathbf{e}^{*}_{q_k\tau_k}(\bar{\omega}_k)\mathbf{e}_{m_l\sigma_l}(\bar{\omega}_l)dS. \tag{7.30f}$$

While Eqs. (7.29) seem complicated, in cases of practical interest they can be considerably simplified. To be more specific, these equations describe a multitude of optical effects pertaining to both linear and nonlinear gratings, including linear coupling between modes with the same frequency, nonlinear coupling between modes with the same frequency, due to SPM and XPM effects, XPM-induced coupling between modes with different frequency, and FWM interactions. In most experimental set-ups, however, not all these linear and nonlinear effects occur simultaneously as in a generic case not all of them lead to efficient pulse interactions.

These ideas becomes clear if one inspects the exponential factors in Eqs. (7.30b)-(7.30e). Thus, they vary over a characteristic length comparable to the lattice constant of the PhC, namely much more rapidly as compared to the spatial variation rate of the pulse envelopes. As a result, except for the mode (n_i,ρ_i), these linear and nonlinear coefficients cancel. There are, however, particular cases when some of these interactions are phase-matched and consequently are resonantly enhanced. To be more specific, the integrals in Eqs. (7.30b)-(7.30e) are periodic functions of z, with period a, so that it is possible that a Fourier component of these integrals phase-matches a specific linear or nonlinear interaction between modes (e.g., the linear coupling between two modes with the same frequency and SPM- or XPM-induced nonlinear coupling between modes). In this study, we do not consider such accidental phase-matching of mode interactions. With this in mind, we discard all terms in Eqs. (7.29) that average to zero to obtain the final form of the coupled-mode equations for the pulse envelopes:

$$i\left[\rho_i\frac{\partial A^{(i)}_{n_i\rho_i}}{\partial z}+\frac{\delta^i_{n_i}(z)}{v^i_{g,n_i}}\frac{\partial A^{(i)}_{n_i\rho_i}}{\partial t}\right]-\frac{\delta^i_{n_i}(z)\bar{\beta}_{2,n_i}}{2}\frac{\partial^2A^{(i)}_{n_i\rho_i}}{\partial t^2}+\frac{\bar{\omega}_i\delta n_{\mathrm{fc}}\bar{\kappa}^i_{n_i}(z)}{nv^i_{g,n_i}}A^{(i)}_{n_i\rho_i}$$

$$+\frac{ic\bar{\kappa}^i_{n_i}(z)}{2nv^i_{g,n_i}}(\alpha_{\rm fc}+\alpha_{\rm in})A^{(i)}_{n_i\rho_i}+\gamma^i_{n_i\rho_i}(z)|A^{(i)}_{n_i\rho_i}|^2A^{(i)}_{n_i\rho_i}+\sum_{\substack{(p_i\rho_i)\neq(n_i\rho_i)\\ p_i>n_i}}2\gamma^i_{n_i\rho_i,p_i\rho_i}(z)$$

$$\times|A^{(i)}_{p_i\rho_i}|^2A^{(i)}_{n_i\rho_i}+\sum_{\substack{j=1\\ j\neq i}}^{4}\sum_{p_j\rho_j}2\gamma^{ij}_{n_i\rho_i,p_j\rho_j}(z)|A^{(j)}_{p_j\rho_j}|^2A^{(i)}_{n_i\rho_i}+\sum_{\substack{p_jq_km_l\\ \rho_j\tau_k\sigma_l}}2e^{i\Delta\bar{\beta}_{n_ip_jq_km_l}z}$$

$$\gamma^{jkl}_{n_i\rho_i,p_j\rho_jq_k\tau_km_l\sigma_l}(z)\times A^{(j)}_{p_j\rho_j}A^{(k)*}_{q_k\tau_k}A^{(l)}_{m_l\sigma_l}\Big|_{j\neq k\neq l\neq i}=0,\ i=1,\ldots,4, \tag{7.31}$$

where the new parameters introduced in this equation are defined as:

$$\bar{\kappa}^i_{n_i}(z)=\frac{\varepsilon_0an^2}{2\bar{W}^i_{n_i}}\int_{S_{\rm nl}}|\mathbf{e}_{n_i\rho_i}(\bar{\omega}_i)|^2dS, \tag{7.32a}$$

$$\gamma^i_{n_i\rho_i}(z)=\frac{3\bar{\omega}_i\varepsilon_0a^2}{16v^{i2}_{g,n_i}}\frac{1}{\bar{W}^{i2}_{n_i}}\int_{S_{\rm nl}}\mathbf{e}^*_{n_i\rho_i}(\bar{\omega}_i)$$
$$\cdot\hat{\chi}^{(3)}(\bar{\omega}_i,-\bar{\omega}_i,\bar{\omega}_i)\vdots\mathbf{e}_{n_i\rho_i}(\bar{\omega}_i)\mathbf{e}^*_{n_i\rho_i}(\bar{\omega}_i)\mathbf{e}_{n_i\rho_i}(\bar{\omega}_i)dS, \tag{7.32b}$$

$$\gamma^i_{n_i\rho_i,p_i\rho_i}(z)=\frac{3\bar{\omega}_i\varepsilon_0a^2}{16v^i_{g,n_i}v^i_{g,p_i}}\frac{1}{\bar{W}^i_{n_i}\bar{W}^i_{p_i}}\int_{S_{\rm nl}}\mathbf{e}^*_{n_i\rho_i}(\bar{\omega}_i)$$
$$\cdot\hat{\chi}^{(3)}(\bar{\omega}_i,-\bar{\omega}_i,\bar{\omega}_i)\vdots\mathbf{e}_{p_i\rho_i}(\bar{\omega}_i)\mathbf{e}^*_{p_i\rho_i}(\bar{\omega}_i)\mathbf{e}_{n_i\rho_i}(\bar{\omega}_i)dS, \tag{7.32c}$$

$$\gamma^{ij}_{n_i\rho_i,p_j\rho_j}(z)=\frac{3\bar{\omega}_i\varepsilon_0a^2}{16v^i_{g,n_i}v^j_{g,p_j}}\frac{1}{\bar{W}^i_{n_i}\bar{W}^j_{p_j}}\int_{S_{\rm nl}}\mathbf{e}^*_{n_i\rho_i}(\bar{\omega}_i)$$
$$\cdot\hat{\chi}^{(3)}(\bar{\omega}_j,-\bar{\omega}_j,\bar{\omega}_i)\vdots\mathbf{e}_{p_j\rho_j}(\bar{\omega}_j)\mathbf{e}^*_{p_j\rho_j}(\bar{\omega}_j)\mathbf{e}_{n_i\rho_i}(\bar{\omega}_i)dS, \tag{7.32d}$$

$$\gamma^{jkl}_{n_i\rho_i,p_j\rho_jq_k\tau_km_l\sigma_l}(z)=\frac{3\bar{\omega}_i\varepsilon_0a^2}{16(v^j_{g,p_j}v^k_{g,q_k}v^l_{g,m_l}v^i_{g,n_i})^{\frac{1}{2}}}$$
$$\frac{1}{(\bar{W}^j_{p_j}\bar{W}^k_{q_k}\bar{W}^l_{m_l}\bar{W}^i_{n_i})^{\frac{1}{2}}}\int_{S_{\rm nl}}\mathbf{e}^*_{n_i\rho_i}(\bar{\omega}_i)\cdot\hat{\chi}^{(3)}(\bar{\omega}_j,-\bar{\omega}_k,\bar{\omega}_l)$$
$$\vdots\mathbf{e}_{p_j\rho_j}(\bar{\omega}_j)\mathbf{e}^*_{q_k\tau_k}(\bar{\omega}_k)\mathbf{e}_{m_l\sigma_l}(\bar{\omega}_l)dS. \tag{7.32e}$$

In these equations, $S_{\rm nl}(z)$ is the transverse surface of the region filled with nonlinear material. Note that the exponential factor in the term describing the FWM does not average to zero because the FWM interaction is assumed to be nearly phase-matched and therefore the exponential factor varies over a characteristic length that is much larger than the lattice constant, a. Importantly, the linear and nonlinear effects in Eq. (7.31) appear as being inverse proportional to the v_g and v_g^2, respectively. In other words, one does not need to rely on any phenomenological considerations to describe

slow-light effects, as they are naturally captured by our model.

7.3.4 Carriers dynamics

The last step in our derivation of the theoretical model describing FWM in Si-PhCWs is to determine the influence of photogenerated FCs on pulse dynamics. To this end, we first find the rate at which electron-hole pairs are generated optically, *via* degenerate and nondegenerate TPA, and as a result of FWM. More specifically, we first multiply Eqs. (7.29), after all linear terms have been discarded, by $A^{(i)*}_{n_i\rho_i}$, then multiply the complex conjugate of Eqs. (7.29) by $A^{(i)}_{n_i\rho_i}$, and sum the results over all carrier frequencies and modes. The outcome of these simple manipulations can be cast as:

$$\frac{\partial}{\partial z}\sum_{i=1}^{4}\sum_{n_i\rho_i}\rho_i|A^{(i)}_{n_i\rho_i}|^2=-\frac{3}{8\varepsilon_0 a^2}\sum_{i=1}^{4}\sum_{n_i\rho_i}\bar{\omega}_i\times\Im\mathfrak{m}\Bigg\{\sum_{m_i\sigma_i}\Bigg[\frac{\Gamma^{i}_{n_i\rho_i,m_i\sigma_i}(z)}{v^{i}_{g,m_i}\sqrt{v^{i}_{g,m_i}v^{i}_{g,n_i}}}|A^{(i)}_{m_i\sigma_i}|^2A^{(i)}_{m_i\sigma_i}A^{(i)*}_{n_i\rho_i}$$
$$+\sum_{\substack{(p_i\rho_i)\neq(m_i\sigma_i)\\ p_i>m_i}}\frac{2\Gamma^{i}_{n_i\rho_i,m_i\sigma_i p_i\rho_i}(z)}{v^{i}_{g,p_i}\sqrt{v^{i}_{g,m_i}v^{i}_{g,n_i}}}|A^{(i)}_{p_i\rho_i}|^2A^{(i)}_{m_i\sigma_i}A^{(i)*}_{n_i\rho_i}+\sum_{\substack{j=1\\ j\neq i}}^{4}\sum_{p_j\rho_j}\frac{2\Gamma^{ij}_{n_i\rho_i,m_i\sigma_i p_j\rho_j}(z)}{v^{j}_{g,p_j}\sqrt{v^{i}_{g,m_i}v^{i}_{g,n_i}}}$$
$$|A^{(j)}_{p_j\rho_j}|^2A^{(i)}_{m_i\sigma_i}A^{(i)*}_{n_i\rho_i}\Bigg]+\sum_{\substack{p_jq_km_l\\ \rho_j\tau_k\sigma_l}}e^{i\Delta\bar{\beta}_{n_ip_jq_km_l}z}\frac{2\Gamma^{jkl}_{n_i\rho_i,p_j\rho_jq_k\tau_km_l\sigma_l}(z)}{\sqrt{v^{j}_{g,p_j}v^{k}_{g,q_k}v^{l}_{g,m_l}v^{i}_{g,n_i}}}$$
$$\times A^{(j)}_{p_j\rho_j}A^{(k)*}_{q_k\tau_k}A^{(l)}_{m_l\sigma_l}A^{(i)*}_{n_i\rho_i}\Big|_{j\neq k\neq l\neq i}\Bigg\}. \tag{7.33}$$

The sum in the l.h.s. of this equation represents the rate at which optical power is transferred to FCs. This power is absorbed by carriers generated in the silicon slab, in the infinitesimal volume $dV(z)=A_{\rm nl}(z)dz$, where $A_{\rm nl}(z)$ is an effective area. This area is defined in terms of the Poynting vector of the field propagating inside the silicon slab,

$$A_{\rm nl}(z)=\frac{\left[\int_{S_{\rm nl}}|\langle\mathbf{E}(\mathbf{r},t)\times\mathbf{H}(\mathbf{r},t)\rangle_t|dS\right]^2}{\int_{S_{\rm nl}}|\langle\mathbf{E}(\mathbf{r},t)\times\mathbf{H}(\mathbf{r},t)\rangle_t|^2dS}. \tag{7.34}$$

In this equation, $\langle f\rangle_t$ means the time average of f. Using Eq. (7.20), and taking into account the fact that $A^{(i)}_{n_i\rho_i}$ varies in time much slower than $e^{-i\bar{\omega}_it}$, one can express

Eq. (7.34) in the following form:

$$A_{\mathrm{nl}}(z)=\frac{\left[\int_{S_{\mathrm{nl}}}\left|\sum_{i=1}^{4}\sum_{n_i\rho_i}\frac{|A^{(i)}_{n_i\rho_i}|^2}{\bar{P}_{n_i}}\mathfrak{Re}(\mathbf{e}_{n_i\rho_i}\times\mathbf{h}^*_{n_i\rho_i})\right|dS\right]^2}{\int_{S_{\mathrm{nl}}}\left|\sum_{i=1}^{4}\sum_{n_i\rho_i}\frac{|A^{(i)}_{n_i\rho_i}|^2}{\bar{P}_{n_i}}\mathfrak{Re}(\mathbf{e}_{n_i\rho_i}\times\mathbf{h}^*_{n_i\rho_i})\right|^2dS}. \tag{7.35}$$

In spite of the fact that it might seem difficult to use this formula to calculate the effective area, we will show in the next section that in cases of practical interest it can be simplified considerably. We also stress that Eq. (7.35) gives the effective transverse area of the region in which FCs are generated, so that it should not be confused with the modal effective area. In fact, since in the FWM process there are several co-propagating beams, a single effective modal area is not well defined.

The energy transferred to FCs when an electron-hole pair is generated *via* absorption of two photons with frequencies $\bar{\omega}_i$ and $\bar{\omega}_j$ is equal to $\hbar(\bar{\omega}_i+\bar{\omega}_j)$. Using this result and neglecting again all terms in Eq. (7.33) that average to zero, it can be easily shown that the carriers dynamics are governed by the following rate equation:

$$\begin{aligned}\frac{\partial N}{\partial t}=&-\frac{N}{\tau_c}+\frac{1}{\hbar A_{\mathrm{nl}}(z)}\sum_{i=1}^{4}\sum_{n_i\rho_i}\left\{\frac{\gamma''^{i}_{n_i\rho_i}(z)}{\bar{\omega}_i}|A^{(i)}_{n_i\rho_i}|^4+\sum_{\substack{(p_i\rho_i)\neq(n_i\rho_i)\\ p_i>n_i}}\frac{2\gamma''^{i}_{n_i\rho_i,p_i\rho_i}(z)}{\bar{\omega}_i}|A^{(i)}_{p_i\rho_i}|^2|A^{(i)}_{n_i\rho_i}|^2\right.\\
&+\sum_{\substack{j=1\\ j\neq i}}^{4}\sum_{p_j\rho_j}\frac{4\gamma''^{ij}_{n_i\rho_i,p_j\rho_j}(z)}{\bar{\omega}_i+\bar{\omega}_j}|A^{(j)}_{p_j\rho_j}|^2|A^{(i)}_{n_i\rho_i}|^2+\sum_{\substack{p_jq_km_l\\ \rho_j\tau_k\sigma_l}}\mathfrak{Im}\left[e^{i\Delta\bar{\beta}_{n_ip_jq_km_l}z}\frac{4\gamma^{jkl}_{n_i\rho_i,p_j\rho_jq_k\tau_km_l\sigma_l}(z)}{\bar{\omega}_i+\bar{\omega}_k}\right.\\
&\left.\left.\times A^{(j)}_{p_j\rho_j}A^{(k)*}_{q_k\tau_k}A^{(l)}_{m_l\sigma_l}A^{(i)*}_{n_i\rho_i}\right|_{j\neq k\neq l\neq i}\right]\right\},\end{aligned} \tag{7.36}$$

where $\tau_c\approx 500\,\mathrm{ps}$ [7. 77] is the FC recombination time in Si-PhCWs and ζ' (ζ'') means the real (imaginary) part of the complex number, ζ.

7.4 Degenerate four-wave mixing

The system of coupled nonlinear partial differential equations, Eqs. (7.31) and Eq. (7.36), fully describes the FWM of optical pulses and FCs dynamics and represents the main result derived in this study. In practical experimental set-ups, however, the most used pulse configuration is that of degenerate FWM. In this particular case, the

optical frequencies of the two pump pulses are the same, $\bar{\omega}_1 = \bar{\omega}_2 \equiv \omega_p$, whereas the two generated pulses, the signal and the idler, have frequencies $\bar{\omega}_3 \equiv \omega_s$ and $\bar{\omega}_4 \equiv \omega_i$, respectively. Moreover, we assume that all modes are forward-propagating modes and that at each carrier frequency there is only one guided mode in which the optical pulses that enter in the FWM process can propagate – others, should they exist, would not be phase-matched – so that we set $N_i = 1$, $i = 1,\ldots,4$. Under these circumstances, Eqs. (7.31) and Eq. (7.36) can be simplified to:

$$
\begin{aligned}
&i\left[\frac{\partial A_p}{\partial z} + \frac{\delta_p(z)}{v_{g,p}}\frac{\partial A_p}{\partial t}\right] - \frac{\delta_p(z)\bar{\beta}_{2,p}}{2}\frac{\partial^2 A_p}{\partial t^2} + \frac{\omega_p \delta n_{\mathrm{fc}}\bar{\kappa}_p(z)}{n v_{g,p}}A_p + \frac{ic\bar{\kappa}_p(z)}{2nv_{g,p}}(\alpha_{\mathrm{fc}}+\alpha_{\mathrm{in}})A_p \\
&+ \left[\gamma_p(z)|A_p|^2 + 2\gamma_{ps}(z)|A_s|^2 + 2\gamma_{pi}(z)|A_i|^2\right]A_p + 2e^{i\Delta\bar{\beta}z}\gamma_{psi}(z)A_sA_iA_p^* = 0, \quad (7.37a)\\
&i\left[\frac{\partial A_s}{\partial z} + \frac{\delta_s(z)}{v_{g,s}}\frac{\partial A_s}{\partial t}\right] - \frac{\delta_s(z)\bar{\beta}_{2,s}}{2}\frac{\partial^2 A_s}{\partial t^2} + \frac{\omega_s \delta n_{\mathrm{fc}}\bar{\kappa}_s(z)}{n v_{g,s}}A_s + \frac{ic\bar{\kappa}_s(z)}{2nv_{g,s}}(\alpha_{\mathrm{fc}}+\alpha_{\mathrm{in}})A_s \\
&+ \left[\gamma_s(z)|A_s|^2 + 2\gamma_{sp}(z)|A_p|^2 + 2\gamma_{si}(z)|A_i|^2\right]A_s + e^{-i\Delta\bar{\beta}z}\gamma_{spi}(z)A_p^2A_i^* = 0, \quad (7.37b)\\
&i\left[\frac{\partial A_i}{\partial z} + \frac{\delta_i(z)}{v_{g,i}}\frac{\partial A_i}{\partial t}\right] - \frac{\delta_i(z)\bar{\beta}_{2,i}}{2}\frac{\partial^2 A_i}{\partial t^2} + \frac{\omega_i \delta n_{\mathrm{fc}}\bar{\kappa}_i(z)}{n v_{g,i}}A_i + \frac{ic\bar{\kappa}_i(z)}{2nv_{g,i}}(\alpha_{\mathrm{fc}}+\alpha_{\mathrm{in}})A_i \\
&+ \left[\gamma_i(z)|A_i|^2 + 2\gamma_{ip}(z)|A_p|^2 + 2\gamma_{is}(z)|A_s|^2\right]A_i + e^{-i\Delta\bar{\beta}z}\gamma_{ips}(z)A_p^2A_s^* = 0, \quad (7.37c)
\end{aligned}
$$

$$
\begin{aligned}
\frac{\partial N}{\partial t} = &-\frac{N}{\tau_c} + \frac{1}{\hbar A_{\mathrm{nl}}(z)}\Bigg\{\sum_{\mu=p,s,i}\left[\frac{\gamma''_\mu(z)}{\omega_\mu}|A_\mu|^4 + \sum_{\substack{\nu=p,s,i\\ \nu\neq\mu}}\frac{4\gamma''_{\mu\nu}(z)}{\omega_\mu+\omega_\nu}|A_\mu|^2|A_\nu|^2\right] \\
&+ \frac{1}{\omega_p}\Im\mathfrak{m}\left[2\gamma_{psi}(z)\times A_p^{*2}A_sA_ie^{i\Delta\bar{\beta}z} + [\gamma_{spi}(z)+\gamma_{ips}(z)]A_p^2A_s^*A_i^*e^{-i\Delta\bar{\beta}z}\right]\Bigg\}, \quad (7.38)
\end{aligned}
$$

where $\Delta\bar{\beta} = \beta_s + \beta_i - 2\beta_p$. The coefficients of the linear and nonlinear terms in Eqs. (7.37) and Eq. (7.38) are:

$$
\begin{aligned}
\bar{\kappa}_\mu(z) &= \frac{\varepsilon_0 a n^2}{2\bar{W}_\mu}\int_{S_{\mathrm{nl}}}|\mathbf{e}_\mu(\omega_\mu)|^2 dS, \quad (7.39a)\\
\gamma_\mu(z) &= \frac{3\omega_\mu\varepsilon_0 a^2}{16v_{g,\mu}^2}\frac{1}{\bar{W}_\mu^2}\int_{S_{\mathrm{nl}}}\mathbf{e}_\mu^*(\omega_\mu) \\
&\quad\cdot\hat{\chi}^{(3)}(\omega_\mu,-\omega_\mu,\omega_\mu)\vdots\mathbf{e}_\mu(\omega_\mu)\mathbf{e}_\mu^*(\omega_\mu)\mathbf{e}_\mu(\omega_\mu)dS, \quad (7.39b)\\
\gamma_{\mu\nu}(z) &= \frac{3\omega_\mu\varepsilon_0 a^2}{16v_{g,\mu}v_{g,\nu}}\frac{1}{\bar{W}_\mu\bar{W}_\nu}\int_{S_{\mathrm{nl}}}\mathbf{e}_\mu^*(\omega_\mu) \\
&\quad\cdot\hat{\chi}^{(3)}(\omega_\nu,-\omega_\nu,\omega_\mu)\vdots\mathbf{e}_\nu(\omega_\nu)\mathbf{e}_\nu^*(\omega_\nu)\mathbf{e}_\mu(\omega_\mu)dS, \quad (7.39c)
\end{aligned}
$$

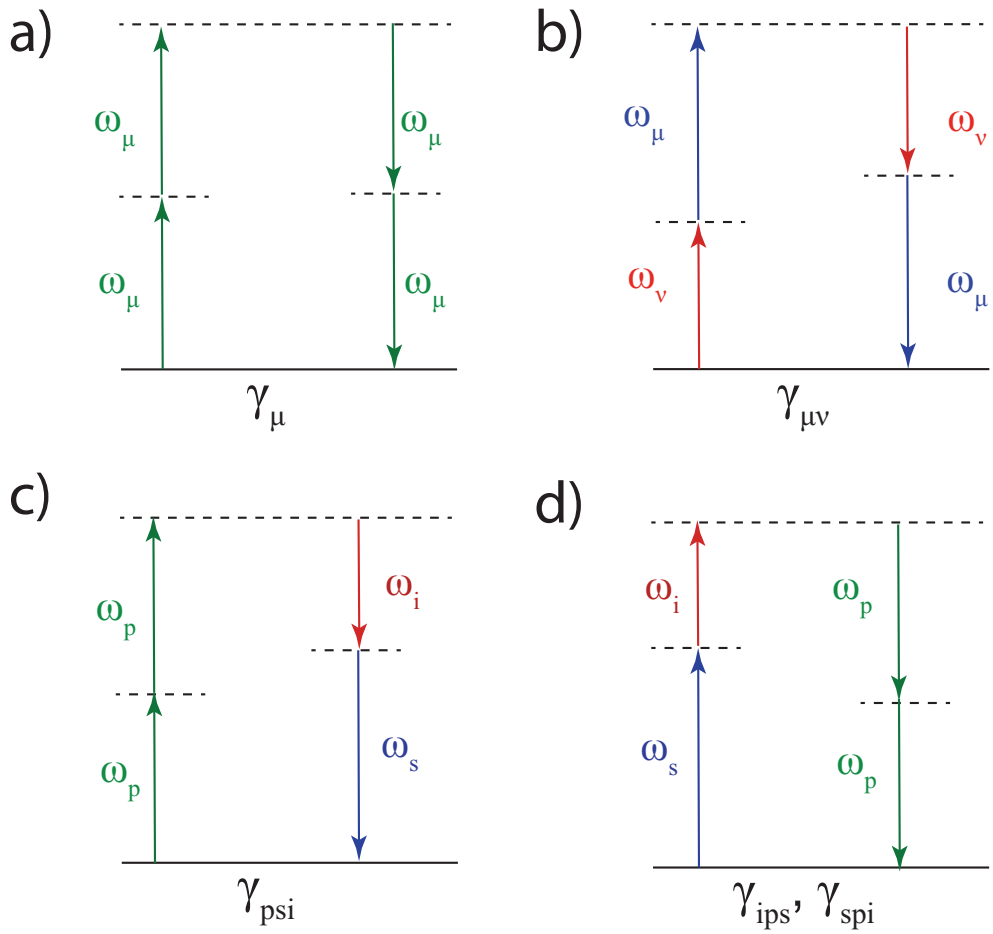

Figure 7.4: Energy diagrams representing the nonlinear optical processes included in Eqs. (7.37). (a) SPM and degenerate TPA corresponding to γ'_{μ} and γ''_{μ}, respectively. (b) XPM and XAM corresponding to $\gamma'_{\mu\nu}$ and $\gamma''_{\mu\nu}$, respectively. Two possible ways of energy transfer that can occur during a degenerate FWM process: (c) two pump photons generate a signal and an idler photon, a process described by γ_{psi}; (d) the reverse process, described by γ_{ips} and γ_{spi}, in which a signal and an idler photon generate two pump photons.

$$\gamma_{psi}(z) = \frac{3\omega_p \varepsilon_0 a^2}{16 v_{g,p} (v_{g,s} v_{g,i})^{\frac{1}{2}}} \frac{1}{\bar{W}_p (\bar{W}_s \bar{W}_i)^{\frac{1}{2}}}$$
$$\times \int_{S_{\mathrm{nl}}} \mathbf{e}_p^*(\omega_p) \cdot \hat{\chi}^{(3)}(\omega_s, -\omega_p, \omega_i) \vdots \mathbf{e}_s(\omega_s) \mathbf{e}_p^*(\omega_p) \mathbf{e}_i(\omega_i) dS, \tag{7.39d}$$

$$\gamma_{spi}(z) = \frac{3\omega_s \varepsilon_0 a^2}{16 v_{g,p} (v_{g,s} v_{g,i})^{\frac{1}{2}}} \frac{1}{\bar{W}_p (\bar{W}_s \bar{W}_i)^{\frac{1}{2}}}$$
$$\times \int_{S_{\mathrm{nl}}} \mathbf{e}_s^*(\omega_s) \cdot \hat{\chi}^{(3)}(\omega_p, -\omega_i, \omega_p) \vdots \mathbf{e}_p(\omega_p) \mathbf{e}_i^*(\omega_i) \mathbf{e}_p(\omega_p) dS, \tag{7.39e}$$

$$\gamma_{ips}(z) = \frac{3\omega_i \varepsilon_0 a^2}{16 v_{g,p} (v_{g,s} v_{g,i})^{\frac{1}{2}}} \frac{1}{\bar{W}_p (\bar{W}_s \bar{W}_i)^{\frac{1}{2}}}$$
$$\times \int_{S_{\mathrm{nl}}} \mathbf{e}_i^*(\omega_i) \cdot \hat{\chi}^{(3)}(\omega_p, -\omega_s, \omega_p) \vdots \mathbf{e}_p(\omega_p) \mathbf{e}_s^*(\omega_s) \mathbf{e}_p(\omega_p) dS, \tag{7.39f}$$

where μ and $\nu \neq \mu$ take one of the values p, s, and i and the frequency degeneracy at the pump frequency has been taken into account.

Note that, as expected, when the nonlinear coefficients γ's are real quantities, namely when nonlinear optical absorption effects can be neglected, the optical pumping term in Eq. (7.38) vanishes. More specifically, if the frequencies of the interacting waves are far from the transition frequencies of the medium, a condition that is satisfied in our case, the time-reversal and overall permutation symmetry properties of the nonlinear susceptibility hold [7. 74], so that one can easily demonstrate that:

$$\gamma^{*}_{psi}(z) = \gamma_{spi}(z) = \gamma_{ips}(z). \tag{7.40}$$

This relation, which can be proven to be equivalent to the Manley-Rowe relations associated to the FWM process, shows that in these circumstances the FWM interaction does not contribute to generation of FCs and consequently the last term in Eq. (7.38) can be dropped.

Moreover, since in experiments usually $P_p \gg P_s, P_i$, the effective area given by Eq. (7.35) can be reduced to the following simplified form:

$$A_{\mathrm{nl}}(z) = \frac{\left(\int_{S_{\mathrm{nl}}} \left| \mathfrak{Re}\left[\mathbf{e}_p(\omega_p) \times \mathbf{h}^{*}_p(\omega_p) \right] \right| dS \right)^2}{\int_{S_{\mathrm{nl}}} \left| \mathfrak{Re}\left[\mathbf{e}_p(\omega_p) \times \mathbf{h}^{*}_p(\omega_p) \right] \right|^2 dS}. \tag{7.41}$$

The types of nonlinear interactions incorporated in our theoretical model described by Eqs. (7.37) are summarized in Fig. 7.4 *via* the energy diagrams defined by the frequencies of the specific pairs of interacting photons. Thus, as per Fig. 7.4(a), the terms proportional to the γ'_μ and γ''_μ coefficients describe SPM and degenerate TPA effects, respectively, whereas Fig. 7.4(b) illustrates XPM and XAM (also called nondegenerate TPA) interactions whose strength is proportional to $\gamma'_{\mu\nu}$ and $\gamma''_{\mu\nu}$, respectively. Finally, there are two distinct types of FWM processes, represented in Fig. 7.4(c) and Fig. 7.4(d). In the first case two pump photons combine and generate a pair of photons, one at the signal frequency and the other one at the idler, a process described by the term proportional to γ_{psi}. The reverse process, represented by the γ_{ips} and γ_{spi} terms, corresponds to the case in which a signal and an idler photon combine to generate a

pair of photons at the pump frequency.

As Eqs. (7.39) show, the linear and nonlinear optical coefficients of the waveguide depend on the index of refraction of silicon, both explicitly and implicitly *via* the optical modes of the waveguide. In our calculations the implicit modal frequency dispersion is not taken into account because it cannot be incorporated in the PWE method used to compute the modes. On the other hand, the explicit material dispersion is accounted for *via* the following Sellmeier equation describing the frequency dependence of the index of refraction of silicon [7. 78]:

$$n^2(\lambda) = \varepsilon + \frac{A}{\lambda^2} + \frac{B\lambda_1^2}{\lambda_1^2 - \lambda^2}, \tag{7.42}$$

where $\lambda_1 = 1.1071\,\mu\text{m}$, $\varepsilon = 11.6858$, $A = 0.939816\,\mu\text{m}^2$, and $B = 8.10461 \times 10^{-3}$.

The system of coupled equations, Eqs. (7.37) and Eq. (7.38), form the basis for our analysis of degenerate FWM in silicon PhC waveguides. In our simulations, based on numerical integration of this system of equations using a standard split-step Fourier method combined with a fifth-order Runge-Kutta method for the integration of the linear, carriers dependent terms, the z-dependence of the coefficients in these equations is rigorously taken into account. However, one can significantly decrease the simulation time by averaging these fast-varying coefficients over a lattice constant, as this way the integration step for the resulting, averaged system can be increased considerably. The derivation of this averaged model is presented in the Appendix-B.

One of the key differences between our theoretical description of FWM processes in Si-PhCWs and the widely used models for FWM in waveguides with uniform cross-section, such as optical fibres or silicon photonic wires, is that the linear and nonlinear waveguide coefficients are periodic functions of the distance along the waveguide. In what follows, we discuss this feature of the FWM in more detail, starting with the effective area, A_{nl}, defined by Eq. (7.41). The dependence of this area on the longitudinal distance, z, is presented in Fig. 7.5(a), where z spans the length of a unit cell. As we have discussed, a physical characteristic of slow-light modes is their increased spatial extent. This property is clearly illustrated in Fig. 7.5(a), which shows that in the case of the even and odd modes the effective area increases by almost a factor of two when the group index varies from 14 to 120 and from 8.6 to 65, respectively. This property

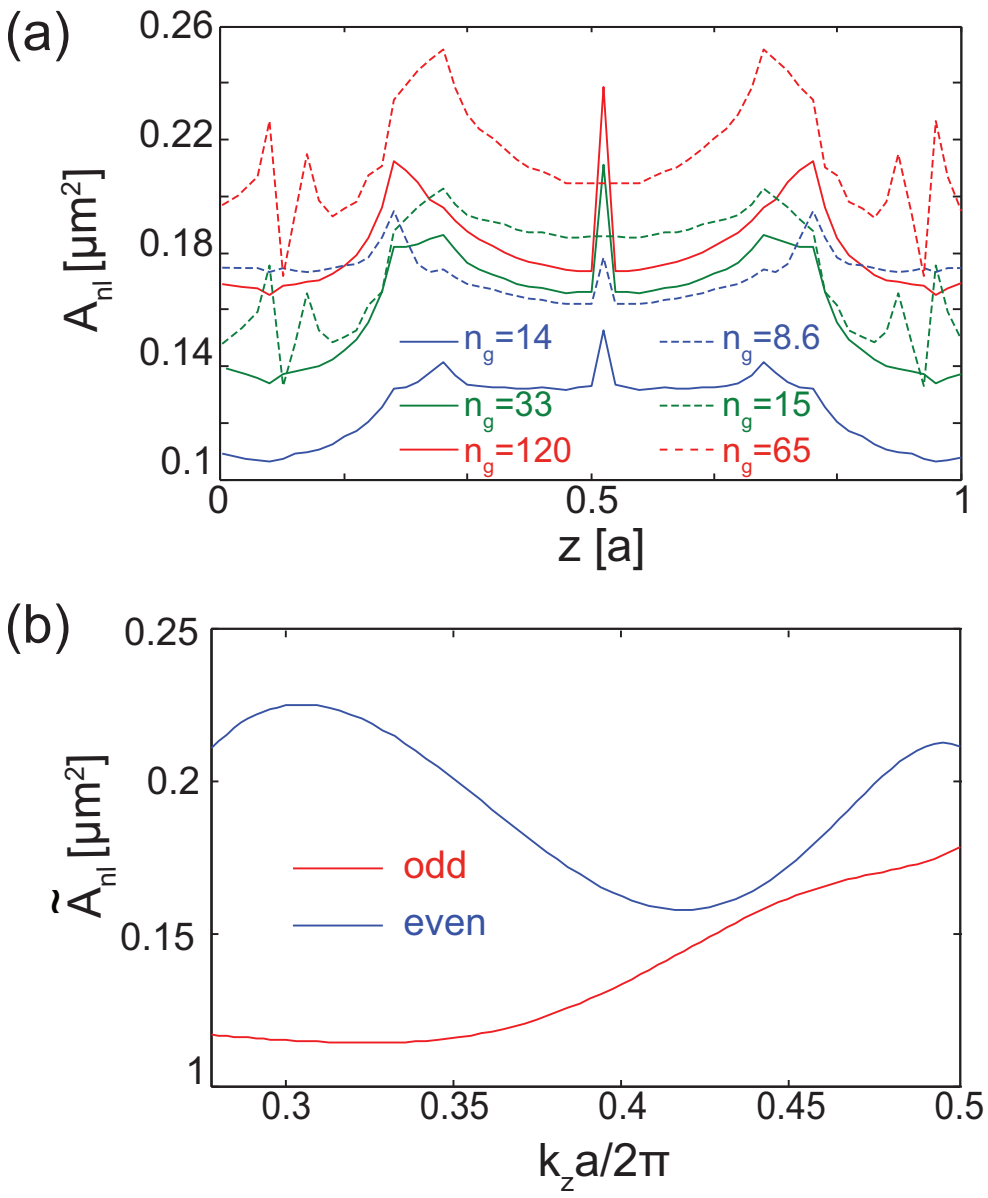

Figure 7.5: (a) Dependence of A_{nl} on z, determined for the odd (solid line) and even (dashed line) modes for several values of the group-index, n_g. (b) Frequency dispersion of $\tilde{A}_{\mathrm{nl}}$ calculated for the two modes, in the spectral domain where they are guiding modes.

is also illustrated by the frequency dispersion of the effective area, averaged over a unit cell, as per Fig. 7.5(b). Thus, it can be seen in this figure that the effective area has a maximum at $k_z \approx 0.3(2\pi/a)$ for the even mode and at the edge of the Brillouin zone for both modes, namely in the regions of slow light indeed.

The z-dependence of the spatial mode overlap, κ, and the frequency dispersion of its spatial average over a unit cell, $\tilde{\kappa}$, are plotted in Figs. 7.6(a) and 7.6(b), respectively. These figures show that the mode overlap varies more strongly with z in the case of the

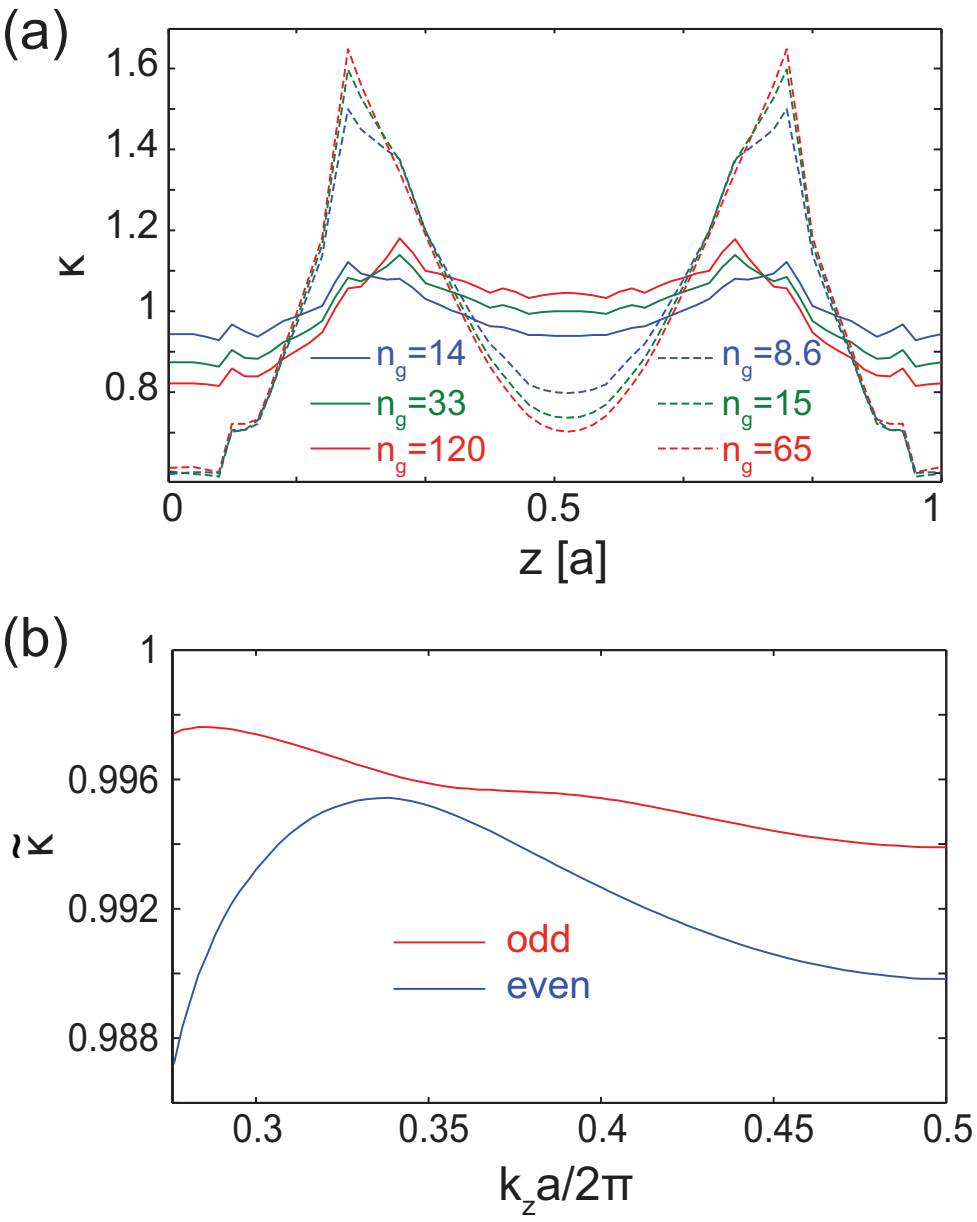

Figure 7.6: (a) Dependence of κ on z, determined for the odd (solid line) and even (dashed line) modes for several values of the group-index, n_g. (b) Frequency dispersion of $\tilde{\kappa}$ calculated for the two modes, in the spectral domain where they are guiding modes.

even mode, whereas in both cases the mode overlap variation increases as the group-index, n_g, increases. Interestingly enough, the averaged overlap coefficient of the even mode has a maximum at $k_z \approx 0.3(2\pi/a)$, i.e. $\lambda \approx 1.52\,\mu$m, which coincides with a minimum of its v_g. Note also that whereas $\kappa(z)$ can be larger than unity within the unit cell, its average, $\tilde{\kappa} < 1$. This result is expected because $\tilde{\kappa}$ quantifies the mode overlap with the slab waveguide.

In Fig. 7.7 we present the dependence on z of another physical quantity that char-

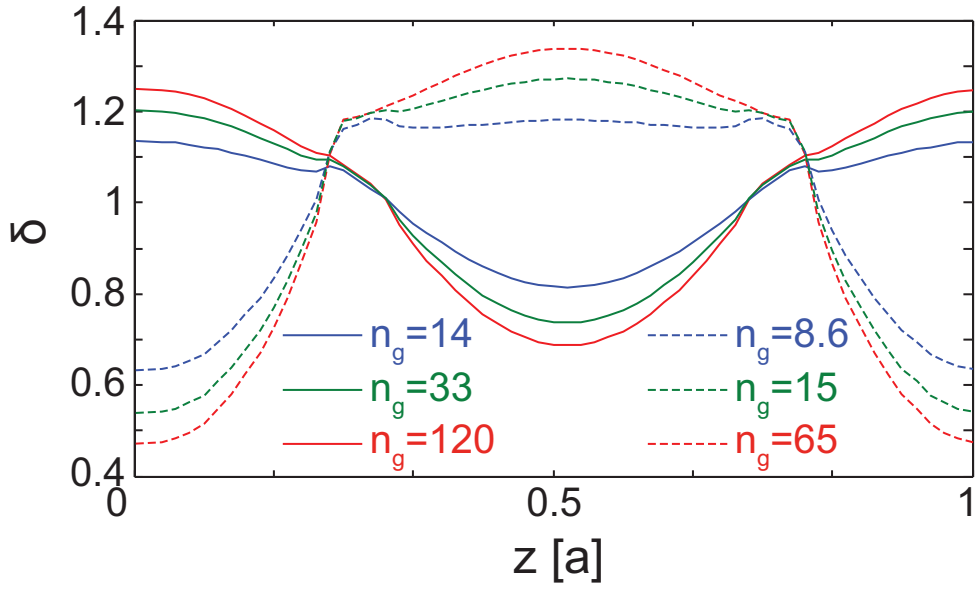

Figure 7.7: Dependence of δ on z, determined for several values of n_g. Solid and dashed lines correspond to the odd and even mode, respectively.

acterizes the linear optical properties of the PhC waveguide, namely its dispersive properties. This parameter, δ, quantifies the extent to which the z-dependent dispersion coefficients differ from their averaged values. Similarly to the mode overlap coefficient κ, $\delta(z)$ shows a more substantial changes with z in the case of the even mode as compared to the odd one and an increase of the amplitude of these oscillations with the increase of n_g. Moreover, as it has been demonstrated in the preceding section, the average of $\delta(z)$ over a unit cell is equal to unity.

The z-dependence of the nonlinear waveguide coefficient that characterizes the strength of SPM and TPA effects and the wavelength dependence of its average over a unit cell are plotted in the top and bottom panels of Fig. 7.8, respectively. One relevant result illustrated by these plots is that the nonlinear waveguide coefficient increases considerably as the GV of the optical mode is tuned to the slow-light regime. Indeed, for the case presented in Figs. 7.8(a) and 7.8(b) the group-index of the odd and even modes are $n_g = 6.4$ and $n_g = 11.5$, respectively. This phenomenon is better illustrated by the wavelength dependence of the spatially averaged values of $\gamma'(z)$ and $\gamma''(z)$, which are shown in Figs. 7.8(c) and 7.8(d), respectively. Thus, these plots indicate that the nonlinear waveguide coefficient increases by more than an order of magnitude as the wavelength is tuned from the fast-light to the slow-light regime, the nonlinear interactions being enhanced correspondingly.

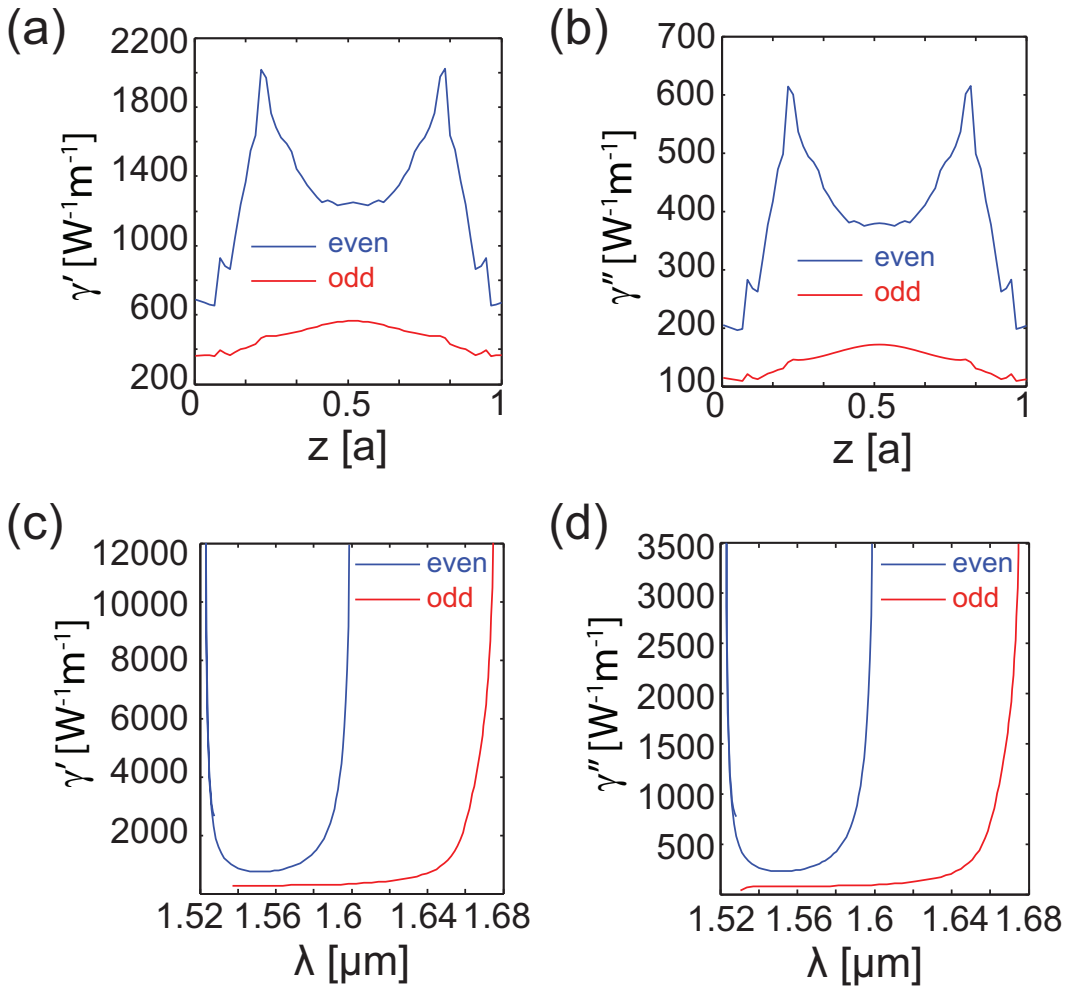

Figure 7.8: (a), (b) Dependence of γ' and γ'' on z, respectively, determined for $k_z = 0.35(2\pi/a)$. (c), (d) Frequency dispersion of spatially averaged values of $\gamma'(z)$ and $\gamma''(z)$, respectively, determined both for the even and odd modes.

7.5 Phase-matching condition

Before we use the theoretical model we developed to investigate the properties of FWM in Si-PhCWs, we derive and discuss the conditions in which optimum nonlinear pulse interaction can be achieved. In particular, efficient FWM is achieved when the interacting pulses are phase-matched, namely when the total (linear plus nonlinear) wavevector mismatch is equal to zero. In the most general case this phase-matching condition depends in an intricate way on the peak power of the pump, P_p, signal, P_s, and idler, P_i, as well as on the linear and nonlinear coefficients of the waveguide [7. 79]. This complicated relation takes a very simple form when one considers an experimental set-up most used in practice, namely when the pump is much stronger than the signal and idler, $P_p \gg P_s, P_i$. Under these circumstances, the phase-matching condition can be expressed

as:

$$2\gamma_p' P_p - 2\beta_p + \beta_s + \beta_i = 0. \tag{7.43}$$

In order to determine the corresponding wavelengths of the optical pulses, this relation must be used in conjunction with the energy conservation relation, that is $2\omega_p = \omega_s + \omega_i$.

An alternative phase-matching condition, less accurate but easier to use in practice, can be derived by expanding the propagation constants, $\beta_{s,i}(\omega)$, in Taylor series around the pump frequency, ω_p:

$$\beta_{s,i}(\omega) = \sum_{n\geq 0} \frac{(\omega-\omega_p)^n}{n!} \left.\frac{d^n\beta_{s,i}}{d\omega^n}\right|_{\omega=\omega_p}. \tag{7.44}$$

Inserting these expressions in Eq. (7.43) and neglecting all terms beyond the fourth-order, one arrives to the following relation:

$$2\gamma_p' P_p + \beta_{2p}(\Delta\omega)^2 + \frac{1}{12}\beta_{4p}(\Delta\omega)^4 = 0, \tag{7.45}$$

where $\Delta\omega \equiv |\omega_p - \omega_s| = |\omega_p - \omega_i|$.

The wavelength diagrams presented in Figs. 7.9(a) and 7.9(b) display the triplets of wavelengths for which the phase-matching conditions expressed by Eq. (7.43) and Eq. (7.45), respectively, are satisfied. These wavelength diagrams were calculated only for the even mode because only this mode possesses spectral regions with anomalous dispersion [cf. Fig. 7.3(b)], which is a prerequisite condition for phase-matching the FWM. More specifically, efficient FWM can be achieved if the pump wavelength ranges from $\lambda_p = 1.52\,\mu\text{m}$ to $1.56\,\mu\text{m}$. Moreover, the diagrams in Fig. 7.9 show that the predictions based on Eq. (7.43) and Eq. (7.45) are in good agreement, especially when $\Delta\omega$ is small. They start to agree less as $\Delta\omega$ increases because the contribution of the terms discarded when the series expansion of $\beta_{s,i}(\omega)$ is truncated increases as $\Delta\omega$ increases.

Figure 7.9 also suggests that the spectral domain in which efficient FWM is achieved depends on the pump power, P_p. To be more specific, it can be seen that for $P_p \lesssim 0.7\,\text{W}$, a spectral gap opens where the phase-matching condition cannot be

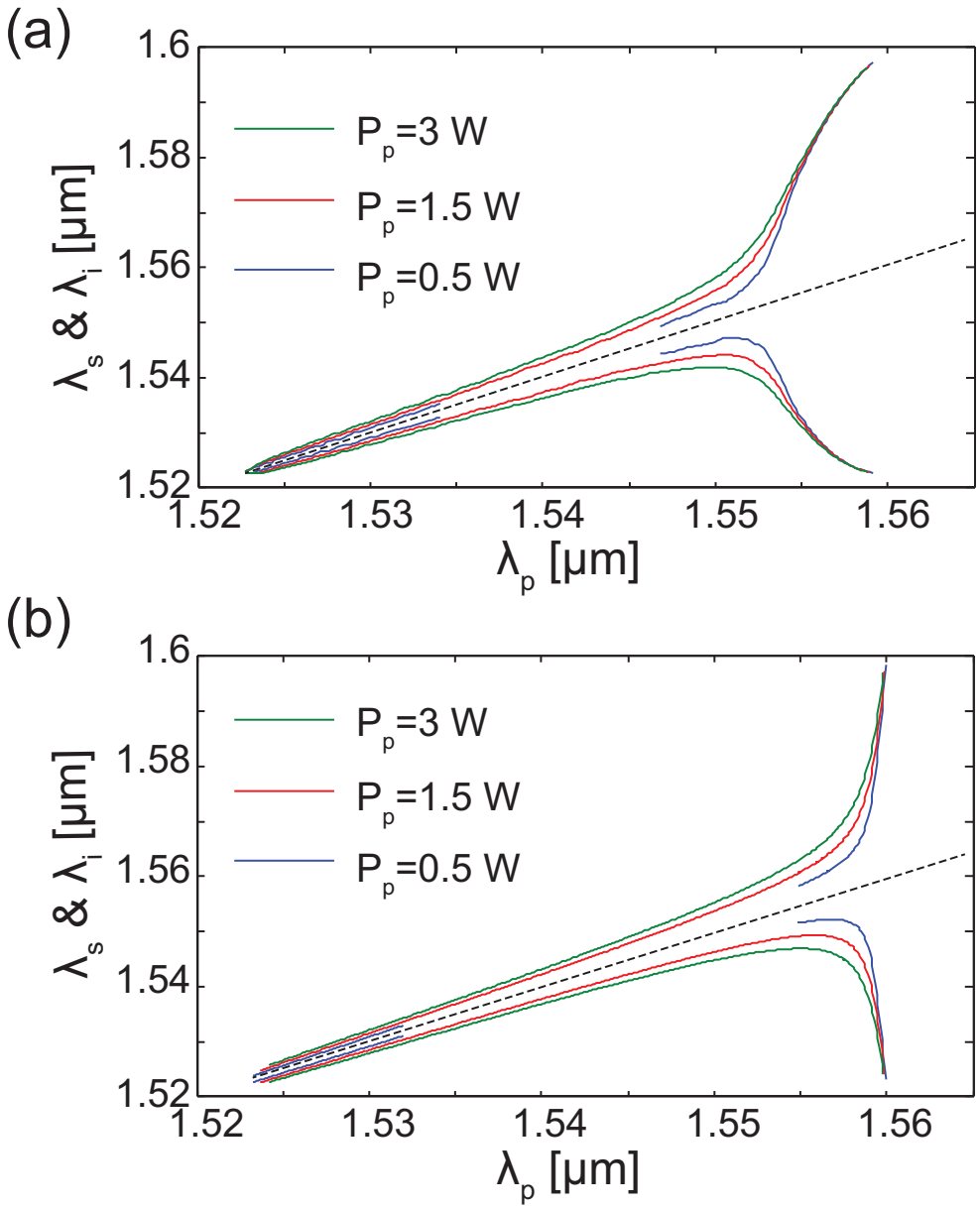

Figure 7.9: (a), (b) Wavelength diagrams defined by Eq. (7.43) and Eq. (7.45), respectively. In both panels dashed lines correspond to $\omega_p = \omega_s = \omega_i$.

satisfied. The spectral width of this gap increases when P_p decreases as the the waveguide was not designed to possess phase-matched modes in the linear regime. Moreover, the diagrams presented in Fig. 7.9 show that in the fast-light regime the wavelengths defined by the phase-matching condition depend only slightly on P_p, whereas a much stronger dependence is observed when the wavelengths of the signal and idler lie in slow-light spectral domains.

7.6 Results and discussion

In this section we illustrate how our theoretical model can be used to investigate various phenomena related to FWM in Si-PhCWs. In particular, we will compare the pulse interaction in slow- and fast-light regimes, calculate the FWM gain, and investigate the influence of various waveguide parameters on the FWM process. The choice of the values of physical parameters of the co-propagating pulses and that of the input pump power has been guided by the exact phase-matching condition given by Eq. (7.43). In all our calculations we assumed that the pulses propagate in the even mode and, unless otherwise specified, the following values for the pulse and waveguide parameters have been used in all our simulations: the input peak pump power, $P_p = 10^2 P_s = 5\,\mathrm{W}$, the input pulse width, $T_p = T_s = 7\,\mathrm{ps}$, and the intrinsic waveguide loss coefficient, $\alpha_{\mathrm{in}} = 50\,\mathrm{dB\,cm^{-1}}$[7. 58].

Let us consider first the evolution of the envelopes of the pulses in the time domain, both in the slow- and fast-light regimes, as illustrated in Fig. 7.10. The triplet of wavelengths for which the phase-matching condition is satisfied is $\lambda_p = 1554\,\mathrm{nm}$, $\lambda_s = 1536\,\mathrm{nm}$, and $\lambda_i = 1571\,\mathrm{nm}$ in the fast-light regime, whereas in the slow-light regime the wavelengths are $\lambda_p = 1559\,\mathrm{nm}$, $\lambda_s = 1524\,\mathrm{nm}$, and $\lambda_i = 1597\,\mathrm{nm}$. We stress that in both cases the pump pulse propagates in the fast-light regime, whereas the signal and idler are both generated either in the fast- or slow-light regime. All the input pulse parameters used for the fast light and slow light simulations are presented in the following Table-7.1 and Table-7.2, respectively.

Under these circumstances, one expects that the pump evolution in the time domain is similar in the two cases, a conclusion validated by the plots shown in Figs. 7.10(c) and 7.10(d). However, the dynamics of the signal and idler are strikingly different when they propagate in the slow-light or fast-light regimes. There are several reasons that account for these differences. First, whereas the FCA coefficient, α_{fc}, has similar values in the two cases, the FCA and intrinsic losses are much larger in the slow-light regime because the strength of both these effects is inverse proportional to v_g. This is reflected in Fig. 7.10 as a much more rapid decay in the slow-light regime of the signal and idler pulses. Second, it can be seen that in the slow-light regime the idler pulse grows at a faster rate. This is again a manifestation of slow-light effects. In particular, the nonlinear coefficient γ_{ips}, which determines the FWM gain, is

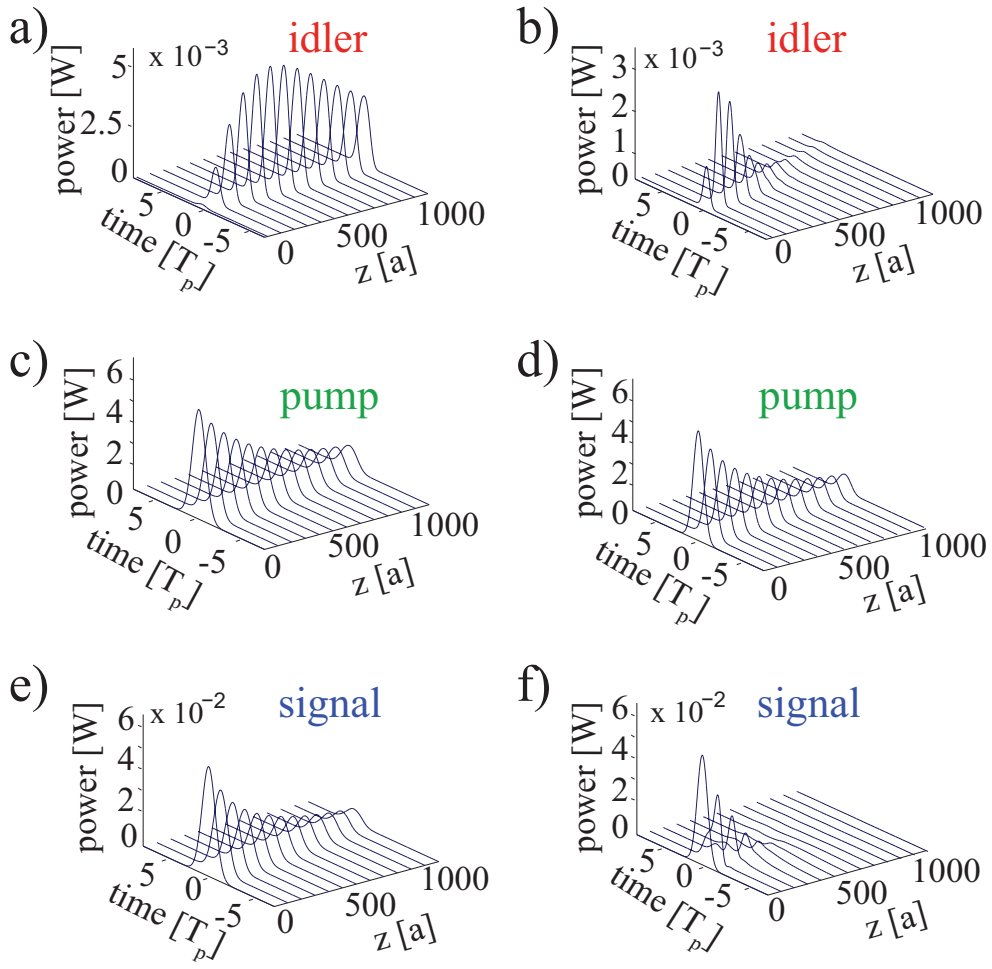

Figure 7.10: Pulse evolution in the time domain. Left (right) panels correspond to fast-light (slow-light) regimes, the group-index of the pulses being: $n_{g,i} = 9.48$ ($n_{g,i} = 20.3$), $n_{g,p} = 8.64$ ($n_{g,p} = 8.69$), $n_{g,s} = 10.37$ ($n_{g,s} = 23.3$).

inverse proportional to $(v_{g,i}v_{g,s})^{1/2}$ [see Eq. (7.39f)]. As a consequence, the FWM gain is strongly enhanced when both the signal and idler propagate in the slow-light regime.

The slow-light effects are reflected not only in the characteristics of the time-domain propagation of the pulses but they also affect the evolution of the pulse spectra. In order to illustrate this idea, we plot in Fig. 7.11 the z-dependence of the spectra of the pulses. Similarly to the time-domain dynamics, the spectra of the pump are almost the same in the slow- and fast-light regimes as its GV does not differ much between the two cases. The most noteworthy differences between the slow- and fast-light scenarios can again be observed in the case of the idler and signal. Thus, in the slow-light regime the idler decays faster due to increased losses and grows and broadens more significantly because of enhanced FWM gain and FCD effects, respectively. The influence of FCD

physical parameters	$\lambda_p = 1.554\mu m$	$\lambda_s = 1.536\mu m$	$\lambda_s = 1.571\mu m$
$T_0\ [ps]$	7	7	7
$P_0\ [W]$	5	5e-2	0
$\alpha_{in}\ [dB\ cm^{-1}]$	50	50	50
$\beta_1\ [ps/m]$	$2.88{\cdot}10^4$	$3.04{\cdot}10^4$	$2.97{\cdot}10^4$
$\beta_2\ [ps^2/m]$	-20.47	$-4.2{\cdot}10^4$	2.55
$\beta_3\ [ps^3/m]$	-35.51	$-7.02{\cdot}10^5$	-36
$\beta_4\ [ps^4/m]$	-1.277	9.826	1.326
$\beta_{TPA}\ [cm/GW]$	$1.3{\cdot}10^{-11}$	$1.35{\cdot}10^{-11}$	$1.28{\cdot}10^{-11}$
$n_2\ [cm^2/W]$	$5.4{\cdot}10^{-18}$	$5.39{\cdot}10^{-18}$	$5.42{\cdot}10^{-18}$
$\gamma'_{p,s,i}\ [W^{-1}m^{-1}]$	748.56	793.97	840.87
$\gamma''_{p,s,i}\ [W^{-1}m^{-1}]$	228.11	241.94	256.24
$\gamma'_{ps,sp,ip}\ [W^{-1}m^{-1}]$	765.11	814.158	803.48
$\gamma''_{ps,sp,ip}\ [W^{-1}m^{-1}]$	233.33	248.098	244.84
$\gamma'_{pi,si,is}\ [W^{-1}m^{-1}]$	164.07	160.21	789.36
$\gamma''_{pi,si,is}\ [W^{-1}m^{-1}]$	49.99	48.82	240.54
$\gamma'_{psi,spi,ips}\ [W^{-1}m^{-1}]$	800.66	781.95	771.69
$\gamma'_{psi,spi,ips}\ [W^{-1}m^{-1}]$	238.77	243.29	240.1
$L\ [\mu m]$	412	412	412

Table 7.1: Input pulse parameters for the fast light case of degenerate FWM of Fig. 7.10.

physical parameters	$\lambda_p = 1.559\mu m$	$\lambda_s = 1.524\mu m$	$\lambda_s = 1.597\mu m$
$T_0\ [ps]$	7	7	7
$P_0\ [W]$	5	0.05	0
$\alpha_{in}\ [dB\ cm^{-1}]$	50	50	50
$\beta_1\ [ps/m]$	$2.88{\cdot}10^4$	$7.04{\cdot}10^4$	$9.31{\cdot}10^4$
$\beta_2\ [ps^2/m]$	-57	$-77.18{\cdot}10^3$	$7.58{\cdot}10^3$
$\beta_3\ [ps^3/m]$	-38.49	$-4.41{\cdot}10^5$	$-2.24{\cdot}10^3$
$\beta_4\ [ps^4/m]$	-2.43	$-2{\cdot}10^7$	9.63
$\beta_{TPA}\ [cm/GW]$	$1.29{\cdot}10^{-11}$	$1.42{\cdot}10^{-11}$	$1.22{\cdot}10^{-11}$
$n_2\ [cm^2/W]$	$5.4{\cdot}10^{-18}$	$4.9{\cdot}10^{-18}$	$6.19{\cdot}10^{-18}$
$\gamma'_{p,s,i}\ [W^{-1}m^{-1}]$	778.56	$4.66{\cdot}10^3$	$5.65{\cdot}10^3$
$\gamma''_{p,s,i}\ [W^{-1}m^{-1}]$	237	$1.42{\cdot}10^3$	$1.72{\cdot}10^3$
$\gamma'_{ps,sp,ip}\ [W^{-1}m^{-1}]$	$1.75{\cdot}10^3$	$4.49{\cdot}10^3$	$4.29{\cdot}10^3$
$\gamma''_{ps,sp,ip}\ [W^{-1}m^{-1}]$	532.6	$1.37{\cdot}10^3$	$1.31{\cdot}10^3$
$\gamma'_{pi,si,is}\ [W^{-1}m^{-1}]$	$2.05{\cdot}10^3$	$1.79{\cdot}10^3$	$2.0{\cdot}10^3$
$\gamma''_{pi,si,is}\ [W^{-1}m^{-1}]$	626	545.12	611
$\gamma'_{psi,spi,ips}\ [W^{-1}m^{-1}]$	937.6	-531.3	-506.93
$\gamma''_{psi,spi,ips}\ [W^{-1}m^{-1}]$	$-2.92{\cdot}10^3$	$1.84{\cdot}10^3$	$1.76{\cdot}10^3$
$L\ [\mu m]$	412	412	412

Table 7.2: Input pulse parameters for the slow light case of degenerate FWM of Fig. 7.10.

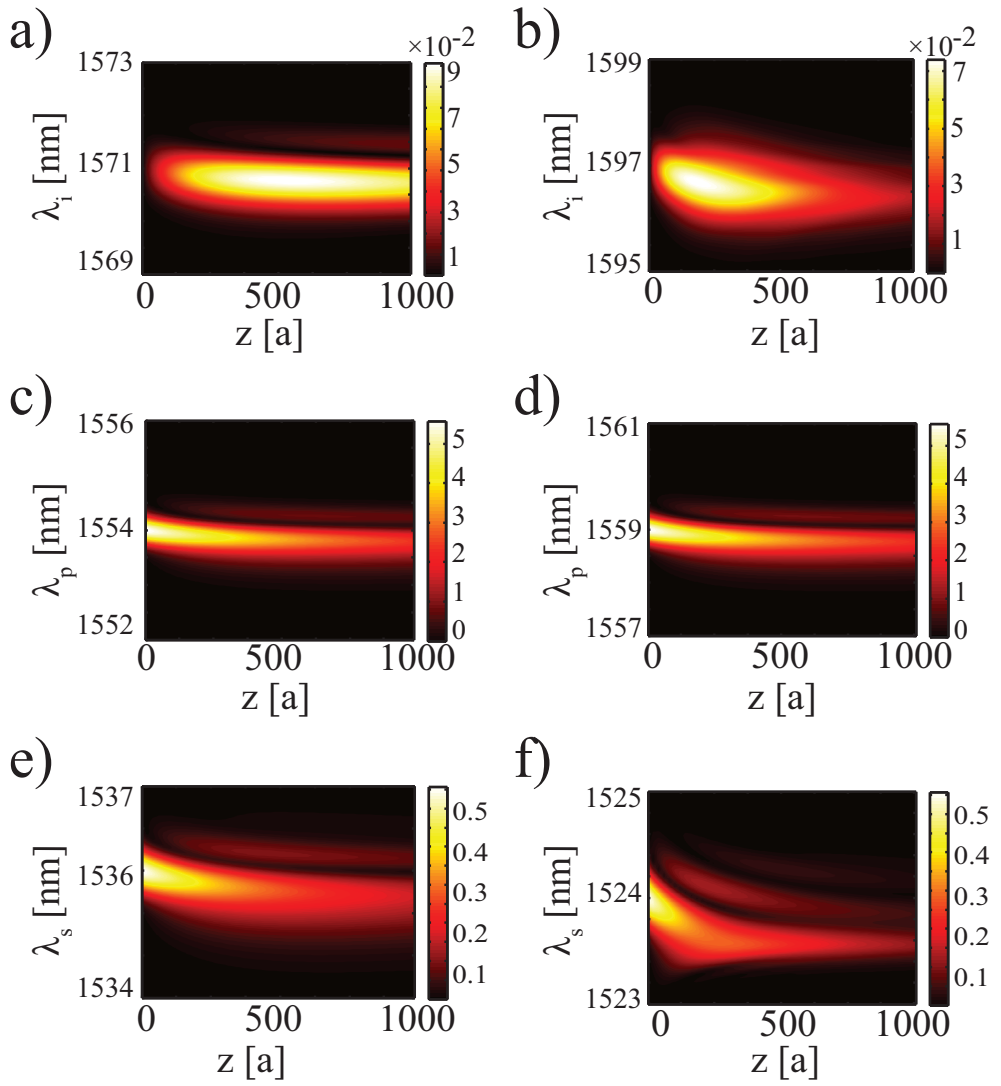

Figure 7.11: From top to bottom, the left (right) panels show the evolution of the spectra of the idler, pump, and signal in the case of fast-light (slow-light) regimes. The waveguide and pulse parameters are the same as in Fig. 7.10.

on the spectral features of the pulses can also be seen in the case of the signal and, to a smaller extent, the pump. More specifically, Eq. (7.9a) shows that the index of refraction of the waveguide decreases due to the generation of FCs. This in turn leads to a phase-shift and, consequently, a blue-shift of the pulse [7. 14]. Interestingly enough, one can also see in Fig. 7.11 that as the frequency of the pulses shifts during their propagation new spectral peaks are forming at the initial wavelengths for which the phase-matching condition was satisfied.

In order to gain a deeper insight into the influence of slow-light effects on the FWM process, we computed the z-dependence of the pulse energies when the frequencies of the signal and idler were tuned in the slow-light regions of the even mode of

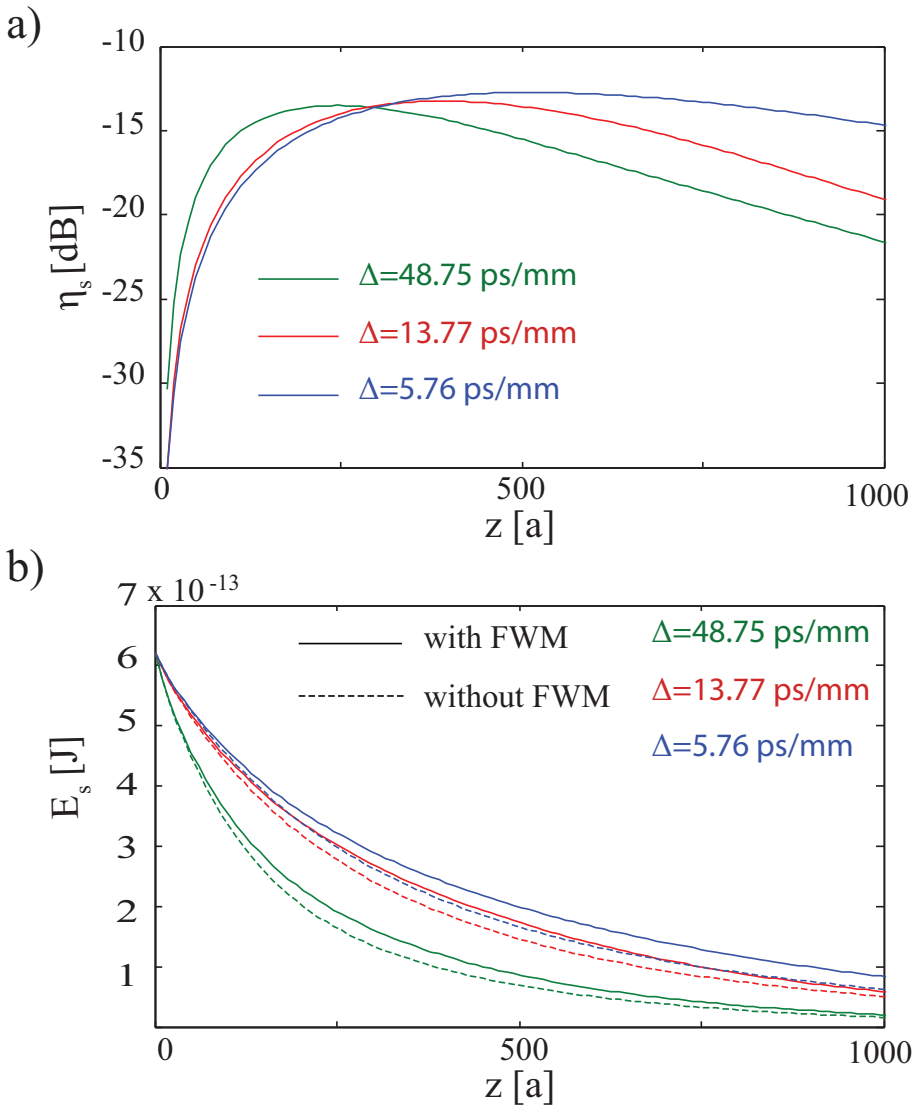

Figure 7.12: (a) FWM enhancement factor vs. propagation distance, determined for different values of the walk-off parameter, $\Delta = 1/v_{g,s} - 1/v_{g,p}$. (b) Signal energy vs. propagation distance, calculated by including FWM terms in Eqs. (7.37) and Eq. (7.38) and by setting them to zero. The blue (green) curve corresponds to the fast-light (slow-light) regime considered in Fig. 7.10(a) [Fig. 7.10(b)], whereas the remaining triplet of phase-matched wavelengths is $\lambda_p = 1556\,\text{nm}$, $\lambda_s = 1530\,\text{nm}$, and $\lambda_i = 1582\,\text{nm}$ (red).

the waveguide. We considered two scenarios, namely these energies were calculated by including FWM terms in Eqs. (7.37) and Eq. (7.38) and, in the other case, by setting them to zero, that is $\gamma_{psi} = \gamma_{spi} = \gamma_{ips} = 0$. In the former case, the FWM terms are responsible for transferring energy from the pump pulse to the signal and idler. Therefore, a suitable quantity to characterize the efficiency of this energy transfer is what we call the FWM enhancement factor, η, which in the case of the signal is defined as $\eta_s = 10\log[(E_{SXF} - E_{SX})/E_{s,in}]$. Here, E_{SXF} and E_{SX} are the signal energies calculated

by taking into account, in one case, SPM, XPM, and FWM effects, and only SPM and XPM terms in the other case (i.e. FWM terms are neglected in the latter case), and $E_{s,in}$ is the input energy of the signal.

The results of these calculations are summarized in Fig. 7.12. In particular, it can be clearly seen in Fig. 7.12(a) that the FWM enhancement factor is strongly dependent on pulse propagation regime. To be more specific, as the signal and idler are shifting in the slow-light regime a smaller amount of energy is transferred from the pump pulse to the signal. There are two effects whose combined influence leads to this behaviour. First, as we discussed, the pulses experience larger optical losses in the slow-light regime and therefore the signal losses energy at higher rate. Equally important, as the pulses are tuned in the slow-light regime the walk-off parameter, Δ, defined as $\Delta = 1/v_{g,s} - 1/v_{g,p}$, increases, meaning that the pulses interact for a shorter time and consequently less energy is transferred to the signal. These conclusions are clearly validated by the results summarized in Fig. 7.12(b), where we plot the energy of the signal vs. the propagation distance, determined for several values of the walk-off parameter. In addition, this figure somewhat surprisingly suggests that the FWM process is more efficient in the fast-light regime, which is again due to the fact that the pump and signal overlap over longer time.

It is well known that in the slow-light regime linear optical effects are enhanced by a factor of c/v_g, whereas cubic nonlinear interactions increase by a factor of $(c/v_g)^2$. For example, FCA and TPA are proportional to v_g^{-1} and v_g^{-2}, respectively. Our theoretical model predicts, however, that when the mutual interaction between FCs and the optical field is taken into account these scaling laws can significantly change. This can be understood as follows: the amount of FCs generated via TPA, N, is proportional to v_g^{-2} and since FCA is proportional to the product $v_g^{-1}N$, it scales with the GV as v_g^{-3}.

In order to validate this argument we have determined the optical total loss experienced by a pulse when it propagates in the presence of TPA and FCA or, in a different scenario, when only TPA is present [the latter case is realized by simply setting $\alpha_{\mathrm{fc}} = 0$ in Eqs. (7.37)]. Moreover, to simplify our analysis, we consider the propagation of only one pulse by setting all parameters describing XPM and FWM interactions to zero. Finally, we also reduced the input power to 100 mW in order to avoid strong SPM-induced pulse reshaping. Under these conditions, the effect of the FCA on the

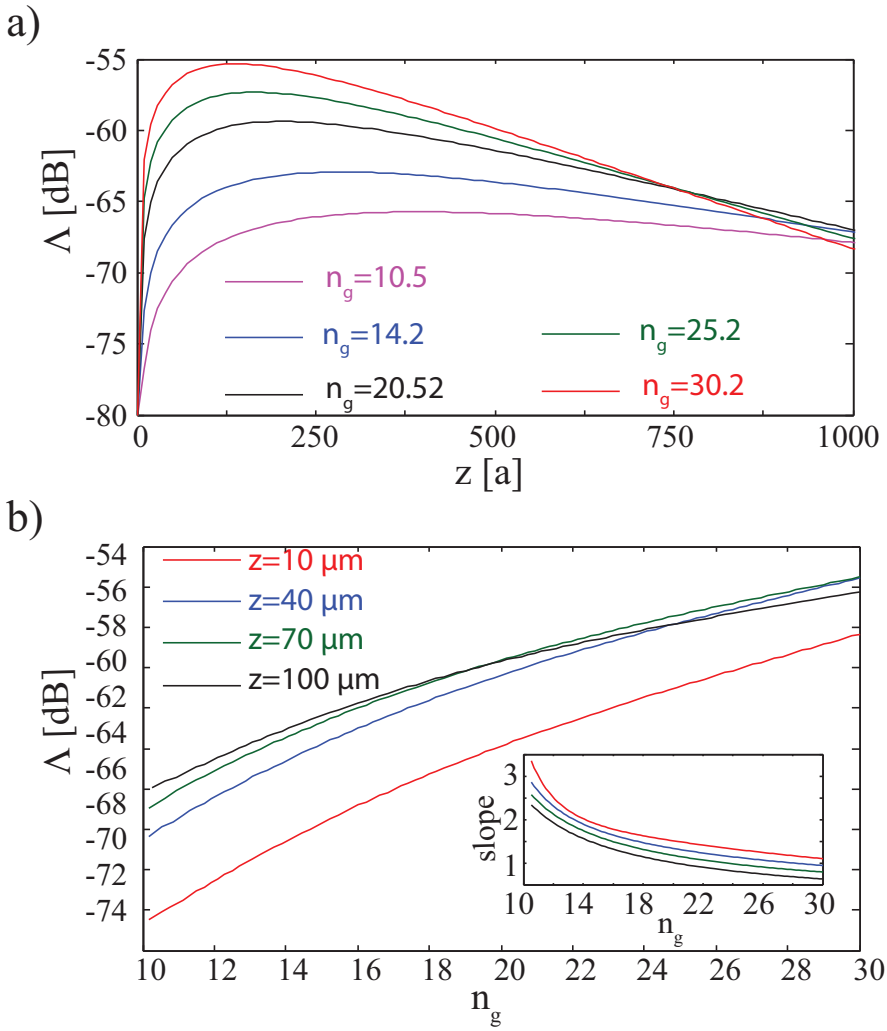

Figure 7.13: (a) Dependence of loss factor, Λ, on the propagation distance, z, determined for different values of the group-index, n_g. (b) Dependence of Λ on n_g, determined for different values of z. The slopes of the curves corresponding to $z = 10\,\mu$m and $z = 70\,\mu$m are shown in the inset.

pulse dynamics can be conveniently characterized by introducing a loss factor, Λ, defined as $\Lambda = 10\log[(E_T - E_{TF})/E_{in}]$, where E_{TF} and E_T are the pulse energies in the case when both TPA and FCA terms are included in the model and when only TPA is present, respectively, and E_{in} is the input energy of the pulse. The results of these calculations are presented in Fig. 7.13.

The variation of the loss factor, Λ, with the propagation distance, determined for several values of the GV is presented in Fig. 7.13(a). As one would have expected, the loss factor increases with the group-index, n_g, which is a reflection of the fact that the FC-induced losses increase with the decrease of the GV. One can observe, however, that when the propagation distance is larger than about $139a$ the loss factor begins to

decrease when the GV decreases. This behaviour is a direct manifestation of slow-light effects, namely as the frequency is tuned to the slow-light regime the optical losses increase significantly irrespective of the fact that only TPA is considered or both TPA and FCA effects are incorporated in the numerical simulations.

This subtle dependence of FC-induced losses on v_g is perhaps better reflected by the plots presented in Fig. 7.13(b). Thus, for several values of the propagation distance, we have determined the variation of Λ with the group-index, n_g. Then, by calculating the slope of the function $\Lambda(n_g)$ represented on a logarithmic scale one can determine how FC-induced losses scale with v_g [cf. the inset in Fig. 7.13(b)]. The results of this analysis clearly demonstrate that FC losses are proportional to v_g^{-3}, which agrees with the predictions of our qualitative evaluation of this dependence. We stress that for large n_g (i.e., small v_g) the v_g^{-3} dependence no longer holds at large propagation distance, chiefly because the pulse is strongly reshaped in the slow-light regime due to enhanced nonlinear optical effects, and thus its peak power is no longer exclusively determined by optical losses.

In order to gain more information about the influence of FCs on optical losses, we launch a new set of simulations where the pulse and waveguide parameters used for the slow light case of this simulation have already been presented in Table 7.2 (except that the input pump power is $P_p = 3\ W$ and $P_s = 0.03\ W$) while for the case of fast light regime are summarized in Table 7.3.

According to Fig. 7.14(a) it can be seen that α_{fc} is slightly larger at the idler, which is due to the smaller frequency, and that no significant difference is observed between the slow- and fast light regimes, mainly due to the fact that FCs are mostly generated by the pump. Importantly, however, since the FCA is proportional to α_{fc}/v_g, it is about two times larger in the slow-light regime as compared to its value in the fast-light regime.

As the signal is tuned into the slow-light regime Δ increases, which results in the degradation of the FWM conversion efficiency, $CE = 10\log(E_i(z)/E_{s,\text{in}})$, the maximum CE being reached at shorter distance [see Fig. 7.14(b)]. This scenario can be understood as follows: as Δ increases the pump and signal pass through each other in a shorter time, which results in weaker FWM, while at large distance increased losses in the slow-light regime lead to smaller CE.

Thus, as per Fig. 7.15(a), our analysis shows that the CE only slightly depends

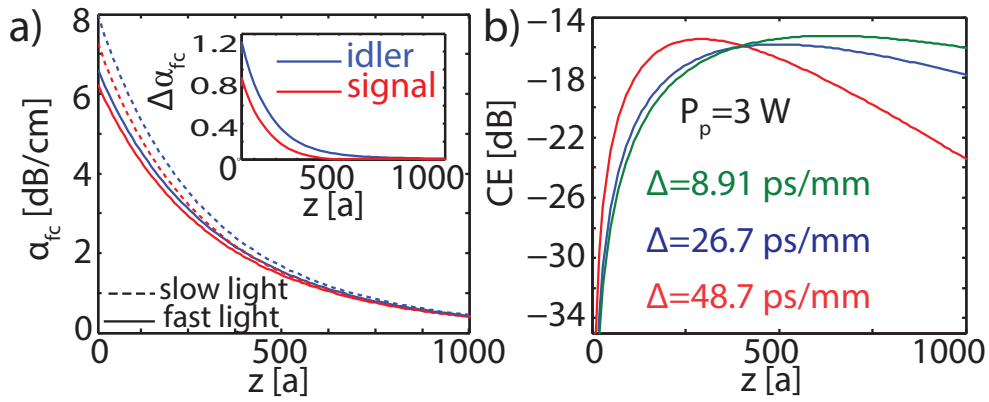

Figure 7.14: (a) FCA of the idler and signal vs. distance. In inset, difference of FCA between slow- and fast-light regimes, $\Delta\alpha_{\rm fc} = \alpha_{s,i}^{\rm sl} - \alpha_{s,i}^{\rm fl}$. (b) CE vs. distance.

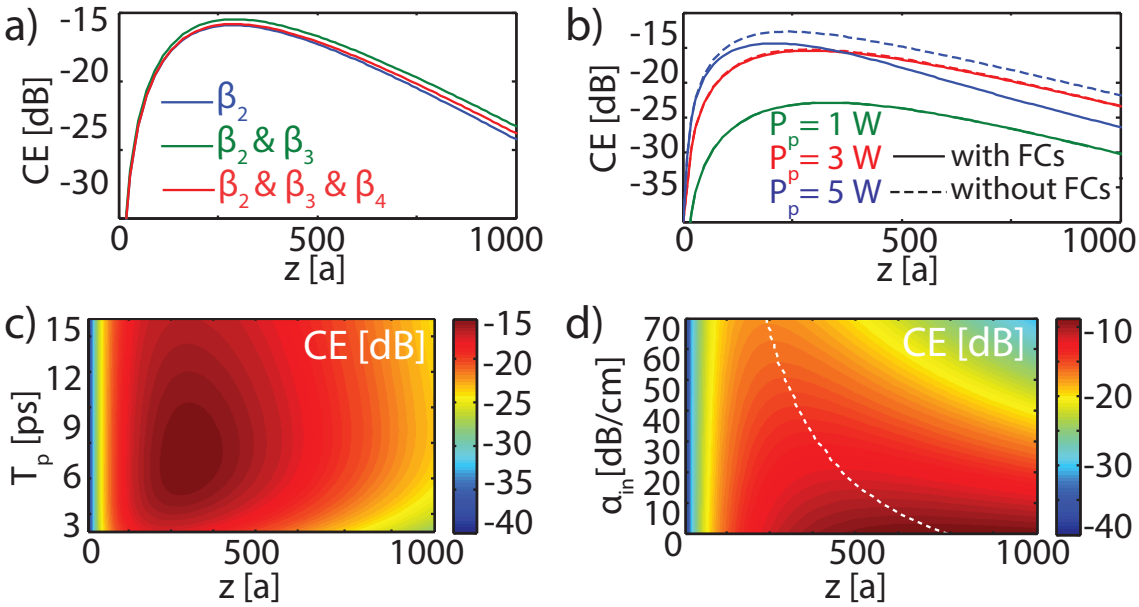

Figure 7.15: Dependence of CE on: (a), linear parameters, β_2, β_3, and β_4; (b), input pump power, P_p; (c), pulse width, T_p; and (d), waveguide loss coefficient, $\alpha_{\rm in}$. In (d), the dashed curve is the loci of maximum CE.

on the dispersion coefficients and although the (approximate) Eq. (7.45) predicts that it must depend only on even-order coefficients it can be seen that β_3 affects to some extent the CE. Moreover, it can be seen in Fig. 7.15(b) that, as expected, the CE increases with the pump power, and that the larger P_p the more FCs affect the CE. Note that for power values considered here the phase-matching condition Eq. (7.43) depends weakly on P_p. Our study also suggests that a maximum CE can be achieved for $T_p = 7.1\,$ps and $z = 285a$, as per Fig. 7.15(c). Finally, Fig. 7.15(d) shows that irrespective of the waveguide loss, $\alpha_{\rm in}$, there is a certain distance, $z_{\rm max}$, at which CE reaches a maximum value, whereas for fixed z the CE monotonously decreases with $\alpha_{\rm in}$.

Input pulse parameters	$\lambda_p = 1.555\mu m$	$\lambda_s = 1.533\mu m$	$\lambda_s = 1.578\mu m$
$T_0\ [ps]$	7	7	0
$P_0\ [W]$	3	0.03	0
$\alpha_{in}\ [dB\ cm^{-1}]$	50	50	50
c/v_g	8.64	11.3	10.4
$\beta_2\ [ps^2/m]$	170	$2.2{\cdot}10^3$	576
$\beta_3\ [ps^3/m]$	-46.48	-659.86	-54.35
$\beta_4\ [ps^4/m]$	-4.59	-372.55	3.98
$\beta_{TPA}\ [cm/GW]$	$1.3{\cdot}10^{-11}$	$1.35{\cdot}10^{-11}$	$1.28{\cdot}10^{-11}$
$n_2\ [cm^2/W]$	$5.4{\cdot}10^{-18}$	$5.39{\cdot}10^{-18}$	$5.42{\cdot}10^{-18}$
$\gamma'_{p,s,i}\ [W^{-1}m^{-1}]$	753.9	$1.17{\cdot}10^3$	$1.25{\cdot}10^3$
$\gamma''_{p,s,i}\ [W^{-1}m^{-1}]$	229.7	356.2	381.1
$\gamma'_{ps,sp,pi}\ [W^{-1}m^{-1}]$	917	$1.17{\cdot}10^3$	967
$\gamma''_{ps,sp,pi}\ [W^{-1}m^{-1}]$	279i	355i	295i
$\gamma'_{ip,si,is}\ [W^{-1}m^{-1}]$	$1.13{\cdot}10^3$	929	953
$\gamma''_{ip,si,is}\ [W^{-1}m^{-1}]$	346	283	291
$\gamma'_{psi,spi,ips}\ [W^{-1}m^{-1}]$	323.6	-286.9	-279
$\gamma''_{psi,spi,ips}\ [W^{-1}m^{-1}]$	$-1.06{\cdot}10^3$	941.4	915.4
$L\ [\mu m]$	412	412	412

Table 7.3: Input pulse parameters for the fast light case of degenerate FWM of Figs. 7.14 and 7.15.

7.7 Conclusion

In conclusion, we have derived a rigorous theoretical model, which describes pulsed four-wave-mixing in one-dimensional photonic crystal slab waveguides made of silicon. Our theoretical model rigorously incorporate all key linear and nonlinear optical effects affecting the optical pulse dynamics, including modal dispersion, free-carrier dispersion, free-carrier absorption, self- and cross-phase modulation, two-photon absorption, cross-absorption modulation, and four-wave mixing. In addition, the mutual interaction between photogenerated free-carriers and optical field is incorporated in our theoretical analysis in a natural way by imposing the conservation the total energy of the optical field and free-carriers. Importantly, our theoretical formalism allows one to derive rigorous formulae for the optical coefficients characterizing the linear and nonlinear optical properties of the photonic crystal waveguides, avoiding thus any of the approximations that are commonly used in the investigation of nonlinear pulse dynamics in semiconductor waveguides based on photonic crystals.

As a practical application of the theoretical results developed in this study, we

have used our theoretical model to investigate the properties of degenerate four-wave-mixing of optical pulses propagating in photonic crystal waveguides made of silicon, with a special focus being on highlighting the differences between the pulse dynamics in the slow- and fast light regimes. This analysis has revealed not only that linear and nonlinear effects are enhanced in the slow-light regime by a factor of n_g and n_g^2, respectively, but also that these scaling laws are markedly affected in the presence of free-carriers. Moreover, since our study has been performed in a very general framework, i.e. generic optical properties of the waveguides (multi-mode waveguides) and pulse configuration (multi-frequency optical field), our findings can also be used to describe many phenomena not considered in this work. For example, important nonlinear effects, including stimulated and spontaneous Raman scattering, coherent anti-Stokes Raman scattering, and third-harmonic generation, can be included in our model by simply adding the proper nonlinear polarizations.

The present chapter has revealed the dependence of the optical properties of silicon photonic crystal waveguides on the group velocity of the copropagating pulses. It has also briefly demonstrated that the efficiency of degenerate FWM is strongly enhanced in Si-PhCWs. However a more solid and detailed analysis of FWM is required in order to gain a complete insight of this nonlinear process. To this end, we present a comparative analysis of FWM in slow and fast light regime in the next chapter.

References

[7. 1] R. Ho, K. W. Mai, and M. A. Horowitz, "The future of wires," Proc. IEEE **89**, 490–504 (2001).

[7. 2] K. K. Lee, D. R. Lim, H. C. Luan, A. Agarwal, J. Foresi, and L. C. Kimerling, " Effect of size and roughness on light transmission in a Si/SiO2 waveguide: Experiments and model," Appl. Phys. Lett. **77**, 1617–1619 (2000).

[7. 3] R. U. Ahmad, F. Pizzuto, G. S. Camarda, R. L. Espinola, H. Rao, and R. M. Osgood, "Ultracompact Corner-Mirrors and T-Branches in Silicon-on-Insulator," IEEE Photon. Technol. Lett. **14**, 65–67 (2002).

[7. 4] R. Claps, D. Dimitropoulos, V. Raghunathan, Y. Han, and B. Jalali, "Observation of stimulated Raman amplification in silicon waveguides," Opt. Express **11**, 1731–1739 (2003).

[7. 5] R. Espinola, J. I. Dadap, R. M. Osgood, S. J. McNab, and Y. A. Vlasov, "Raman amplification in ultrasmall silicon-on-insulator wire waveguides," Opt. Express **12**, 3713–3718 (2004).

[7. 6] H. S. Rong, R. Jones, A. S. Liu, O. Cohen, D. Hak, A. Fang, and M. Paniccia, "A continuous-wave Raman silicon laser," Nature **433**, 725–728 (2005).

[7. 7] M. A. Foster, A. C. Turner, J. E. Sharping, B. S. Schmidt, M. Lipson, and A. L. Gaeta, "Broad-band optical parametric gain on a silicon photonic chip," Nature **441**, 960–963 (2006).

[7. 8] X. Liu, R. M. Osgood, Y. A. Vlasov, and W. M. J. Green, "Mid-infrared optical parametric amplifier using silicon nanophotonic waveguides," Nat. Photonics **4**, 557–560 (2010).

[7. 9] G. Cocorullo, M. Iodice, I. Rendina, and P. M. Sarro, "Silicon thermooptical micromodulator with 700-kHz3-dB bandwidth," IEEE Photon. Technol. Lett. **7**, 363–365 (1995).

[7. 10] A. Liu, R. Jones, L. Liao, D. Samara-Rubio, D. Rubin, O. Cohen, R. Nicolaescu, and M. Paniccia, " ," Nature **427**, 615–618 (2004).

[7. 11] Q. Xu, B. Shmidt, S. Pradhan, and M. Lipson, "A high-speed silicon optical modulator based on a metaloxidesemiconductor capacitor," Nature **435**, 325–327 (2005).

[7. 12] X. Chen, N. C. Panoiu, I. W. Hsieh, J. I. Dadap, and R. M. Osgood, "Third-order dispersion and ultrafast-pulse propagation in silicon wire waveguides," IEEE Photon. Technol. Lett. **18**, 2617–2619 (2006).

[7. 13] M. Mohebbi, " Silicon Photonic Nanowire Soliton-Effect Compressor at 1.5μm," IEEE Photon. Technol. Lett. **20**, 921–923 (2008).

[7. 14] O. Boyraz, P. Koonath, V. Raghunathan, and B. Jalali, "All optical switching and continuum generation in silicon waveguides," Opt. Express **12**, 4094–4102 (2004).

[7. 15] I. W. Hsieh, X. Chen, X. P. Liu, J. I. Dadap, N. C. Panoiu, C. Y. Chou, F. Xia, W. M. Green, Y. A. Vlasov, and R. M. Osgood, "Supercontinuum generation in silicon photonic wires," Opt. Express **15**, 15242–15249 (2007).

[7. 16] L. Yin, Q. Lin, and G. P. Agrawal, " Soliton fission and supercontinuum generation in silicon waveguides," Opt. Lett. **32**, 391–393 (2007).

[7. 17] N. C. Panoiu, X. Liu, and R. M. Osgood, "Self-steepening of ultrashort pulses in silicon photonic nanowires," Opt. Lett. **34**, 947–949 (2009).

[7. 18] N. C. Panoiu, X. Chen, and R. M. Osgood, "Modulation instability in silicon photonic nanowires," Opt. Lett. **31**, 3609–3611 (2006).

[7. 19] H. Fukuda, K. Yamada, T. Shoji, M. Takahashi, T. Tsuchizawa, T. Watanabe, J. Takahashi, and S. Itabashi, "Four-wave mixing in silicon wire waveguides," Opt. Express **13**, 4629–4637 (2005).

[7. 20] R. Espinola, J. Dadap, R. M. Osgood, S. McNab, and Y. Vlasov, "C-band wavelength conversion in silicon photonic wire waveguides," Opt. Express **13**, 4341–4349 (2005).

[7. 21] Q. Lin, J. Zhang, P. M. Fauchet, and G. P. Agrawal, "Ultrabroadband parametric generation and wavelength conversion in silicon waveguides," Opt. Express **14**, 4486–4799 (2006).

[7. 22] M. A. Foster, A. C. Turner, R. Salem, M. Lipson, and A. L. Gaeta, "Broad-band continuous-wave parametric wavelength conversion in silicon nanowaveguides," Opt. Express **15**, 12949–12958 (2007).

[7. 23] S. Zlatanovic, J. S. Park, S. Moro, J. M. C. Boggio, I. B. Divliansky, N. Alic, S. Mookherjea, and S. Radic, "Mid-infrared wavelength conversion in silicon waveguides using ultracompact telecom-band-derived pump source," Nat. Photonics **4**, 561–564 (2010).

[7. 24] J. B. Driscoll, N. Ophir, R. R. Grote, J. I. Dadap, N. C. Panoiu, K. Bergman, and R. M. Osgood, "Width-modulation of Si photonic wires for quasi-phase-matching of four-wave-mixing: experimental and theoretical demonstration," Opt. Express **20**, 9227–9242 (2012).

[7. 25] R. M. Osgood, N. C. Panoiu, J. I. Dadap, X. Liu, X. Chen, I-W. Hsieh, E. Dulkeith, W. M. J. Green,and Y. A. Vlassov, "Engineering nonlinearities in nanoscale optical systems: physics and applications in dispersion-engineered silicon nanophotonic wires," Adv. Opt. Photon. **1**, 162–235 (2009).

[7. 26] Q. Lin, O. J. Painter, and G. P. Agrawal, "Nonlinear optical phenomena in silicon waveguides: Modeling and applications," Opt. Express **15**, 16604–16644 (2007).

[7. 27] E. Yablonovitch, "Inhibited Spontaneous Emission in Solid-State Physics and Electronics," Phys. Rev. Lett. **58**, 2059–2062 (1987).

[7. 28] S. John, "Strong localization of photons in certain disordered dielectric superlattices," Phys. Rev. Lett. **58**, 2486–2489 (1987).

[7. 29] A. Mekis, J. C. Chen, I. Kurland, S. Fan, P. R. Villeneuve, and J. D. Joannopoulos, "High Transmission through Sharp Bends in Photonic Crystal Waveguides," Phys. Rev. Lett. **77**, 3787–3790 (1996).

[7. 30] S. Y. Lin, E. Chow, V. Hietala, P. R. Villeneuve, J. D. Joannopoulos, "Experimental Demonstration of Guiding and Bending of Electromagnetic Waves in a Photonic Crystal," Science **282**, 274–276 (1998).

[7. 31] T. Baba, N. Fukaya, and J. Yonekura, "Observation of light propagation in photonic crystal optical waveguides with bends," Electron. Lett. **35**, 654–655 (1999).

[7. 32] S. G. Johnson, S. Fan, P. R. Villeneuve, J. D. Joannopoulos, and L. A. Kolodziejski, "Guided modes in photonic crystal slabs," Phys. Rev. B **60**, 5751–5758 (1999).

[7. 33] A. Chutinan and S. Noda, "Waveguides and waveguide bends in two-dimensional photonic crystal slabs," Phys. Rev. B **62**, 4488–4492 (2000).

[7. 34] J. S. Foresi, P. R. Villeneuve, J. Ferrera, E. R. Thoen, G. Steinmeyer, S. Fan, J. D. Joannopoulos, L. C. Kimerling, H. I. Smith, and E. P. Ippen, "Photonic-bandgap microcavities in optical waveguides," Nature **390**, 143–145 (1997).

[7. 35] O. Painter, R. K. Lee, A. Scherer, A. Yariv, J. D. O'Brien, P. D. Dapkus, and I. Kim, "Two-dimensional photonic band-gap defect mode laser," Science **284**, 1819–1821 (1999).

[7. 36] Y. Akahane, T. Asano, B. S. Song, and S. Noda, "High-Q photonic nanocavity in a two-dimensional photonic crystal," Nature **425**, 944–947 (2003).

[7. 37] J. P. Reithmaier, G. Sek, A. Loffler, C. Hofmann, S. Kuhn, S. Reitzenstein, L. V. Keldysh, V. D.Kulakovskii, T. L. Reinecke, and A. Forchel, "Strong coupling in a single quantum dotsemiconductor microcavity system," Nature **432**, 197–200 (2004).

[7. 38] T. Yoshie, A. Scherer, J. Hendrickson, G. Khitrova, H. M. Gibbs, G. Rupper, C. Ell, O. B. Shchekin, and D. G. Deppe, "Vacuum Rabi splitting with a single quantum dot in a photonic crystal nanocavity," Nature **432**, 200–203 (2004).

[7. 39] M. Notomi, A. Shinya, S. Mitsugi, G. Kira, E. Kuramochi, and T. Tanabe, "Optical bistable switching action of Si high-Q photonic-crystal nanocavities," Opt. Express **13**, 2678–2687 (2005).

[7. 40] S. Fan, P. R. Villeneuve, J. D. Joannopoulos, M. J. Khan, C. Manolatou, and H. A. Haus, "Theoretical analysis of channel drop tunneling processes," Phys. Rev. B **59**, 15882–15892 (1999).

[7. 41] A. Chutinan, M. Mochizuki, M. Imada, and S. Noda, "Surface-emitting channel drop filters using single defects in two dimensional photonic crystal slabs," Appl. Phys. Lett. **79**, 2690–2692 (2001).

[7. 42] S. W. Leonard, H. M. van Driel, J. Schilling, and R. B. Wehrspohn, "Ultrafast band-edge tuning of a two-dimensional silicon photonic crystal via free-carrier injection," Phys. Rev. B **66**, 161102–161106(R) (2002).

[7. 43] M. Soljacic and J. D. Joannopoulos, "Enhancement of nonlinear effects using photonic crystals," Nat. Mater. **3**, 211–219 (2004).

[7. 44] T. F. Krauss, "Why do we need slow light?," Nat. Photonics **2**, 448–450 (2008).

[7. 45] T. Baba, "Slow light in photonic crystals," Nat. Photonics **2**, 465–473 (2008).

[7. 46] M. Notomi, K. Yamada, A. Shinya, J. Takahashi, C. Takahashi, and I. Yokohama, " Extremely Large Group-Velocity Dispersion of Line-Defect Waveguides in Photonic Crystal Slabs," Phys. Rev. Lett. **87**, 253902–253906 (2001).

[7. 47] M. Soljacic, S. G. Johnson, S. Fan, M. Ibanescu, E. Ippen, and J. D. Joanopoulos, "Photonic-crystal slow-light enhancement of nonlinear phase sensitivity," J. Opt. Soc. Am. B. **19**, 2052–2059 (2002).

[7. 48] N. C. Panoiu, M. Bahl, and R. M. Osgood, "Optically tunable superprism effect in nonlinear photonic crystals," Opt. Lett. **28**, 2503–2505 (2003).

[7. 49] N. C. Panoiu, M. Bahl, and R. M. Osgood, "All-optical tunability of a nonlinear photonic crystal channel drop filter," Opt. Express **12**, 1605–1610 (2004).

[7. 50] Y. A. Vlasov, M. O. Boyle, H. F. Hamann, and S. J. McNab, "Active control of slow light on a chip with photonic crystal waveguides," Nature **438**, 65–69 (2005).

[7. 51] J. F. McMillan, X. Yang, N. C. Panoiu, R. M. Osgood, and C. W. Wong, "Enhanced stimulated Raman scattering in slow-light photonic crystal waveguides," Opt. Lett. **31**, 1235–1237 (2006).

[7. 52] R. J. P. Engelen, Y. Sugimoto, Y. Watanabe, J. P. Korterik, N. Ikeda, N. F. van Hulst, K. Asakawa, and L. Kuipers, "The effect of higher-order dispersion on slow light propagation in photonic crystal waveguid es," Opt. Express **14**, 1658–1672 (2006).

[7. 53] B. Corcoran, C. Monat, C. Grillet, D. J. Moss, B. J. Eggleton, T. P. White, L. O'Faolain, and T. F. Krauss, "Green light emission in silicon through slow-light enhanced third-harmonic generation in photonic-crystal waveguides," Nat. Photonics **3**, 206–210 (2009).

[7. 54] I. H. Rey, Y. Lefevre, S. A. Schulz, N. Vermeulen, and T. F. Krauss, "Scaling of Raman amplification in realistic slow-light photonic crystal waveguides," Phys. Rev. B **84**, 035306–035312 (2011).

[7. 55] R. H. Stolen, J. E. Bjorkholm, and A. Ashkin, "PhaseMatched Three-Wave Mixing in Silica Fiber Optical Waveguides," Appl. Phys. Lett. **24**, 308–310 (1974).

[7. 56] J. F. McMillan, M. Yu, D. L. Kwong, and C. W. Wong, "Observation of four-wave mixing in slow-light silicon photonic crystal waveguides," Opt. Express **18**, 15484–15497 (2010).

[7. 57] M. Santagiustina, C. G. Someda, G. Vadala, S. Combrie, and A. De Rossi, "Theory of slow light enhanced four-wave mixing in photonic crystal waveguides," Opt. Express **18**, 21024–21029 (2010).

[7. 58] C. Monat, M. Ebnali-Heidari, C. Grillet, B. Corcoran, B. J Eggleton, T. P. White, L. O'Faolain, J. Li, and T. F. Krauss, "Four-wave mixing in slow light

engineered silicon photonic crystal waveguides," Opt. Express **18**, 22915–22927 (2010).

[7. 59] V. Eckhouse, I. Cestier, G. Eisenstein, S. Combrie, P. Colman, A. De Rossi, M. Santagiustina, C. G. Someda, and G. Vadala, "Highly efficient four wave mixing in GaInP photonic crystal waveguides," Opt. Lett. **35**, 1440–1442 (2010).

[7. 60] J. Li, L. O'Faolain, I. H. Rey, and T. F. Krauss, "Four-wave mixing in photonic crystal waveguides: slow light enhancement and limitations ," Opt. Express **19**, 4458–4463 (2011).

[7. 61] T. Chen, J. Sun, and L. Li, "Modal theory of slow light enhanced third-order nonlinear effects in photonic crystal waveguides," Opt. Express **20**, 20043–20058 (2012).

[7. 62] S. Lavdas, S. Zhao, J. B. Driscoll, R. R. Grote, R. M. Osgood, and N. C. Panoiu, "Wavelength conversion and parametric amplification of optical pulses via quasi-phase-matched four-wave mixing in long-period Bragg silicon waveguides," Opt. Lett. **39**, 4017–4020 (2014).

[7. 63] J. D. Joannopoulos, S. G. Johnson, J. N. Winn, and R. D. Meade, *Photonic Crystals: Molding the Flow of Light*, 2nd ed. (Princeton University Press, Princeton, NJ, 2008).

[7. 64] S. G. Johnson and J. D. Joannopoulos, "Block-iterative frequency-domain methods for Maxwell's equations in a planewave basis," Opt. Express **8**, 173–190 (2001).

[7. 65] X. Chen, N. C. Panoiu, and R. M. Osgood, "Theory of Raman-mediated pulsed amplification in silicon-wire waveguides," IEEE J. Quantum Electron. **42**, 160–170 (2006).

[7. 66] N. C. Panoiu, J. F. McMillan, and C. W. Wong, "Theoretical Analysis of Pulse Dynamics in Silicon Photonic Crystal Wire Waveguides," IEEE J. Sel. Top. Quantum Electron. **16**, 257–266 (2010).

[7. 67] A. W. Snyder and J. D. Love, *Optical Waveguide Theory* (Chapman and Hall, London, 1983).

[7. 68] D. Michaelis, U. Peschel, C. Wachter, and A. Brauer, "Reciprocity theorem and perturbation theory for photonic crystal waveguides," Phys. Rev. E **68**, 065601(R)(1-4) (2003).

[7. 69] A. W. Snyder, "Coupling of modes on a tapered dielectric cylinder," IEEE Trans. Microw. Theory Tech. **18**, 383–392 (1970).

[7. 70] J. E. Sipe, C. M. de Sterke, and B. J. Eggleton, "Rigorous derivation of coupled mode equations for short, high-intensity grating-coupled, co-propagating pulses," J. Mod. Opt. **49**, 1437–1452 (2002).

[7. 71] R. A. Soref and B. R. Bennett, "Electrooptical Effects in Silicon," IEEE J. Quantum Electron. **23**, 123–129 (1987).

[7. 72] R. W. Boyd, *Nonlinear Optics*, 3rd ed. (Academic Press, San Diego, 2008).

[7. 73] J. Zhang, Q. Lin, G. Piredda, R. W. Boyd, G. P. Agrawal, and P. M. Fauchet, "Dispersion of silicon nonlinearities in the near infrared region," Appl. Phys. Lett. **91**, 071113(1-3) (2007).

[7. 74] P. N. Butcher and D. Cotter, *The Elements of Nonlinear Optics* (Cambridge University Press, 1991).

[7. 75] T. Kamalakis and T. Sphicopoulos, "A new formulation of coupled propagation equations in periodic nanophotonic waveguides for the treatment of Kerr-induced nonlinearities," IEEE J. Quantum Electron. **43**, 923–933 (2007).

[7. 76] P. Bienstman, " Rigorous and efficient modelling of wavelength scale photonic components," Ph. D. Thesis (University of Ghent, 2001).

[7. 77] C. Monat, B. Corcoran, M. Ebnali-Heidari, C. Grillet, B. J. Eggleton, T. P. White, L. O'Faolain, and T. F. Krauss, "Slow light enhancement of nonlinear effect s in silicon engineered photonic crystal waveguides," Opt. Express **17**, 2944–2953 (2009).

[7. 78] E. D. Palik, *Handbook of Optical Constants of Solids* (Academic Press, San Diego, 1998).

[7. 79] G. P. Agrawal, *Nonlinear Fibre Optics*, 5th ed. (Academic Press, San Diego, 2013).

Chapter 8

Conclusions and future work

The field of silicon photonics has attracted great attention during the recent years. The striking linear and nonlinear features of silicon have inspired many researchers to elaborate on a large range of applications in optical telecommunications, computer systems or even in medicine for therapeutic purposes. Further to that, silicon photonics provide a unique ability to fabricate novel devices with properties and functionalities which are dynamic and can tailored in a very convenient way. This work has totally focused on exploring and exhibiting interesting nonlinear effects emerged from optical pulse propagation in silicon nanopatterned waveguides. To this end, theoretical semi-analytic and analytic models have been developed in this work in order to describe rigorously and accurately nonlinear pulse dynamics that occur either in silicon wires or silicon photonic crystal slab waveguides.

Unlike the majority of the already published work in the field of photonics, the objective of the current project focused on the study and analysis of nonlinear phenomena which occur when one or more pulses propagate in silicon waveguide media. The driving force for launching pulses and not continuous waves comes from the fact that the real contemporary applications in computer and telecommunication systems formulate the circulating information as bits which represent essentially a pulse shape. Therefore, the evolution of the pulse shape along the propagation distance constitutes the cornerstone of current communication systems. It is worth mentioning that the current work has not only developed the mathematical software for simulating optical pulse propagation but also has studied efficient ways to eliminate significant pulse degradation which is the most common limit in many optical applications.

By developing mathematical models for the description of nonlinear optical pulse

propagation in silicon waveguides, we have tried to overcome some serious problems emerged in optical applications which are mainly related to their physical size and efficient operational bandwidth. Based on that, I will discuss how our work has directly contributed either to improve or push the limits of these research challenges and how it has managed to achieve its intended objectives. In what it follows, I will present the contributions of the current work as well as the next potential step for the solution of the remaining problems.

8.1 Contribution of this work to the field of silicon photonics

In this thesis I have presented theoretical analysis and numerical simulations for different nonlinear phenomena in silicon photonics related to nonlinear optical pulse copropagation in silicon nanowires and silicon photonic crystal slab waveguides. Regarding the silicon nanowires, similariton generation and collision, degenerate FWM as well as pulse compression has been described and compared with the corresponding nonlinear phenomena in silica fibres. At the same time, a detailed mathematical analysis of nonlinear pulse dynamics in silicon photonic crystal slab waveguides has been demonstrated focusing on degenerate FWM. Interesting scientific conclusions have been drawn from the latter nonlinear phenomena enforcing researchers to design and fabricate novel optical applications. One should note here that our theoretical model incorporates all relevant linear optical effects, including waveguide loss, free-carrier (FC) dispersion and FC absorption, nonlinear optical effects such as SPM, XPM, TPA and XAM, as well as the coupled dynamics of FCs and optical field.

In order to make clear the novelty of this work, I present in the following bulleted list the main contribution of the current PhD project to the field of silicon photonics.

- This work has proved that parabolic pulses (similaritons) or similariton collision can be achieved in millimeter-long tapered silicon nanowires with engineered decreasing normal GVD. One should note here that similar phenomenon in silica fibres requires much longer propagation distances as the linear and nonlinear dispersive properties of silica fibres are much weaker than of these in silicon nanowires.

- The efficiency of similariton generation process is strongly dependent on the geometry of the silicon nanowires. This property implies that silicon nanowires provide an additional degree of freedom for tailoring such nonlinear phenomena as the non flexible geometry of fibres pose a limit on such kind of manipulations and improvements.

- We showed that significant pulse compression can be obtained in just few millimeters of optical pulse propagation unlike the case of silica fibres where the neccessary distance is much longer. The current analysis also revealed that significant pulse compression can be achieved not only when the dispersion parameter ($|\beta_2|$, $\beta_2 < 0$) decreases, as it occurs in the case of soliton compression in fibres, but also when $|\beta_2|$ increases. Our investigation suggested a new scheme for obtaining pulse compression by launching, initially, an optical pulse in normal dispersion regime ($GVD > 0$) and after a specific propagation distance in anomalous dispersion regime ($GVD < 0$).

- A novel scheme was suggested in this work related to quasi phase-matched FWM. In particular a periodically width modulated nanowire was proposed in order to achieve an efficient FWM. In particular, the phase-matching condition can be attained at more than one pair of wavelengths, which can be used to implement optical stability. In the same context, FWM can be achieved not only in anomalous dispersion regime but also in normal dispersion. This is a striking feature which is not usually exhibited in silica fibres.

- A very general mathematical framework was developed which incorporates not only all the linear and nonlinear pulse dynamics that occur in silicon photonic crystals but also is able to describe the interaction of many co-propagating optical pulses which are of the same or different electromagnetic mode.

- Regarding the theoretical model of ultrashort pulse propagation in silicon nanowires, we have developed a parallel C++ OpenMP code (OpenMP stands for open multi-processing) in order to be able to simulate multiple independent propagation scenarios at the same time. This code like this could be easily embedded in a commercial software after some improvements of the data input interface.

8.2 Future prospects

As it has been stated many times in this work, the silicon photonics technology is oriented to the design and fabrication of chips capable of optically transmitting and receiving information at large data rates such 100 gigabits of data per second. Essentially silicon photonics technology will allow silicon chips to rely on pulses of light, rather than electrical signals. Such chips could construct systems that will store information in the cloud, analyze enormous amounts of data, and think more like a brain than a standard computer. A development like this may be an important step toward commercializing the next generation of computing technology. Further to this step is the integration of silicon photonic chips with the computer processor in the same package, avoiding the need for transceiver assemblies. This allows for faster, cheaper and lower energy solution for computing, cloud and data centres. This design would improve the performance and power efficiency of the optical interconnects while reducing the cost of assembly. A vision of an optically connected 3-D supercomputer chip is shown in the scheme of Fig.8.1.

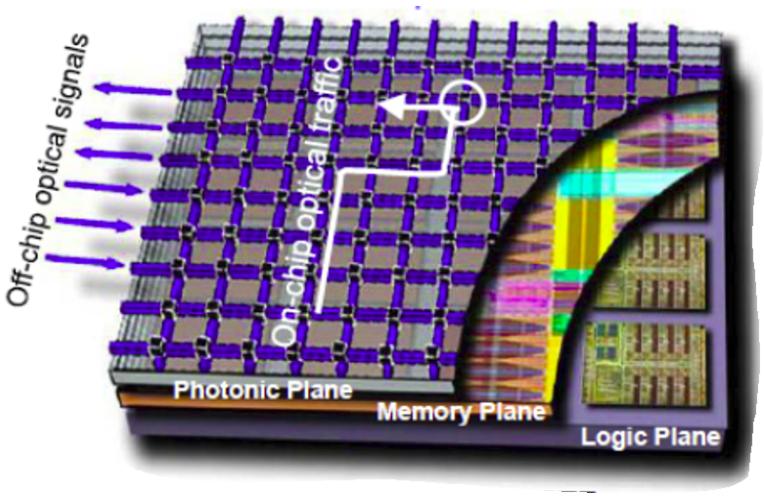

Figure 8.1: Optically connected 3-D supercomputer chip

This design shows that silicon photonics layer will be integrated with high performance logic and memory layers. Note here that photonic layer not only connects the multiple cores, but also routes the traffic of the data. In such schemes challenges arise because alignment tolerances are critical, typically in the sub-micron range, and optical interfaces are sensitive to debris and imperfections, thus requiring the best in packaging technology.

Based on the mentioned future chip scale applications our work can be extended to the study of more complicated optical schemes such as optical interconnects, receivers and transmitters. An interesting aspect of this work would be to study the bit-error rate of multiple pulse propagation in multiple optical channels. Such study can manifest the optimum parameters that determine an efficient pulse propagation in a wide range of applications such as super-computing, data centres etc. As the current work has revealed the optical properties and the potential pulse dynamics of silicon nanowires and silicon photonic crystals, it is more convenient for researchers to employ our recent developed theoretical model to novel applications.

A more technical alternative extension of this work is the formulation of a more compact C++ code which will be able to be embedded in commercial software in the field of photonics. In addition to that, it would be important to reform the current developed source code into a parallel code compatible with a message passing interface (MPI) system. This would facilitate the study and design of more complicated optical schemes such one shown in Fig.8.1. The interaction of optical pulses in advanced optical structures may reveals new optical phenomena which will have crucial influence in the forthcoming era of optical computer technology.

Appendix A

Mathematical formulation of the semi-analytical model

By taking the z-derivatives in Eqs. (5.1a)-(5.1e) and inserting Eq. (3.1), in which the first two terms in the RHS are neglected, into the resulting integrals, one obtain after some mathematical manipulations the following system of ordinary differential equations for the pulse parameters:

$$\frac{dE}{dz} = -2(\gamma)'' \int_{-\infty}^{\infty} |u|^4 dt - 4\int_{-\infty}^{\infty} |u|^2 (\gamma\tau_s u^* u_t)' dt - 2\int_{-\infty}^{\infty} |u|^2 (\gamma\tau_s u u_t^*)' dt, \quad \text{(A1a)}$$

$$\begin{aligned}\frac{d\tau}{dz} =& -\frac{\delta}{2\tau E^2}\frac{dE}{dz}\int_{-\infty}^{\infty}(t-T)^2|u|^2 dt - \frac{\delta}{2\tau E}\frac{dT}{dz}\int_{-\infty}^{\infty}(t-T)|u|^2 dt + \frac{\pi^2}{12}\delta\beta_2\frac{C}{\tau}\\ &+ \frac{\delta\beta_3}{2\tau E}\int_{-\infty}^{\infty}(t-T)|u_t|^2 dt - \frac{2\delta}{E\tau}\int_{-\infty}^{\infty}(t-T)^2|u|^2(\gamma\tau_s u^* u_t)' dt\\ &- \frac{\delta\gamma'}{\tau E}\int_{-\infty}^{\infty}(t-T)^2|u|^4 dt - \frac{\delta}{\tau E}\int_{-\infty}^{\infty}(t-T)^2|u|^2(\gamma\tau_s u u_t^*)' dt, \end{aligned} \quad \text{(A1b)}$$

$$\begin{aligned}\frac{dC}{dz} =& \frac{\delta\beta_2}{E}\int_{-\infty}^{\infty}|u_t|^2 dt + \frac{i\delta\beta_3}{4E}\int_{-\infty}^{\infty}(u_{tt}u_t^* - u_{tt}^* u_t)\, dt\\ &- \frac{2\delta}{E}\int_{-\infty}^{\infty}(t-T)|u|^2(\gamma u^* u_t)' dt - \frac{2\delta}{E}\int_{-\infty}^{\infty}(t-T)\left[\gamma\tau_s u_t^*\left(|u|^2 u\right)_t\right]'' dt\\ &- \frac{2\delta}{E}\int_{-\infty}^{\infty}|u|^2(\gamma\tau_s u^* u_t)'' dt - \frac{\delta}{E}\int_{-\infty}^{\infty}|u|^2(\gamma\tau_s u u_t^*)'' dt\\ &- \frac{i\delta}{2E^2}\frac{dE}{dz}\int_{-\infty}^{\infty}(t-T)(u^* u_t - u u_t^*)\, dt - \frac{i\delta}{2E}\frac{dT}{dz}\int_{-\infty}^{\infty}(u^* u_t - u u_t^*)\, dt, \end{aligned} \quad \text{(A1c)}$$

$$\begin{aligned}\frac{d\Omega}{dz} =& -\frac{i}{2E^2}\frac{dE}{dz}\int_{-\infty}^{\infty}(u^* u_t - u u_t^*)\, dt - \frac{2}{E}\int_{-\infty}^{\infty}(\gamma u^* u_t)'|u|^2 dt\\ &- \frac{4(\gamma\tau_s)''}{E}\int_{-\infty}^{\infty}|u u_t|^2 dt - \frac{2}{E}\int_{-\infty}^{\infty}\left[\gamma\tau_s(u u_t^*)^2\right]'' dt, \end{aligned} \quad \text{(A1d)}$$

$$\begin{aligned}\frac{dT}{dz} =& -\frac{1}{E^2}\frac{dE}{dz}\int_{-\infty}^{\infty}t|u|^2 dt + \beta_2\Omega + \frac{\beta_3}{2E}\int_{-\infty}^{\infty}|u_t|^2 dt - \frac{2\gamma'}{E}\int_{-\infty}^{\infty}t|u|^4 dt\\ &- \frac{4}{E}\int_{-\infty}^{\infty}t|u|^2(\gamma\tau_s u^* u_t)' dt - \frac{2}{E}\int_{-\infty}^{\infty}t|u|^2(\gamma\tau_s u u_t^*)' dt. \end{aligned} \quad \text{(A1e)}$$

This nonlinear system of equations depends on the specific pulse shape, $u(z,t)$. For hyperbolic secant pulses given by Eq. (5.2a) $\delta = 12/\pi^2$, so that this system reads,

$$\frac{dE}{dz} = -\frac{2\gamma' E^2}{3\tau} - \frac{2(\gamma\tau_s)''}{3}\frac{E^2\Omega}{\tau}, \quad \text{(A2a)}$$

$$\frac{d\tau}{dz} = (\beta_2 + \beta_3\Omega)\frac{C}{\tau} + \frac{(-6+\pi^2)}{3\pi^2}E(-\gamma'' - (\gamma\tau_s)''\Omega) - \frac{\tau}{2E}\frac{dE}{dz}, \tag{A2b}$$

$$\begin{aligned}\frac{dC}{dz} =& \beta_2\left(\frac{1}{\tau^2}\left(\frac{4}{\pi^2}+C^2\right)+\frac{12\Omega^2}{\pi^2}\right)+\beta_3\Omega\left(\frac{1}{\tau^2}\left(\frac{2}{\pi^2}+\frac{3C^2}{2}\right)+\frac{6\Omega^2}{\pi^2}\right)\\ &+\frac{EC}{3\tau}\left(-\frac{2(-6+\pi^2)}{\pi^2}\gamma''-\frac{-6+\pi^2}{3}(\gamma\tau_s)''\Omega\right)+\frac{E}{\tau\pi^2}\left(2\gamma'+\left(\frac{\pi^2+12}{3}\right)(\gamma\tau_s)'\Omega\right)\\ &-\frac{C}{E}\frac{dE}{dz}-\Omega\frac{dT}{dz}\end{aligned} \tag{A2c}$$

$$\frac{d\Omega}{dz} = \frac{E}{3\tau}\left(-2\gamma''\Omega + (\gamma\tau_s)'\frac{C}{\tau^2} + (\gamma\tau_s)''\left(-\frac{6}{5\tau^2} - 2\Omega^2 - \frac{-6+\pi^2}{6}\frac{C^2}{\tau^2}\right)\right) - \frac{\Omega}{E}\frac{dE}{dz}, \tag{A2d}$$

$$\begin{aligned}\frac{dT}{dz} =& \beta_2\Omega + \frac{\beta_3}{2}\left(\frac{1}{3\tau^2}+\Omega^2+\frac{\pi^2}{12}\frac{C^2}{\tau^2}\right)+\frac{E}{\tau}\left(-\frac{2}{3}\gamma''T+\frac{(\gamma\tau_s)'}{2}\right)\\ &+(\gamma\tau_s)''\frac{E}{\tau}\left(-\frac{2}{3}T\Omega-\frac{-6+\pi^2}{18}C\right)+\frac{T}{E}\frac{dE}{dz}\end{aligned} \tag{A2e}$$

whereas $\delta = 2$ in the case of Gaussian pulses given by Eq. (5.2b), so that (A1) becomes,

$$\frac{dE}{dz} = -\sqrt{\frac{\pi}{2}}\frac{\gamma''E^2}{\pi\tau} - \frac{(\gamma\tau_s)''E^2\Omega}{\pi\tau}, \tag{A3a}$$

$$\frac{d\tau}{dz} = (\beta_2 + \frac{\beta_3\Omega}{\sqrt{2}})\frac{C}{\tau} + \frac{E}{4\sqrt{2\pi}}(-\gamma'' - (\gamma\tau_s)''\Omega) - \frac{1}{2\sqrt{2}}\frac{\tau}{E}\frac{dE}{dz}, \tag{A3b}$$

$$\begin{aligned}\frac{dC}{dz} =& \frac{\beta_2}{\sqrt{2}}\left(\frac{1}{\tau^2}\left(1+C^2\right)+2\Omega^2\right)+\beta_3\Omega\left(\frac{1}{2\tau^2}\left(1+3C^2+\right)+\frac{\Omega^2}{\sqrt{2}}\right)\\ &+\sqrt{\frac{\pi}{2}}\frac{EC}{\tau}\left(-\frac{\gamma''}{\sqrt{2\pi}}-\frac{(\gamma\tau_s)''}{\pi}\Omega\right)+\sqrt{\frac{\pi}{2}}\frac{E}{\tau}\left(\frac{\gamma'}{\sqrt{2\pi}}+\frac{3}{\pi}(\gamma\tau_s)'\Omega\right)\\ &-\frac{C}{E}\frac{dE}{dz}-\sqrt{2}\Omega\frac{dT}{dz},\end{aligned} \tag{A3c}$$

$$\frac{d\Omega}{dz} = \frac{1}{\sqrt{2\pi}}\frac{E}{\tau}\left(-\gamma''\Omega + \frac{(\gamma\tau_s)'}{2}\frac{C}{\tau^2} + (\gamma\tau_s)''\left(-\frac{3}{4\tau^2} - \Omega^2 - \frac{1}{4}\frac{C^2}{\tau^2}\right)\right) - \frac{1}{\sqrt{2}}\frac{\Omega}{E}\frac{dE}{dz}, \tag{A3d}$$

$$\begin{aligned}\frac{dT}{dz} =& \beta_2\Omega + \frac{\beta_3}{2\sqrt{2}}\left(\frac{1}{2\tau^2}+\Omega^2+\frac{1}{2}\frac{C^2}{\tau^2}\right)+\frac{1}{\sqrt{2\pi}}\frac{E}{\tau}\left(-\gamma''T+\frac{3(\gamma\tau_s)'}{4}\right)\\ &+\frac{(\gamma\tau_s)''}{\sqrt{2\pi}}\frac{E}{\tau}\left(-T\Omega-\frac{C}{4}\right)-\frac{1}{\sqrt{2}}\frac{T}{E}\frac{dE}{dz}\end{aligned} \tag{A3e}$$

Appendix B

Derivation of the averaged model

The spatial scale over which the envelope of picosecond pulses varies is much larger than the lattice constant of the PhC and therefore for such optical pulses one can simplify the system of equations governing the pulse interaction, i.e. Eqs. (7.37) and Eq. (7.38), by taking the average over one lattice constant. Under these conditions, the corresponding system of coupled equations can be cast in the following form:

$$i\left(\frac{\partial A_p}{\partial z}+\frac{1}{v_{g,p}}\frac{\partial A_p}{\partial t}\right)-\frac{\bar{\beta}_{2,p}}{2}\frac{\partial^2 A_p}{\partial t^2}+\frac{\omega_p\delta n_{\rm fc}\tilde{\kappa}_p}{nv_{g,p}}A_p+\frac{ic\tilde{\kappa}_p}{2nv_{g,p}}(\alpha_{\rm fc}+\alpha_{\rm in})A_p$$
$$+2e^{i\Delta\bar{\beta}z}\tilde{\gamma}_{psi}A_sA_iA_p^*+\left(\tilde{\gamma}_p|A_p|^2+2\tilde{\gamma}_{ps}|A_s|^2+2\tilde{\gamma}_{pi}|A_i|^2\right)A_p=0, \tag{B1a}$$

$$i\left(\frac{\partial A_s}{\partial z}+\frac{1}{v_{g,s}}\frac{\partial A_s}{\partial t}\right)-\frac{\bar{\beta}_{2,s}}{2}\frac{\partial^2 A_s}{\partial t^2}+\frac{\omega_s\delta n_{\rm fc}\tilde{\kappa}_s}{nv_{g,s}}A_s+\frac{ic\tilde{\kappa}_s}{2nv_{g,s}}(\alpha_{\rm fc}+\alpha_{\rm in})A_s$$
$$+e^{-i\Delta\bar{\beta}z}\tilde{\gamma}_{spi}A_p^2A_i^*+\left(\tilde{\gamma}_s|A_s|^2+2\tilde{\gamma}_{sp}|A_p|^2+2\tilde{\gamma}_{si}|A_i|^2\right)A_s=0, \tag{B1b}$$

$$i\left(\frac{\partial A_i}{\partial z}+\frac{1}{v_{g,i}}\frac{\partial A_i}{\partial t}\right)-\frac{\bar{\beta}_{2,i}}{2}\frac{\partial^2 A_i}{\partial t^2}+\frac{\omega_i\delta n_{\rm fc}\tilde{\kappa}_i}{nv_{g,i}}A_i+\frac{ic\tilde{\kappa}_i}{2nv_{g,i}}(\alpha_{\rm fc}+\alpha_{\rm in})A_i$$
$$+e^{-i\Delta\bar{\beta}z}\tilde{\gamma}_{ips}A_p^2A_s^*+\left(\tilde{\gamma}_i|A_i|^2+2\tilde{\gamma}_{ip}|A_p|^2+2\tilde{\gamma}_{is}|A_s|^2\right)A_i=0, \tag{B1c}$$

$$\frac{\partial N}{\partial t}=-\frac{N}{\tau_c}+\frac{1}{\hbar}\Bigg\{\sum_{\mu=p,s,i}\left[\frac{\Upsilon''_\mu}{\omega_\mu}|A_\mu|^4+\sum_{\substack{\nu=p,s,i\\ \nu\neq\mu}}\frac{4\Upsilon''_{\mu\nu}}{\omega_\mu+\omega_\nu}|A_\mu|^2|A_\nu|^2\right]$$
$$+\frac{1}{\omega_p}\Im\mathrm{m}\left[2\Upsilon_{psi}\times A_p^{*2}A_sA_ie^{i\Delta\bar{\beta}z}+(\Upsilon_{spi}+\Upsilon_{ips})A_p^2A_s^*A_i^*e^{-i\Delta\bar{\beta}z}\right]\Bigg\}. \tag{B2}$$

The coefficients of the linear and nonlinear terms in these equations are given by the following formulae:

$$\tilde{\kappa}_\mu=\frac{\varepsilon_0 n^2}{2\bar{W}_\mu}\int_{V_{\rm nl}}|\mathbf{e}_\mu(\omega_\mu)|^2dV, \tag{B3a}$$

$$\tilde{\gamma}_\mu=\frac{3\omega_\mu\varepsilon_0 a}{16v_{g,\mu}^2}\frac{1}{\bar{W}_\mu^2}\int_{V_{\rm nl}}\mathbf{e}_\mu^*(\omega_\mu)$$
$$\cdot\hat{\chi}^{(3)}(\omega_\mu,-\omega_\mu,\omega_\mu)\vdots\mathbf{e}_\mu(\omega_\mu)\mathbf{e}_\mu^*(\omega_\mu)\mathbf{e}_\mu(\omega_\mu)dV, \tag{B3b}$$

$$\tilde{\gamma}_{\mu\nu} = \frac{3\omega_\mu \varepsilon_0 a}{16 v_{g,\mu} v_{g,\nu}} \frac{1}{\bar{W}_\mu \bar{W}_\nu} \int_{V_{\rm nl}} \mathbf{e}_\mu^*(\omega_\mu)$$
$$\cdot \hat{\chi}^{(3)}(\omega_\nu, -\omega_\nu, \omega_\mu) \vdots \mathbf{e}_\nu(\omega_\nu) \mathbf{e}_\nu^*(\omega_\nu) \mathbf{e}_\mu(\omega_\mu) dV, \tag{B3c}$$
$$\tilde{\gamma}_{psi} = \frac{3\omega_p \varepsilon_0 a}{16 v_{g,p} (v_{g,s} v_{g,i})^{\frac{1}{2}}} \frac{1}{\bar{W}_p (\bar{W}_s \bar{W}_i)^{\frac{1}{2}}}$$
$$\times \int_{V_{\rm nl}} \mathbf{e}_p^*(\omega_p) \cdot \hat{\chi}^{(3)}(\omega_s, -\omega_p, \omega_i) \vdots \mathbf{e}_s(\omega_s) \mathbf{e}_p^*(\omega_p) \mathbf{e}_i(\omega_i) dV, \tag{B3d}$$
$$\tilde{\gamma}_{spi} = \frac{3\omega_s \varepsilon_0 a}{16 v_{g,p} (v_{g,s} v_{g,i})^{\frac{1}{2}}} \frac{1}{\bar{W}_p (\bar{W}_s \bar{W}_i)^{\frac{1}{2}}}$$
$$\times \int_{V_{\rm nl}} \mathbf{e}_s^*(\omega_s) \cdot \hat{\chi}^{(3)}(\omega_p, -\omega_i, \omega_p) \vdots \mathbf{e}_p(\omega_p) \mathbf{e}_i^*(\omega_i) \mathbf{e}_p(\omega_p) dV, \tag{B3e}$$
$$\tilde{\gamma}_{ips} = \frac{3\omega_i \varepsilon_0 a}{16 v_{g,p} (v_{g,s} v_{g,i})^{\frac{1}{2}}} \frac{1}{\bar{W}_p (\bar{W}_s \bar{W}_i)^{\frac{1}{2}}}$$
$$\times \int_{V_{\rm nl}} \mathbf{e}_i^*(\omega_i) \cdot \hat{\chi}^{(3)}(\omega_p, -\omega_s, \omega_p) \vdots \mathbf{e}_p(\omega_p) \mathbf{e}_s^*(\omega_s) \mathbf{e}_p(\omega_p) dV, \tag{B3f}$$
$$\Upsilon_{\varpi} = \frac{1}{a} \int_{z_0}^{z_0+a} \frac{\gamma_{\varpi}(z)}{A_{\rm nl}(z)} dz. \tag{B3g}$$

where $V_{\rm nl}$ is the volume occupied by silicon in a unit cell of the PhC waveguide and z_0 an arbitrary distance. Finally, $A_{\rm nl}(z)$ in Eq. (B3g) is given by Eq. (7.41), whereas the index ϖ takes any of the following values: p, s, i, ps, si, ip, psi, spi, or ips.whereas the index ϖ takes any of the following values: p, s, i, ps, si, ip, psi, spi, and ips. Note that in deriving the averaged equations governing the pulse and FC dynamics, Eqs. (B1) and Eq. (B2), we have assumed that the FWM process is nearly phase-matched, namely $\Delta\bar{\beta} \ll 1/a$. In other words, the phase of the exponential factors in these equations vary much slower with the distance, z, as compared to the variation of the dielectric constant of the PhC waveguide.

A comparison between the predictions of the full and averaged models is illustrated in Fig. B.2. Thus, we have considered the slow-light pulse dynamics presented in Fig. 7.10 and determined the pulse evolution using both the full and averaged models. As it can be seen, both models predict a similar pulse dynamics for the entire propagation length, $z = 1000a$. This result is expected as the envelope of picosecond pulses, as are those chosen in our simulations, spans a large number of unit cells and therefore the pulse amplitude is only slightly affected by the local inhomogeneity of the index of refraction.

The fast variation with z of the pulse envelope is shown in Fig. B.2(g), where we

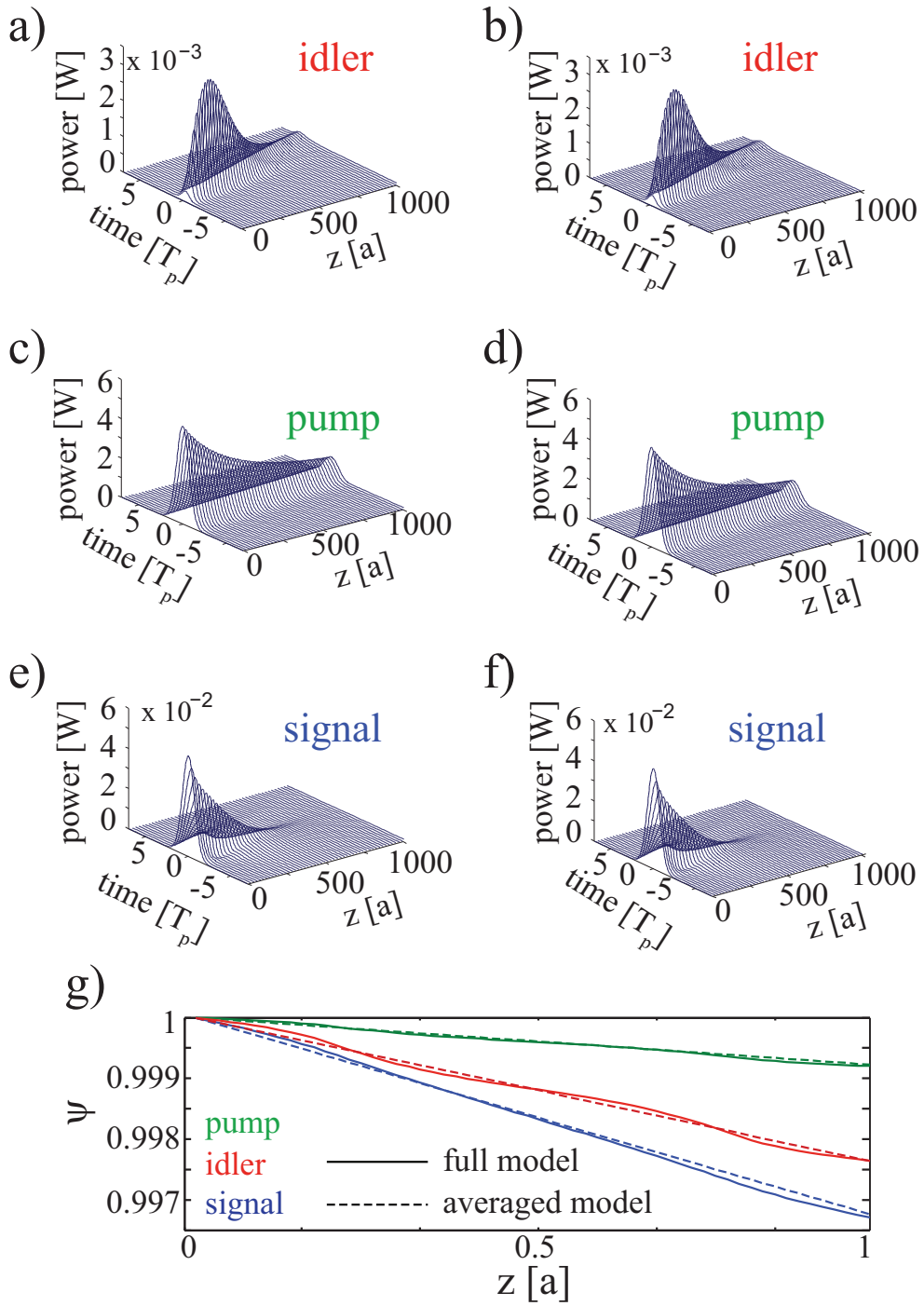

Figure B.2: Comparison between pulse evolution as described by the full and averaged model is presented in the left and right panels, respectively. The group-index of the pulses are $n_{g,i} = 20.3$, $n_{g,p} = 8.69$, and $n_{g,s} = 23.3$ and correspond to the slow-light propagation scenario presented in Fig. 7.10. The bottom panel shows the z-dependence of the normalized pulse amplitude, $\Psi_\mu(z) = A_\mu(z_0+z)/A_\mu(z_0)$, $\mu = p,s,i$, calculated for the unit cell starting at $z_0 = 200a$.

plot the z-dependence of the normalized pulse amplitude, $\Psi_\mu(z) = A_\mu(z_0+z)/A_\mu(z_0)$, $\mu = p,s,i$, calculated for the unit cell starting at $z_0 = 200a$. It can be seen in this figure

that the pulse envelope varies at a spatial scale commensurable with the lattice constant yet the amplitude of these variations is much smaller than the pulse peak amplitude. The magnitude of these variations, however, would comparatively become more significant should the pulse duration would be brought to the femtosecond range.